



**HAL**  
open science

## Interaction between synaptic and structural plasticity

Côme Camus

► **To cite this version:**

Côme Camus. Interaction between synaptic and structural plasticity. Neuroscience. Université de Bordeaux, 2021. English. NNT: 2021BORD0178 . tel-03360539

**HAL Id: tel-03360539**

**<https://theses.hal.science/tel-03360539v1>**

Submitted on 30 Sep 2021

**HAL** is a multi-disciplinary open access archive for the deposit and dissemination of scientific research documents, whether they are published or not. The documents may come from teaching and research institutions in France or abroad, or from public or private research centers.

L'archive ouverte pluridisciplinaire **HAL**, est destinée au dépôt et à la diffusion de documents scientifiques de niveau recherche, publiés ou non, émanant des établissements d'enseignement et de recherche français ou étrangers, des laboratoires publics ou privés.

THÈSE PRÉSENTÉE  
POUR OBTENIR LE GRADE DE

**DOCTEUR DE L'UNIVERSITÉ DE BORDEAUX**

ÉCOLE DOCTORALE DES SCIENCES DE LA VIE ET DE LA SANTÉ  
SPÉCIALITÉ NEUROSCIENCES

Par Côme CAMUS

**Interaction entre plasticité synaptique  
et plasticité structurale**

Sous la direction de : Eric HOSY

Soutenue le 9 juillet 2021

Membres du jury :

Erwan BEZARD	Directeur de Recherche INSERM	Président
Maria PASSAFARO	Directrice de Recherche CNR	Rapporteur
Harold MACGILLAVRY	Professeur Assistant Utrecht University	Rapporteur
Fekrije SELIMI	Directrice de Recherche CNRS	Examineur
Simon WIEGERT	Professeur Hamburg Universität	Examineur

**Institut Interdisciplinaire de Neurosciences (IINS)**  
CNRS UMR 5297

Université de Bordeaux  
Centre Broca Nouvelle-Aquitaine  
146 Rue Léo Saignat  
33076 Bordeaux (France)

## Résumé

Le cerveau est un réseau complexe de neurones interconnectés, responsable de toutes nos fonctions cognitives et de nos comportements. Les neurones reçoivent des signaux au niveau de zones spécialisées appelées synapses, qui convertissent un signal électrique, dit « tout ou rien », en un signal chimique, par la libération de neurotransmetteurs, qui sera retransformé en un signal électrique par les récepteurs aux neurotransmetteurs. Cependant, un seul neurone reçoit des milliers d'entrées provenant de plusieurs neurones en fonction de l'espace et du temps. Le mécanisme précis par lequel les neurones reçoivent, intègrent et transmettent ces entrées synaptiques est très complexe et n'est pas encore parfaitement compris.

Au niveau des synapses excitatrices, les récepteurs AMPA (AMPA) sont responsables de la majorité de la transmission synaptique rapide. Ils ne sont pas distribués au hasard dans les synapses mais sont organisés en nanodomains de ~80 nm de diamètre contenant ~20 récepteurs. Ce contenu va déterminer l'intensité de la réponse synaptique. En raison de leur affinité de l'ordre du mM pour le glutamate, les AMPAR ne peuvent être activés que lorsqu'ils sont situés dans une zone de ~150 nm autour du site de libération du glutamate. De plus, il a été démontré que les nanodomains font face aux sites de libération du glutamate formant des nanocolonnes trans-synaptiques. Ainsi, l'organisation à l'échelle nanométrique des AMPARs par rapport aux sites de libération semble être un paramètre clef pour l'efficacité de la transmission synaptique.

L'objectif global de ma thèse a été de déterminer l'influence de cette organisation à l'échelle nanométrique sur les propriétés intimes de la transmission synaptique à l'état basal et pendant la plasticité.

Nous avons d'abord étudié comment les AMPAR sont co-organisés avec d'autres types de récepteurs du glutamate : NMDARs et mGluRs. Nous avons également montré que cette organisation fine a un impact sur le profil d'activation des récepteurs et donc sur la régulation de la physiologie synaptique. Ce travail a complété la nouvelle vision du rôle de la nano-organisation dans la transmission synaptique à l'état basal. Ensuite, j'ai étudié comment cette nano-organisation permet aux neurones d'adapter leur communication. En effet, les synapses peuvent moduler leur force par la plasticité synaptique à long terme. Par exemple, la dépression à long terme (LTD) correspond à un affaiblissement de la force synaptique et serait importante dans certains processus cognitifs et la flexibilité comportementale. Suite à de précédentes découvertes sur l'impact de la nano-organisation dynamique des AMPAR aux synapses sur la régulation de la force et de la fiabilité de la transmission synaptique, j'ai étudié leur rôle dans la dépression synaptique. Grâce à ce projet, nous avons démontré que le contenu des nanodomains chute rapidement et que cette déplétion dure plusieurs minutes à plusieurs heures. La phase initiale semble être due à une augmentation des événements d'endocytose, mais dans une seconde phase, la mobilité des AMPAR est augmentée suite à une réorganisation de la densité post-synaptique. Ce changement de mobilité permet aux synapses déprimées de maintenir leur capacité à répondre aux stimulations à haute fréquence. Ainsi, nous proposons que l'augmentation de la mobilité des AMPAR induite par la LTD permet de conduire une réponse fiable dans les synapses sous stimulation haute fréquence et donc de les maintenir sélectivement, tout en éliminant celles qui sont inactives. Pour confirmer cela, j'ai étudié comment l'évolution de la nano-organisation synaptique régule

l'élimination synaptique, appelée élagage synaptique, en modulant la relation LTD-élagage synaptique. Finalement, nous avons montré que l'isolement dans le temps et l'espace d'une synapse favorise son élagage suite à des remaniements moléculaires spécifiques induits par la LTD.

**Mots clés** : transmission synaptique, récepteurs AMPA, PSD-95, organisation synaptique, plasticité synaptique, plasticité structurelle.

## Abstract

The brain is a complex network of interconnected neurons responsible for all our cognitive functions and behaviors. Neurons receive inputs at specialized contact zones named synapses which convert an all or none electrical signal to a chemical one, through the release of neurotransmitters. This chemical signal is then turned back in a tunable electrical signal by receptors to neurotransmitters. However, a single neuron receives thousands of inputs coming from several neurons in a spatial- and temporal-dependent manner. The precise mechanism by which neurons receive, integrate and transmit these synaptic inputs is highly complex and is still not perfectly understood.

At excitatory synapses, AMPA receptors (AMPA receptors) are responsible for the fast synaptic transmission. With the recent developments in super-resolution microscopy, the community has changed its vision of synaptic transmission. One breakthrough was the discovery that AMPARs are not randomly distributed at synapses but are organized in nanodomains of ~80 nm of diameter containing ~20 receptors. This content is an important factor since it will determine the intensity of the synaptic response. Due to their mM affinity for glutamate, AMPARs can only be activated when located in an area of ~150 nm in front of the neurotransmitter release site. Moreover, AMPAR nanodomains have been shown to be located in front of glutamate release sites and to form trans-synaptic nanocolumns. Thus, the nanoscale organization of AMPARs regarding release sites seems to be a key parameter for the efficiency of synaptic transmission.

The overall aim of my PhD has been to determine the influence of this nanoscale organization on the intimate properties of synaptic transmission both at basal state and during plasticity.

First, we studied how AMPARs are co-organized with other types of glutamate receptors: NMDARs and mGluRs. We showed as well that this fine organization impacts the profile of activation of receptors and therefore regulate synaptic physiology. This work completed our new vision of the role of nano-organization in the synaptic transmission at the basal state. Then, I studied how this nano-organization enables neurons to adapt their communication. Indeed, synapses can modulate their strength through long-term synaptic plasticity. As an example, Long-Term Depression (LTD) corresponds to a long-lasting weakening of synaptic strength and is thought to be important in some cognitive processes and behavioral flexibility through synapse selective elimination. Following previous discoveries about the impact of AMPAR dynamic nano-organization at synapses on the regulation of the synaptic transmission strength and reliability, I decided to investigate their role in the weakening of synapses. Through this project, we demonstrated that AMPAR nanodomain content drops down rapidly and this depletion lasts several minutes to hours. The initial phase seems to be due to an increase of endocytosis events, but in a second phase, AMPAR mobility is increased following a reorganization of the post-synaptic density. This change in mobility allows depressed synapses to maintain their capacity to answer to high-frequency inputs. Thus, we propose that LTD-induced increase in AMPAR mobility allows to conduct a reliable response in synapses under high-frequency stimulation and thus to selectively maintain them while eliminating the inactive ones. To confirm this, I investigated how evolution of synaptic nano-organization regulates the synaptic elimination, called synaptic pruning, by modulating the relationship LTD-pruning.

Finally, we showed that the isolation in time and space of a synapse favors its pruning following specific molecular reshufflings induced by LTD.

**Keywords:** synaptic transmission, AMPA receptors, PSD-95, synaptic organization, synaptic plasticity, structural plasticity

## Remerciements

Je tiens en premier lieu à remercier l'ensemble des membres de mon jury de thèse pour le temps consacré à évaluer mon travail de thèse.

Je souhaiterais particulièrement remercier mon directeur de thèse, Eric Hosy. A tes côtés, j'ai bien changé depuis le jeune stagiaire que tu épatais en lui expliquant que les récepteurs à la synapse pouvaient bouger et qu'on pouvait les suivre en direct ! Cette thèse aura été une aventure tant scientifique qu'humaine et je suis très heureux que tu aies été à mes côtés. Je te remercie énormément pour ta bienveillance, ton ouverture d'esprit et ta volonté d'adapter ton encadrement à chaque personne ! Un grand merci pour tous les moments scientifiques et personnels partagés !

Je voudrais également exprimer toute ma reconnaissance à Daniel Choquet pour m'avoir accueilli au sein de son équipe de recherche. Merci pour la confiance et l'ouverture dont tu fais preuve pour que les gens de ton équipe puissent travailler dans les meilleures conditions possibles et se sentent bien.

Un grand merci à toute l'équipe ! En particulier, merci à Anna, Matthieu, Françoise, Christelle et Sophie pour leur présence et les discussions toujours enrichissantes !

Merci également à Frédéric Gambino pour sa disponibilité sans faille et ses conseils ! Merci aussi à Mathieu Letellier, mon voisin d'électrophysio, pour son soutien dans les jours de mauvaises manips !

Et que serait le labo sans Rémi, Jordan et Emeline ? Merci beaucoup à vous trois pour votre travail incroyable et votre gentillesse !

Je voudrais aussi remercier des personnes qui sont bien plus que des collègues de labo. Un très grand merci à Julia, Natacha, les Mélanies et Nicolas pour votre présence et votre écoute amicale ! Sans vous, ma vie de labo aurait été bien moins sympa !

Un énorme merci aussi à Benjamin et Tiago ! Vous avez été mes deux mentors pendant mes stages de master et même après, chacun dans son style !

Un immense merci aux personnes avec qui j'ai partagé mon bureau, mes cafés, mes embûches, mes joies, et j'en passe ! Hanna, Konstantina et Matthieu merci pour votre bonne humeur et la bonne ambiance que vous mettez, ne changez rien !

Je voudrais aussi prendre le temps de remercier Marie-Edith Lafon et Thomas Bienvenu, sans qui je n'aurais jamais eu l'idée de faire une thèse. Merci du fond du cœur pour vos conseils et votre bienveillance !

Un très, très grand merci à mes frères et sœur : Virginie, Nicolas, Grégoire, Vivien et Albin ! Merci d'être toujours au rendez-vous quand j'ai besoin de vous, et merci pour ces moments de rires et de bonne humeur qui me sont si précieux !

Enfin, je souhaiterais remercier des personnes qui m'accompagnent (et me supportent) depuis toujours. Merci à vous, Maman et Papa, pour votre soutien et votre présence indéfectible depuis tant d'années ! C'est grâce à vous que j'en suis là, et je vous remercie du fond du cœur pour les valeurs humaines et de travail que vous



m'avez transmises ! Et un gigantesque merci à toi, Maman, pour tes petits plats qui n'ont de petits que le nom !

« L'infini en petitesse est bien moins visible. [...] On se croit naturellement bien plus capable d'arriver au centre des choses que d'embrasser leur circonférence. L'étendue visible du monde nous surpasse visiblement ; mais comme c'est nous qui surpassons les petites choses, nous nous croyons plus capables de les posséder, et cependant il ne faut pas moins de capacité pour aller jusqu'au néant que jusqu'au tout ; il la faut infinie pour l'un et l'autre ; et il me semble que qui aurait compris les derniers principes des choses pourrait aussi arriver jusqu'à connaître l'infini »

Blaise Pascal, *Pensées*

## Abbreviations

ABP: AMPAR Binding Protein

AMPA:  $\alpha$ -Amino-3-hydroxy-5-Methyl-isoxazole-Propionic Acid Receptor

AP: Action Potential

AP2: Adaptor Protein 2

ATP: Adenosine TriPhosphate

AZ: Active Zone

Ca<sup>2+</sup>: Calcium

CaMKII: Ca<sup>2+</sup>/Calmodulin-dependent protein Kinase II

CNS: Central Nervous System

CP-AMPA: Calcium-Permeable AMPA

CTD: C-Terminal Domain

DIV: Day In Vitro

d-STORM: direct-Stochastic Optical Reconstruction Microscopy

EC<sub>50</sub>: half maximal Effective Concentration

EM: Electron Microscopy

EPSC: Excitatory Post-Synaptic Current

fEPSP: field-Excitatory Post-Synaptic Potential

GABA:  $\gamma$ -Amino-Butyric Acid

GKAP: Guanylate-Kinase-Associated Protein

GRIP: Glutamate Receptor Interacting Protein

GSK3: Glycogen Synthase Kinase-3

iGluRs: ionotropic Glutamate Receptors

IPSC: Inhibitory Post-Synaptic Current

KAR: Kainate Receptor

LBD: Ligand-Binding Domain

LTD: Long-Term Depression

LTP: Long-Term Potentiation

MAGUK: Membrane-Associated Guanylate Kinase

mEPSC: miniature Excitatory Post-Synaptic Current

mGluR: metabotropic Glutamate Receptor

NMDAR: N-Methyl-D-Aspartate Receptor

NSF: N-ethylmaleimide-Sensitive Factor

NTD: N-Terminal Domain

P2XR: Purinergic P2X Receptor

PALM: Photo-Activated Localization Microscopy

PICK1: Protein Interacting with C Kinase 1

PKC: Protein Kinase C

PLC: PhosphoLipase C

Pr: release probability

PP1: Protein Phosphatase 1

PP2B: Protein Phosphatase 2B or Calcineurin

PPD: Paired-Pulse Depression

PSD: Post-Synaptic Density

Q: Quantum of response

QD: Quantum Dot

RIM: Rab3-Interacting Molecule

RIM-BP: RIM-Binding Protein

SMLM: Single Molecule Localization Microscopy

SNARE: Soluble N-ethylmaleimide-sensitive-factor Attachment protein Receptor

SPT: Single-Particle Tracking

STED: Stimulated-Emission Depletion microscopy

STF: Short-Term Facilitation

STD: Short-Term Depression

STDP: Spike Timing-Dependent Plasticity

STP: Short-Term Plasticity

TARP: Transmembrane AMPAR Regulatory Protein

TMD: Trans-Membrane Domain

u-PAINT: universal-Point Accumulation for Imaging in Nanoscale Topography

VGCC: Voltage-Gated Calcium Channel

# Table of contents

Résumé.....	3
Abstract.....	5
Remerciements.....	7
Abbreviations.....	10
Table of contents.....	13
<b>INTRODUCTION.....</b>	<b>15</b>
<b>Chapter 1: The excitatory synaptic transmission.....</b>	<b>16</b>
1. The synapse.....	19
2. The post-synapse.....	21
a. Glutamate receptors.....	21
b. AMPAR structure.....	23
c. Regulation and function of PSD-95.....	25
d. Assembly and macromolecular complex.....	29
e. AMPAR-mediated currents.....	33
3. Synaptic input integration.....	36
4. Short-term plasticity.....	42
a. Pre-synaptic origins of STP.....	43
b. Post-synaptic contribution to STD.....	43
5. AMPAR dynamic.....	45
<b>Chapter 2: Regulation of synaptic inputs.....</b>	<b>50</b>
1. Synaptic plasticity.....	51
2. Long Term Potentiation.....	54
3. Long Term Depression.....	56
a. Input-specific LTD.....	58
b. Neuromodulator-induced LTD.....	60
<b>Chapter 3: Regulation of synaptic structure.....</b>	<b>62</b>
1. Spines' type and morphology.....	62
2. Structural plasticity.....	65
3. Synaptic pruning.....	66
Thesis problematic.....	71
<b>MATERIAL AND METHODS.....</b>	<b>74</b>
1. Primary hippocampal neurons culture.....	75
2. Transfections.....	76
3. Electrophysiology.....	76
a. Whole-cell patch clamp on cultured neurons.....	77
b. Acute slice electrophysiology.....	79
	13

4. Immunolabeling .....	80
5. LTD induction.....	81
6. Single Molecule Localization Microscopy.....	82
a. Principle of fluorescence microscopy .....	82
b. Diffraction limit & resolution in fluorescent microscopy.....	84
c. Principle of SMLM .....	84
d. Resolution in SMLM .....	86
7. direct - Stochastic Optical Reconstruction Microscopy .....	88
a. d-STORM general principle .....	88
b. d-STORM application .....	89
c. Imaging solution for d-STORM .....	90
d. Analysis and quantification .....	91
8. Single-Particle Tracking .....	92
a. General principle of stochastic labelling methods.....	92
b. u-PAINT application.....	94
9. Confocal imaging .....	95
a. Principles of confocal imaging .....	95
b. Application of confocal imaging .....	96
c. Synaptotagmin-1 uptake measurement.....	97

## **RESULTS .....** 99

Chapter 1 - Nanoscale co-organization and coactivation of AMPAR, NMDAR, and mGluR ..... 100

Chapter 2 - NMDAR-dependent long-term depression is associated with increased short-term plasticity through autophagy mediated loss of PSD-95..... 123

Chapter 3 - Synaptic pruning following NMDAR-dependent LTD preferentially affects isolated PSD-95-depleted synapses ..... 159

## **CONCLUSION AND PERSPECTIVES.....** 182

## **BIBLIOGRAPHY.....** 190

## **INTRODUCTION**



## Chapter 1: The excitatory synaptic transmission

The brain is a highly complex organ composed of ~100 billion neurons, each one connected and communicating to thousands of neuronal partners. The fundamental building block of neuron-to-neuron communication is the synapse, a micrometer size organelle, where the membranes of two cells come in close apposition to favor information transfer. Our deep understanding of this structure, named for the first time in 1897 by Foster and Sherrington, has evolved in parallel with the development of new technologies. Most of the main conceptual advances in our understanding of synaptic organization and function have originated from new imaging developments. Based on the new silver staining developed by Camillo Golgi, Cajal demonstrated that nerve cells are not continuous but contiguous, invalidating the cable theory of the nervous system. At the same time, he introduced the notion that a synapse is composed of three independent compartments: the pre-synapse, the post-synapse, and the space between them: the synaptic cleft. This organization remained hypothetical until the first precise image of a synapse was obtained in parallel in the 1950s by two laboratories using electron microscopy (De Robertis and Bennett, 1955; Palay and Palade, 1955). The first image of a synapse revealed an asymmetric organization, with one compartment enriched in ~50 nm sized vesicles (De Robertis and Bennett, 1954, 1955). This discovery and the demonstration one year later that these vesicles contained neurotransmitters (Palay, 1956), coupled to Katz's electrophysiological recordings of unitary postsynaptic voltage changes, established most of the basis for our current knowledge of the mechanisms of synaptic transmission (Castillo and Katz, 1954; Fatt and Katz, 1951). The pre-synapse releases a "quantum" of neurotransmitters in the synaptic cleft due to discrete vesicle fusion,

triggering a reproducible postsynaptic current. Despite the large number of newly available techniques, our present vision of the synapse is not very different from the one described by Palay, even though the invention of the patch-clamp technique offered a more robust way to measure synaptic currents (Hamill et al., 1981) and the revolution in genomics and proteomics allowed to allocate proteins, their interactions, and structures, into the various synaptic compartments. From the cloning of the first glutamate receptor in 1994 and the identification of PSD-95 as the main scaffold element of the postsynaptic density (Cho et al., 1992; Hunt et al., 1996; Kornau et al., 1995), to the extensive proteomic characterization of synaptic elements (Grant, 2013), it is probably safe to say that by now, most protein constituents of the synapse have been identified. However, we still do not fully understand how synapses work and many shadow zones remain.

An important misconception in shaping our original understanding of synaptic transmission was the omission of dynamic regulation at various levels. Indeed, since 1973 and the discovery of the concept of synaptic plasticity by Bliss and Lomo, new dynamic levels of regulation of synaptic transmission have regularly been identified. From this moment, synaptic transmission is accepted as a dynamic mechanism, which can be modified through plastic events on both short and long terms to adapt the synaptic transmission to various types of received inputs (Bliss and Lømo, 1973; Dudek and Bear, 1992; Nicholls et al., 2008). Later on, the first use of single-particle tracking, the precursor of super-resolution microscopy, revealed the individual dynamic of post-synaptic proteins, notably AMPA-type glutamate receptors (Borgdorff and Choquet, 2002; Choquet and Triller, 2013; Tardin et al., 2003). The application of the revolutionary single-particle and single-molecule-tracking approaches has granted access to understanding the behavior of single proteins. After a series of first steps

based on imaging latex beads, then organic dyes and semiconductor quantum dots, the last decade has seen a large development of super-resolution imaging techniques largely based on massively increasing the throughput of single-molecule detection assays, offering a new vision of synapse organization.

To conclude, comprehension of the synapse structure and function is intimately related to methodological improvements, from first staining techniques to the revolution of super-resolution microscopy.

In the coming chapters, I will first present the current knowledge about excitatory synapses. I will start by introducing its structure and different components, and then how they contribute to the function of the synapse.

## 1. The synapse

The excitatory synapse is formed by the association of a pre-synaptic axonal bouton with glutamate-containing vesicles, in front of a post-synaptic protrusion named dendritic spine. Pre- and post-synaptic membranes are separated by a ~20 nm synaptic cleft. At this contact zone, the pre-synapse organizes a specialized area in the regulation of the neurotransmitter vesicular release named Active Zone (AZ). AZ faces the Post-Synaptic Density (PSD), an area enriched in various proteins, rendering it electron-dense as seen by electron microscopy (EM) (Harris and Weinberg, 2012) (Figure 1). The pre-to-post-synaptic association is stabilized through interaction of several adhesion proteins. A major protein implicated in this phenomenon is the pre-synaptic protein Neurexin, as again showed very recently (Fukata et al., 2021). It can bind with the post-synaptic protein Neuroligin forming a trans-synaptic complex, and this interaction is, in instance, tightly regulated by MDGA (Elegheert et al., 2017; Südhof, 2017; Moretto et al., 2019; Wu et al., 2019). In 2009, two major papers showed as well the importance of the interaction between LRRTM2 and Neurexin in the formation and further stabilization of the synapse (Ko et al., 2009; de Wit et al., 2009). Briefly, these molecular examples show that the rigidity of apposition between pre and post synapses is highly regulated and I will show later that it crucially impacts synaptic transmission.

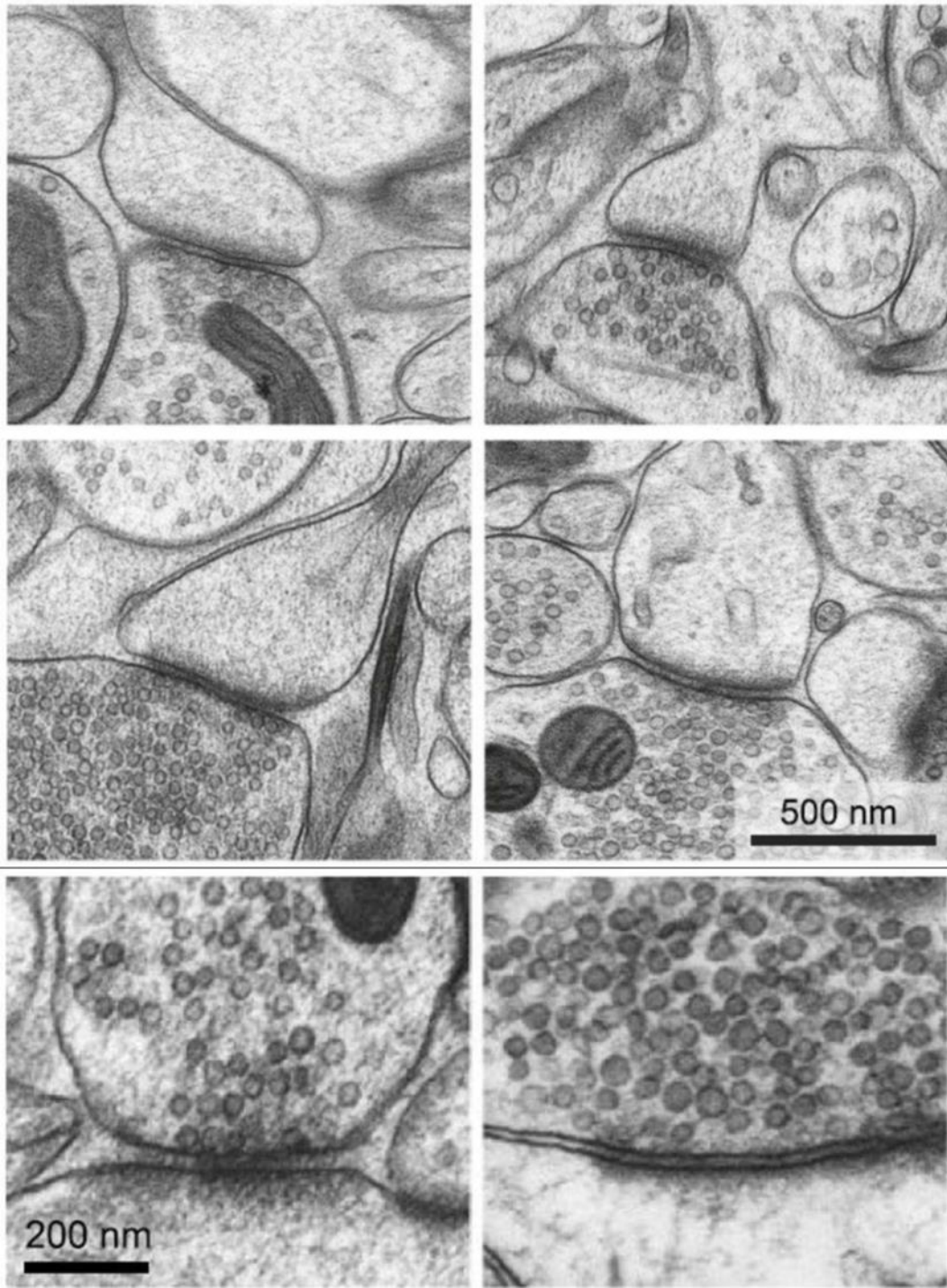


**Figure 1.** Cryo-EM images of CNS excitatory synapse. The pre-synaptic bouton is filled with glutamate containing vesicles which can be docked at the Active Zone which faces the Post-Synaptic Density. (From Korogod et al 2015)

## 2. The post-synapse

### a. Glutamate receptors

At the post-synapse occurs the conversion of the chemical signals coming from the pre-synapse via glutamate release into tunable electrical signals. To this end, the post-synapse accumulates receptor proteins that are in majority activated by glutamate binding. These receptors can be either ionotropic glutamate receptors (iGluRs) or metabotropic glutamate receptors (mGluRs). The classes of iGluRs have been named relatively to their specific agonist:  $\alpha$ -Amino-3-hydroxy-5-Methyl-isoxazole-Propionic Acid Receptors (AMPA), N-Methyl-D-Aspartate Receptors (NMDARs) and Kainate Receptors (KARs) (Lodge, 2009). One exception is the delta type glutamate (GluD) receptors. They are a functionally enigmatic subfamily of ionotropic glutamate receptors: despite sharing similar sequences and structures with AMPA, NMDA, and kainate receptors, GluD receptors do not function as ligand-gated ion channels. Binding d-serine and engaging in trans-synaptic protein-protein interactions, GluD receptors are thought to undergo complex conformational rearrangements for non-ionotropic signaling. (Chin and Lau, 2021; Naur et al., 2007). For the other iGluRs, they are ligand-gated ion channels that mediate most of the excitatory neurotransmission. Glutamate-binding triggers the opening of the channel pore, allowing ions to diffuse down to their electro-chemical gradient. AMPARs are responsible for the fast synaptic transmission and mainly mediate  $\text{Na}^+/\text{K}^+$  currents (Buonarati et al., 2019). Their structure and function will be further detailed in chapter 2. NMDARs differ from AMPARs in several important manners. At rest, the ion channel of NMDARs is blocked by  $\text{Mg}^{2+}$ . This  $\text{Mg}^{2+}$  block is released when the post-synaptic membrane is sufficiently depolarized, after AMPAR activation or back propagated action potential (Vyklícky et

al., 2014). Therefore, NMDARs is not the main actor of fast basal synaptic transmission and are rather considered as coincidence detectors for pre- and post-synaptic activity. The second feature which marks a difference between AMPARs and NMDARs is the permeability of NMDARs to  $\text{Ca}^{2+}$  ions. Even if some AMPARs are calcium-permeable (CP-AMPA), NMDARs play a key role at synapses to activate many intracellular calcium-dependent cascades (Traynelis et al., 2010). This calcium permeability of NMDARs gives them a central role in the modification of synaptic strength referred as synaptic plasticity which relies on calcium-dependent mechanisms. Finally, NMDARs differ by their gating mode. NMDAR are constituted by 2 NR1 and 2 NR2 subunits. The NR2 subunits are activated by glutamate with a high affinity but require in parallel the presence of a co-agonist which is either glycine or D-serine, and which bound to NR1 subunit (Traynelis et al., 2010). NMDAR present relatively slow activation kinetics, implicating them more in long-term signaling than directly in the electrical fast synaptic transmission. The KARs seem more implicated as regulators of synaptic transmission than as real direct effectors, but their exact role is still poorly understood (Traynelis et al., 2010).

In addition to the role of iGluRs on synaptic transmission, mGluRs modulate synaptic EPSCs by their presence at both sides of the synapse. Indeed, mGluRs family is composed of eight different receptors (mGluR1-8) which can be localized at the pre- or post-synaptic membrane, mainly outside of the synaptic cleft. Their functions are multiple as they convert glutamate release into protein G responses, leading to complex and various transduction signaling pathways according to the mGluR subtype (Koehl et al., 2019). Their roles depend on their composition, glutamate affinity (from hundreds of nM to mM) and partners but they are implicated in synapse maturation, plasticity, and calcium homeostasis (Ferraguti and Shigemoto, 2006).

These various receptors present a highly variable affinity for glutamate, from the nM range for NMDARs to almost mM range for AMPARs. After pre-synaptic release at the active zone, glutamate diffuses inside of the synaptic cleft, its concentration into the synaptic cleft being non-homogenous and decreasing with the distance from release sites (Raghavachari and Lisman, 2004). Therefore, the localization of receptors regarding glutamate release site will determine their saturation by glutamate. This parameter, added to the differential affinity of receptors to glutamate, influence the level of activation of receptors during synaptic signaling (Scheefhals and MacGillavry, 2018).

Our group historically studied the dynamic of AMPARs. During my thesis, I notably interested myself to their regulation and interaction with other post-synaptic proteins.

## **b. AMPAR structure**

AMPARs are tetrameric cation channels that mediate fast excitatory synaptic transmission upon glutamate binding. AMPAR assemblies are complex signaling machines that function as homo- or heterotetramers (which corresponds to the majority in the CNS) built from combinations of four subunits, GluA1-4 (Greger et al., 2017). Most of AMPARs are synthesized in the soma. To form a mature receptor, four subunits need to assemble together in a dimer-to-dimer process (Greger and Esteban, 2007). Each subunit differs in its contribution to channel kinetics, ion selectivity and receptor trafficking properties. AMPARs show a widespread distribution in the brain, as expected from their key role in excitatory transmission. Unlike GluA4 that is abundant in the cerebellum, GluA1, GluA2 and GluA3 are enriched in most of the CNS regions



(Schwenk et al., 2014). Each AMPAR subunit is composed of around 900 amino acids and has a molecular weight of about 100 kDa (Hollmann, 1994). Subunits are coded by their own genes but share ~70 % amino acid sequence identity. They display a unique modular architecture as each subunit consists of four distinct domains (Sobolevsky et al., 2009): an extracellular N-Terminal Domain (NTD, also referred to as ATD for Amino-Terminal Domain), a Ligand-Binding Domain (LBD), a Trans-Membrane Domain (TMD) that forms the pore of the ion channel, and a cytoplasmic C-Terminal Domain (CTD) (Figure 2). The CTD varies in length between subunits and plays an important role in AMPAR trafficking. Indeed, this CTD is subject to various activity-dependent post-translational modifications able to influence synaptic strength

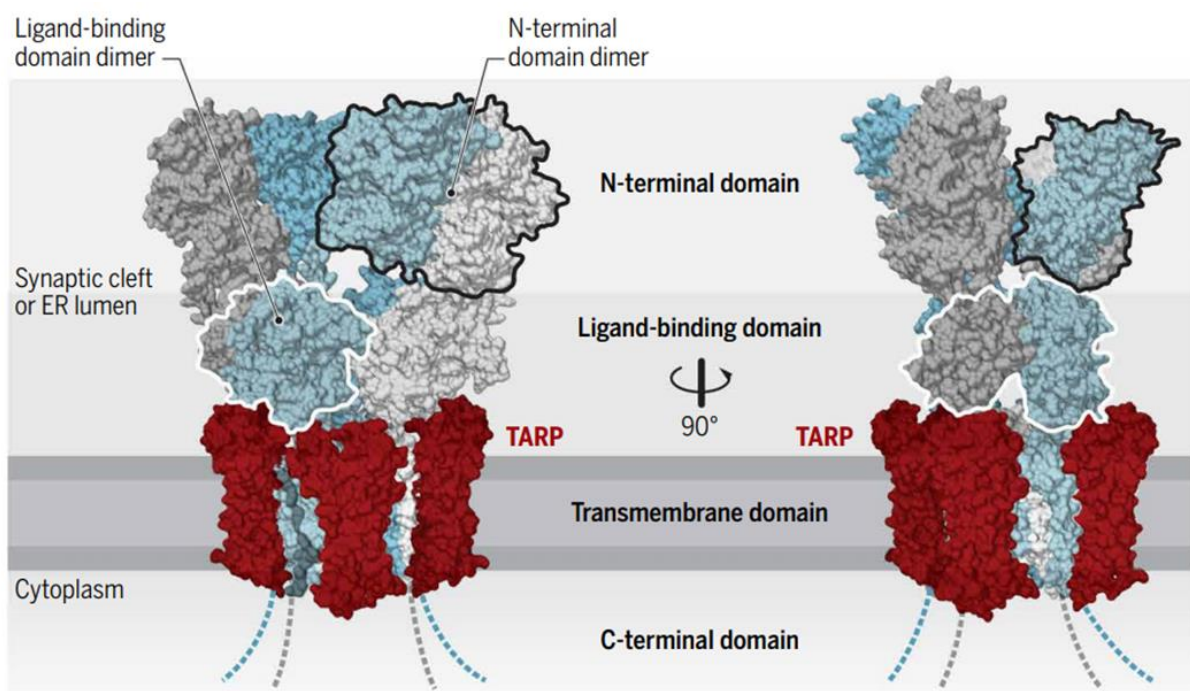


**Figure 2.** Structure of AMPAR subunits. AMPARs are formed by four subunits, which are conformationally (and functionally) distinct (“pore-proximal” subunits are in gray, and “pore-distal subunits” are in blue). These subunits consist of an extracellular N-terminal domain, the ligand-binding domain, an integral membrane domain, and an intracellular C-terminal domain and form tetrameric receptors (chains A to D). The large extracellular region faces the ER-lumen during receptor biogenesis and ultimately projects into the synaptic cleft. The TARPs interact with the receptor at up to four positions around the transmembrane domain. From Buonarati et al., 2019.

Each subunit brings a specificity in term of gating properties. Another level of variability is due to various post-transcriptional modifications. Briefly, receptors present a flip/flop alternative splicing in a 38 amino acid region located just before the M4 segment and this activity-dependent alternative splicing affects the channel gating kinetics and pharmacological properties (Penn et al., 2012). In addition, AMPARs display post-transcriptional processing or mRNA editing. Maybe the most important one concerns specifically the GluA2 subunit. Indeed, its M2 segment contains a Q/R (Glutamine Q to Arginine R) mRNA editing site. This post-transcriptional modification renders GluA2-containing AMPARs impermeable to calcium, reduces AMPAR channel conductance and open probability (Derkach et al., 2007; Greger et al., 2017; Coombs et al., 2019). This editing occurs during brain development and ~99 % of GluA2 subunits are edited in the adult CNS. Finally, a last editing site is present in GluA2-4 subunits just before the flip/flop domain. This second mRNA editing site switches an Arginine (R) to a Glycine (G). Most of expressed subunits are in the editing form. This editing affect AMPAR gating kinetics, subunit assembly and trafficking (Greger et al., 2017; Penn et al., 2012).

### **c. Regulation and function of PSD-95**

For a while, glutamate receptors were thought immobile inside the synapse, until first single particle tracking experiment which reveal that 20 to 30% of the AMPAR receptors were mobile while the other one were immobilize at the synapse (Borgdorff and Choquet, 2002). This glutamate receptor overaccumulation and immobilization at the synapse and more particularly at the PSD has been rapidly attributed to its direct

or indirect interaction with the constituents of the PSD, which are the scaffolding proteins.

The PSD is composed of thousands of scaffolding proteins tightly organized and regulated (figure 3). They are involved in the synaptic development, basal synaptic transmission and are key players in synaptic plasticity (Choquet and Triller, 2013; Sheng and Kim, 2011). Among them, the deeper part of the PSD is mainly composed of Homer, Shank and Guanylate-Kinase-Associated Protein (GKAP), while the Membrane-Associated GUanylate Kinases (MAGUK) family proteins seem highly concentrated closer to the post-synaptic membrane. The main members of synaptic MAGUK proteins are PSD-95, PSD-93, SAP97 and SAP102.

PSD-95 plays a primary role in the PSD organization because (i) it accumulates before and is located closer to the post-synaptic membrane compared to other PSD proteins, (ii) its level of expression affects synapse maturation and strength, (iii) spine shrinkage or pruning is correlated with a decrease of synaptic PSD-95 (Chen et al., 2011; El-Husseini et al., 2000; Woods et al., 2011; Subramanian et al., 2019). However, it has been suggested that the absence of PSD-95 could be compensated by the other members of the MAGUK family as they display a large homology (Elias et al., 2006; Levy et al., 2015). In this chapter, I will focus on PSD-95, as its regulation has been at the heart of my thesis.

PSD-95 is composed of series of protein interaction domains enabling the formation of clusters of various synaptic proteins. PSD-95 possesses three PDZ domains, a SH3 domain and a Guanylate-Kinase (GK) like domain (Okabe, 2007; Sheng and Kim, 2011). From a functional point of view, PSD-95 is able to recruit and stabilize several synaptic proteins at the post-synaptic membrane mainly through its PDZ domains. For instance, the first two PDZ domains, working as a tandem (Sainlos

et al., 2011), play a crucial role in the organization of the two main glutamate receptors (AMPA and NMDARs) at synapses.

Post-translational modifications of PSD-95 play important roles in its functionality. In particular, on its N-terminal part, PSD-95 can be anchored to the postsynaptic membrane via the palmitoylation of two cysteine residues in position 3 and 5 (El-Husseini *et al.*, 2002; Fukata *et al.*, 2013; Matt *et al.*, 2019). The regulation of PSD-95 location concerns two important points. First, its presence at the synaptic or extra-synaptic sites. This regulation is reported to dramatically rely on its phosphorylation state, in instance the phosphorylation of T19 that decreases its synaptic stability (Hruska *et al.*, 2015; Nelson *et al.*, 2013). Then, when present at the synapse, the anchoring of PSD-95 at the membrane is mainly regulated by the palmitoylation as mentioned above: when palmitoylated, PSD-95 is anchored at the membrane. This is due to the fact that palmitoylation changes PSD-95 from a compact conformation, as presumably prevalent outside synapses, to an extended one perpendicular to the PSD membrane, with its palmitoylated N-terminal domain at the membrane (Chen *et al.*, 2011; Jeyifous *et al.*, 2016).

In order to ensure its scaffolding role, PSD-95 is highly stable at synapses with a low turnover rate as demonstrated by FRAP experiments (Kuriu *et al.*, 2006; Sharma *et al.*, 2006). Once PSD-95 is anchored at synapses in an open conformation, its interaction domains are outstretched, allowing interactions to several proteins crucial for synaptic transmission as glutamate receptors or adhesion proteins.

First of all, PSD-95 stabilizes NMDARs at synapses via a direct interaction between the last four amino acids of the C-terminal domain of GluN2 subunit of NMDAR and the first two PDZ domains of PSD-95 (Groc *et al.*, 2004, 2006). PSD-95 has also been identified as one of the main organizers of AMPARs. Briefly, although

AMPA subunits own a PDZ-binding motif, they are unable to interact directly with PSD-95. Indeed, it has been shown in the group that truncation of the C-terminal domain of GluA2 subunit of AMPAR does not impact its surface diffusion or synaptic stabilization but only affects its expression at the cell surface (Bats et al., 2007). AMPAR interacts with PSD-95 through an intermediate, identified as the Transmembrane AMPAR Regulatory Proteins (TARPs) (Bats et al., 2007; Chen et al., 2000; Nicoll et al., 2006; Schnell et al., 2002).

In addition to simply localizing PSD-95 at the synapse and thus providing AMPAR anchoring “slots” at the PSD, PSD-95 palmitoylation may contribute to the regulation of synaptic strength by (re)organization of the entire PSD structure. Dynamic palmitoylation cycling changes PSD-95 conformation and TARP binding, thereby regulating the number of AMPAR slots in AMPAR nanodomains. This hypothesis is consistent with the observation that changing PSD-95 palmitoylation in PSDs altered PSD-95 and AMPAR (Jeyifous et al., 2016). Adopting an extended conformation likely also contributes to binding of PSD-95 to stargazing (Bats et al., 2007) and potentially other TARPs, whose C-termini also undergo an extension away from the plasma membrane upon.

To conclude, the PSD is not an unstructured aggregate of scaffolding proteins, but it follows tight organization rules which are still not understood. For example, PSD-95 presents multiple phosphorylation sites, each targeted by kinases or phosphatases that are activated during synaptic development, maturation or plasticity. They regulate PSD-95 nanoscale organization and its interactions with proteins. This complex structure will be able to organize acutely the various glutamate receptors and so to define synaptic transmission properties. The precise molecular organization of both

scaffolding proteins and glutamate receptors regarding the release site determines the number of receptors activated during a synaptic input.

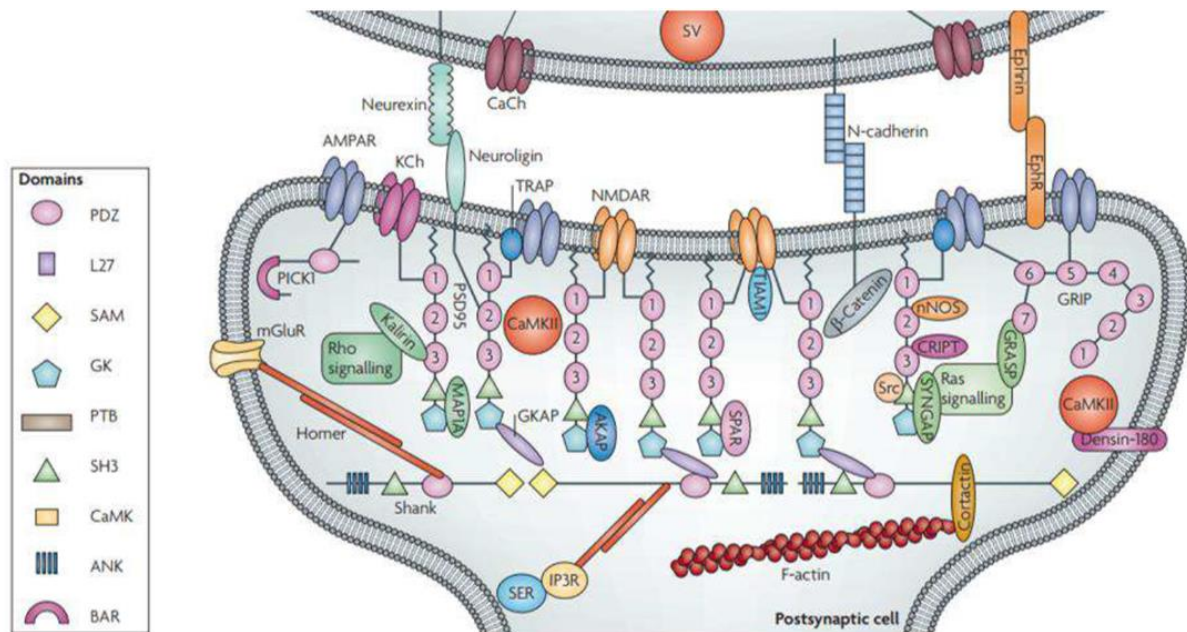


**Figure 3.** General scheme of molecular organization of the PSD of excitatory synapses. From Feng and Zhang, 2009.

#### d. Assembly and macromolecular complex

The assembly of AMPARs, as for most membrane proteins, starts in the ER. In neurons, the organelles of the secretory route are uniquely organized in a way that they are not only located centrally in the soma, but also span into the dendrites. This organization allows assembly and modification of synaptic proteins close to their site of action (Jacobi and von Engelhardt, 2018). The AMPAR subunits GluA1-GluA4 assemble to the premature receptors in the ER (Mignogna et al., 2015). The initial step in AMPAR biogenesis is mediated by the N-terminal domains of the single subunits that drive dimerization of the receptors. This early interaction largely dictates the

subunit composition of the final receptors on the cell surface (Greger et al., 2017; Penn et al., 2012). However, AMPAR assembly is not random, as specific subunit combinations are preferred (Greger et al., 2003; Lu et al., 2009). Very recently, Gouaux's lab identified the GluA1–GluA2, GluA1–GluA2–GluA3 and GluA2–GluA3 receptors as the predominant assemblies in the hippocampus (Yu et al., 2021). It has been proposed that the process of preferential assembly of AMPARs depends largely on intrinsic interactions of the different domains of the involved GluA subunits. This interaction of the GluA-subunits again depends on their RNA-editing, their post-translational modifications and on chaperon activity (Fukata et al., 2005; Greger et al., 2003, 2006; Hayashi et al., 2005).

To form a mature receptor, four subunits need to assemble together in a dimer-to-dimer process (Greger and Esteban, 2007). In the CNS, the majority of AMPARs exists as heterotetramers and most of them contain edited GluA2 subunits, restricting  $\text{Ca}^{2+}$  permeability (Henley and Wilkinson, 2016). The first assembly as dimer is attributed to NTD affinities while the tetramer formation and stabilization is attributed to LBD and TMD interactions. Regarding the dimer assembly, GluA1 NTD has an affinity for GluA2 NTD that is >200-fold stronger than for another GluA1 NTD. The effect of these affinity differences in the hippocampus where GluA1-3 subunits are expressed results in the assembly of almost exclusively GluA1/GluA2 (~80 %) and GluA2/GluA3 (< 20%) heterotetramers (Lu et al., 2009). Still, the presence of low level of homotetrameric GluA1 (CP-AMPARs) has been observed. While their contribution to basal synaptic transmission is unlikely to occur, a role during synaptic plasticity has been reported since they could allow a better control of calcium influx that is at the origin of those mechanisms (Huganir and Nicoll, 2013; Sanderson et al., 2016).

In the CNS, AMPAR are almost never isolated from their assembly to their synaptic localization where they mediate synaptic transmission. They are described as macromolecular complexes comprising various auxiliary proteins (Schwenk et al., 2012; Miguez-Cabello et al., 2020). The receptor core could be surrounded by up to four members of four distinct families of membrane proteins: the TARPs ( $\gamma$ -2,  $\gamma$ -3,  $\gamma$ -4,  $\gamma$ -5,  $\gamma$ -7,  $\gamma$ -8) (Jackson and Nicoll, 2011; Tomita et al., 2003; Miguez-Cabello et al., 2020), the cornichon homologs 2 and 3 (CNIH2, 3), GSG1L protein (Schwenk et al., 2012) and Shisa family (CKAMP44/Shisa9 and Shisa6) (Engelhardt et al., 2010; Klaassen et al., 2016). Gouaux's lab showed in a recent study that the functional properties of AMPARs are regulated by the non-stochastic assembly of receptor and auxiliary protein components, notably the TARP  $\gamma$ -8 (Yu et al., 2021).

A definition of AMPAR auxiliary protein based on three criteria has been proposed by Tomita's lab: (i) to be a non-pore forming subunit, (ii) to have a direct and stable interaction with the pore-forming subunits, and (iii) to modulate AMPAR trafficking and/or biophysical properties (Yan and Tomita, 2012). While it appears evident that the presence of this bench of proteins around AMPAR regulates its trafficking, its synaptic localization and its gating properties, the precise role of each one remains unclear (Jacobi and von Engelhardt, 2018). Due to the redundant role of the various auxiliary proteins in AMPAR trafficking and gating, it is difficult to understand the precise role of each in region where several members of the same family are expressed. However, regarding TARP  $\gamma$ -2 (stargazin) which is the most characterized, several interesting results regarding the regulation of AMPAR functions have been obtained. Briefly, the first result has been obtained by Roger Nicoll's group on Stargazer mice (mice lacking  $\gamma$ -2). They showed that in the cerebellum where stargazin is the main TARP, neurons display an intense decrease of the surface



AMPA level, suggesting a role of stargazin in AMPAR trafficking and surface expression (Chen et al., 2000). However, it has been recently hypothesized that this suppression of AMPARs in the cerebellum of the stargazer mouse was not only due to the suppression of stargazin but also to the over-activity of  $\gamma$ -7 which favors AMPAR endocytosis (Bats et al., 2012). Other studies have demonstrated that the interaction between stargazin PDZ-binding motif and PSD-95 allows the anchoring of AMPAR at synapses (Bats et al., 2007; Opazo et al., 2010; Sainlos et al., 2011; Schnell et al., 2002). As previously reported, AMPAR seems unable to interact directly with PSD-95. Bats et al. demonstrated that the loss of interaction between stargazin and PSD-95 impairs AMPAR immobilization and accumulation at synapses and leads to a decrease of synaptic transmission. This regulation of AMPAR mobility and synaptic anchoring is dependent on synaptic activity and phosphorylation state of stargazin. Schematically, the phosphorylation level of the stargazin cytoplasmic tail controls its interaction with the negative charge of the lipid bilayer. An increase in the phosphorylation level outstretches the tail and favors interaction with the anchored PSD-95 (Hafner et al., 2015; Sumioka et al., 2011; Tomita et al., 2005a).

To finish, stargazin does not only impact AMPAR trafficking and stabilization at synapses but also tunes AMPAR synaptic responses by slowing channel deactivation and desensitization (Jackson and Nicoll, 2011; Tomita et al., 2005a). Similar regulations are introduced to AMPAR complex by the other auxiliary proteins. Moreover, it has been reported that endogenous AMPAR currents seem dependent on the presence of a combination of at least two different associated proteins (Gill et al., 2011; Kato et al., 2010). Finally, our group also demonstrated that the unbinding of AMPAR and stargazin facilitates recovery from short-term changes in synaptic currents

(Constals et al., 2015), showing that interaction between AMPARs and TARPs profoundly regulate synaptic transmission.

This clearly reveals that synaptic current properties are due to the highly regulated combination between AMPAR composition, post-translational modifications, position regarding glutamate release, and presence of various regulatory proteins (Bassani et al., 2012; González-Calvo et al., 2021; Mignogna et al., 2015). Until now, a clear view of AMPAR complex composition in various brain areas and the physiological effect of such variability on the synaptic transmission properties are far to be understood.

#### **e. AMPAR-mediated currents**

AMPARs present a low affinity for glutamate with a half-maximal effective concentration (EC<sub>50</sub>) of ~0.5 mM compare to NMDARs which has a nanomolar range affinity for glutamate. When exposed to a pulse of 1 mM glutamate a current is generated with a rapid rise time of 100-600  $\mu$ s (Raghavachari and Lisman, 2004). This reflects the very fast binding/activation kinetic and high opening probability of AMPARs (Figure 4A). The single channel conductance is highly variable, from <1 pS to ~30 pS, because of AMPAR subunit composition, RNA editing and alternative splicing (Swanson et al., 1997), but also due to the number of glutamate molecules that bound to the receptor. Two glutamate molecules must bind the receptor to open it, and then the channel conductance increases proportionally to the number of bound glutamate (Figure 4B). The more efficient is the agonist, the more frequently the receptor will occupy the high-conductance state (Rosenmund et al., 1998). This particularity

underlines the importance of AMPAR localization regarding glutamate release sites, independently of the AMPAR composition to determine the synaptic response intensity (Q value). Once open, receptors deactivate rapidly following clearance of synaptic glutamate. The deactivation occurs in ~2.5 ms and is probably sufficient to explain the termination of AMPAR-mediated EPSC. Indeed, glutamate is cleared from the synaptic cleft in few hundreds of  $\mu$ s following a single vesicle release (Colquhoun et al., 1992; Raghavachari and Lisman, 2004). During high frequency release or strong stimulation, if glutamate is not cleared rapidly enough, AMPAR channel closes rapidly and the receptor enters in a desensitized state which lasts for tens to hundreds of ms. The desensitized state corresponds to a conformational state of the receptor in which glutamate can still bind to the receptor but the channel is closed (Dürr et al., 2014; Sun et al., 2002) even though a recent study challenged this last point (Coombs et al., 2019). Desensitization appears to play a role in the regulation of synaptic strength on a synapse-specific basis, especially during high-frequency stimuli (Constals et al., 2015; Koike-Tani et al., 2008; Otis et al., 1996).

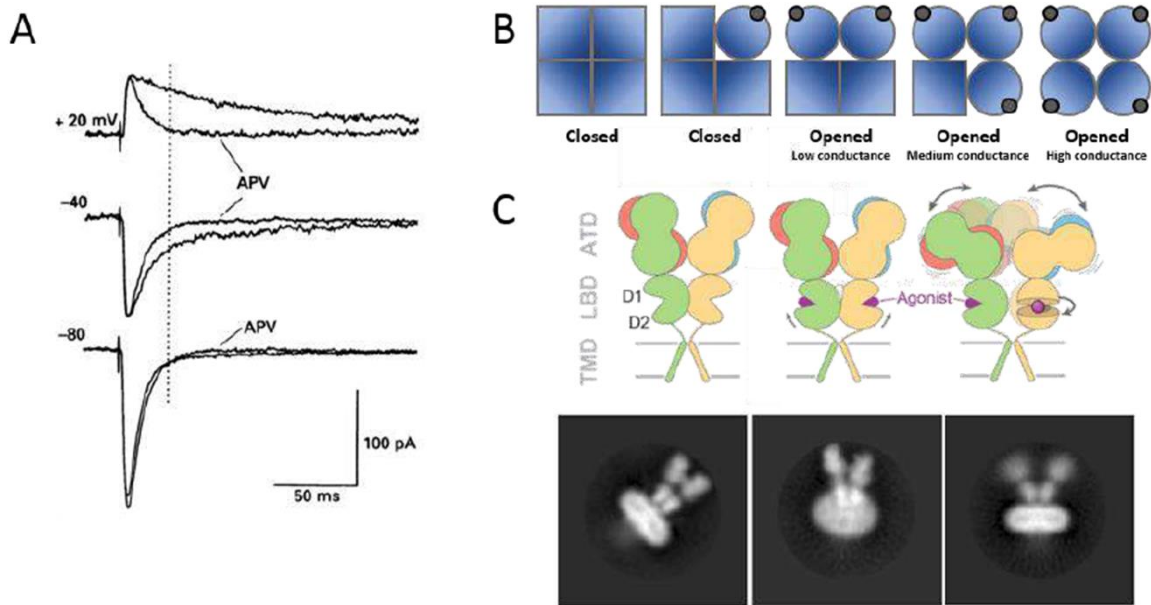


**Figure 4.** AMPAR gating properties. (A) Excitatory post-synaptic currents are mainly mediated by AMPAR at resting potential (-70 mV). The contribution of NMDAR is almost null as shown by the similar EPSC obtained in the presence of NMDAR blocker (APV) at -70 mV (From Hestrin et al 1990). (B) Activation of AMPAR requires at least two bound glutamate (black circle). Activation of more subunits (Blue square) opens the channel to a higher conductance level. (C) AMPAR conformational states: close (left), open (middle) and desensitized (right) in schematic representation or cryo-EM visualization (Durr et al 2014 & Chen et al 2017)

To conclude, the simple model where AMPAR is closed, opened and get desensitized appears to be more complex. It has been shown that AMPAR displays different stages of channel opening depending on the number of bound glutamate molecules leading to several desensitized states (Meyerson et al., 2014; Robert and Howe, 2003). This structural complexity relies on AMPAR composition, regulation by post-translational modification and interactome, leading to a more complex view of how AMPARs participate to the integration of synaptic inputs.

In the next chapters, I will introduce the functional consequences of the previously shown synaptic organization. In particular, I will outline how the nano-organization of synapses regulates the synaptic signaling.

### 3. Synaptic input integration

Synaptic vesicles are clustered into the pre-synaptic bouton and despite the fact that their organization seems to be random, three pools of vesicles can be distinguished depending on their functions (Nosov et al., 2020). Half of the vesicles belongs to the "recycling pool" as they are able to exocytose neurotransmitters upon moderate stimulation. A part of those recycling vesicles is docked at the active zone (AZ) and is thus ready to be exocytosed. This second fraction of vesicles belongs to the "readily releasable pool". Finally, the second half of synaptic vesicles forms the "reserve pool" which is left unreleased even after strong stimulation (Denker and Rizzoli, 2010; Rizzoli and Betz, 2005). The release of glutamate contained in synaptic vesicle is restricted to the AZ which contains the necessary machinery for vesicle exocytosis. The AZ has four main functions: (i) to dock and prime the readily releasable pool of synaptic vesicles, (ii) to recruit voltage-gated calcium channels (VGCCs) to synchronize excitation with glutamate release, (iii) to localize the release of neurotransmitters in front of the PSD via trans-synaptic proteins, and (iv) to organize and reorganize the pre-synapse during basal transmission and synaptic plasticity (Harris et al., 2013; Südhof, 2012).

Glutamate release at excitatory synapses depends on the fusion of synaptic vesicles with the plasma membrane through a complex mechanism which requires the action of several proteins at specific locations. The fusion between glutamatergic vesicles and the pre-synaptic membrane is operated by the SNARE (Soluble N-ethylmaleimide-sensitive-factor Attachment protein Receptor) complex which tightens

after the influx of  $\text{Ca}^{2+}$ , sensed by the vesicular protein synaptotagmin (Jahn and Fasshauer, 2012; Zhou et al., 2017a).

In parallel to the first observation of the pre-synapse organization in the 1950s, Katz demonstrated that neurotransmitter release was at the origin of the post-synaptic electrical response (Fatt and Katz, 1951; Huxley, 2002). After confirming the notion of the action potential (AP) threshold during electrical stimulation, he showed that this AP triggers the action of neurotransmitters on the post-synaptic element and introduced the notion of "quantum of action". The smallest quantum is equal to a miniature spontaneous post-synaptic current and the synaptic response is composed of a sum of quantal units (Del Castillo and Katz, 1954; Fatt and Katz, 1951). Later on, it has been shown by coupling electrophysiological recordings and EM that a single quantum is the result of a single vesicle release event at the AZ (Heuser et al., 1979). It is well known that each quantum is independent of one another and that the number of quanta released upon AP stimulation is dependent on the release probability ( $P_r$ ) of single vesicles.

To summarize decades of studies about the concept of synaptic currents, there are two main types of vesicular release (Kavalali, 2015). The first one depends on the action potential propagation and is called "evoked" release (figure 5). AP triggers the pre-synaptic increase of calcium, which in turn activates the pre-synaptic machinery for vesicle fusion and glutamate release. The efficiency of a dedicated synapse to release a vesicle following an AP varied from one to another synapse and is named release probability ( $P_r$ ). The vast majority of the pre-synaptic plasticity mechanisms aim to regulate this  $P_r$  to increase the role of given pre-synapses in the network activity. Due to the massive increase of calcium, several docked vesicles will fuse, and as AP

propagates all along the pre-synaptic axon, this will occur at several synapses. This release can occur synchronously or asynchronously (delayed) in respect to the AP duration. The post-synaptic response to this release of glutamate is called excitatory post-current or EPSC and can be recorded after somatic summation by whole-cell patch clamp recording (see material and methods part) as a macroscopic event of hundreds of pA.

The second type of vesicular release is independent on AP propagation and is called “spontaneous” release (figure 5). It is thought to be mainly independent of intracellular calcium changes, even if this point is still debated (Raghavachari and Lisman, 2004). It corresponds to the spontaneous fusion of a single vesicle, leading to a quantal release of glutamate at a single synapse. The post-synaptic response is called miniature EPSC (mEPSC) and can be measured at the soma as a small event of tens of pA. The differences between EPSCs and mEPSCs are therefore the dependence on calcium, the mechanism that triggers their apparition, and of course the quantity of glutamate being released (Gonzalez-Islas et al., 2018). However, a debate is still open concerning the localization of the release site during EPSC or mEPSC. Some argues go in favor of two different localizations, at the AZ for the EPSC and at the entire pre-synapse for the mEPSC, some indicates more a unique release site.

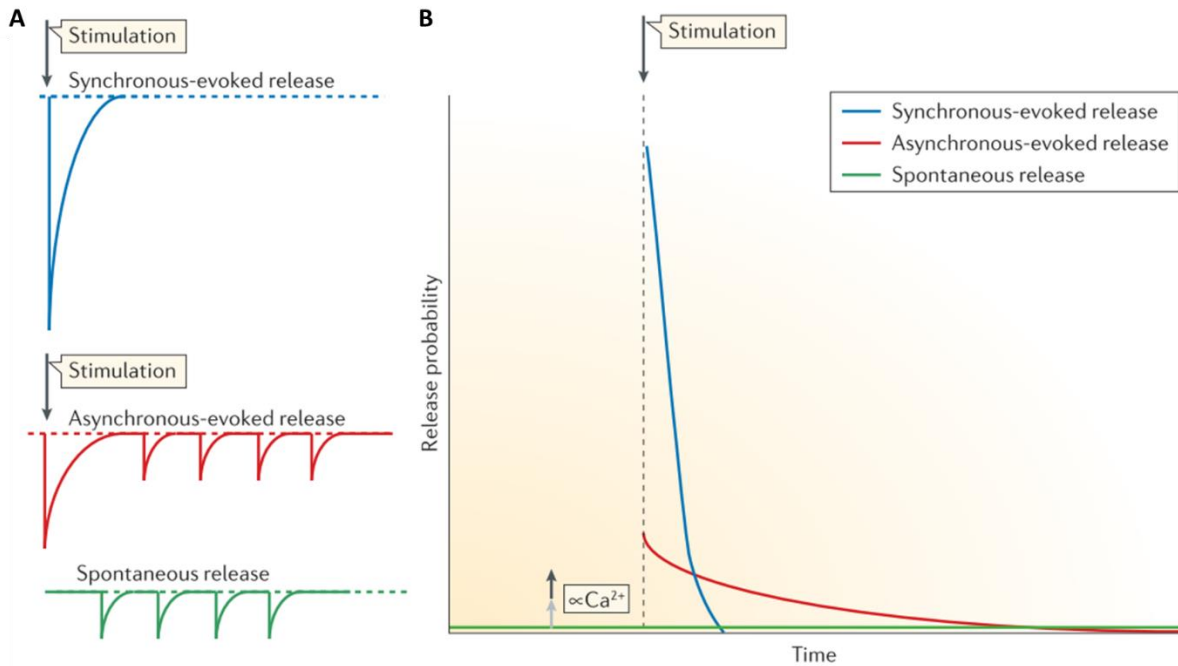


**Figure 5.** Two distinct forms of neurotransmitter release. A. Graphical recording traces show representative examples of events that are detected in response to synchronous- and asynchronous-evoked release, and to spontaneous release during a typical electrophysiological experiment. B. The graph shows the relative time courses of decay in neurotransmitter release probability seen after presynaptic stimulation. Presynaptic action potentials and the resulting  $Ca^{2+}$  influx cause synchronous vesicle fusion within 1 ms. In some synapses, vesicle fusion is only loosely coupled to the timing of a presynaptic action potential and may thus outlast the duration of the action potential for 1 s or more, which leads to asynchronous neurotransmitter release. In addition, neurotransmitter release can occur spontaneously in the absence of presynaptic action potentials, even though the rate of such spontaneous release is proportional to intracellular  $Ca^{2+}$  levels. From Kavalali, 2015.

From these post-synaptic currents' recordings, several key parameters can be extracted to study the characteristics of synapse. I will now introduce them.

Previous chapters briefly present an overview of basic knowledge on the principal components of the synaptic transmission. These components are coordinated to regulate and define the inputs received by the post-synaptic neuron when pre-synaptic inputs are delivered.

The **N** corresponds to the number of connected synapses.



The pre-synapse regulates the amount of released glutamate but more importantly, the probability of this release to occur following an AP (**Pr**).

Finally, the amplitude of a mEPSC, which has been initially attributed to the quantity of glutamate per vesicle, but is now more considered as an effect of the organization and the composition of glutamate receptor complexes, determine the post-synaptic quantum of synaptic response (**Q**). Indeed, the neurotransmitter content appears to be quite stable from one vesicle to another (Franks et al., 2002; Heine et al., 2008; Lisman et al., 2007; Raghavachari and Lisman, 2004). In addition, recent works demonstrated that glutamate receptor complexes are not homogeneously organized inside the synapse. They can change their composition and thus modulate their glutamate affinity and their conductance. In this condition, Q is not only a pre-synaptic property but relies mainly on the quantity of glutamate receptors inside the synapse, their proper organization, their location regarding the release site, and their molecular composition.

These parameters define the currents that pass at the post-synapses and that will be summed at the soma (**I**), corresponding to the amplitude of post-synaptic response to a pre-synaptic event. As described previously, the generation of an AP output depends on a temporal and spatial integration of synaptic signals. Thus, the intensity of the somatic current (**I**) depends on the number of activated synapses/release sites (**N**), the probability of vesicular release (**Pr**) at each stimulated release site and the quantum of response (**Q**) such as  **$I = N \cdot Pr \cdot Q$**

It is rather noting that in the particular case of mEPSCs,  $N = 1$ , as quantal release occurs at one synapse at a time, because of random distribution of this phenomenon.

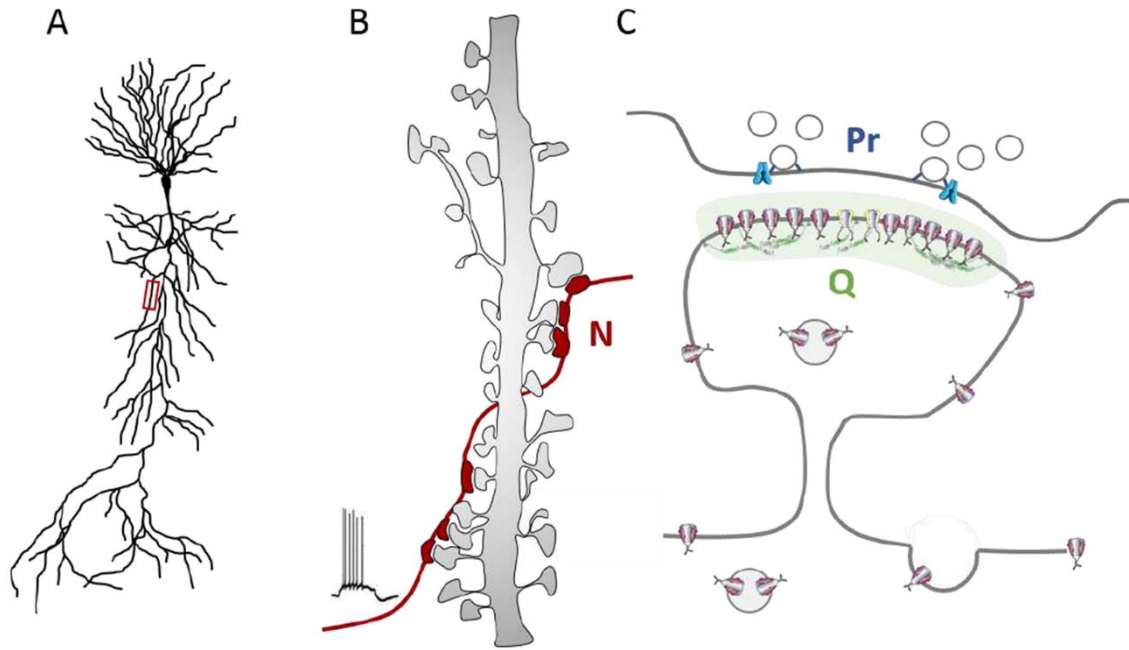


**Figure 6.** The NPQ paradigm. (A) CA1 pyramidal neuron. A dendritic segment (red rectangle) is detailed in the panel B. (B) Dendritic segment (grey) with spines. A single axon (red) coming from another neuron connect several times the dendritic segment forming synapses. When APs arrive in the axonal boutons it activates the N synapses formed with the CA1 pyramidal neuron. (C) Structure of a synapse with in the pre-synaptic vesicles, which can be docked through the molecular release machinery and can be released when an AP arrives at the axonal bouton with a certain probability (Pr). In front are located glutamatergic receptors. Their density, composition and location will determine the quantum of response Q.

As already mentioned, neurons have the capacity to modulate the efficacy of synaptic transmission to adapt to new conditions. To do so, all the previously parameters N, Pr and Q, far from being fixed for a synapse, are susceptible to be modified by neurons. In the coming chapters, I will introduce the phenomenon by which this regulation occurs.

## 4. Short-term plasticity

Synapses display the ability to adapt their efficiency depending on the inputs that they receive. This dynamic gain control occurs on short time scales (tens to thousands of milliseconds). This Short-Term Plasticity (STP) exists in two forms called Short-Term Facilitation and Short-Term Depression (STF and STD, respectively) which correspond to a short-lasting strengthening or weakening of synaptic gain in response to high-frequency glutamate release (Zucker and Regehr, 2002). STP-induced modifications of synaptic efficacy do not last and the synaptic efficacy returns quickly to its baseline level without continued pre-synaptic activity. The form of STP which is induced upon high-frequency stimulation depends on the neuronal cell type and can also vary within a same type of neuron. For instance, pyramidal neurons of the CA1 region in the hippocampus have both STD- and STF-dominated synapses. In contrast, in the cerebellum, climbing fiber synapses express mainly STD while STF dominates in parallel fiber synapses (Dittman et al., 2000; Dobrunz and Stevens, 1997). Although the precise role of STP is not clearly understood, it is thought to have filtering functions that are used in information processing and could be simplified as a dynamic gain control of synaptic inputs (Abbott et al., 1997; Dittman et al., 2000; Fortune and Rose, 2000, 2001; Rotman et al., 2011).

### **a. Pre-synaptic origins of STP**

STF and STD share an identical pre-synaptic origin. Facilitation of synaptic transmission on short time scale is caused by over-accumulation of  $\text{Ca}^{2+}$  at the AZ vicinity during high frequency stimuli, leading to an increase of Pr. Substantial evidence has accumulated in support of this residual  $\text{Ca}^{2+}$  hypothesis: (i) pre-synaptic  $\text{Ca}^{2+}$  concentration correlates with STF of synaptic transmission, (ii) buffering pre-synaptic  $\text{Ca}^{2+}$  or reducing  $\text{Ca}^{2+}$  influx reduces STF (Salin et al., 1996; Schneggenburger Ralf and Neher Erwin, 2000; Scimemi and Diamond, 2012; Zucker and Regehr, 2002). Concerning STD, it is also attributed to a pre-synaptic mechanism but postsynaptic properties can contribute to it. The most widespread mechanism is attributed to a decrease of the glutamate release which is likely related to a depletion of the readily releasable pool of vesicles even if a decrease in pre-synaptic quantal size has been proposed (Burrone and Lagnado, 2000; Chen et al., 2002, 2004; Zucker and Regehr, 2002). From a general point of view, pre-synaptic short-term plasticities are based on transient Pr modifications.

### **b. Post-synaptic contribution to STD**

Although it is well accepted that STPs originate from a pre-synaptic mechanism, desensitization of AMPARs has been implied at least partly in STD (Otis, Zhang and Trussell, 1996; Chen, Blitz and Regehr, 2002; Zucker and Regehr, 2002; Heine et al., 2008; Constals et al., 2015). Indeed, after the first stimulus, some AMPARs do not recover from desensitization before the following release, implying that less receptors

can be activated during the second release. In the presence of AMPAR desensitization inhibitors, Paired-Pulse Depression (PPD) is impaired (Brenowitz and Trussell, 2001; Heine et al., 2008). In addition, the enhancement of residual glutamate in the synaptic cleft by blocking glutamate transporters increased PPD, while glutamate scavengers reduced it (Turecek and Trussell, 2000). Thus, most of studies explain STD as a combination of depression of presynaptic glutamate release and desensitization of AMPARs upon glutamate binding. Return from depression is believed to arise from the replenishment of the readily releasable pool and from the recovery from desensitization (Trussell et al., 1993; Xu-Friedman and Regehr, 2004). More recently, Heine et al. and then Constals et al., reported that AMPAR lateral diffusion was able to tune the recovery from post-synaptic depression induced at high-frequency glutamate release. They observed that blocking AMPAR lateral diffusion increased the PPD. The explanation was that lateral diffusion is fast enough to allow an exchange of some receptors in and out synapses between two consecutive releases of glutamate. Based on diffusion properties of AMPARs at synapses, the replacement of synaptic receptors after the first glutamate release by lateral diffusion occurs faster than the recovery of individual AMPAR from desensitization. Thus, short-term depression does not depend on two but three parameters: (i) depression of pre-synaptic glutamate release, (ii) AMPAR desensitization and (iii) AMPAR lateral diffusion (Constals et al., 2015; Heine et al., 2008). These studies, confirmed by other ones, showed the physiological importance of AMPAR surface mobility in controlling the synaptic gain during high-frequency inputs (Frischknecht et al., 2009; Opazo et al., 2010).

## 5. AMPAR dynamic

As started to be developed in the previous chapters, AMPARs regulation is a very important parameter for the control of synaptic transmission and maturation (Bassani et al., 2012; González-Calvo et al., 2021; Wagner et al., 2019). Before entering in the heart of the topic of AMPARs control of synaptic transmission, I will introduce their nanoscopic behavior in term of organization and dynamic.

Although the concept of a fluid mosaic membrane has been proposed since 1972 by Singer and Nicholson (Singer and Nicolson, 1972), and that the application of the FRAP technique has demonstrated a rapid exchange via Brownian lateral diffusion of the various membrane constituents (Axelrod et al., 1976b, 1976a), it is only since the early 2000s, with the development of single-particle tracking techniques, that lateral diffusion has started to be considered as a non-negligible physiological parameter, particularly in neuronal cells. In 2001, for the first time, our group together with Antoine Triller applied single-particle tracking techniques on neurons to reveal and analyze the properties of the mobility of an inhibitory neurotransmitter receptor (Meier et al., 2001). One year later, the group published the characterization of AMPAR surface mobility (Borgdorff and Choquet, 2002). The use of single-particle tracking drastically changed our vision of AMPAR dynamic and organization inside synapses. The dogma that neurotransmitter receptors were immobile at synapses, their number in the PSD being affected only by endo- and exocytosis, was shown to be insufficient. Indeed, various experiments revealed that AMPARs constantly alternate between fast Brownian diffusion and confined motion (Borgdorff and Choquet, 2002; Tardin et al., 2003). Each receptor may adopt successively both of these behaviors, and activity regulates the

time spent in one or the other diffusive state (Constals et al., 2015; Heine et al., 2008; Tardin et al., 2003). Importantly, these experiments revealed the presence of specific and saturable binding sites for AMPAR inside the synapse. Therefore, the following years in the field have been dedicated to identify which molecular mechanisms are responsible for the AMPAR trapping at synapses. Unraveling the nature of the traps was intimately linked to the initial progress in genome sequencing and decoding and then the improvement in high throughput and sensitive proteomic technique (Von Engelhardt et al., 2010; Schwenk et al., 2012). Stargazin has been identified as the first AMPAR regulatory protein, implicated in both their cellular traffic to the membrane, the regulation of their electrophysiological properties and responsible for their synaptic trapping (Chen et al., 2000). AMPARs do not travel alone, but they are part of a macromolecular complex composed of many different auxiliary proteins, as presented in the previous chapters. The precise role of each auxiliary subunit is not well established, even if many studies using knock-out mice or protein mutations have tried to clarify the impact of some AMPAR associated proteins on synaptic function both at basal state and during plastic events.

First attempts at describing the AMPARs organization have been performed using single-particle tracking with quantum dots. In these conditions, random second to minute time scale immobilization of AMPAR in the PSD was reported, revealing a potential local subsynaptic organization (Ehlers et al., 2007). But it is only the recent application of the new super-resolution microscopy techniques on AMPAR that succeeded to reveal the AMPAR nano-organization inside synapses (Broadhead et al., 2016; Fukata et al., 2013; Hosy et al., 2014; Macgillavry et al., 2013; Nair et al., 2013). The emergence of those super-resolution imaging techniques and their application in neuroscience allows a better understanding of the dynamic distribution of synaptic

proteins at the nanoscale. Using a combination of super-resolution techniques, on fixed or living hippocampal cultured neurons, Nair et al. focused on AMPARs' dynamic nano-organization (Nair et al., 2013). Using u-PAINT and sptPALM, they tracked AMPARs at high density and showed for the first time the presence at synapses of AMPARs nanodomains. They observed that AMPARs are immobilized in fixed hotspots and are mobile between those. Super-resolution imaging on fixed cells, as well as electron microscopy, confirmed the presence of one to three 80 nm clusters per synapse containing 20 to 25 receptors each. Those AMPAR nanodomains can be stable for tens of minutes at the synapse. On the other hand, MacGillavry et al. (Macgillavry et al., 2013) studied the dynamic organization of PSD-95-mEOS by PALM and sptPALM and showed the presence of one to two 80-nm clusters per synapse. Fukata et al. via an elegant approach, observed ~150-nm cluster of the palmitoylated form of PSD-95 tagged using for the first time a genetically encoded antibody sensitive to palmitoylated form of PSD95 and imaged by STED microscopy (Fukata et al., 2013). Nair et al. also investigated the organization of PSD-95 fused to mEOS by PALM and found ~150-nm clusters. Blanpied's group reported an average of two nanoclusters of endogenous PSD-95 per synapse (Tang et al., 2016) In brain slices, these PSD95 subclusters have been recently reported as well, and both Broadhead et al. and Tang et al. found that 20% to 40% of PSDs contain more than one PSD-95 nanocluster, on PSD-95-mEOS or GFP knock-in mice or endogenous PSD 95, respectively (Broadhead et al., 2016; Tang et al., 2016). Due to the large number of laboratories that have reported the postsynaptic nano-organization of PSD95 and AMPAR, this new concept discovered 8 years ago is now being currently accepted. One important question regarding this synaptic organization has been answered recently by the work of Blanpied's group and more recently by our team, demonstrating the presence of presynaptic–postsynaptic



nanocolumns, where AMPARs nanodomains face pre-synaptic release sites (Haas et al., 2018; Tang et al., 2016). Hruska et al. showed this organization to rely also on pre-to-post synaptic nanomodules constituted notably by PSD-95, and that regulate synaptic transmission and relate synaptic function to structure (Hruska et al., 2018)

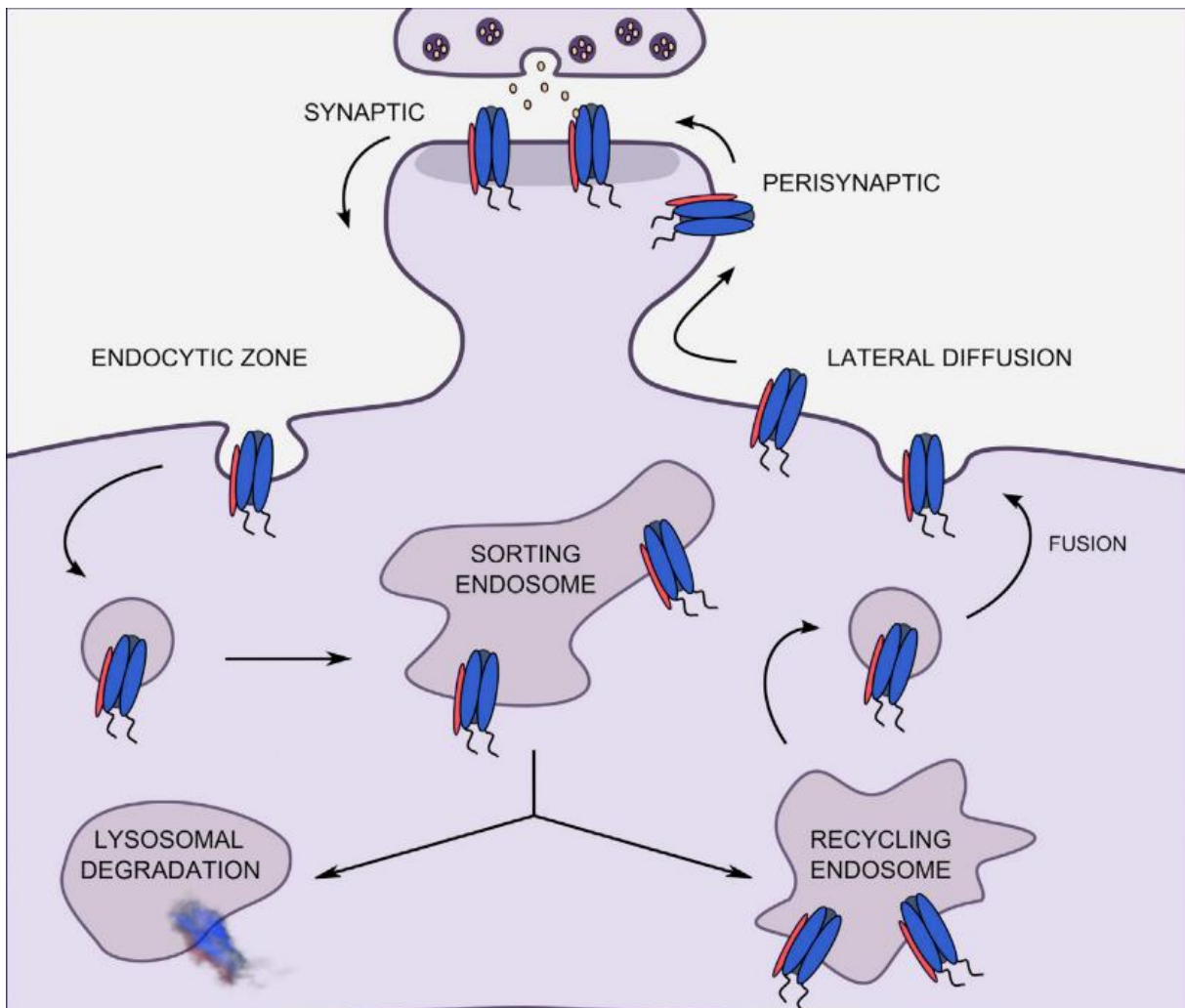


**Figure 7** AMPAR dynamic organization at the synapse. AMPAR traffic between the plasma membrane and the intracellular compartment through endocytosis and exocytosis. Once at the cell surface, AMPARs reach the PSD through lateral diffusion and get trapped by interacting with PSD-95 via their associated stargazin. At synapses, AMPARs are organized in nanodomains located in front of glutamate release sites. From Hugarir and Nicoll, 2013.

This discovery of AMPAR nano-organization, coupled to the concept of lateral diffusion, changed our vision of the synaptic organization and function, but raises

multiple questions. The previously reported studies present a new vision of the synapse at its stable state, but synapses are plastic organelles, able to adapt both to short- and long-term stimulation. Hence, one can postulate that modifications of AMPAR nanoscale organization could underlie various forms of synaptic plasticity. Many studies have brought indications of the molecular rearrangements taking place during plasticity at the whole synapse—diffraction limited—level; we now need to fuse these studies with the concept of lateral diffusion and nanoclustering of AMPAR to deliver a new vision of synaptic transmission regulation during plastic events.

## Chapter 2: Regulation of synaptic inputs

Neurons communicate with their neuronal partners by sampling and integrating the thousands of synaptic inputs that they receive (Sigoillot et al., 2015). They display several mechanisms to specifically modulate the strength of a specific input among the entire bulk of synapses. This leads to an increase/decrease of a particular stimulation input weight compared to all the other inputs received by the neuron. To do so, a neuron can modulate independently or jointly the three parameters of the NPQ paradigm. In particular, the post-synaptic organization of AMPARs plays a key role to tune the quantum unit of synaptic transmission (Q value) (Compans et al., 2016). Due to the development of super-resolution microscopy and its recent application to the field of Neuroscience, it has been possible to decipher the precise organization of the main actors of synaptic transmission. Notably, AMPARs and their main scaffolding protein PSD-95 have been shown to be organized in nanodomains of less than 100 nm (Fukata et al., 2013; Macgillavry et al., 2013; Nair et al., 2013).

Such nanoscale organization modify our concept concerning the regulation of the Q parameter. Indeed, several studies have suggested that not only the number of receptor inside the synapse was determinant for synaptic strength but also the density of the receptor, and the alignment of the receptor cluster regarding the release site (Macgillavry et al., 2013; Nair et al., 2013; Savtchenko and Rusakov, 2014). Recently, it has been demonstrated that those AMPAR nanodomains are physically aligned in front of glutamate release sites, introducing the notion of trans-synaptic nanocolumns (Tang et al., 2016). The impact of this alignment accuracy has initially been studied with Monte-Carlo based simulation, suggesting that it could have an

important role in tuning synaptic transmission (Franks et al., 2003; Macgillavry et al., 2013; Nair et al., 2013; Tarusawa et al., 2009). This hypothesis has been finally investigated in 2018, our group used various molecular and genetical tools to disturb interaction between the neuroligin (a post-synaptic adhesion protein interacting with the pre-synaptic neurexin) and PSD95, altering pre-post alignment (Haas et al. 2018). We demonstrated that a 100 nm misalignment between pre synaptic active zone (labelled with RIM) and AMPAR nanodomains leads to a 25 to 30 % decrease of synaptic currents.

In addition to the direct control of the amplitude (Q) of unitary synaptic currents, synaptic connections may increase their contribution to the neuronal integrated input by being active at higher rates through variation of the Pr, or by modifying the number of active synapses on the postsynaptic neuron (modification of the N parameter).

## 1. Synaptic plasticity

It has been suggested by Ramon y Cajal and then by Hebb that learning and memory depend critically on long-lasting changes in synaptic strength (Hebb, 1949; Ramon y Cajal, 1909). Hebb postulated that "when an axon of cell A is near enough to excite a cell B and repeatedly or persistently takes part in firing it, some growth process or metabolic change takes place in one or both cells such that A's efficiency, as one of the cells firing B, is increased". In other words, the Hebbian postulate is that if a pre-synaptic neuron A is repeatedly taking part in activating the post-synaptic neuron B, along with a set of other pre-synaptic neurons, then the strength of the synaptic connection between A and B should be increased. This mechanism is believed to store

memory traces. The first experimental evidences came from Bliss and Lomo in 1973. They demonstrated that EPSPs evoked in the hippocampus were increased by repeated high-frequency electrical stimulation, a phenomenon called Long-Term Potentiation (LTP) (Bliss and Lømo, 1973). Thus, repeated firing of a pre-synaptic neuron can induce a long-lasting increase of the activity of a post-synaptic neuron through synaptic strengthening. The fact that this mechanism was discovered in the hippocampus, a region involved in the process of learning and memory formation, has led to extensive studies on the role of LTP in learning (Bliss, T.V.P. & Collingridge, 1993; Huganir and Nicoll, 2013), even though its role in other adaptive conditions is more and more reported (Campelo et al., 2020; Gambino et al., 2014). Several elements suggested LTP to be the engram of memory formation, as interfering *in vivo* with its induction impaired some learning tasks (Holtmaat and Caroni, 2016; Nabavi et al., 2014; Takeuchi et al., 2014). However, the direct implication of LTP in learning and memory remains so far to be conclusively demonstrated.

Although Hebb's postulate appears exact, the inverse mechanism was not considered. At the time when LTP was discovered, it was suggested that an inverse of LTP could exist in the brain, termed Long-Term Depression (LTD). Based on monocular deprivation experiments in kittens (Hubel and Wiesel, 1965; Wiesel and Hubel, 1965), Stent postulated that "when the presynaptic axon of cell A repeatedly and persistently fails to excite the post-synaptic cell B while cell B is firing under the influence of other pre-synaptic axons, metabolic change takes place in one or both cells such that A's efficiency, as one of the cells firing B, is decreased" (Stent, 1973). As the depressing synapse is not active during this mechanism, this synaptic weakening was termed "heterosynaptic" LTD. It has been experimentally confirmed when LTD has been induced on an inactive pathway while inducing LTP in another

(Abraham and Goddard, 1983; Lynch et al., 1977). More commonly, input-specific LTD (or “homosynaptic” LTD) can be observed in the cortex and hippocampus following low-frequency stimulation (Dudek and Bear, 1992; Mulkey and Malenka, 1992; Stanton and Sejnowski, 1989). LTD is thought to be a key mechanism to optimize information storage in a neuronal network, for behavioral flexibility and during sensory-experience adaptation, development and network refinement (Collingridge et al., 2010; Nabavi et al., 2014; Nicholls et al., 2008)

It is now clear that bidirectional long-lasting changes in synaptic strength can be induced by frequency-dependent stimulations. However, those protocols do not reflect realistic firing patterns observed *in vivo*. On the contrary, some LTP paradigms are pathological as they reflect epileptic activity. Other paradigms, based on temporal order between pre-synaptic and postsynaptic firing, are accepted as more physiological and have been observed in several brain regions from different animal species. This plasticity mechanism termed Spike Timing- Dependent Plasticity (STDP) allows strengthening/weakening of synapses in a frequency- and timing-dependent manner. Typically, if the pre-synaptic neuron fires an AP a few milliseconds before or at the same time than the post-synaptic neuron, LTP is produced. The opposite temporal order triggers LTD (Levy and Steward, 1983; Magee and Johnston, 1997; Markram et al., 1997; Sjöström et al., 2008; Stanton and Sejnowski, 1989). STDP does not depend solely on the temporal order between pre- and post-synaptic firing but also on the input-frequency (Lisman and Spruston, 2005; Sjöström et al., 2001, 2008). High-frequency (>20 Hz) burst of pre-before-post pairing produced LTP, while low-frequency (<10 Hz) burst of pre-before-post pairing failed to produced LTP. In contrast, low-frequency (<20 Hz) post-before-pre pairing produced LTD, while high-frequency (>40 Hz) post-before-pre pairing produced LTP (Sjöström et al., 2001). The coincidence

between pre- and post-synaptic activities is detected at synapses and is widely accepted to rely on NMDARs. As explained previously, NMDARs require post-synaptic depolarization to remove their  $Mg^{2+}$  block and allow  $Ca^{2+}$  influx. Therefore, they can detect coincidence between glutamate release due to pre-synaptic activity and depolarization due to post-synaptic spiking (back propagating AP or dendritic spike due to AMPAR activation in synaptic cluster area). Thus, the coincidence between pre- and post-synaptic activity (or pre-before-post) leads to the opening of NMDARs via depolarization-induced removal of  $Mg^{2+}$  block, resulting in a high level  $Ca^{2+}$  influx required to trigger LTP. In contrast, post-before-pre pairing leads to a lower level of  $Ca^{2+}$  rise by the limited opening of NMDARs (Dan and Poo, 2004; Magee and Johnston, 1997; Markram et al., 1997). Although both LTP and LTD are calcium-dependent phenomena, the signaling cascades involved are different and trigger distinct molecular modifications at the origin of the increase or decrease of synaptic strength, respectively.

## 2. Long Term Potentiation

Originally thought to be only a pre-synaptic mechanism, the discovery of silence synapses and their unsilencing during LTP changed the global vision of this process. The elements suggesting a pre-synaptic mechanism for LTP are a decrease of failure rate which in fact have been fully explained by synapse unsilencing (Isaac et al., 1995; Liao et al., 1999), and increase in release probability (Pr) (Jung et al., 2021; Reid et al., 2004). Other experiments using glutamate-uncaging conclusively demonstrated the post-synaptic expression mechanism of LTP (Matsuzaki et al., 2004).

LTP is triggered through repetitive activations of NMDARs leading to a high  $\text{Ca}^{2+}$  influx into the spine. This influx results in the activation of a specific  $\text{Ca}^{2+}$ -dependent signaling cascade within the spine allowing two main processes. The first one is the stabilization of the surface diffusive AMPARs at the PSD through their phosphorylation and through phosphorylation of their TARPs (Bats et al., 2007; Lee et al., 2000; Opazo et al., 2010; Penn et al., 2017; Sumioka et al., 2011; Tomita et al., 2005b). High increase of  $\text{Ca}^{2+}$  concentration within the post-synapse during LTP activates first the  $\text{Ca}^{2+}$ /Calmodulin-dependent protein kinase II (CaMKII). This kinase is then recruited at the PSD where it phosphorylates AMPARs and their TARPs to favor their interaction with PSD-95 and thus trigger their accumulation at the PSD. This leads ultimately to the potentiation of AMPAR-mediated EPSCs in a long-lasting manner (Huganir and Nicoll, 2013; Lee et al., 2000, 2010; Lisman et al., 2012; Murakoshi et al., 2017; Opazo et al., 2010). The fast initial recruitment of AMPARs is only possible thanks to the receptor lateral diffusion from extra-synaptic to synaptic sites (Bats et al., 2007; Borgdorff and Choquet, 2002; Makino and Malinow, 2009; Opazo et al., 2010; Penn et al., 2017). This increase in synaptic AMPAR content is accompanied by an increase of spine volume, a process known as structural LTP (sLTP) (Nägerl et al., 2004; Nishiyama and Yasuda, 2015). The second important process triggered by the influx of  $\text{Ca}^{2+}$  is the exocytosis of AMPARs from recycling and/or reserve vesicular pool. It has been suggested that the newly exocytosed receptors are enriched in GluA1 homomers, as they are calcium permeant. This could help synapses to maintain a higher cytoplasmic calcium level in order to stabilize the CaMKII activity (Granger et al., 2013; Lledo et al., 1998; Lu et al., 2001; Makino and Malinow, 2009; Park et al., 2004; Petrini et al., 2009). To conclude, LTP corresponds mainly to a post-synaptic



event which tends to increase the number/efficiency of AMPARs under the glutamate release site.

### **3. Long Term Depression**

Unlike LTP, LTD is a neuronal mechanism by which synaptic strength is decreased. Actually, several forms of LTD have been characterized. It can be induced following LTP in a process called depotentiation and it can be either homosynaptic (input-specific) or heterosynaptic (Collingridge et al., 2010). While these different forms of plasticity may seem similar as they all trigger weakening of synaptic strength, they use distinct molecular signaling pathways and probably have different functions. Here, the term “LTD” will be used to discuss about input-specific LTD only.

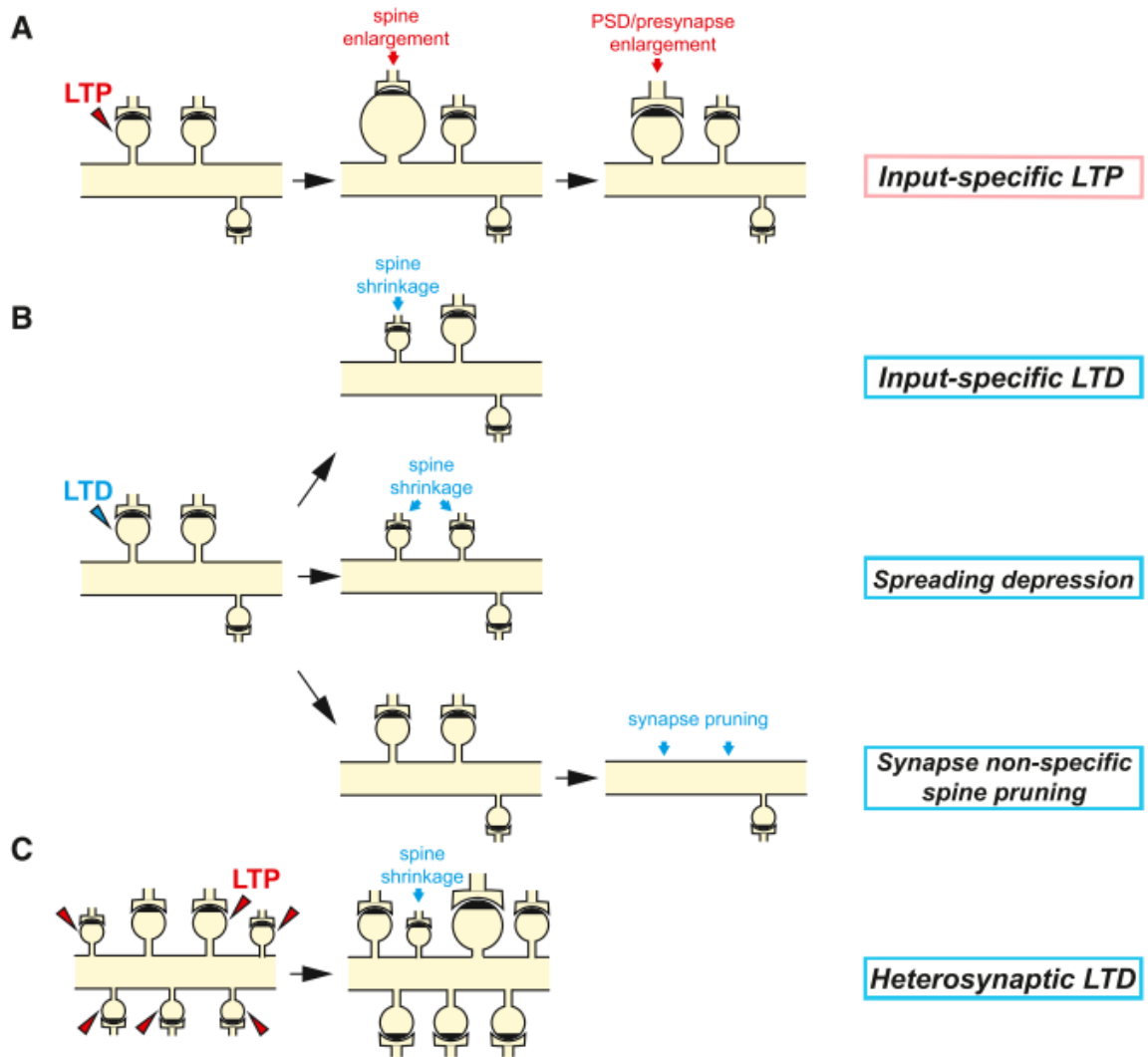


**Figure 8.** Long-term plasticity. (A) Input-specific LTP triggers increase in spine volume. (B) Input-specific LTD triggers either spine shrinkage or spine pruning. (C) Heterosynaptic LTD triggers spine shrinkage when surrounded spines undergo LTP. Figure adapted from Nishiyama and Yasuda, 2015.

## a. Input-specific LTD

LTD has been described in the hippocampus as a post-synaptic mechanism dependent on NMDAR activation (NMDAR-dependent LTD) (Dudek and Bear, 1992). Few studies investigated the role of the pre-synaptic element in the weakening of synaptic transmission. The existence of pre-synaptic mechanisms has been reported following a retrograde signaling (endocannabinoids, nitric oxide ...) and are thought to modify the Pr or the readily releasable pool size. However, this pre-synaptic mechanism is controversial, probably because the studies are performed in various brain regions and at different developmental stages (Collingridge et al., 2010; Goda and Stevens, 1998; Hjelmstad et al., 1997; Kreitzer and Malenka, 2007).

NMDAR-dependent LTD can be induced by low-frequency stimulation, STDP or chemical treatments using specific agonist of NMDARs, which all result in a low or moderate increase of  $Ca^{2+}$  concentration into the post-synapse (Cummings et al., 1996; Dudek and Bear, 1992; Lee et al., 1998; Mulkey and Malenka, 1992; Sjöström et al., 2001). This low increase of calcium concentration in the spine triggers the activation of complex downstream signaling pathways that are not fully characterized yet. A simplified model is that during NMDAR-dependent LTD,  $Ca^{2+}$  binds to calmodulin to activate the Protein Phosphatase 2B (PP2B, also named Calcineurin) which dephosphorylates Inhibitor-1 and thus releases the Protein Phosphatase 1 (PP1) from inhibition (Mulkey et al., 1993, 1994). On the one hand, PP1 dephosphorylates S845 on the GluA1 C-terminal domain and stargazin (Lee et al., 2003, 1998; Sumioka et al., 2010; Tomita et al., 2005b). These dephosphorylations release AMPARs from synaptic trapping sites and thus decrease the amount of receptors at synapses, leading to synaptic depression. However, no direct element has been found about the

involvement of lateral diffusion following AMPAR and TARPs dephosphorylations during LTD. In addition, PP1 has been described to rapidly dephosphorylate S295 on PSD-95, a phosphorylation site known to promote its synaptic accumulation (Kim et al., 2007). On the other hand, PP1 dephosphorylates some kinases such as the Glycogen Synthase Kinase-3 (GSK3) which in turn phosphorylates PSD-95 on T19. This phosphorylation on T19 requires S295 dephosphorylation and promotes PSD-95 removal from synapses (Nelson et al., 2013). It has also been proposed that another important kinase could be involved in LTD. CaMKII, involved in the induction of LTP, could be activated during LTD and phosphorylate GluA1 subunit of AMPAR in its first intracellular loop at S567 (Coultrap et al., 2014; Goodell et al., 2017). This phosphorylation has been shown to decrease synaptic localization of AMPARs (Sainlos et al., 2011; Lua et al., 2010). Thus, CaMKII could sense and discriminate  $Ca^{2+}$  concentration, and phosphorylate specific AMPAR sites and play a bidirectional role in long-term synaptic plasticities. So far, the decrease of synaptic AMPAR number during LTD has been mainly attributed to an endocytosis process (Bhattacharyya et al., 2009; Carroll et al., 1999, 2001; Lüscher et al., 2000). The precise localization between extra-synaptic and peri-synaptic sites for AMPAR to get endocytosed remains unclear. Also, the precise mechanism responsible for AMPAR endocytosis is poorly understood. The main evidence for AMPAR endocytosis is that the N-ethylmaleimide-Sensitive Factor (NSF), which stabilizes AMPARs at the membrane, is replaced by the Adaptor Protein 2 (AP2), that is involved in the recruitment of the machinery required for clathrin-dependent endocytosis (Man et al., 2000). AP2 also binds to dephosphorylated stargazin. Disrupting the association between AP2 and stargazin blocks NMDAR-dependent LTD by preventing AMPAR internalization (Matsuda et al., 2013).

A second major form of LTD requires the activation of group 1 mGluRs (mGluR-dependent LTD) (Bashir et al., 1993). Group 1 mGluRs are widely expressed in the CNS. Both NMDAR- and mGluR-dependent LTD exist in the hippocampus and the patterns of activation required to induce them are similar (Oliet et al., 1997). They also both depend on calcium signaling even if the origin of the calcium increase is different. Group 1 mGluR activation leads to the activation  $Ca^{2+}$  channels and of the phosphoinositide-specific PhosphoLipase C (PLC) which can trigger  $Ca^{2+}$  release from intracellular stores and activate the Protein Kinase C (PKC) (Collingridge et al., 2010; Gladding et al., 2009; Oliet et al., 1997). This increase in intracellular  $Ca^{2+}$  concentration results in the internalization of AMPARs through the possible recruitment of the Protein Interacting with C Kinase 1 (PICK1)-PKC complex at synapses in order to phosphorylate GluA2 subunit of AMPAR and dissociate GluA2-containing AMPAR from the AMPAR Binding Protein (ABP) – Glutamate Receptor Interacting Protein (GRIP) complex, leading to the receptor endocytosis (Casimiro et al., 2011; Collingridge et al., 2010; Gladding et al., 2009; Xiao et al., 2001).

## **b. Neuromodulator-induced LTD**

More recently, a new form of hippocampal LTD has been identified. It can be induced by the activation of post-synaptic purinergic receptor P2XR by noradrenalin-dependent astrocytic release of ATP (Pouget et al., 2014; Yamazaki et al., 2002). This P2XR-dependent LTD, as the classical form of LTD, depends on  $Ca^{2+}$  to trigger AMPAR internalization and synaptic depression. However, in this form of LTD,  $Ca^{2+}$  enters in the post-synaptic element through P2XRs and activates both CaMKII and the

phosphatases PP1 and PP2A. Unlike NMDAR-dependent LTD, calcineurin is not involved. It was showed that both P2XR-dependent LTD and NMDAR-dependent LTD are independent from each other as the induction of one do not occlude the induction of the other one. P2XR stimulation through ATP application or noradrenergic stimulation of astrocytes (to trigger release of endogenous ATP) leads to a rapid removal of synaptic AMPARs and receptor internalization. This ATP-induced AMPAR internalization produces a long-lasting decrease of AMPAR-mediated EPSCs (Pouget et al., 2014). Astrocytes are known to regulate synaptic transmission. Release of gliotransmitters (ATP, glutamate and D-serine) has already been shown to be important for basal transmission and synaptic plasticity (Panatier et al., 2006, 2011; Pascual et al., 2005; Yang et al., 2003). Indeed, in addition to ATP, astrocytes can release D-serine, an endogenous co-agonist of NMDARs (Martineau et al., 2006; Mothet et al., 2000). By releasing D-serine, astrocytes can modulate the activity of synaptic NMDARs and control NMDAR-dependent long-term synaptic plasticity (Panatier et al., 2006; Yang et al., 2003). In conclusion, neurons display two independent ways to decrease synaptic strength either via a synaptic input-specific response or through a more global neuromodulation by astrocytes. Although both lead to a decrease of AMPAR number at synapses, their distinct signaling pathways suggest a specific regulation of AMPAR organization and currents, as well as different physiological roles. It is thus important to decipher their specific impact on the regulation of the synaptic input.

## Chapter 3: Regulation of synaptic structure

The majority of glutamatergic synapses are carried by dendritic spines, which mediate the vast majority of excitatory synaptic transmission in the mammalian brain (Holtmaat and Svoboda, 2009). They represent fundamental computational units of information processing that underlie sensory perception, emotions, and motor behavior. In this chapter, I will present the general features of spines structure and function, before introducing the reshufflings that their support during development and experience.

### 1. Spines' type and morphology

Spines stand out as unique neuro-anatomical specializations, and apart from their general head-and-neck design, no spine looks quite like any other. In fact, spine morphology is highly diverse, covering a broad distribution of shapes and sizes, which conduct to a categorization far from being clear cut. For instance, spine head volumes range from 0.01 to 1  $\mu\text{m}^3$ , while spine necks measure between 50 and 500 nm in diameter and are roughly up to 3  $\mu\text{m}$  in length (Arellano et al., 2007; Harris and Stevens, 1989; Trommald and Hulleberg, 1997). Moreover, these morphological parameters show little correlation with each other.

Despite of this morphological continuum, spines are commonly grouped into a small number of distinct categories, such as stubby, mushroom, thin, and filopodial, based on their appearance. While this categorization scheme may be practical for analysis purposes, it is a gross over-simplification, where the categorization results depend strongly on image quality, which vary between studies. Moreover, image

projection artifacts and limited spatial resolution mask short spine necks, which leads to the false identification of stubby spines (Tønnesen et al., 2014). There are consistent differences in the spectrum of their morphology across different dendritic locations and laminar positions, cell types, brain areas, animal age, and disease states (Nimchinsky et al., 2002), while the density of spines on dendrites is also highly variable; aspiny interneurons lack spines altogether, while cerebellar Purkinje cells carry more than 200,000 spines. The ubiquity of dendritic spines across the phylogenetic tree points to a highly specialized and fundamental role; however, the rhyme and reason behind their remarkable structure and diversity remains enigmatic.

Dendritic spines are very specialized neuronal compartments, which fine morphological and functional analysis still represents a huge challenge in the field. Finally, it is rather noting that structure of spines, notably their morphology, impacts their function (Tønnesen and Nägerl, 2016). Indeed, Tønnesen et al. showed that the neck width enables the isolation of spines from the rest of the dendrite. In those conditions, they behave as isolated compartments where molecular as well as electrical modifications maximize their effects because protected from immediate dilution into the dendritic shaft (Tønnesen et al., 2014).



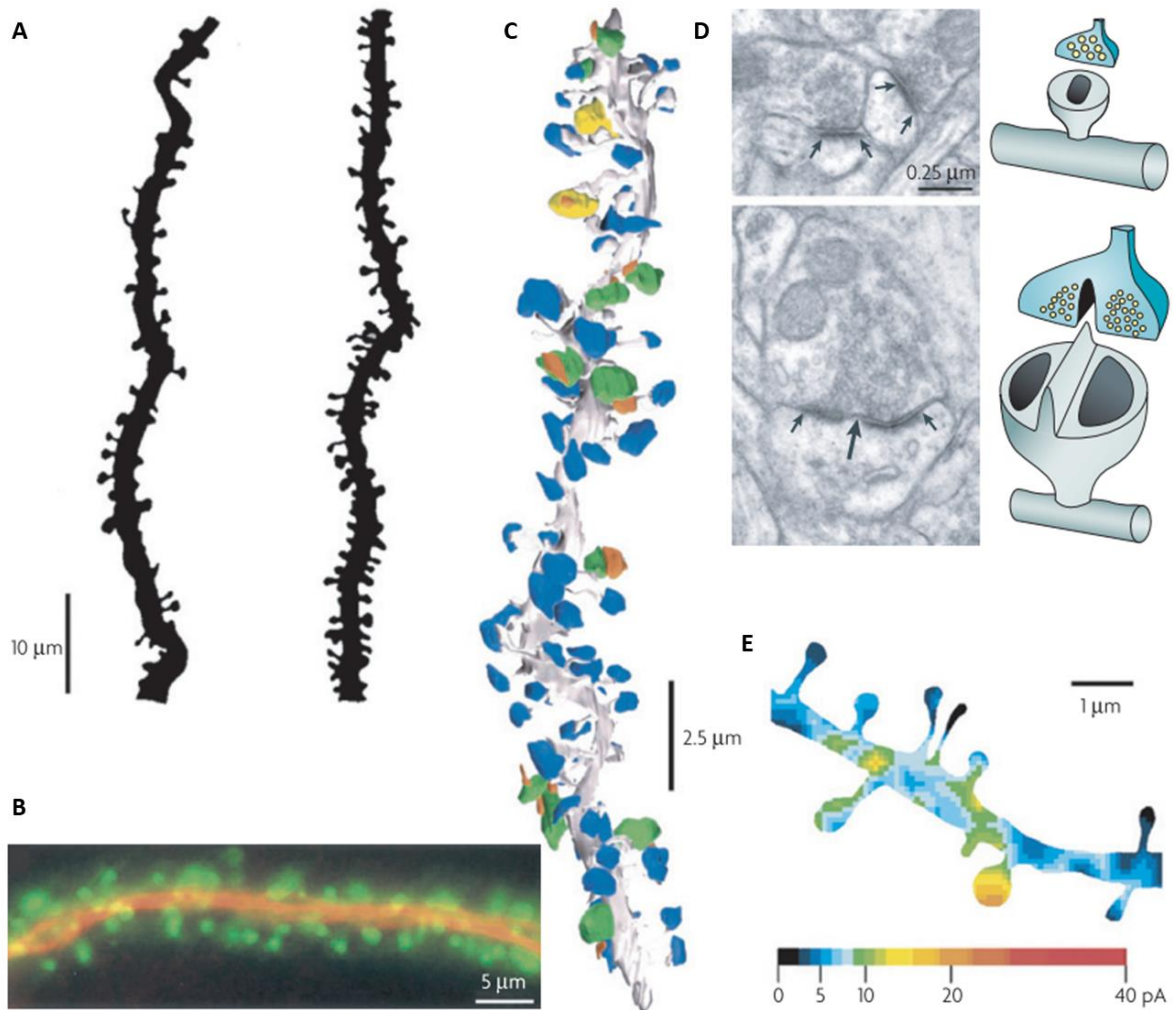


**Figure 9.** Dendritic spines and synapses on pyramidal neurons. A. Two spine-studded dendrites of a stained CA1 pyramidal neuron. B. A dendrite that has been labelled for microtubule-associated protein 2 (MAP2; red) and actin (green). MAP2 is concentrated in the dendritic shafts. Actin filaments in the spine head mediate spine motility. C. A three-dimensional reconstruction of spines and synapses in a typical pyramidal cell, based on electron micrographs of a single stretch of dendrite from a filled cell. Every spine is contacted by at least one synapse. The dendrite and its spines are shown in grey; synaptic boutons forming single synapses are shown in blue; boutons forming multiple synapses onto more than one cell are shown in green; boutons forming multiple synapses onto the same cell are shown in yellow; spines from other dendrites are shown in orange. D. The left-hand panels show electron micrographs of two non-perforated postsynaptic densities (PSDs; top panel, indicated by arrows) and a perforated PSD (bottom panel, the perforation is indicated by the large arrow). The right-hand panel contains schematic diagrams of a non-perforated synapse (top) and a perforated synapse (bottom). E. Two-photon glutamate uncaging at various locations on a dendritic segment. The colors indicate the somatically recorded current amplitude that was measured when uncaging was carried out at each location. Note that the largest response (yellow/orange) occurred when the glutamate was uncaged on a large spine head. From Spruston, 2008.

## 2. Structural plasticity

Time-lapse observation of dendritic spines reveals constant modification of spine morphology on various time scales. Given such dynamic nature of dendritic spines, it is of particular interest to understand how dendritic spines can be regulated by synaptic changes as it is the case during their morphogenesis (Lanoue et al., 2013).

Over the last decade, extensive experimental studies using EM or two-photon imaging combined with glutamate uncaging and electrophysiological approaches have established several ground rules for the relationship between their structure and function. First and foremost, there is a broad consensus that the size of the spine head scales with the size of the PSD (Arellano et al., 2007; Harris and Stevens, 1989; Trommald and Hulleberg, 1997), and the amplitude of the excitatory post synaptic current (Matsuzaki et al., 2001). Accordingly, the induction of synaptic long-term potentiation leads to spine head enlargement that scales with the potentiation of the EPSC (Lang et al., 2004). This structural effect primarily occurs in smaller spines (Matsuzaki et al., 2004), and is saturable as repeated rounds of induction lose their effectiveness, much like LTP. While synaptic potentiation and spine enlargement occur within seconds after the induction protocol, the increase in PSD size develops more slowly over tens of minutes (Bosch *et al.*, 2014; Holtmaat *et al.*, 2006), indicating that multiple, kinetically distinct processes underlie the molecular and morphological remodeling of synapses. In addition to modifications of existing spines, spines can grow *de novo* in response to a variety of triggers, including LTP-inducing electrical stimulation, two-photon glutamate uncaging, or altered sensory experience (Nägerl et al., 2004), leading to the formation of new functional synapses (Knott et al., 2006;

Nägerl et al., 2007). Conversely, electrical induction of LTD leads to shrinkage of the spine head and increased spine loss (Holtmaat et al., 2006; Zhou et al., 2004), which can also be induced by glutamate uncaging (Hayama et al., 2013; Oh et al., 2013) and optogenetic stimulation (Wiegert and Oertner, 2013). Wiegert and colleagues also showed that induction in sequence of LTD and LTP at the same synapse could promote either growth or suppression of spines, depending on the order of the sequence of induction (Wiegert et al., 2018). Taken together, these studies support the view that during synaptic plasticity spine heads undergo size changes followed by remodeling of the PSD to accommodate a higher or lower number of receptors, depending on whether LTP or LTD is induced. According to this view, spines serve primarily as place holders for the PSD and changes in post synaptic strength are mediated by modulating the efficacy or number of synaptic receptors.

### **3. Synaptic pruning**

Different molecular re-organization and pathways activation have been reported to be responsible for spine elimination, ranging from LTD-associated mechanisms as mentioned previously, activity-mediated competition between spines, microglia or astrocytes-mediated mechanisms (Stein and Zito, 2019). It is clear that these mechanisms correspond to different phenomenon that occur at diverse developmental stage and physio-pathological situations. However, they all lead to a re-organization of neuronal network (Holtmaat and Svoboda, 2009).

In fact, although most studies have focused on the outgrowth and stabilization of dendritic spines, spine shrinkage and elimination also play a vital role in the neural circuit plasticity that underlies learning. Indeed, the formation and stabilization of new

dendritic spines as new circuits are formed during learning is accompanied by elimination of preexisting spines (Chen et al., 2015; Lai et al., 2012; Nakayama et al., 2015; Sanders et al., 2012; Xu et al., 2009; Yang et al., 2009); a subset of these studies in addition reported that the effectiveness of learning was correlated with the observed degree of spine elimination (Lai et al., 2012; Yang et al., 2009). Notably, induction of complete hearing loss in zebra finches resulted in decreased spine size and subsequent stability, and larger decreases in spine size accompanied stronger vocal deterioration of pre-learned songs (Tschida and Mooney, 2012). In addition, spines gained in the visual cortex following monocular deprivation shrank after binocular vision had been restored, suggesting that the decrease in spine size reflected the deactivation of neural circuits established during monocular deprivation (Hofer et al., 2009). Furthermore, during development, an early phase of dendritic spine addition and synaptogenesis is followed by a period of spine pruning and synaptic refinement, during which inappropriate and redundant spiny synapses are eliminated (De Felipe et al., 1997; LaMantia and Rakic, 1990; Zuo et al., 2005). Thus, spine shrinkage and elimination appear to be essential for fine tuning of neural circuits both when they are established during development and during learning in adults.

A series of recent articles also highlighted a vital daily, or better nightly, role for spine shrinkage mechanisms in restoring synaptic homeostasis. Global synaptic downscaling during sleep is thought to be important to counterbalance the increases in spine size and density that are occurring during sensory processing and learning in the wake state, renormalizing synaptic strength, and spine size to allow for new learning on the next day (Diering *et al.*, 2017; Li *et al.*, 2017; De Vivo *et al.*, 2017; Valnegri et al., 2011). Interestingly, this synaptic downscaling was restricted to small spines and spared larger spines (De Vivo et al., 2017), which have been associated

with memory. These results are consistent with those from recent *in vivo* imaging studies, where the authors found that spine pruning during rapid eye movement (REM) sleep balanced the number of motor skill learning-induced new spines that were strengthened and maintained (Li et al., 2017).

Initial studies of the activity-dependent mechanisms that drive spine elimination examined the consequences of LTD-inducing low-frequency stimulation (LFS; 900 stimuli at 1 Hz) (Dudek and Bear, 1992) on the size and stability of dendritic spines. Using a local stimulating electrode placed within ~10-30  $\mu\text{m}$  of a fluorescently labeled dendrite, three independent studies published in 2004 found that LFS induced shrinkage and elimination of dendritic spines (Nägerl et al., 2004; Okamoto et al., 2004; Zhou et al., 2004), supporting the hypothesis that synaptic weakening is associated with a reduction in spine size. Later, Wiegert and colleagues revisited the LFS by replacing the electrical stimulation by optogenetic to LTD-induced synaptic selection (Wiegert and Oertner, 2013). Importantly, Zhou and colleagues showed that shrinkage was observed only in dendritic spines near to the stimulating electrode (<30  $\mu\text{m}$ ); distant spines (>90  $\mu\text{m}$ ) did not shrink, consistent with findings of Wiegert and colleagues (Wiegert and Oertner, 2013). LFS-induced spine shrinkage and elimination (Zhou et al., 2004), like LFS-induced LTD (Dudek and Bear, 1992), required activation of NMDARs and the downstream  $\text{Ca}^{2+}$ -dependent activation of calcineurin (protein phosphatase 2B, PP2B). Unlike synaptic depression, spine shrinkage was independent of protein phosphatase 1 (PP1), a downstream effector of calcineurin; instead, spine shrinkage was mediated by the actin severing protein cofilin and the shift of the F-actin/G-actin equilibrium toward G-actin (Okamoto et al., 2004; Zhou et al., 2004). A subsequent study in hippocampal pyramidal neurons furthermore showed

that intracellular perfusion of activated cofilin was sufficient to induce dendritic spine shrinkage (Noguchi et al., 2016). These initial studies found widespread spine shrinkage and loss on stimulated dendritic segments. However, because they relied on broad synaptic stimulation, it was not possible to determine whether the widespread spine shrinkage observed was due to input-specific mechanisms operating at several simultaneously stimulated spines, or rather due to spreading depression to nearby unstimulated spines. Oh and colleagues recognized that this issue could be addressed using two-photon glutamate uncaging (Matsuzaki et al., 2001; Oh et al., 2013), which allows for targeted activation of individual dendritic spines. Low-frequency uncaging (LFU) of glutamate at a single dendritic spine induced input-specific long-lasting synaptic weakening and spine shrinkage at individual dendritic spines, but not at neighboring unstimulated spines (Oh et al., 2013). This input-specific spine shrinkage was dependent on NMDAR activation and, intriguingly, was differentially regulated in small and large spines; shrinkage of large spines also required signaling through group I mGluR activation and the activation of inositol trisphosphate receptors (IP3Rs) (Oh, Hill and Zito, 2013). Thus, LTD-inducing stimulation at individual dendritic spines was sufficient to drive input-specific spine shrinkage and synaptic weakening.

Dendritic spine shrinkage and elimination has also been shown to occur downstream of activation of group I mGluRs, which have been well-established to drive a form of LTD that coexists with NMDAR-dependent LTD (Oliet et al., 1997). LFU experiments also supported a role for mGluRs in spine shrinkage, but instead suggested that mGluR- and IP3R-dependent signaling selectively drives spine shrinkage in large spines (Oh et al., 2013). Unexpectedly, a recent additional study reported no effects on spine elimination after a single DHPG application, but instead

observed increased spine elimination in response to repeated DHPG stimulations given on consecutive days (Hasegawa et al., 2015). Despite inconsistencies in the induction protocols and the downstream signaling mechanisms required to induce spine shrinkage and elimination, mGluR-dependent LTD has been clearly associated with dendritic spine shrinkage and elimination.

To conclude, in parallel to molecular re-organization, LTD triggers morphological changes. LTD triggers either spine shrinkage or pruning (Nägerl et al., 2004; Nishiyama and Yasuda, 2015; Wiegert and Oertner, 2013; Woods et al., 2011). This network reorganization during LTD is thought to be at the origin of its physiological role.

## **Thesis problematic**



Integrated in a network, a neuron receives at synapses thousands of signals coming from its partners in a spatial and temporal dependent manner and therefore need to integrate them for transmission in the form of an action potential.

Over the last decades, the view of the synapse has evolved, from a fix entity receiving signaling in a passive manner, to an extremely dynamic structure, able to re-organize itself at the molecular level. Indeed, application of *in vivo* and *ex vivo* 2P imaging coupled with electrophysiology has shown that such molecular reshufflings are related to structural changes of synapses.

However, several points remain unclear. First, parts of the molecular organization of glutamatergic synapses are elusive, notably how the different types of receptors are organized together at the synapse. If the nano-organization of AMPARs starts to be well understood, the one of NMDAR and mGluR remains hypothetical, even though this could crucially impact their activation. Second, how this organization evolves during synaptic plasticity is unknown. Beyond the report of endocytosis changes of AMPARs and consequent changes of synaptic currents, how is the nano-organization of synapses reshuffled during synaptic plasticity? Finally, structure and function of synapses interact together, but function study has been mainly limited to electrophysiological recordings, which are insufficient to understand the precise impact of the synaptic nano-organization on the structure of spines.

During my PhD, I studied therefore how the dynamic nano-organization of synapses regulate its function and structure. I notably focused on the post-synaptic interaction of LTD and pruning.

In the first chapter of the results, we studied how AMPARs, NMDARs and mGluRs are organized and co-activated with each other group. We showed as well that this fine organization impacts the profile of activation of receptors and therefore regulate synaptic physiology.

This work completed our new vision of the role of nano-organization of glutamate receptors on the synaptic transmission at the basal state. In the second part of the results, we used super-resolution imaging techniques combined with electrophysiology to decipher the AMPAR re-organization induced during Long-Term Depression. Through this project, we demonstrated that compared to P2XR-dependent LTD, NMDAR-dependent LTD cannot be restricted to an increase of AMPAR endocytosis, but corresponds to a precise new equilibrium between the main synaptic molecular components.

Finally, in the last chapter, we investigated how evolution of synaptic nano-organization regulates synaptic pruning by modulating the relationship LTD-pruning. We showed indeed, by combining confocal imaging with electrophysiological recordings, that the isolation in time and space of a synapse favors its pruning following specific molecular reshufflings.

## **MATERIAL AND METHODS**

## 1. Primary hippocampal neurons culture

Cultures of dissociated hippocampal neurons were prepared from E18 Sprague-Dawley rats embryos of either sex, as described in (Kaech and Banker, 2006). First, brains were extracted and hippocampi were isolated in HBSS containing Penicillin-Streptomycin (PS) and HEPES. For dissociation, all hippocampi were incubated in 5 mL of Trypsin-EDTA/PS/HEPES solution for 15 min at 37°C. After two washes with warm HBSS, a mechanical dissociation with Pasteur pipet pre-coated with horse serum was performed. The number of cells was counted in a Malassez grid in order to plate the appropriate number of cells according to the following requirement.

Glial cell feeder layers were prepared from dissociated hippocampi too, plated between 20 000 to 40 000 cells per 60 mm dish (according to the Horse Serum batch used), and cultured in MEM (Fisher Scientific) containing 4.5 g/L glucose, 2 mM L-glutamine and 10% horse serum (Invitrogen) for 14 days.

For cultured hippocampal neurons, cells were plated at a density of 200 000 cells per 60 mm dish containing four 18 mm coverslips (Mariefield). Cells were plated in supplemented Neurobasal Plus medium containing 1.5% Horse serum heat inactivated. After 2h, time required for neurons to adhere to coverslips, coverslips were transferred in 60 mm dish containing the 14 days old glial feeder layer, and MEM was replaced by Neurobasal Plus medium supplemented with 0.5 mM GlutaMAX and 1X B-27 Plus supplement (Thermo Fischer Scientific). 2  $\mu$ M Ara-C was added after 3 days in vitro (DIV) to stop glia's proliferation. Before experiments, cultured hippocampal neurons were maintained at 36.6°C with 5% CO<sub>2</sub> for 14-16 DIV.

## 2. Transfections

Neurons have been chemically transfected at 9-11 DIV using Calcium phosphate transfection method. Most of the time, experiments have been done on endogenous proteins. However, when it was not possible, neurons were transfected with constructs listed above:

- Soluble EGFP from Clontech Company was used as a cytosolic marker and as a transfection reporter.
- Two constructs were overexpressed to study reshufflings of PSD-95 and were produced in the lab: 1) WT PSD-95 plasmid containing IRES EGFP to identify transfected neurons was used as a control, 2) T19A PSD95 plasmid containing IRES EGFP (Nelson et al., 2013).

## 3. Electrophysiology

Electrophysiology is a technique that possesses a good temporal resolution. Indeed, it is a good way to assess the function of a neuron or a network. As mentioned in the introduction, different events can be recorded. Notably, the measurement of mEPSCs enables to assess the evolution of activatable AMPARs at the level of the single synapse, as the number of AMPARs is proportional to the amplitude of mEPSCs. On their side, spontaneous EPSCs are informative concerning the N, Pr and Q values, as detailed in the introduction. It is here important to mention that the Pr is sensible to the calcium level, and that therefore experimenter can play with it by changing calcium

concentration in the extra-cellular solution. During my PhD, I measured electrically stimulated events, mEPSCs, and spontaneous events. First, I measured NMDAR-mediated mEPSCs in order to assess the consequences of NMDAR synaptic location on its function in the first chapter of the results. Then, I measured AMPAR-mediated mEPSCs to assess induction of LTD at synapses, and stimulated EPSCs to measure its impact on short-term plasticity. Finally, I recorded spontaneous EPSCs to understand how LTD and pruning affect the three parameters that define summative inputs: N, Pr and Q.

#### **a. Whole-cell patch clamp on cultured neurons**

Coverslips of neurons were placed in a Ludin Chamber on an inverted motorized microscope (Nikon Eclipse Ti). For mEPSCs recording, extracellular solution was composed of the following (in mM): 110 NaCl, 5 KCl, 2 CaCl<sub>2</sub>, 2 MgCl<sub>2</sub>, 5 MgCl<sub>2</sub>, 10 HEPES, 10 D-Glucose, 0.0005 Tetrodotoxin and 0.1 Picrotoxin (pH 7.4; ~262 mOsm/L). Patch pipettes were pulled using a horizontal puller (P-97, Sutter Instrument) from borosilicate capillaries (GB150F-8P, Science Products GmbH) to obtain a resistance of 4-6 MΩ and filled with intracellular solution composed of the following (in mM): 118 K-gluconate, 10 HEPES, 1.1 EGTA, 3 ATP, 0.3 GTP, 0.1 CaCl<sub>2</sub>, 3 P-Creatine (pH 7.3; 260 mOsm). Transfected neurons were identified under epifluorescence from the GFP signal. Recordings were performed using an EPC10 patch clamp amplifier operated with Patchmaster software (HEKA Elektronik). Whole-cell voltage clamp recordings were performed at room temperature and at a holding potential of -70 mV.

Unless specified otherwise, all chemicals were purchased from Sigma-Aldrich except for drugs, which are provided by Tocris Bioscience.

In order to record spontaneous EPSCs in neuronal culture, similar methods were used. Extracellular recording solution was composed of the following (in mM): 110 NaCl, 5 KCl, 0.2 / 2 / 4 CaCl<sub>2</sub>, 2 MgCl<sub>2</sub>, 10 HEPES, 10 D-Glucose, 0.1 Picrotoxin (pH 7.4; ~256 mOsm/L). The pipettes are filled with intracellular solution composed of the following (in mM): 100 K-gluconate, 10 HEPES, 1.1 EGTA, 3 ATP, 0.3 GTP, 0.1 CaCl<sub>2</sub>, 5 MgCl<sub>2</sub> (pH 7.3; 230 mOsm).

Miniature EPSCs analysis were performed using a software developed by Michel Goillandeau, Detection Mini. The principle of the detection used is the median filter. The program takes a window sets by the experimenter and for each point of the biological signal, it calculates the median of values in the window before and after the point. The detection is not made on the biological signal but on another signal (called Detection Signal), calculated from the difference between the filtered signal and the baseline signal. For further analysis, only detected events which amplitude is comprised between 5 and 50 pA are taken into account.

For spontaneous EPSCs, the area and duration from individual events were measured using the software Clampfit 10.7 (Molecular Devices). A template-based search of events was used to obtain the parameters.

## **b. Acute slice electrophysiology**

### ***a) Slice preparation***

Acute slices were prepared from P16 Sprague-Dawley rats of both sexes. Rats were anesthetized with 5% isoflurane prior to decapitation. Brains were quickly extracted and the two hemispheres were separated and placed in ice-cold, oxygenated (95% O<sub>2</sub>/5% CO<sub>2</sub>) sucrose-based artificial cerebrospinal fluid (ACSF) containing (in mM): 250 Sucrose, 2 KCl, 7 MgCl<sub>2</sub>, 0.5 CaCl<sub>2</sub>, 11 Glucose, 1.15 NaH<sub>2</sub>PO<sub>4</sub> and 26 NaHCO<sub>3</sub> (pH 7.4; ~305 mOsm/L). Sagittal slices were cut (350 μm thick) and incubated for 30 minutes at 32°C in carbogenated (95% O<sub>2</sub>/5% CO<sub>2</sub>) ACSF containing (in mM): 126 NaCl, 3.5 KCl, 2 CaCl<sub>2</sub>, 1 MgCl<sub>2</sub>, 1.2 NaH<sub>2</sub>PO<sub>4</sub>, 25 NaHCO<sub>3</sub> and 12.1 Glucose (pH 7.4; ~310 mOsm/L). Subsequently, slices were incubated for 30 minutes at room temperature and used for 5 hours after preparation. Experiments were performed in a submerged recording chamber at 30-32°C with continuous perfusion of carbogenated ACSF.

### ***b) Whole-cell patch clamp recording and analysis***

Whole-cell voltage-clamp recordings (borosilicate pipettes, 4-6 MΩ) were made at 30-32°C from CA1 pyramidal neurons. Slices were perfused with the previously described carbogenated ACSF with added Gabazine (2 μM). The intracellular solution was composed of (in mM): 125 Cs methane sulfonate, 4 NaCl, 10 HEPES, 10 EGTA, 2 MgCl<sub>2</sub>, 5 P-Creatine, 4 Na-ATP (pH 7.3; ~300 mOsm/L). Synaptic responses were obtained by 2 stimulations of Schaffer collateral with 0.2 ms pulses at 50 Hz. 20 series



spaced by 20 seconds were performed and averaged. Each response was normalized to the first one amplitude. Paired-Pulse Ratios were measured using Stimfit software.

## 4. Immunolabeling

In order to investigate protein nanoscale organization with d-STORM technique, an immunolabeling was first realized on either surface or intracellular proteins. The following protocol describes the main steps for both types of immunolabeling.

For surface labeling, 14 DIV neurons were first incubated for 7 min at 37°C with the surface primary antibody diluted in culture medium. Then, cells were fixed by a solution of PFA/Sucrose at 4% for 10 minutes. After 3 PBS washes, neurons were incubated in 50 mM NH<sub>4</sub>Cl (Sigma Aldrich) solution for 10 min to block PFA aldehyde groups and reduce background autofluorescence induced by these aldehyde groups.

For intracellular proteins, neurons were initially fixed with PFA/Sucrose at 4% for 10 minutes, and after 3 PBS washes, neurons were incubated in 50 mM NH<sub>4</sub>Cl solution for 5 minutes. After 3 PBS washes, cells were treated for 5 minutes with triton at 0.1% to permeabilize cell membranes then washed 3 times with PBS, they were incubated with 2% Bovine Serum Albumin (BSA) solution for 1 hour to saturate unspecific binding sites. Neurons were then incubated with primary antibody diluted in 2% BSA solution, and incubated for 1 hour at room temperature.

Then, protocol is identical for both surface and intracellular labeling: following 3 BSA washes, another 2% BSA incubation was performed for 1 hour to precede the incubation with both secondary antibodies. A dye coupled secondary antibody at 1/500

in BSA was incubated for 1 hour at room temperature. Following 3 BSA and 3 PBS washes, a post-fixation in 2% PFA/Sucrose solution was performed. Finally, 3 PBS washes followed by 5 minutes in 50 mM NH<sub>4</sub>Cl and 3 PBS washes. Finally, neurons were kept at fridge in PBS for maximum two weeks before imaging.

Target	Company	Full name of antibody	Reference
<b>GluA2</b>	Gift from Gouaux Lab	Anti-GluA2	
<b>Homer1</b>	Synaptic Systems	Anti-Homer 1 Polyclonal Guinea Pig Antibody	160 004
<b>LC3B</b>	Sigma	Anti-LC3B antibody produced in rabbit	L7543
<b>PSD-95</b>	Thermo Fisher	PSD-95 Monoclonal Antibody (7E3-1B8)	MA1046
<b>Synaptotagmin-1</b>	Synaptic Systems	Anti-synaptotgamin 1 lumenal domain, coupled to CypHer5E (pH sensitive)	105 311CpH

## 5. LTD induction

In order to investigate the organization or mobility of AMPAR during Long-Term Depression, 14 DIV transfected neurons were used. Neurons were maintained at 37°C before the fixation step. To induce LTD through P2XR stimulation, neurons were also incubated with the adrenergic receptor antagonist CGS15943 to avoid the activation of this other pathway by ATP treatment as referred in (Pouget et al., 2016, 2014).

NMDAR-dependent LTD				
Condition	Treatment	Duration	Location	Time
<b>30 min</b>	30µM NMDA in culture media	3min	12 well plate	30 to 27 min
		27min	Dish	27 to 0 min
<b>Control</b>	Culture media	3 min	12 well plate	30 to 27 min
		27 min	Dish	27 to 0 min

P2XR-dependent LTD				
Condition	Treatment	Duration	Location	Time
30 min	3 $\mu$ M CGS15943	10 min	Dish	40 to 30 minutes
	10 $\mu$ M ATP + 3 $\mu$ M CGS15943 in culture media	1 min	12 well plate	30 to 29 min
	3 $\mu$ M CGS15943	29 min	Dish	29 to 0 min
Control	3 $\mu$ M CGS15943	10 min	Dish	
	Culture media+ 3 $\mu$ M CGS15943	1 min	12 well plate	30 to 29 min
	3 $\mu$ M CGS15943	29 min	Dish	29 to 0 min

**Table 1.** Long-Term Depression induction protocols.

## 6. Single Molecule Localization Microscopy

### a. Principle of fluorescence microscopy

Fluorescence microscopy is the most widely used method to study protein organization on both fixed and living sample. The excitation of the fluorescent dye, resulting from the absorption of a photon, brings it from its electronic ground state (S<sub>0</sub>) to an excited state (S<sub>1</sub>). The energy of the photon must match the energy difference between the ground (lower energy) and the excited state (higher energy). Both S<sub>0</sub> and S<sub>1</sub> are singlet states, which means that all electrons of the dye are spin-paired. During the few nanoseconds in excited state, the fluorescent molecule undergoes into a vibrational relaxation or internal conversion, which corresponds to a loss of energy through vibration or heat. Dye is at this moment in the lowest excited state and can return to ground state by emission of a photon of lower energy than the absorbed one (because of the vibrational relaxation). This last notion is called the Stokes shift. In addition to S<sub>0</sub> and S<sub>1</sub>, other states can be reached following spin-unpairing of the dye

(intersystem crossing) and bring the dye from the singlet excited state to an excited triplet state ( $T_n$ ). This state is metastable which means that it can stay from nanosecond to second or even minutes. The relaxation from  $T_n$  to  $S_0$  is at the origin of the phosphorescence. The exploitation of this excited triplet state is at the base of the d-STORM technique, a powerful method used in SMLM as it is described in the coming chapters.

The photo-bleach corresponds to the disruption of the dye due to illumination. Its properties are specific from each type of dye and correspond to a loss of an electron, when they are either in  $S_1$  or  $T_n$ , which interacts with oxygen to form reactive oxygen species. In function of time, local accumulation of ROS tends to break the dye by chemical reaction.

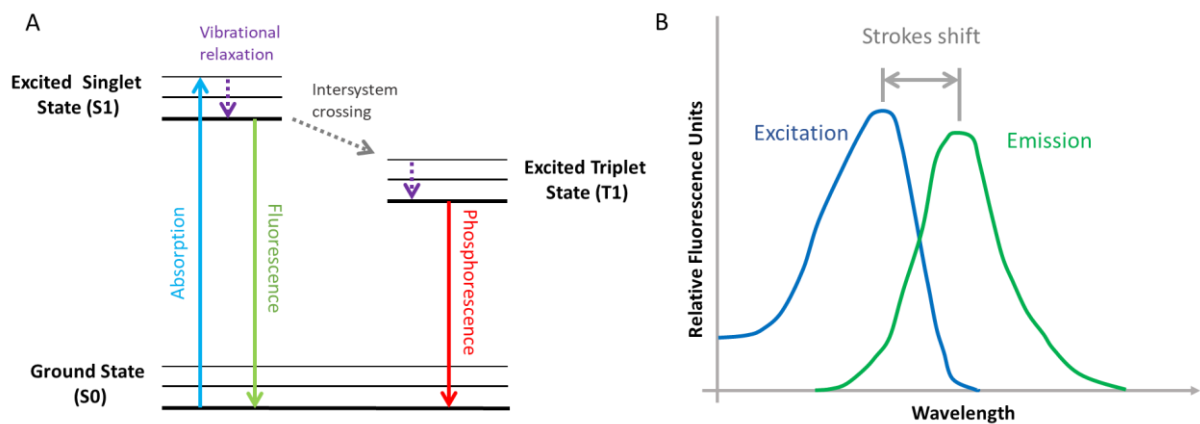


**Figure 10.** The principle of Fluorescence. (A) Jablonski diagram showing the timeline of fluorescence and the different energetic level in which the fluorescent dye can transit through. (B) Excitation and Emission spectrum of the Green Fluorescent Protein (GFP). The energy lost through vibrational relaxation is responsible for the increased wavelength of the emission spectrum. This displacement is named the Stokes shift.

## **b. Diffraction limit & resolution in fluorescent microscopy**

A fluorescent molecule can be considered as a point source emitting light waves. The fluorescent wavefronts emanating from the point source become diffracted at the edges of the objective aperture and lenses. This phenomenon of light diffraction, established by Huygens and Fresnel, is due to the waveform property of light. When light waves encounter an obstacle or an aperture, they tend to bend around it and spread at oblique angles. The spreading of the diffracted wavefronts produces an image composed by a central spot with a high intensity, and several interference rings of lower intensity. This diffracted point is called Airy disk and represents the idealized in focus 2D Point Spread Function (PSF) for a fluorescence microscope.

The Abbe theory says that the lateral resolution ( $r_{x,y}$ ) correspond to the center of the Airy disk or  $r_{x,y} = \lambda/2NA$  where  $\lambda$  corresponds to the wavelength and NA to the Numerical Aperture of the objective. Technically, the resolution can be defined as the minimal separation distance between two point-like objects in which they can still be distinguished as individual emitters. This definition is provided by the Rayleigh criterion where the resolution corresponds to:  $r_{x,y} = 0.61\lambda/NA$ . In other terms, two points can be distinguished if the maximum intensity of one Airy pattern coincides with the first minimum of the other Airy pattern.

## **c. Principle of SMLM**

Over the last decade, new microscope techniques have been developed to bypass the diffraction limit and improve the resolution to observe the precise

organization of proteins in biological samples. This part will only focus on Single Molecule Localization Microscopy (SMLM), even if other techniques as Stimulated Emission Depletion (STED) or Structured Illumination Microscopy (SIM) can be used to bypass the diffraction limit. It is important to note here that the development of this so-called super-resolution imaging techniques is closely linked to the discovery and creation of fluorescent dyes such as the Green Fluorescent Protein (GFP), its derivatives and many organic fluorophores.

SMLM aims to decorrelate over the time the emission of fluorescence of single emitters. This allows to observe individual PSF and to fit mathematically this signal to determine the x,y coordinates of the source point (PSF centroid). In SMLM, the resolution obtained is not dependent anymore on our capacity to distinguish two close points, but relies on the precision to localize the object from its diffracted image. The resolution achieved in SMLM is in the range of 10-50 nm against ~250 nm with conventional fluorescence microscopy. For that, the first aim is to ensure that the emission of fluorescence of the biological sample is in a condition of single molecule detection. To achieve this goal, three approaches can be used: (i) the control of the labeling efficiency to maintain a fluorescent molecules concentration lower enough to be in single molecule condition, (ii) the use of fluorescent protein which require photo-activation to emit fluorescence (Photo-Activated Localization Microscopy, PALM), or (iii) the use of the ability for some organic fluorophore to reach a triplet state to control the density of emitting dyes over the time (direct-STochastic Optical Reconstruction Microscopy, d-STORM).

## d. Resolution in SMLM

In SMLM, the resolution is linked to the precision in localizing the object from its airy pattern. However, it is important to know that the localization precision does not correspond to the resolution. The resolution can be approximated in SMLM to  $r = 2.3p$ , where  $p$  is the localization precision. Several factors can affect this precision: the number of photons emitted by the fluorophore, the background signal, the stability of the system during the acquisition, the labeling density and the labeling accuracy

Methods to determine the centroid coordinates are generally based on statistical curve-fitting algorithms to fit the measured photon distribution (the PSF) by a Gaussian function. The localization precision ( $\sigma$ ) can be described by this complex relationship (Deschout et al., 2014):

$$\sigma^2 = s^2 + \frac{p^2}{12N} + \frac{8\pi s^4 b^2}{p^2 N^2}$$

where  $s$  is the standard error of the Gaussian fit,  $p$  is the camera pixel size,  $N$  is the number of photons,  $b$  is the background photon count per pixel. To simplify, the localization precision can be resumed to:

$$\sigma = s/\sqrt{N}$$

Three other factors are critical to accurately reveal a structure with SMLM:

- As acquisitions are not instantaneous but can last couple of minutes to hours, it is crucial to correct the lateral drift induced by the set-up properties. Better the xy drift correction is, better will be the precision of single molecule or biological object localization. To this aim, we used fluorescent beads as fiducial markers such that we can track and then correct all images by the bead nanoscale position.

- The affinity of the labeling is a critical point. It has been reported that mEos only has 50 to 60% well folded proteins, meaning that only half of the fused-proteins expressed will be detected. In parallel, antibody-based labeling requires high quality antibodies, with high specificity and affinity. The required density of fluorescent probes, to label correctly a specific structure/protein of interest, should satisfy the Shannon-Nyquist theorem which says that the distance between neighboring fluorescent probes (sampling interval) should be at least twice shorter than the desired resolution. In other terms, to resolve a structure of 50 nm of diameter, a fluorophore should be localized every 25 nm.
- Finally, antibody based SMLM presents an intrinsic bias due to the antibody size. The use of primary and secondary antibodies method of labeling implies that the fluorophore is positioned at ~20 nm from the target (when the pointing accuracy could be of 10 nm). Several ways to decrease the size of the labeling have been developed in the last few years as described in the following part.



## 7. direct - Stochastic Optical Reconstruction Microscopy

### a. d-STORM general principle

The technique takes advantage of biophysical properties of some organic fluorophores to reach triplet state as explained above. Using high power laser and specific imaging solution containing thiols, some dyes can be sent from ground state to triplet state. The stabilization of this triplet state thanks to oxygen scavengers (that protect from photo-bleaching), allows the stochastic relaxation to ground state of few fluorophores over the time and thus to have a sparse fraction of fluorophore emitting fluorescence at one time point. Each fluorophore is able to cycle several times between fluorescent ( $S_0-S_1-S_0$ ) and non-fluorescent triplet state ( $T_n$ ) before photobleaching. Several fluorophores can be used for d-STORM, however, for now, the best in term of resolution and capability to easily reach the triplet state, is the Alexa647. Other fluorophores can be used to perform multicolor d-STORM experiments such as Alexa568 or Alexa532. Finally, it is important to note that d-STORM is not compatible with live imaging as it requires imaging solution containing thiols and oxygen scavengers. d-STORM has been extensively used to investigate the organization of endogenous and exogenous proteins into fixed biological sample with a resolution of ~10 nm.

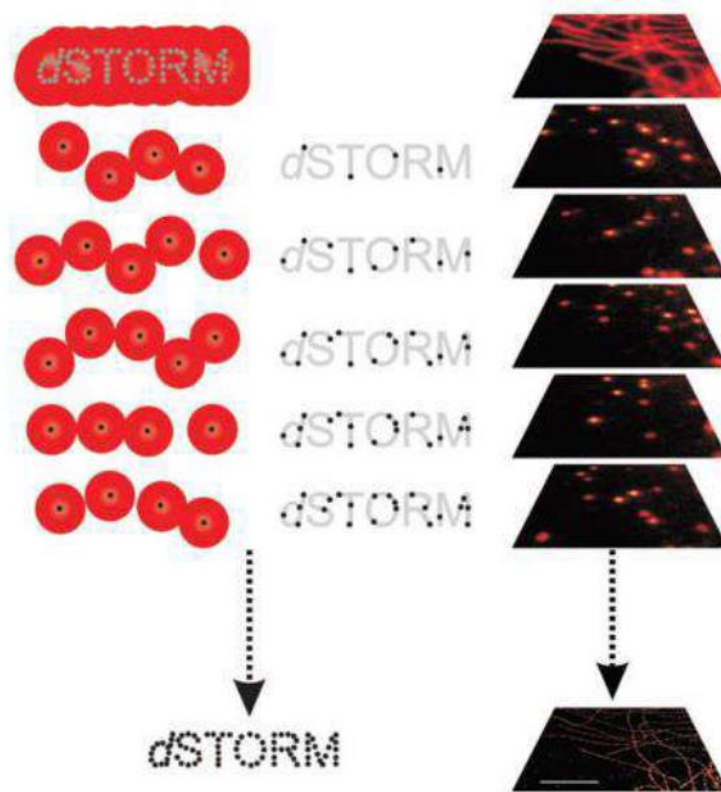


**Figure 11.** d-STORM principle. Figure from van de Linde et al 2011

## **b. d-STORM application**

d-STORM experiments have been done on fixed neurons labeled as described in subchapter 3. d-STORM imaging was performed on a LEICA DMI8 mounted on an anti-vibrational table (TMC, USA) used to minimize drift, Leica HCX PL APO 160x 1.43 NA oil immersion TIRF objective and laser diodes with following wavelength: 405 nm, 488 nm, 532 nm, 561 nm and 642 nm (Roper Scientific, Evry, France). Fluorescent signal was detected with sensitive EMCCD camera (Evolve, Roper Scientific, Evry, France). Image acquisition and control of microscope were driven by Metamorph

software (Molecular devices, USA). Image stack contained typically 40,000 frames. Selected ROI (region of interest) had dimension of 512x512 pixels (one pixel = 100 nm). Pixel size of reconstructed super-resolved image was set to 25 nm. Multi-color fluorescent microspheres (Tetraspeck, Invitrogen) were used as fiducial markers to register long-term acquisitions and correct for lateral drifts.

### c. Imaging solution for d-STORM

18 mm coverslip covered by immune-labelled neurons was mounted in a Ludin chamber (Life Imaging Services, Switzerland) and 500  $\mu$ L of imaging buffer are added. Another 18 mm coverslip was placed on top of the chamber to minimize oxygen exchanges during the acquisition and so maintain the efficacy of the buffer to prevent photobleaching.

The imaging buffer used for d-STORM experiments was the classical Glucose oxidase (Glox) buffer described in (van de Linde et al., 2011). The Glox buffer is composed of 1 mL G, 125  $\mu$ L E and 125  $\mu$ L M, and the final pH is adjusted to  $\sim$ 7.8 with NaOH.

Glucose base solution (G)			Enzyme solution (E)			Thiol solution (M)		
50 mL			50 mL			10 mL		
45 mL	H2O milliQ		100 $\mu$ L	Catalase	Sigma C100	1.136 g	MEA-HCl	Sigma M6500
5 g	Glucose	Sigma G8270	200 $\mu$ L	TCEP	Sigma C4706	10 mL	H2O milliQ	
5 mL	Glycerin	Sigma G2289	25 mL	Glycerin	Sigma G2289	<b>adjust pH to 8 with NaOH</b>		
			22.5 mL	H2O milliQ				
			1.25 mL	KCl (1M)	Sigma P9541			
			1 mL	Tris-HCl (1M) pH 7.5	Euromedex EU0011			
			50 mg	Glucose oxidase	Sigma G2133			

## **d. Analysis and quantification**

### **a) Localization processing**

Single molecule detection recordings were processed using a Metamorph plugin called PalmTracer and developed by the group of Jean-Baptiste Sibarita (Izeddin et al., 2012). The x,y coordinates were localized using image wavelets segmentation and centroid estimation methods. First, an intensity threshold was defined to detect single molecule signals. Once each single molecule has been localized in each frames of the recording, their centroid x,y coordinates were automatically written on a text file. An intensity map was created with a desire pixel size (25 nm) by positioning the several thousands of points localized during the first step.

### **b) Cluster analysis**

To analyze the clustering of proteins, we used two methods. The first one consist to detect cluster on the super-resolution image using PalmTracer Cluster Analysis. On the same manner that the localization detection, Cluster Analysis use wavelets segmentation to detect individual clusters based on set intensity threshold. Following clusters detection, a Gaussian fit was applied and their standard deviation  $\sigma$  was measured. This allowed to calculate the FWHM of clusters ( $\text{FWHM} = 2.3 \sigma$ ) and to give clusters length and width. The intensity of these clusters was measured by the sum of all pixel values and the intensity of single emitters as well using Metamorph Integrated Morphometry Analysis. By dividing the intensity of each cluster by the median intensity of single emitters, we can approximate the number of proteins per

cluster. This method is commonly used in localization-based super resolution microscopy. However, clusters quantification depends on the sampling chosen to reconstruct the super resolution image.

Recently, Levet et al. introduced a framework named SR-Tesseler, based on Voronoï diagrams, for a more precise automatic segmentation and quantification of protein organization at different scales from the same set of molecular coordinates, using a local density parameter (Levet et al., 2015). SR-Tesseler creates polygonal regions centered on localization centroid previously established with PalmTracer. These polygons are defined in an Euclidean space and provides information on the neighboring localization. The density is measured and can be a parameter used to identify clusters. After successive segmentation steps, SR-Tesseler allows to obtain the intensity of single emitters (isolated fluorophores on the coverslip and isolated proteins) and to quantify the protein cluster diameter and content (Figure 18B-H).

## **8. Single-Particle Tracking**

### **a. General principle of stochastic labelling methods**

The universal-Point Accumulation for Imaging in Nanoscale Topography (u-PAINT) technique has been developed to visualize single protein mobility behavior.

The principle comes from the PAINT technique which consists in the precise lateral localization of individual fluorophores which transiently attach the membrane and become fluorescent only at the contact of the lipid layer (Sharonov and Hochstrasser, 2006). This principle of a stochastic labeling over the time during the

imaging process raised the idea of u-PAINT (Giannone et al., 2010). Regarding the optical part, the SeTau 647 dye (red-emitting squaraine-rotaxane), and in some consideration ATTO dyes, are sufficiently stable to photobleaching to be detected as single molecules with a localization precision of ~40-50 nm for couple of seconds to minutes. The small size of organic fluorophore like ATTO, compared to previously used ones as Quantum Dot (1-2 nm vs 5-10 nm), allows a better tracking of the protein of interest in confined space as the synaptic cleft. The PAINT aspect allows to renew the labeling of the protein population over the time. By adding a low concentration of fluorescent probes in the imaging chamber, this leads to a low-density stochastic labeling. The number of trajectories will increase in function of the duration of imaging, giving access to a high-density dynamic information. An oblique illumination to decrease the background signal due to the presence of floating fluorescent probes in the solution is required. However, it is important to note that molecules freely moving in water have a diffusion coefficient (D) of  $\sim 100 \mu\text{m}^2.\text{s}^{-1}$  rather than a membrane protein have a D comprised in a range between 0.0001 to  $0.1 \mu\text{m}^2.\text{s}^{-1}$ . Thus, detections of freely moving molecules cannot be clearly detected by the camera and most of floating dyes are not activated by the illumination.

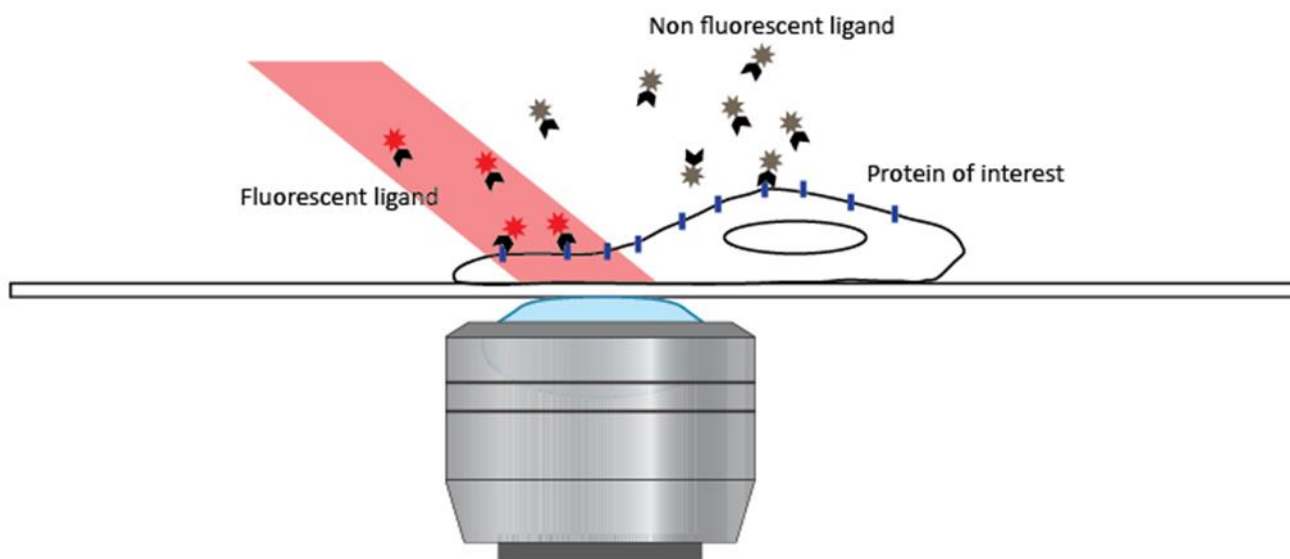


**Figure 12.** uPAINT principle

## **b. u-Paint application**

u-Paint experiments were performed on a Ludin chamber (Life Imaging Service, Switzerland). Cells were maintained in a Tyrode solution composed of the following (in mM): 15 D-Glucose, 100 NaCl, 5 KCl, 2 MgCl<sub>2</sub>, 2 CaCl<sub>2</sub>, 10 HEPES (pH7.4; 247mOsm). Imaging was performed on a LEICA DMi8 mounted on an anti-vibrational table (TMC, USA) used to minimize drift, Leica HCX PL APO 160x 1.43 NA oil immersion TIRF objective and laser diodes with following wavelength: 405 nm, 488 nm, 532 nm, 561 nm and 642 nm (Roper Scientific, Evry, France). Fluorescent signal was detected with sensitive EMCCD camera (Evolve, Roper Scientific, Evry, France). A TIRF device (Ilas, Roper Scientific, Evry, France) is placed on the laser path to modify the angle of illumination. Image acquisition and control of microscope were driven by Metamorph software (Molecular devices, USA). The microscope is caged and heated in order to maintain the biological sample at 37°C.

The first step consists to find a transfected neuron by using the GFP signal. After selection of the dendritic segment of interest, SeTau647 or Atto 647 coupled anti-GluA2 antibody (mouse antibody, gift from E. Gouaux, Portland, USA) at low concentration was added in the Ludin chamber to sparsely and stochastically label endogenous GluA2-containing AMPARs. The TIRF angle was adjusted in oblique configuration to detect fluorescent signal at the cell surface and to decrease background noise due to freely moving fluorophore coupled antibodies. 647 nm laser was activated at a low power to avoid phototoxicity but allowing a pointing accuracy of around 50 nm, and 4000 frames at 50Hz were acquired to record AMPAR lateral diffusion at basal state.

## **9. Confocal imaging**

### **a. Principles of confocal imaging**

Confocal microscopy offers several advantages over conventional widefield optical microscopy, including the ability to control depth of field, elimination or reduction of background information away from the focal plane (that leads to image degradation), and the capability to collect serial optical sections from thick specimens, before reconstruction. The basic key to the confocal approach is the use of spatial filtering techniques to eliminate out-of-focus light or glare in specimens whose thickness exceeds the immediate plane of focus.

The confocal principle in epi-fluorescence laser scanning microscopy is diagrammatically presented in figure 13. Coherent light emitted by the laser system (excitation source) passes through a pinhole aperture that is situated in a conjugate



plane (confocal) with a scanning point on the specimen and a second pinhole aperture positioned in front of the detector (a photomultiplier tube). As the laser is reflected by a dichromatic mirror and scanned across the specimen in a defined focal plane, secondary fluorescence emitted from points on the specimen (in the same focal plane) pass back through the dichromatic mirror and are focused as a confocal point at the detector pinhole aperture.

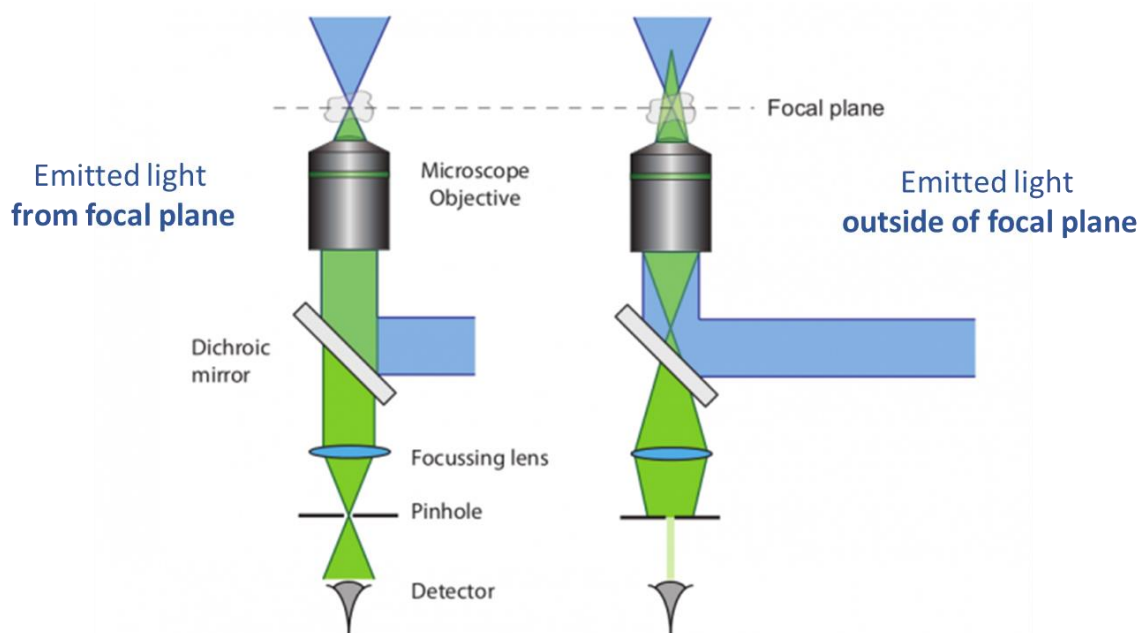


**Figure 13.** confocal principle .Adapted from Scientific Volume Imaging B.V (Netherlands)

## b. Application of confocal imaging

For confocal imaging of PSD-95, primary neuronal cultures were treated either with 30  $\mu\text{M}$  NMDA (Tocris) for 3 minutes or with 100  $\mu\text{M}$  ATP in presence of CGS15943 (3  $\mu\text{M}$ ) (Pougnnet et al., 2016, 2014) (Sigma-aldrich) for 1 minute and fixed with PFA 30 minutes or 3 hours after. Then, classical immunolabeling protocol with permeabilization

is realized as described above. Briefly, PFA was quenched, a permeabilization step with 0.2% triton was then performed. After washing and BSA incubation, cells were incubated with monoclonal mouse anti-PSD-95 antibody (MA1-046, ThermoFischer), diluted in 1% BSA at 1/500, at room temperature for 4 hours. After washes, primary antibodies were revealed with Alexa 647 coupled anti-mouse IgG secondary antibodies (ThermoFisher, A21235).

Images were acquired with a microscope Leica TCS SP8 confocal head mounted on an upright stand DM6 FS (Leica Microsystems, Mannheim, Germany), an objective HC Plan Apo CS2 40X oil NA 1.3 and an internal hybrid detector.

Images were acquired on different Z plans and reconstructed as Z projections using the software ImageJ. Reconstructed images were then analyzed using the software MetaMorph (Molecular Devices). For puncta density measurement, puncta were thresholded and then manually counted.

### **c. Synaptotagmin-1 uptake measurement**

For live imaging of EGFP transfected primary neuronal cultures and synaptotagmin-1 uptake measurement, neurons were treated with 30  $\mu$ M NMDA (Tocris) for 3 minutes. After 30 minutes of incubation, they were placed in a Ludin chamber with culture media from their original dish, and a fluorescently labelled mouse anti-Synaptotagmin-1 antibody (Synaptic System, 105311CpH monoclonal) was applied in the bath at 1/200 for 30 minutes. The neurons are then put back in cultured medium for 2.30 hours in the incubator.

Images were acquired 3 hours after treatment using spinning disk microscope Leica DMI8 (Leica Microsystems, Wetzlar, Germany) equipped with a confocal Scanner Unit CSU-W1 T2 (Yokogawa Electric Corporation, Tokyo, Japan) using a HCX PL Apo CS2 63X oil NA 1.4 TIRF objective. The system comprised a sCMOS Prime 95B camera (Photometrics, Tucson, USA). The LASER diodes used were at 488 nm (400 mW), and 642 nm (100 mW). Z stacks were done with a galvanometric stage (Leica Microsystems, Wetzlar, Germany). The 37°C and 5% CO<sub>2</sub> atmosphere was created with an incubator box and an air heating system (PeCon GmbH, Germany). This system was controlled by MetaMorph software (Molecular Devices, Sunnyvale, USA).

Images were analyzed using the software MetaMorph. Using the EGFP signal, spines were manually selected as region of interests of a size sufficient to comprise the full spine. All visible spines from a neuron were selected.

## RESULTS

# Chapter 1

## Nanoscale co-organization and co-activation of

### AMPA, NMDAR, and mGluR

The application of high-density super-resolution microscopy to neuroscience, initiated by Dani et al. (Dani et al., 2010), changes our vision of synaptic transmission. The limitations of electrophysiological experiments, which were for more than 20 years, the only way to get access to synapse physiology at the receptor level, created some dogma, as the importance of the quantity of glutamate per vesicle. Super-resolution microscopy shed the light on the nanoscale organization inside the synapse and even more inside the PSD, modifying our interpretation of electrophysiological results. Years after years, new bricks of knowledge built a new concept of synaptic transmission properties. My PhD is in direct line with such work of re-interpretation of synaptic physiology based on the combination of both electrophysiology, super-resolution and modeling.

At the beginning of my PhD I participated to a project initiated by Julia Goncalves which aimed to decipher the nanoscale organization of synapses. More specifically, we characterized the co-organization and the co-activation of the three main glutamate receptors (AMPA, NMDAR and mGluR) under basal conditions.

AMPA are organized at the synapse as nanodomains of around 100nm containing 20 to 25 receptors, facing pre-synaptic release sites (Macgillavry et al., 2013; Nair et al., 2013). This pre-post apposition is crucial for AMPARs activation, as they present a low affinity for glutamate (range of mM). On their side, NMDARs are

also accumulated at the postsynaptic density as nanodomains which size and content properties vary in function of the sub-units composition of NMDAR (Kellermayer et al., 2018). However, their location regarding the pre-synapse is unknown. Finally, mGluR5 have been described as localized predominantly in the peri-synapse, even though they have been found to interact with Homer1 and more recently to be regulated by Shank, which are important scaffold proteins of the PSD (Scheefhals et al., 2019).

As previously reported, receptors present differences in glutamate affinity, and therefore their synaptic localization regarding the release sites is thought to have an important role on their activation. This is why deciphering the nanoscale organization of the various glutamate receptors and their possible co-organization and co-activation would bring decisive information for synaptic physiology.

By combining dual-color super-resolution imaging with electrophysiology and modeling we determined how the various glutamate receptors are organized at the nanoscale and to what extent they are activated by a single vesicle release. More particularly, I realized all electrophysiological recordings of NMDAR-mediated currents, in order to characterize their activation profile. Then, I also participated with Michel Vivaudou to the extraction of single-channel properties in order to determine the mean number of activated receptors in response to glutamate release.

Through this project, we showed the central position of a unique NMDAR cluster inside of the PSD, surrounded by one to two AMPAR clusters, while mGluR5 diffuses rapidly inside the entire synapse. Moreover, we found that a single glutamate release activates between 10 and 15 AMPARs and between one to two NMDARs, which is in agreement with previous publications. Finally, even though the glutamate release sites are not aligned with NMDAR cluster, a very recent paper indicates that asynchronous release occur in front of NMDARs, unlike synchronous release (Li et al., 2021).

To conclude, this paper brings a new vision of the synaptic nano-organization. Notably, it relates for the first time the tight interaction between the properties of the receptors and their precise location at the synapse, influencing their co-activation. It is also the first time that the organization of glutamate receptors are characterized altogether. Despite the fact that this is not the major part of PhD, I have been involved in many experiments, and this project has been for me a good opportunity to study the relation between structure and function at the nanoscale.



# Nanoscale co-organization and coactivation of AMPAR, NMDAR, and mGluR at excitatory synapses

Julia Goncalves<sup>a,b</sup>, Tomas M. Bartol<sup>c,1</sup>, Côme Camus<sup>a,b,1</sup>, Florian Levet<sup>a,b,d</sup>, Ana Paula Menegolla<sup>a,b</sup>, Terrence J. Sejnowski<sup>e</sup>, Jean-Baptiste Sibarita<sup>a,b</sup>, Michel Vivaudou<sup>e,f</sup>, Daniel Choquet<sup>a,b,d</sup>, and Eric Hosy<sup>a,b,2</sup>

<sup>a</sup>Interdisciplinary Institute for Neuroscience, University of Bordeaux, 33077 Bordeaux, France; <sup>b</sup>Interdisciplinary Institute for Neuroscience, CNRS UMR 5297, 33077 Bordeaux, France; <sup>c</sup>Howard Hughes Medical Institute, Salk Institute for Biological Studies, La Jolla, CA 92037; <sup>d</sup>Bordeaux Imaging Center, CNRS UMS 3420, University of Bordeaux, INSERM U504, 33077 Bordeaux, France; <sup>e</sup>Institut de Biologie Structurale, Université Grenoble Alpes, Commissariat à l'Énergie Atomique, CNRS, 38000 Grenoble, France; and <sup>f</sup>Laboratory of Excellence, Ion Channel Science and Therapeutics, 06560 Nice, France

Edited by Ehud Y. Isacoff, University of California, Berkeley, CA, and approved May 13, 2020 (received for review December 29, 2019)

**The nanoscale co-organization of neurotransmitter receptors facing presynaptic release sites is a fundamental determinant of their coactivation and of synaptic physiology. At excitatory synapses, how endogenous AMPARs, NMDARs, and mGluRs are co-organized inside the synapse and their respective activation during glutamate release are still unclear. Combining single-molecule superresolution microscopy, electrophysiology, and modeling, we determined the average quantity of each glutamate receptor type, their nanoscale organization, and their respective activation. We observed that NMDARs form a unique cluster mainly at the center of the PSD, while AMPARs segregate in clusters surrounding the NMDARs. mGluR5 presents a different organization and is homogeneously dispersed at the synaptic surface. From these results, we build a model predicting the synaptic transmission properties of a unitary synapse, allowing better understanding of synaptic physiology.**

synaptic transmission | glutamate receptors | superresolution microscopy

The discrete chemical signals mediated by glutamate release at presynapses are computed into various pathways such as rapid depolarization induced by AMPA receptors (AMPARs), calcium entry through NMDA receptors (NMDARs), and activation of long-term signaling pathways via metabotropic receptors (mGluRs). The ability of the postsynapse to integrate the presynaptic message is thought to be part of the memory storage mechanism. However, due mainly to technical limitations, glutamate receptor organization and activation profiles have not been clearly described yet. For example, most studies on the functional relationship between AMPAR and NMDAR have been performed with electrophysiology by stimulating a large number of axons, thereby mixing per se the presynaptic release probabilities, synapses where AMPARs are absent (1), and variations in postsynaptic properties.

The general view, based on imaging, electrophysiology, and biochemical experiments, is that a spine contains between 50 and 100 AMPARs (2, 3). However, only 20 to 25% of this pool of AMPARs is activated by a single vesicle release, revealing the nonsaturation of synaptic AMPARs by glutamate (4). Similar experiments on NMDARs concluded that among the 20 to 30 NMDARs present inside a spine (5), only 2 to 3 are activated by a vesicle release in the absence of magnesium block (6–8).

The nonsaturation of AMPARs and NMDARs has been explained by modeling the glutamate gradient, which rapidly fades away (9, 10). While a glutamate concentration of 4 mM is reached at the vesicle fusion pore, it decreases to 0.5 mM 100 nm away from it 100 μs after release. For this reason, the nanoscale organization of the receptors with respect to the release site shapes the amplitude of synaptic transmission (11, 12). This is particularly true for AMPARs, which have a low affinity for glutamate and whose activation is thus exquisitely sensitive to their location in the gradient. The emergence of superresolution imaging has improved our understanding of the nanoscale organization of glutamate receptors. Around half of the synaptic

AMPARs are clustered in domains of around 80 nm, with the rest diffusing freely (3). This organization is stabilized by subdomains of the scaffolding protein PSD95 present inside the PSD (3, 13, 14). These AMPAR domains are co-organized with the presynaptic glutamate release site via transsynaptic adhesion proteins like neurexin and neuroligin (11, 15). Such a tight molecular organization improves the synaptic transmission efficiency, and modeling has suggested that a 100 nm shift in this prepost alignment decreases synaptic transmission by more than 30% (11).

More recently, the intimate synaptic organization of NMDARs was imaged (16, 17). They are distributed in small clusters inside the PSD, although their co-organization with respect to the release sites has not been established. Some data are available regarding the co-organization of AMPARs and NMDARs; electron microscopy studies have demonstrated a slightly higher density of NMDARs at the center of the PSD, while AMPARs are enriched in a ring at the periphery (18–20). In parallel, several studies have reported the subsynaptic organization of metabotropic receptors. In 1994, Nusser and colleagues demonstrated that AMPAR clusters are more in the center of the synapse, while mGluR1, belonging to the same subgroup as mGluR5, is found more at the periphery (21). Other electron microscopy studies also reported this perisynaptic localization of metabotropic type I family members (22).

Despite attempts to decipher the nanoscale organization of the various glutamate receptors, a clear vision of their co-organization

NEUROSCIENCE

## Significance

Neuron-to-neuron communication is based on synapse activity where presynapses release neurotransmitters, which activate postsynaptic neurotransmitter receptors. The various families of glutamate receptors at the excitatory synapses are responsible of the fast synaptic transmission as well as the regulation of the long-term signaling implicated in information storage and memory. The organization at the nanometer scale of these postsynaptic receptors is a key determinant for synaptic transmission efficiency. Here, we combined dual-color super-resolution imaging with electrophysiology and modeling to determine how the various glutamate receptors are co-organized at the nanoscale and to what extent this organization regulates the receptor activation by a single vesicle release.

Author contributions: T.J.S., J.-B.S., and E.H. designed research; J.G., T.M.B., C.C., F.L., and A.P.M. performed research; F.L. and J.-B.S. contributed new reagents/analytic tools; J.G., C.C., M.V., and E.H. analyzed data; and D.C. and E.H. wrote the paper.

The authors declare no competing interest.

This article is a PNAS Direct Submission.

Published under the PNAS license.

<sup>1</sup>T.M.B. and C.C. contributed equally to this work.

<sup>2</sup>To whom correspondence may be addressed. Email: eric.hosy@u-bordeaux.fr.

This article contains supporting information online at <https://www.pnas.org/lookup/suppl/doi:10.1073/pnas.1922563117/-DCSupplemental>.



and coactivation is still missing. Here, we combined dual-color superresolution imaging with electrophysiology and modeling to determine how the various glutamate receptors are organized at the nanoscale and to what extent they are activated by a single vesicle release.

## Results

**NMDARs and AMPARs Are Clustered in Spines, While mGluR5 Is Homogeneously Distributed.** We first determined the nanoscale synaptic organization of each receptor type in hippocampal neuronal cultures using single-color immunocytochemistry and direct stochastic optical reconstruction microscopy (dSTORM). In live cells, we labeled endogenous GluA2 to visualize AMPAR (Fig. 1A), NR1 for NMDAR (Fig. 1B), and mGluR5 for mGluR (Fig. 1C) with monoclonal primary antibodies, then with secondary antibodies tagged with Alexa-647. Both GluA2- and NR1-containing receptors were organized in clusters, while mGluR5 was homogeneously distributed in the entire synapse.

In contrast to epifluorescence microscopy images which are blurred by diffraction, dSTORM images are more punctate and each punctum, called a nano-object, varies in size and intensity as a function of its fluorophore content. To resolve the nanoscale organization of the various receptors at the synapse, we quantified the receptor content of each synaptic nano-object from intensity-based image reconstructions (SI Appendix, Fig. 1.1A). Briefly, we first estimated the number of localizations per single receptor on the dendrite. On dendrites, there is a clear peak of distribution of individual nano-objects that, we assume, represents an individual receptor. Then, we extracted all of the individual nano-objects by image segmentation using a threshold of five localizations per  $25 \times 25$  nm pixels to extract noise (SI Appendix, Fig. 1.1A). Finally, the number of detections in individual nano-objects was divided by the average number of detections emitted by the average smallest nano-object, which we consider to be a single receptor (11).

The distribution of the total number of GluA2-containing AMPAR receptors per spine (SI Appendix, Fig. 1.1B) presents a peaked shape with a median of  $108 \pm 3$  GluA2-containing receptors but does not present a normal distribution, probably due to the variations in PSD size and the existence of spines with multiple PSDs (23). We then determined the receptor content for all individual nano-objects, single and clustered receptors, per synapse. This distribution revealed that more than 60% of nano-objects are composed of one or two receptors (SI Appendix, Fig. 1.1B, Inset). To further refine our analysis, we then classified the nano-object populations within each individual synapse from the one containing the highest number of receptors to the lowest. Fig. 1D represents the distribution of the largest (dark blue), second-largest (light blue), and third-largest (gray) clusters per spine. The other ones were mainly singles or pairs of receptors, as illustrated (SI Appendix, Fig. 1.1A).

The distribution of the different synaptic AMPAR clusters classified from largest to smallest (Fig. 1D) revealed that each synapse has a main domain containing between 15 and 40 receptors (average of  $36 \pm 1$ ) with an average full width at half maximum (FWHM) of  $97 \pm 3$  nm (SI Appendix, Fig. 1.1C). These main synaptic clusters correspond to the AMPAR nanodomains previously described in Nair et al. (3). The second-largest clusters contained around 12 AMPARs ( $12.6 \pm 0.5$ ), the third has  $7 \pm 0.3$ , and the others were isolated or distributed in clusters containing fewer than 5 AMPARs.

Concerning NMDARs, spines contained mainly between 10 and 40 NR1-containing NMDARs (median of  $32 \pm 3$ , SI Appendix, Fig. 1.1D) organized in various clusters. The largest cluster presented a FWHM of  $110 \pm 2$  nm and was composed of about  $15 \pm 2$  receptors. Unlike AMPARs, no significant secondary clusters were observed (Fig. 1E), with the other NMDARs being organized in

objects containing few receptors. For example, the second-largest cluster contained  $4 \pm 0.3$ , and the third had  $2 \pm 0.2$ .

mGluR5 was organized differently; between 5 and 30 receptors were found per spine, with a median of  $21 \pm 2$ , and they presented a more homogeneous distribution (SI Appendix, Fig. 1.1F). Indeed, comparison of the nearest-neighbor distance between mGluR from experimental data and from simulated data (SI Appendix, Fig. 1.1G) reveals that mGluR5 distribution has a random distribution. Interestingly, the number of detections per object in the dendrites and spines ( $1.5 \pm 0.3$ ) was 50% larger than that of the secondary antibodies attached to the coverslip ( $1 \pm 0.2$ ). This could be due to either the presence of mGluR5 dimers or to the fact that multiple secondary antibodies labeled a single monoclonal antibody.

mGluR5 is widely known to interact inside the synapse with the protein Homer, which aggregates at the PSD (24). To understand the discrepancy between the previously reported role of Homer as a scaffolding protein of the PSD and the spread and homogeneous organization of mGluR5, we performed dSTORM experiments on Homer to characterize its nanoscale organization and single-particle tracking photoactivated localization microscopy (sptPALM) experiments on mGluR5 to measure its membrane diffusion properties (SI Appendix, Figs. 1.2 and 1.3). Homer displayed a highly clustered organization in disks measuring approximately the size of the PSD (area of  $0.1 \pm 0.003 \mu\text{m}^2$ ). sptPALM experiments on mGluR5, performed by expressing a protein fusion of mGluR5 with the photoactivatable fluorophore mEOS2, demonstrated a high mobility in both the dendrites and the spines, revealing no long-term trapping at the synapse. Step analysis performed to identify potential transient immobilization did not reveal any particular restriction in the diffusive behavior of mGluR5 in the vicinity of the PSD.

Hence, AMPARs, NMDARs, and mGluR5 display widely different organizations in synapses, with AMPARs displaying clusters of different sizes, while NMDARs display mainly a single cluster and mGluR5 presents a more diffuse distribution.

**NMDAR and AMPAR Clusters Do Not Colocalize but Are Co-organized in a 300-nm Area.** We then assessed the co-organization of the various glutamate receptors. As we failed to obtain a third color allowing superresolution imaging, we separately analyzed AMPAR/NMDAR and AMPAR/mGluR co-organization by using secondary antibodies labeled, respectively, with Alexa 647 nm and Alexa 532 nm. In our experimental conditions, we measured an average pointing accuracy of 12 nm with Alexa 647 nm dye and 28 nm with Alexa 532 nm [based on nearest-neighbor localization precision (25)]. Chromatic aberrations were corrected by using a correction matrix calculated before each experiment by taking an image of TetraSpeck beads adsorbed on the coverslip, as described in (26). The average distance over the entire field of view between the same beads in the two colors was 146 nm (interquartile range [IQR] 138–163) before correction and reached 12 nm (IQR 8–16) after correction.

To evaluate our precision in measuring the co-organization, we initially performed colabeling of endogenous GluA2/GluA1. These two AMPAR subunits are present in the same nano-objects because they mainly belong to the same tetrameric receptor (SI Appendix, Fig. 2.2 and ref. 27). Using dual-color tessellation-based colocalization analysis (26), we measured the distance between the center of the closest cluster of each color. This center is determined as a function of the repartition of the density of the detection and not only as a function of the shape of the cluster. This, centroid-to-centroid distance between GluA2 and GluA1 nanoclusters ranged from 10 to 110 nm, with an average of  $58 \pm 2.3$  nm.

We then determined the distances between the main synaptic clusters of endogenous GluA2-containing AMPARs and NR1-containing NMDARs (Fig. 2A), considering only the clusters

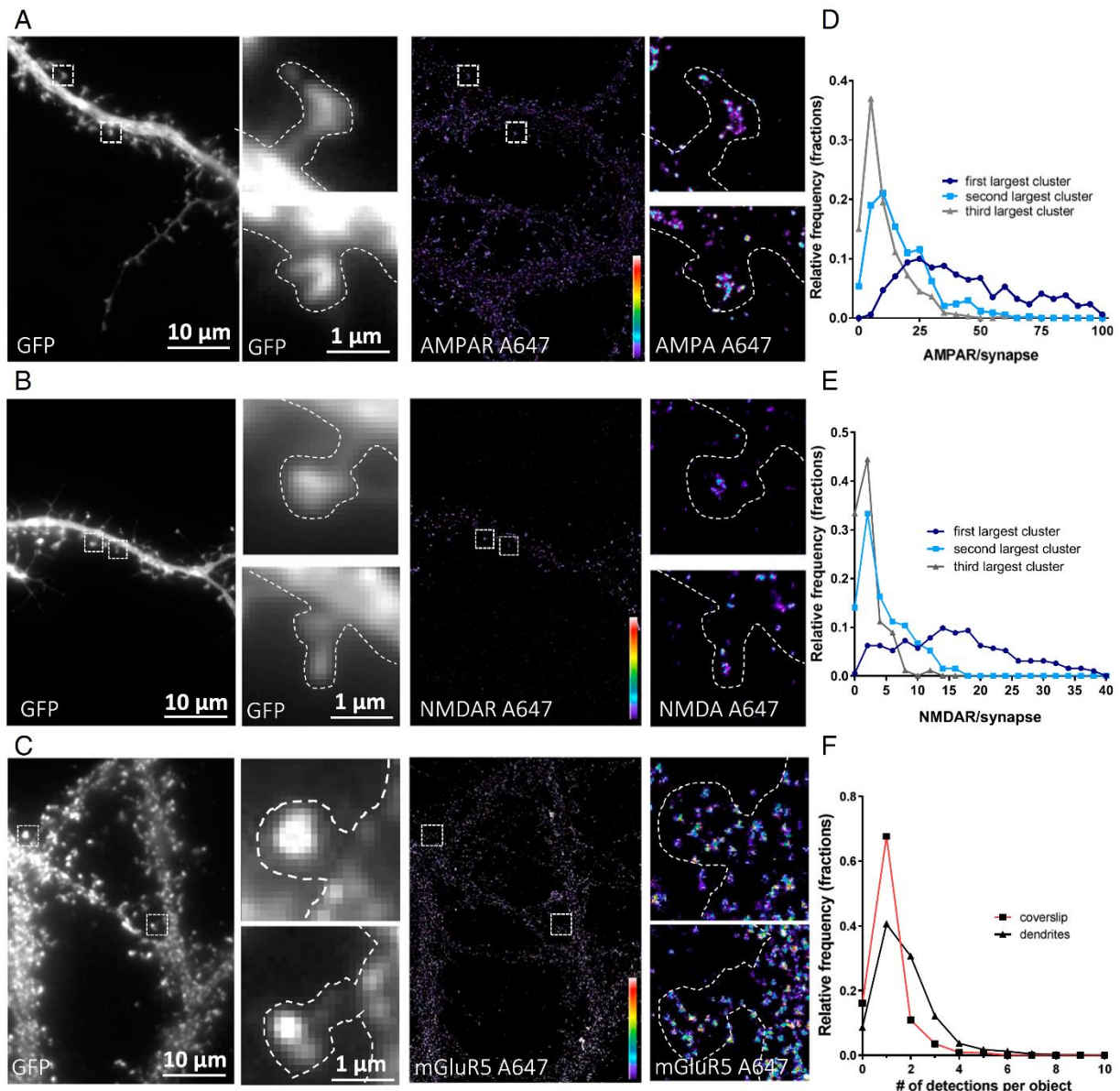


**Fig. 1.** Epifluorescence (*Left*) and dSTORM images (*Right*) of endogenous glutamate receptors: GluA2-containing AMPAR (*A*), NR1-containing NMDAR (*B*), and mGluR5-containing mGluR (*C*). Intensity is color-coded, and the scale goes from 1 (purple) to 100 (white) detections per pixel. Average spine density (*D* and *E*) represents the distribution of the estimated number of receptors per nano-object inside the synapse. Only the three largest clusters per spine are taken into account, with the others being mainly single receptors. (*F*) Comparison between the intensity of nano-objects on the coverslip (single secondary antibody) and on the neuron (primary and secondary antibodies on the mGluR5-containing mGluR). Both AMPAR and NMDAR present a clustered organization, while mGluR5 seems more evenly distributed.

containing more than five receptors. The cluster-to-cluster distance distribution displays a bell-shaped curve, with an average of  $100 \pm 1.5$  nm. Only a few clusters were closer than 40 nm, and none were farther than 200 nm. Moreover, the distribution of the cluster area overlap showed that only 20% of the clusters colocalized over more than 40% of their area, revealing a separation between the two types of clusters (*SI Appendix, Fig. 2.2F*). No such organization could be observed on dendrites, which can present some AMPAR clusters that are less dense and present almost no NMDAR clusters.

To report the relative position between AMPAR and NMDAR clusters, we computed the NMDAR–AMPAR centroid-to-centroid distances and display their spatial distribution with respect to the axis defined between the largest AMPAR cluster and the NMDAR cluster (blue dots) for each synapse (*Fig. 2D*). We observed that secondary clusters containing more than five receptors (orange dots) are homogeneously distributed around NMDAR clusters (*Fig. 2D*).

The distance distribution between the AMPAR clusters and the mGluR5 objects ranged between 100 and 600 nm, with an average of  $187 \pm 6$  nm (*Fig. 2E*). Interestingly, there were 50%

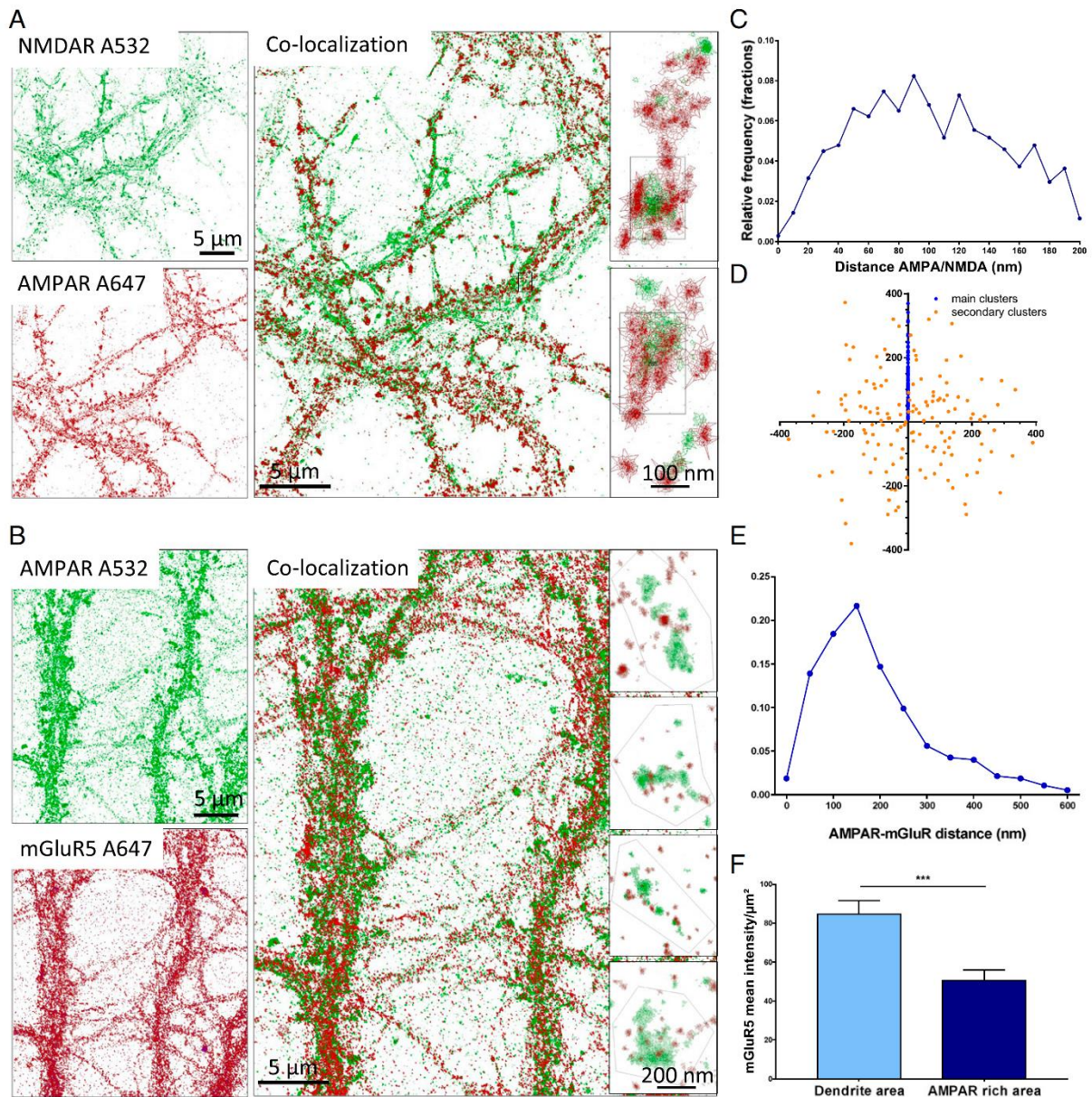


**Fig. 2.** Co-organization of the various glutamate receptors. Dual-color dSTORM imaging is represented with Coloc-Tesseler software of NR1-containing NMDAR and GluA2-containing AMPAR (A) and mGluR5-containing mGluR and GluA2-containing AMPAR (B). For A and B, the *Upper Left* panel represents the 532 nm channel, and the *Lower Left* panel represents the 647 nm channel; the overlay is shown at the center, and synapses are zoomed in the *Right*. In A it appears clearly that the NMDAR cluster (in green) is surrounded by one to two AMPAR clusters (in red). C and E represent the distribution of the cluster centroid-to-cluster centroid distance for AMPAR/NMDAR (C) and AMPAR/mGluR (E). D is the distribution of the AMPAR domains around the NMDAR clusters (located at the origin of the graph). The x and y coordinates are expressed in nanometers. The larger AMPAR cluster distance is projected by rotation on the positive y axis (blue dots); the other cluster coordinates are obtained by applying similar rotation vectors (orange dots). Data represent 91 individuals synapses and 325 AMPAR clusters. (F) Because mGluR does not present clustering, its overlapping with AMPAR is not relevant, so we represent the density of mGluR single objects on the dendrite and in the area enriched in AMPAR. \*\*\* $P < 0.001$ .

fewer mGluR5 objects inside the AMPAR domains than in the other part of the spines or inside the dendrites (Fig. 2F).

**Determining the Activation of NMDAR and AMPAR by Glutamate Release during Miniature Excitatory Postsynaptic Currents (EPSCs).** After characterizing the co-organization of the glutamate receptors, we measured their activation by single vesicle release.

To this aim, we initially bathed the cell in classical Tyrode's solution deprived of  $\text{Mg}^{2+}$  and in the presence of tetrodotoxin (TTX). The miniature currents of AMPARs were recorded for 1 to 2 min; we then perfused 2,3-dioxo-6-nitro-7-sulfamoyl-benzo [f]quinoxaline (NBQX) ( $10 \mu\text{M}$ ) to block them. Five micromolar glycine was added to activate the NMDARs, and the miniature currents were recorded for 1 to 2 min. The obtained NMDAR

currents were very noisy; hence, to verify their specificity, we perfused them with (2*R*)-amino-5-phosphonovaleric acid (APV) (50  $\mu$ M) to block NMDAR activity (examples of traces in Fig. 3*A*). The Detection Mini software was used to extract the properties of the AMPAR and NMDAR miniature currents. Fig. 3*C* shows an average amplitude of  $14.9 \pm 0.22$  pA for AMPAR miniature currents and  $9.5 \pm 0.1$  pA for NMDAR ones.

To establish the number of activated NMDARs in a single miniature EPSC, we first estimated the single-channel conductance. To this aim, single-conductance analysis was applied to currents recorded either in the presence of TTX + NBQX + glycine or when APV was added to this mixture. *SI Appendix, Fig. 3.1* shows that APV application suppressed a conductance of around 4 pA. Such currents due to a channel having approximately a conductance of 50 pS and being blocked by APV can be attributed to NMDARs. To obtain the number of activated NMDARs per miniature current, we divided the distribution of NMDAR miniature currents by the single-receptor current (*SI Appendix, Fig. 3.1D*). In agreement with previously reported findings, we observed that an average of  $2.5 \pm 0.02$  NMDARs were activated by a single vesicle release. This value is probably overestimated; indeed, when we compared, on the same neurons, the frequency of AMPAR- and NMDAR-detected miniatures, we obtained  $4.5 \pm 0.9$  Hz for AMPAR miniatures and  $2.3 \pm 0.2$  Hz for NMDAR miniatures. As the release frequency is quite stable all along a recording, this suggests that almost half of the glutamate releases either trigger NMDAR miniatures which are below the detection threshold or do not even activate any NMDARs.

**Modeling of Receptor Co-organization and Coactivation with the MCell Model.** To improve our understanding of the impact of the glutamate receptor nanoscale organization on synaptic transmission, we created a model using the MCell/CellBlender software. The synaptic architecture was based on three-dimensional reconstruction of electron microscopy (EM) (3DEM) data, and the localization and the size of the PSD were determined on the basis of 3DEM images (*SI Appendix, fig. 1* and ref. 28). The simulations were divided in two sequences. The purpose of the first sequence was to initialize the steady-state organization of

proteins inside the synapse for 10 s with a simulation time step of 1 ms (*SI Appendix, Fig. 4.1 A and B*). The second sequence simulated the activation of the various receptors upon glutamate release for 200 ms with a simulation time step of 1  $\mu$ s (*SI Appendix, Fig. 4.1 C and D*).

For initial conditions, the average numbers of AMPARs, NMDARs, and mGluRs experimentally measured with dSTORM were released at the virtual synapse, i.e., 60 AMPARs, 30 NMDARs, and 20 mGluRs. All receptors were set to diffuse freely on the surface at  $0.1 \mu\text{m}^2/\text{s}$  as classically observed with single-particle tracking experiments. Inside the PSD area, NMDARs and AMPARs were trapped by predefined spots in randomly spaced clusters. The affinity of the receptors for the traps was adjusted to obtain an average receptor content per domain similar to that observed in dSTORM (around 18 for AMPARs and 15 for NMDARs, see Fig. 4*A*). Fig. 4*B* shows the centroid-to-centroid distance of AMPAR to NMDAR clusters from experimental (black line) and simulated (red line) data. The simulated random organization between the two cluster types matched the experimental data.

After 10 s of simulation, the proper steady-state organization of the various receptors was established, and glutamate was released to estimate the number of activated receptors. The release site was obtained by aligning the presynaptic site in front of the centroid of the AMPAR cluster. Between 1,500 and 3,000 glutamate molecules were released, and the number of activated AMPARs and NMDARs is shown in Fig. 4*C*.

The release of 2,000 glutamate molecules activated 17.5% of AMPARs and 7% of NMDARs, i.e., about 10 AMPARs and 2.5 NMDARs, as obtained experimentally. Interestingly, each step increase of 500 glutamate molecules per vesicle triggered the additional activation of 1 AMPAR and 0.5 NMDAR on average, revealing the relatively low impact of glutamate content per vesicle on synaptic currents.

To complete the validation of the model, we compared the experimentally measured distribution of the number of activated NMDARs per miniature with the simulated one, when released vesicles contained 2,000 glutamate molecules. Both distributions

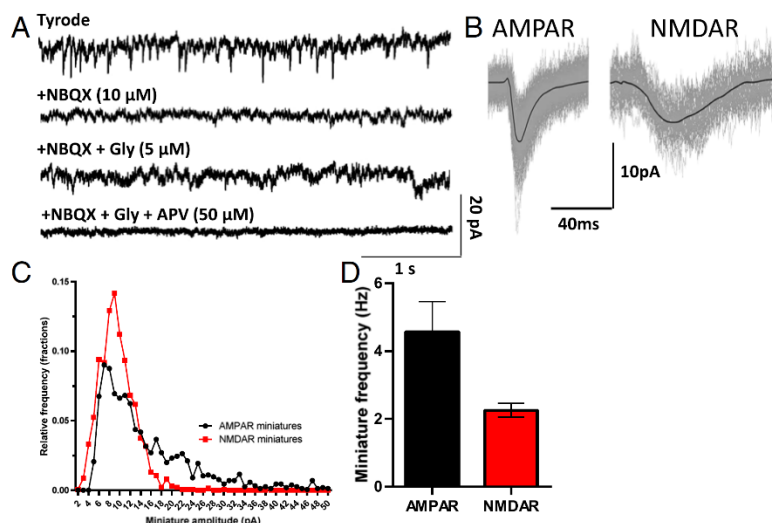


**Fig. 3.** Example of AMPAR and NMDAR miniature currents. (*A*) From top to bottom, TTX and bicuculline are present but  $\text{Mg}^{2+}$  is absent (first trace), then NBQX is added to block AMPARs (second trace), glycine is added to favor activation of NMDARs (third trace), and, finally, APV is added to block NMDARs and estimate the noise level (fourth trace). (*B*) Average trace of AMPAR (*Left*) and NMDAR (*Right*) miniature currents. (*C*) Distribution of the AMPAR (black line) and NMDAR (red line) miniature current amplitudes (pA). (*D*) Miniature frequency (in Hz) of AMPARs (black) and NMDARs (red) on the same neurons, showing that only half of the frequency of AMPAR currents can be detected when recording NMDAR currents.

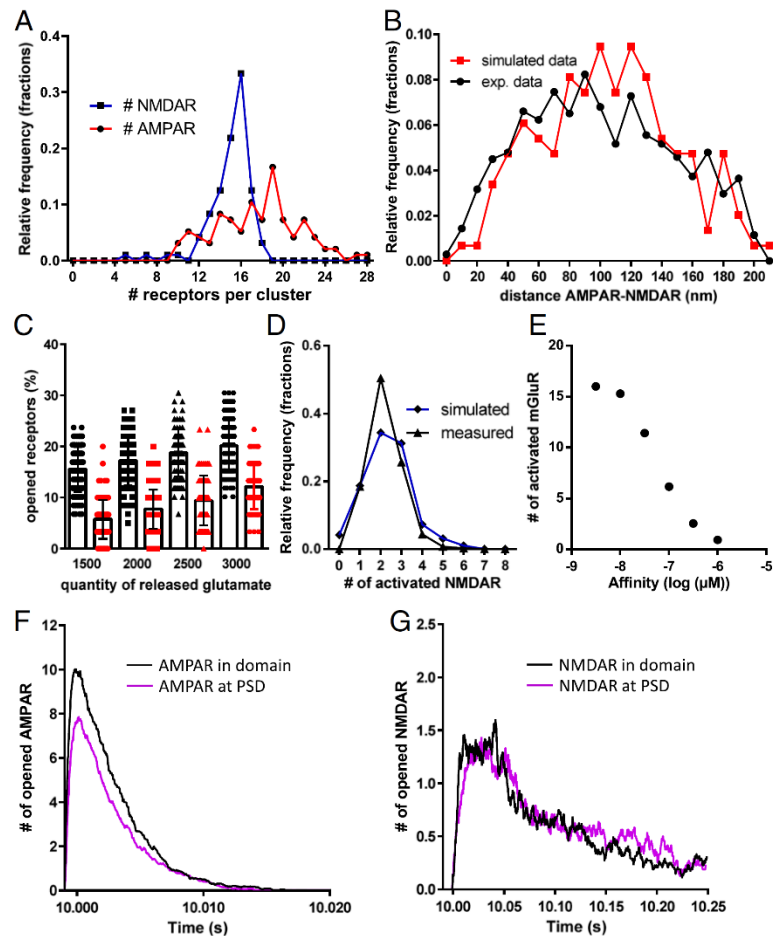


**Fig. 4.** (A) Simulated data representing the distribution of the accumulation of AMPARs (red line) and NMDARs (blue line) inside synaptic nanoclusters. (B) Distribution of simulated (red line) and measured (black line) data of the centroid-to-centroid distance between AMPAR and NMDAR clusters. (C) Evolution of the number of activated AMPARs (black line) and NMDARs (red line) as a function of the quantity of released glutamate. (D) Comparison between the distribution of simulated (blue line) and measured (dark line) activated NMDARs. (E) Dose–response curve of the simulated number of mGluRs activated per synapse when 2,500 glutamate molecules are released as a function of the mGluR affinity. (F and G) Simulated traces of AMPAR (F) and NMDAR (G) currents when the same number of receptors is accumulated either in nanodomains or for the entire PSD.

had comparable averages,  $2.2 \pm 0.02$  for measured values and  $2.32 \pm 0.1$  for simulated ones (Fig. 4D).

The similarities between the simulated and experimental data validated our model and allowed us to estimate the number of bound mGluR5 during glutamate release. Fig. 4E shows the number of activated mGluR5 as a function of their affinity for glutamate when 2,000 glutamate molecules were released. In these conditions, half of the mGluRs were activated if they had a 50 nM affinity for glutamate. With an affinity of 1  $\mu$ M as described in the literature, only one receptor was activated on average (29).

Finally, we used the model to determine the efficiency of receptor activation depending of their nanoscale organization (Fig. 4F and G). We compared the AMPAR and NMDAR activation when the same number of receptors was either clustered in a nanodomain (black lines) or randomly accumulated at the PSD (purple lines). Interestingly, AMPARs and NMDARs do not behave similarly. For AMPARs, their random accumulation at the entire PSD causes a 22% decrease in their activation compared to a nanocluster, while such organization of NMDARs

does not affect NMDAR activation, meaning that NMDARs are less sensitive to their nanoscale organization than AMPARs.

In conclusion, the nanoscale clusterization of NMDARs is less important for their activation than their total number at the PSD, while for AMPARs, the clustering clearly improves their activation and thus the synaptic response efficiency.

## Discussion

**Nanoscale Organization of AMPARs, NMDARs, and mGluRs.** Using dSTORM, we deciphered the nanoscale organization of the three main glutamate receptor subtypes, individually and relative to each other. Endogenous GluA2, NR1, and mGluR5 were labeled, and their quantity and nanoscale organization inside spines were characterized. As described previously, GluA2-containing AMPARs are unevenly distributed in the synapse; 50% of the identified objects are composed of one to two receptors, representing probably the mobile fraction of the receptors. The other 50% are organized in domains, with a main domain containing around 25 receptors. Other smaller domains were found to contain 5 to 15 receptors. It is not clear whether

these secondary domains play a physiological role and are co-organized with presynaptic release sites or whether they form a reserve pool of receptors inside the synapse. Given the relatively low affinity of AMPARs for glutamate, in the millimolar range, it is unlikely that release in front of one AMPAR domain can activate a significant number of AMPARs in a neighboring domain (11). The larger synapses present multiple domains, but their detailed characterization is rendered difficult by the high density of receptors. They may correspond to synapses containing multiple PSDs, as described previously (23).

Concerning the organization of NR1-containing NMDARs, their organization in clusters is similar to that recently described (30), with a single main cluster and surrounding isolated receptors. Quantitative analysis revealed a single main domain composed of half of the synaptic NMDARs (~15 receptors), with the rest being mainly in the form of single or pairs of receptors. These isolated single receptors might represent the pool of mobile receptors already reported in the literature (30, 31).

Interestingly, mGluR5 was not organized in clusters but was distributed more homogeneously, probably due to the rapid and constant lateral diffusion, as observed with sptPALM technique. This is somewhat in contradiction to the measured strong interaction with Homer 1b and 1c proteins, which are considered scaffolding proteins. This paradox could be due to a dual role of Homer, first as an interactor of mGluRs acting as a regulator of mGluR signaling (32) and, in parallel, as a scaffolding protein inside the PSD, involved in the trapping of other types of proteins. We cannot rule out that the overexpression of mGluR5-mEos used for sptPALM limited our ability to detect the few trapped receptors. However, the nonclustered organization of endogenous receptors found with dSTORM experiments is in favor of the hypothesis that mGluR5 is not tightly attached to the PSD.

**Co-organization of Glutamate Receptors.** AMPAR and NMDAR co-organization was already studied with classical fluorescent microscopy techniques and electron microscopy, revealing a colocalization inside the PSD (18, 20). Here, we demonstrate that AMPAR and NMDAR clusters barely colocalize at the nanometric scale, their centroid-to-centroid distance ranging from 50 to 250 nm. This maximum distance of 200 nm could correspond to the presence of both clusters inside the PSD. Moreover, NMDAR clusters were localized mainly centrally and were surrounded by one or more AMPAR clusters. We used simulations to reproduce the bell-shaped distribution of the AMPAR-NMDAR distance. A similar curve was obtained when NMDAR clusters were placed at the center of the PSD and after placing the AMPAR clusters randomly inside the PSD (Fig. 4B).

Physiologically, this pattern of organization would be obtained if NMDARs create the initial aggregation of scaffold proteins and then AMPARs are recruited at the PSD. In that scenario, the release site would be fixed subsequently at the top of the AMPAR clusters, as previously reported (11, 15, 33). This is just one hypothesis that can be formulated to explain this random AMPAR/NMDAR colocalization inside the PSD. In any case, even if both receptor types interact with similar scaffolding proteins (mainly PSD95), they do not present colocalization. This indicates that synapses are physically able to discriminate the trapping sites for AMPAR and NMDAR. This is in line with previous experiments indicating that AMPAR and NMDAR binding to PSD95 can be differentially completed (34). It is also in line with recent results indicating that sequences upstream of the extreme PDZ ligand in AMPAR auxiliary proteins can control their binding to PSD95 (35), hence opening the possibility of differential binding of various PSD95 interactors.

The different types of organization between AMPARs and mGluRs, with AMPARs clustered and mGluRs highly mobile, clearly account for the random distribution of the distance between the AMPAR cluster centroids and the closest mGluR5.

None of these receptor types presents any form of co-organization. We even observed an exclusion of mGluR5 outside of the AMPAR clusters (Fig. 2F). As this exclusion is only partial, it might simply present a form of steric exclusion due to the highly dense cluster of AMPAR complexes. Interestingly, the previously reported enrichment in mGluRs at the perisynapse could be explained by this exclusion. Indeed, exclusion of mGluRs outside of the PSD would mimic an accumulation at the perisynapse.

In conclusion, the present findings point to the central position of a unique NMDAR cluster inside the PSD with AMPAR clusters surrounding it, while mGluR5 diffuses rapidly inside the entire synapse.

**Coactivation of the Various Receptor Types.** The specific organization of glutamate receptor subtypes with respect to the release site determines the signature of their distinctive activation properties. By combining electrophysiological data and simulations, we were able to estimate the number of receptors activated by the release of glutamate. Electrophysiologically, we found that each release triggers a current of 14 pA for AMPARs and 9 pA for NMDARs. The single-channel current driven by the glutamate receptor is around 1 pA for AMPARs and 4 pA for NMDARs. This means that a single glutamate release activates between 10 and 15 AMPARs and around 2 NMDARs. Such values, which are in agreement with published values (6–8), are validated by the results of simulations based on well-defined single-channel gating properties and the observed nanoscale organization.

The relatively low activation of NMDARs is partly due to the nonalignment of NMDAR clusters with glutamate release sites. Indeed, when we simulated a release in front of a NMDAR cluster, we obtained around six to seven activated NMDARs (24 to 28 pA of current), representing 20 to 25% of the total number of synaptic NMDARs. As such a current was not observed experimentally, this indicates that miniature release does not occur in front of NMDAR clusters.

Interestingly, the activation of NMDAR is more sensitive to their total number at the PSD than to their nanoscale organization. Indeed, modeling shows that the same number of NMDARs is activated whether they are inside a nanodomain or trapped at the PSD. However, similar experiments with AMPARs triggers a more than 20% decrease in the number of activated AMPARs.

In view of our model which accurately predicts AMPAR and NMDAR activation, we evaluated the number of mGluRs bound to glutamate according to their affinity. Even if their exact affinity is difficult to measure, it is in the micromolar range (29). This would lead to the low activation of mGluRs by miniature release, in the range of zero to two receptors.

Through this work, we describe the nanoscale co-organization and activation of three glutamate receptor types. While the synapse seems efficient at activating AMPARs, the organization observed in this study seems inefficient to properly activate both NMDARs and mGluR5. Their full activation would necessitate the summation of a train of inputs. Since this synaptic model seems to be able to reflect receptor activation obtained on hippocampal cell culture, it would now be interesting to determine whether such a form of organization is common to all glutamatergic synapses or is specific to this synaptic type. Simulation demonstrated that varying from 1,500 to 3,000 glutamate molecules per vesicle does not strongly affect the amplitude of the response, reinforcing the idea that the quantum value of the synaptic response is not solely dependent on the quantity of glutamate but more on the quantity of receptors and their nanoscale organization. Out of 2,000 released glutamate molecules, only 60 to 80 are used for postsynaptic glutamate receptor activation, so it could be important to determine to what extent

the remaining 95% are involved in undefined signaling, such as activation of the astrocytes, feedback on the presynapse, and other pathways.

## Material and Methods

**Hippocampal Neuron Culture and Transfection.** Sprague–Dawley pregnant rats (Janvier Labs) were killed according to the European Directive rules (2010/63/EU). Primary hippocampal cultures were prepared according to the Banker protocol. For imaging, neurons were transfected with GFP in days in vitro 9. For sptPALM experiments, neurons were transfected with an mEOS3.2–mGluR5 construct following a Ca–phosphate protocol [described in Haas et al. (11)].

**dSTORM Experiments.** For dSTORM imaging, primary neuronal cultures were labeled with monoclonal antibodies: mouse anti-GluA2 IgG2b isotype antibody, mouse anti-GluN1 IgG1 isotype antibody (provided by E. Gouaux, Vollum Institute and Howard Hughes Medical Institute, Oregon Health and Science University, Portland, Oregon), rabbit anti-GluA1 antibody (Agrobio), and rabbit anti-mGluR5 (AB5675, Merck Millipore). AMPAR and NMDAR labeling is realized on living cells at DIVs 14 to 16 by a 7 min incubation at 37 °C before paraformaldehyde fixation. mGluR5 labeling necessitated fixation and then permeabilization with Triton X-100 (0.2%) before labeling. Primary antibodies were revealed with 45 min incubation with goat anti-mouse IgG2b Alexa 647 or 532 for AMPARs (A21242, Thermo Fisher Scientific), goat anti-mouse IgG1 Alexa 532 or 647 for NMDARs (Thermo Fisher Scientific, with coupling done at the laboratory), and goat anti-rabbit Alexa 647 for mGluR5 (A21244, Thermo Fisher Scientific).

dSTORM imaging was performed as described in Haas et al. (11). Multicolor fluorescent microspheres (TetraSpeck, Invitrogen) were used as fiducial markers to register long-term acquisitions and correct for lateral drifts.

Single-molecule localization was achieved using WaveTracer software operating as a plugin of MetaMorph software (36). Intensity-based drift-corrected superresolution images were reconstructed with a 25 nm pixel size, using home-made PALMTracer software operating as a plugin of MetaMorph.

**Dual-Color Analysis.** Dual-color dSTORM images were analyzed using the tessellation-based colocalization analysis software (26). Two color images (532 and 647 nm) were acquired with the same dichroic mirror, and chromatic aberrations were corrected using fiducial markers (TetraSpeck beads) using PALMTracer software.

For each color, clusters were segmented using local density factors computed from the polygons embedding each localization. Nanoclusters were segmented by thresholding the local density parameter. To compare clusters similar to the ones identified Fig. 1 on intensity-based images (of five detections per 25 nm pixel), we used a threshold density factor of 1.5, corresponding approximately to 8,000 detections/ $\mu\text{m}^2$  (SI Appendix, Fig. 2.1). Only AMPAR or NMDAR nanoclusters containing more than five receptors (number of localizations of 80 for Alexa 647 nm and 35 for Alexa 532 nm, calibrated from the intensity-based images analysis) were kept for centroid-to-centroid colocalization analysis. With these conditions, we succeed at analyzing comparable domains between intensity-based and tessellation-based images (SI Appendix, Fig. 2.1).

**Electrophysiology.** Miniature excitatory postsynaptic current recordings in neuronal culture were performed as described in Haas et al. (11). Extracellular recording solution was composed of the following (in mM): 110 NaCl, 5 KCl, 2 CaCl<sub>2</sub>, 10 Hepes, 10 D-glucose, 0.0005 tetrodotoxin, 0.02 bicuculline, 0.01 NBQX, 0.005 glycine, and 0.05 D-APV (pH 7.4; ~256 mOsm/L). The pipettes were filled with intracellular solution composed of the following (in mM): 100 K gluconate, 10 Hepes, 1.1 ethylene glycol-bis( $\beta$ -aminoethyl ether)-N,N,N',N'-tetraacetic acid, 3 adenosine triphosphate, 0.3 guanosine triphosphate, 0.1 CaCl<sub>2</sub>, 5 MgCl<sub>2</sub> (pH 7.3; 230 mOsm). Unless specified otherwise, all chemicals were purchased from Sigma-Aldrich, except for drugs, which were from Tocris Bioscience, and miniature EPSC analysis was performed using software developed by Michel Goillandeau (Detection Mini). Briefly, the principle of the detection used is the median filter. The program takes a window with a width set by the experimenter. For each point of the biological signal, the software calculates the median of values in the window before and after the point. The detection is not made on the biological signal but on another signal (called the detection signal), calculated from the difference between the filtered signal and the baseline signal. For further analysis, only detected events with an amplitude between 5 and 50 pA are taken into account.

1. J. M. Bekkers, C. F. Stevens, NMDA and non-NMDA receptors are co-localized at individual excitatory synapses in cultured rat hippocampus. *Nature* **341**, 230–233 (1989).
2. Y. Fukazawa, R. Shigemoto, Intra-synapse-type and inter-synapse-type relationships between synaptic size and AMPAR expression. *Curr. Opin. Neurobiol.* **22**, 446–452 (2012).

**Single-Channel Analysis.** Data were analyzed with the software Igor Pro-8. Current records were first corrected for baseline drift. The baseline was estimated by smoothing the data (Smooth-Loes, Smoothing = 0.2) and was subtracted from the original data. To reduce high-frequency noise, the records were then digitally filtered at a 200 Hz cutoff. Histograms were acquired using a bin width of 0.1 to 0.18 pA to obtain ~200 bins. Histograms were fitted with sums of Gaussian using the multipeak fit module of Igor Pro-8.

**Modeling.** Computer modeling was performed using the MCell/CellBlender simulation environment with MCell version 3.4. The realistic model of glutamatergic synaptic environment was constructed from 3DEM of hippocampal area CA1 neuropil as described in (28–37). The AMPAR chemical kinetic properties were obtained from the well-established model published in Jonas et al. (38), and the kinetic parameters were adjusted to fit with the recorded mEPSCs (see ref. 11). The NMDAR kinetics were obtained from Vargas-Caballero and Robinson (39). All values are reported in SI Appendix, Fig. 4.1.

Two surface properties were defined: the synapse and the PSD (identified on EM data). According to the literature and to our dSTORM data, 200 PSD95 molecules, 60 AMPARs, 30 NMDARs, and 20 mGluRs were released. They freely diffused at the synapse. Inside the PSD, PSD95 was reversibly palmitoylated (pPSD95) at a defined rate (association constant [ $k_{\text{on}}$ ] = 35, dissociation constant [ $k_{\text{off}}$ ] = 0.7).

A clusterization point called “L” was set at the center of the PSD. pPSD95 aggregates in contact with L ( $k_{\text{on}} = 7$ ,  $k_{\text{off}} = 1$ ) to form a domain. NMDARs interacted with this domain and are trapped in an NMDAR cluster ( $k_{\text{on}} = 10$ ,  $k_{\text{off}} = 1$ ).

A “G” molecule was released inside the PSD and was immobilized when it randomly interacted with a pPSD95. After immobilization, the G molecule recruited the insertion of a presynaptic neurotransmitter release site into the presynaptic membrane at the point closest to the location of G. At the same time, G clustered pPSD95 ( $k_{\text{on}} = 100$ ,  $k_{\text{off}} = 1$ ) which, in turn, clustered AMPARs ( $k_{\text{on}} = 10$ ,  $k_{\text{off}} = 1$ ). The detailed interactions with their  $K_d$  (affinity constant) and the kinetics of accumulation are reported SI Appendix, Fig. 4.2.

All this organization of PSD95, AMPARs, NMDARs, and mGluRs at the synapse was simulated with a time step of 1 ms for 10,000 iterations (10 s), until reaching a steady state (as illustrated in SI Appendix, Fig. 4.1). It is important to note that the means employed here to achieve receptor organization are only intended to give the desired final organization in our model and are not intended to model the physiological mechanisms by which this occurs in real synapses. After reaching the desired organization, the simulations were switched to a time step of 1  $\mu\text{s}$  for 250,000 iterations to model the AMPAR, NMDAR, and mGluR activation when the glutamate was released at the presynaptic level, in front of G.

**Sampling and Statistics.** Statistics are presented as mean  $\pm$  SEM. Statistical significance tests were performed using GraphPad Prism software. At least 10 cells from three independent neuronal preparations are acquired per set of data.

**Ethical Approval.** All experiments were approved by the Regional Ethical Committee on Animal Experiments of Bordeaux.

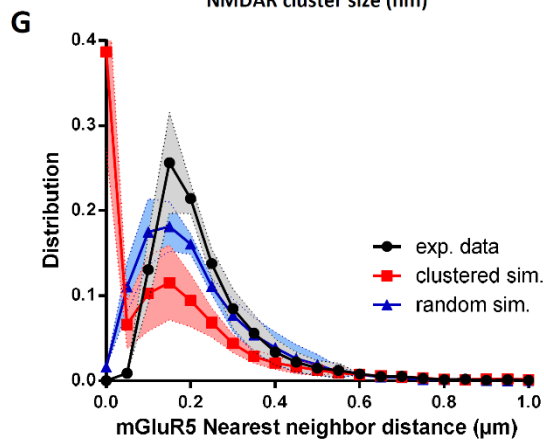
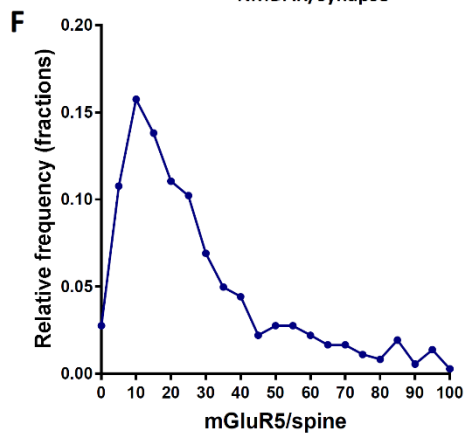
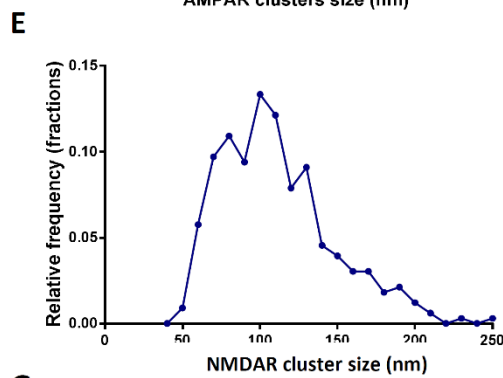
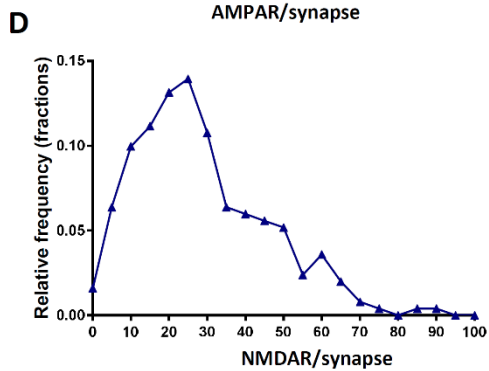
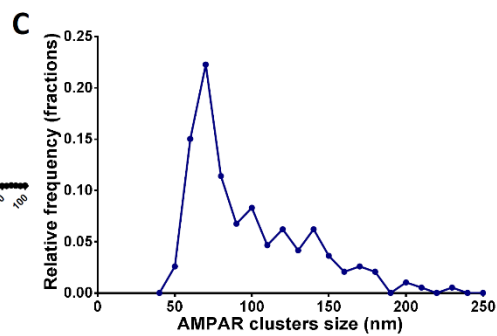
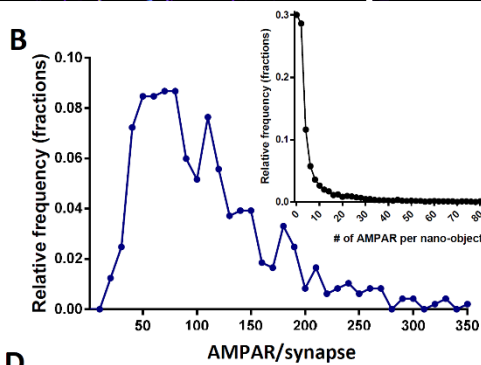
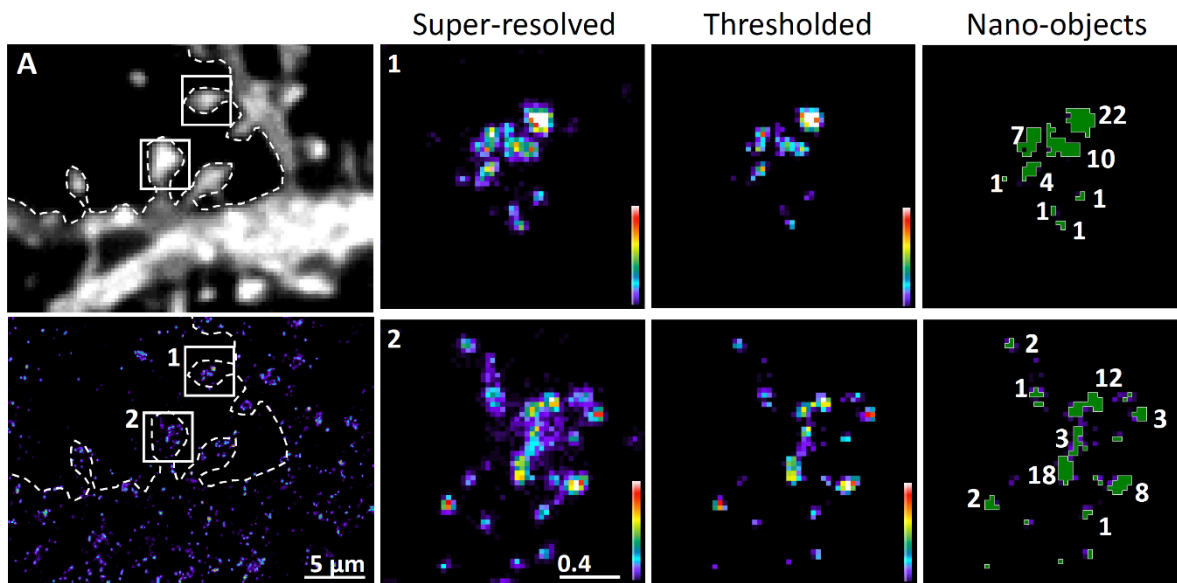
**Data Availability.** The model is accessible at [www.mcell.cnl.salk.edu/models/hippocampus-glutamate-receptor-organization-2020-1](http://www.mcell.cnl.salk.edu/models/hippocampus-glutamate-receptor-organization-2020-1). All other data and associated protocols used for this study are available in the main paper and the SI Appendix.

**ACKNOWLEDGMENTS.** We acknowledge E. Gouaux for the anti-GluA2 and anti-NR1 antibodies. The Bordeaux Imaging Center, part of the France-Bioimaging national infrastructure (Grant ANR-10INBS-04-0) is thanked for support in microscopy. We thank the Initiative for Neurosciences cell biology core facilities (Laboratoire d'Excellence Bordeaux Region Aquitaine [Grant ANR-10-LABX-43]), in particular, C. Breillat, E. Verdier, and N. Retailleau, for cell culture and plasmid production and Jorge Aldana from the Salk Institute for computing support. We thank Corey Butler for his advice on superresolution microscopy and colocalization analysis. This work was supported by funding from the Ministère de l'Enseignement Supérieur et de la Recherche (Grant AMPAR-trapping [ANR AMPAR-T]), Fulbright Program and the Philippe Foundation to E.H. and D.C., Agence Nationale pour la Recherche (NewOptogeneticTools, Grant ANR-15-CE11-0029-01; Laboratory of Excellence, Ion Channel Science and Therapeutics, Grant ANR-11-LABX-0015-01) to M.V., Grant ANR-16-CE13-0018 to J.-B.S., and Centre National de la Recherche Scientifique, European Research Council Grant ADOS (339541) and DynSynMem Grant (787340) to D.C.

3. D. Nair et al., Super-resolution imaging reveals that AMPA receptors inside synapses are dynamically organized in nanodomains regulated by PSD95. *J. Neurosci.* **33**, 13204–13224 (2013).
4. G. Liu, S. Choi, R. W. Tsien, Variability of neurotransmitter concentration and non-saturation of postsynaptic AMPA receptors at synapses in hippocampal cultures and slices. *Neuron* **22**, 395–409 (1999).

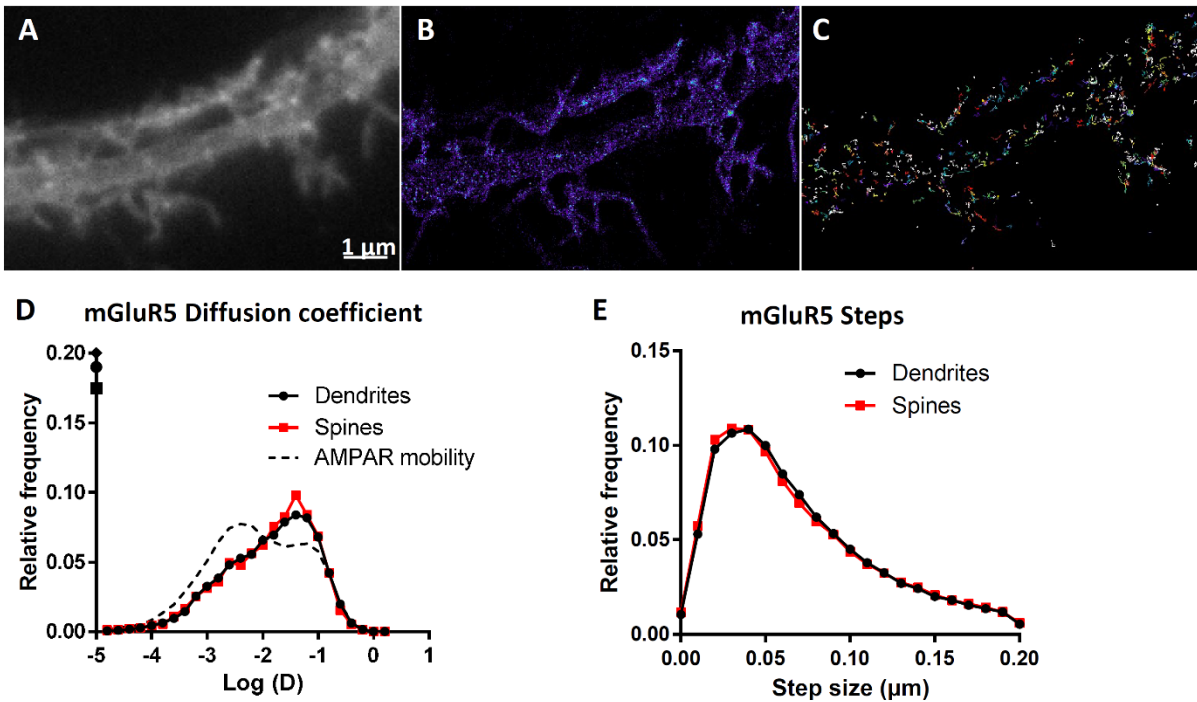
5. Y. Shinohara, Quantification of postsynaptic density proteins: Glutamate receptor subunits and scaffolding proteins. *Hippocampus* **22**, 942–953 (2012).
6. Z. F. Mainen, R. Malinow, K. Svoboda, Synaptic calcium transients in single spines indicate that NMDA receptors are not saturated. *Nature* **399**, 151–155 (1999).
7. A. K. McAllister, C. F. Stevens, Nonsaturation of AMPA and NMDA receptors at hippocampal synapses. *Proc. Natl. Acad. Sci. U.S.A.* **97**, 6173–6178 (2000).
8. E. A. Nimchinsky, R. Yasuda, T. G. Oertner, K. Svoboda, The number of glutamate receptors opened by synaptic stimulation in single hippocampal spines. *J. Neurosci.* **24**, 2054–2064 (2004).
9. S. Raghavachari, J. E. Lisman, Properties of quantal transmission at CA1 synapses. *J. Neurophysiol.* **92**, 2456–2467 (2004).
10. D. A. Rusakov, D. M. Kullmann, Extrasynaptic glutamate diffusion in the hippocampus: Ultrastructural constraints, uptake, and receptor activation. *J. Neurosci.* **18**, 3158–3170 (1998).
11. K. T. Haas *et al.*, Pre-post synaptic alignment through neuroligin-1 tunes synaptic transmission efficiency. *eLife* **7**, e31755 (2018).
12. E. Tarusawa *et al.*, Input-specific intrasynaptic arrangements of ionotropic glutamate receptors and their impact on postsynaptic responses. *J. Neurosci.* **29**, 12896–12908 (2009).
13. Y. Fukata *et al.*, Local palmitoylation cycles define activity-regulated postsynaptic subdomains. *J. Cell Biol.* **202**, 145–161 (2013).
14. H. D. MacGillavry, Y. Song, S. Raghavachari, T. A. Blanpied, Nanoscale scaffolding domains within the postsynaptic density concentrate synaptic AMPA receptors. *Neuron* **78**, 615–622 (2013).
15. A. H. Tang *et al.*, A trans-synaptic nanocolumn aligns neurotransmitter release to receptors. *Nature* **536**, 210–214 (2016).
16. B. Kellermayer *et al.*, Differential nanoscale topography and functional role of GluN2-NMDA receptor subtypes at glutamatergic synapses. *Neuron* **100**, 106–119.e7 (2018).
17. L. Ladepêche *et al.*, Single-molecule imaging of the functional crosstalk between surface NMDA and dopamine D1 receptors. *Proc. Natl. Acad. Sci. U.S.A.* **110**, 18005–18010 (2013).
18. X. Chen *et al.*, PSD-95 family MAGUKs are essential for anchoring AMPA and NMDA receptor complexes at the postsynaptic density. *Proc. Natl. Acad. Sci. U.S.A.* **112**, E6983–E6992 (2015).
19. V. N. Kharazia, R. J. Weinberg, Tangential synaptic distribution of NMDA and AMPA receptors in rat neocortex. *Neurosci. Lett.* **238**, 41–44 (1997).
20. C. Racca, F. A. Stephenson, P. Streit, J. D. Roberts, P. Somogyi, NMDA receptor content of synapses in stratum radiatum of the hippocampal CA1 area. *J. Neurosci.* **20**, 2512–2522 (2000).
21. Z. Nusser, E. Mulvihill, P. Streit, P. Somogyi, Subsynaptic segregation of metabotropic and ionotropic glutamate receptors as revealed by immunogold localization. *Neuroscience* **61**, 421–427 (1994).
22. R. Shigemoto *et al.*, Immunohistochemical localization of a metabotropic glutamate receptor, mGluR5, in the rat brain. *Neurosci. Lett.* **163**, 53–57 (1993).
23. M. Hruska, N. Henderson, S. J. Le Marchand, H. Jafri, M. B. Dalva, Synaptic nanomodules underlie the organization and plasticity of spine synapses. *Nat. Neurosci.* **21**, 671–682 (2018).
24. L. Fagni, F. Ango, J. Perroy, J. Bockaert, Identification and functional roles of metabotropic glutamate receptor-interacting proteins. *Semin. Cell Dev. Biol.* **15**, 289–298 (2004).
25. U. Endesfelder, S. Malkusch, F. Fricke, M. Heilemann, A simple method to estimate the average localization precision of a single-molecule localization microscopy experiment. *Histochem. Cell Biol.* **141**, 629–638 (2014).
26. F. Levet *et al.*, A tessellation-based colocalization analysis approach for single-molecule localization microscopy. *Nat. Commun.* **10**, 2379 (2019).
27. Y. Zhao, S. Chen, A. C. Swensen, W. J. Qian, E. Gouaux, Architecture and subunit arrangement of native AMPA receptors elucidated by cryo-EM. *Science* **364**, 355–362 (2019).
28. T. M. Bartol *et al.*, Computational reconstitution of spine calcium transients from individual proteins. *Front. Synaptic Neurosci.* **7**, 17 (2015).
29. P. Scholler *et al.*, HTS-compatible FRET-based conformational sensors clarify membrane receptor activation. *Nat. Chem. Biol.* **13**, 372–380 (2017).
30. J. Willems *et al.*, ORANGE: A CRISPR/Cas9-based genome editing toolbox for epitope tagging of endogenous proteins in neurons. *PLoS Biol.* **18**, e3000665 (2020).
31. L. Groc *et al.*, Differential activity-dependent regulation of the lateral mobilities of AMPA and NMDA receptors. *Nat. Neurosci.* **7**, 695–696 (2004).
32. Y. H. Suh, K. Chang, K. W. Roche, Metabotropic glutamate receptor trafficking. *Mol. Cell. Neurosci.* **91**, 10–24 (2018).
33. M. Mondin *et al.*, Neurexin-neuroligin adhesions capture surface-diffusing AMPA receptors through PSD-95 scaffolds. *J. Neurosci.* **31**, 13500–13515 (2011).
34. L. Bard *et al.*, Dynamic and specific interaction between synaptic NR2-NMDA receptor and PDZ proteins. *Proc. Natl. Acad. Sci. U.S.A.* **107**, 19561–19566 (2010).
35. M. Zeng *et al.*, Phase separation-mediated TARP/MAGUK complex condensation and AMPA receptor synaptic transmission. *Neuron* **104**, 529–543.e6 (2019).
36. A. Kechkar, D. Nair, M. Heilemann, D. Choquet, J. B. Sibarita, Real-time analysis and visualization for single-molecule based super-resolution microscopy. *PLoS One* **8**, e62918 (2013).
37. J. P. Kinney *et al.*, Extracellular sheets and tunnels modulate glutamate diffusion in hippocampal neuropil. *J. Comp. Neurol.* **521**, 448–464 (2013).
38. P. Jonas, G. Major, B. Sakmann, Quantal components of unitary EPSCs at the mossy fibre synapse on CA3 pyramidal cells of rat hippocampus. *J. Physiol.* **472**, 615–663 (1993).
39. M. Vargas-Caballero, H. P. Robinson, Fast and slow voltage-dependent dynamics of magnesium block in the NMDA receptor: The asymmetric trapping block model. *J. Neurosci.* **24**, 6171–6180 (2004).





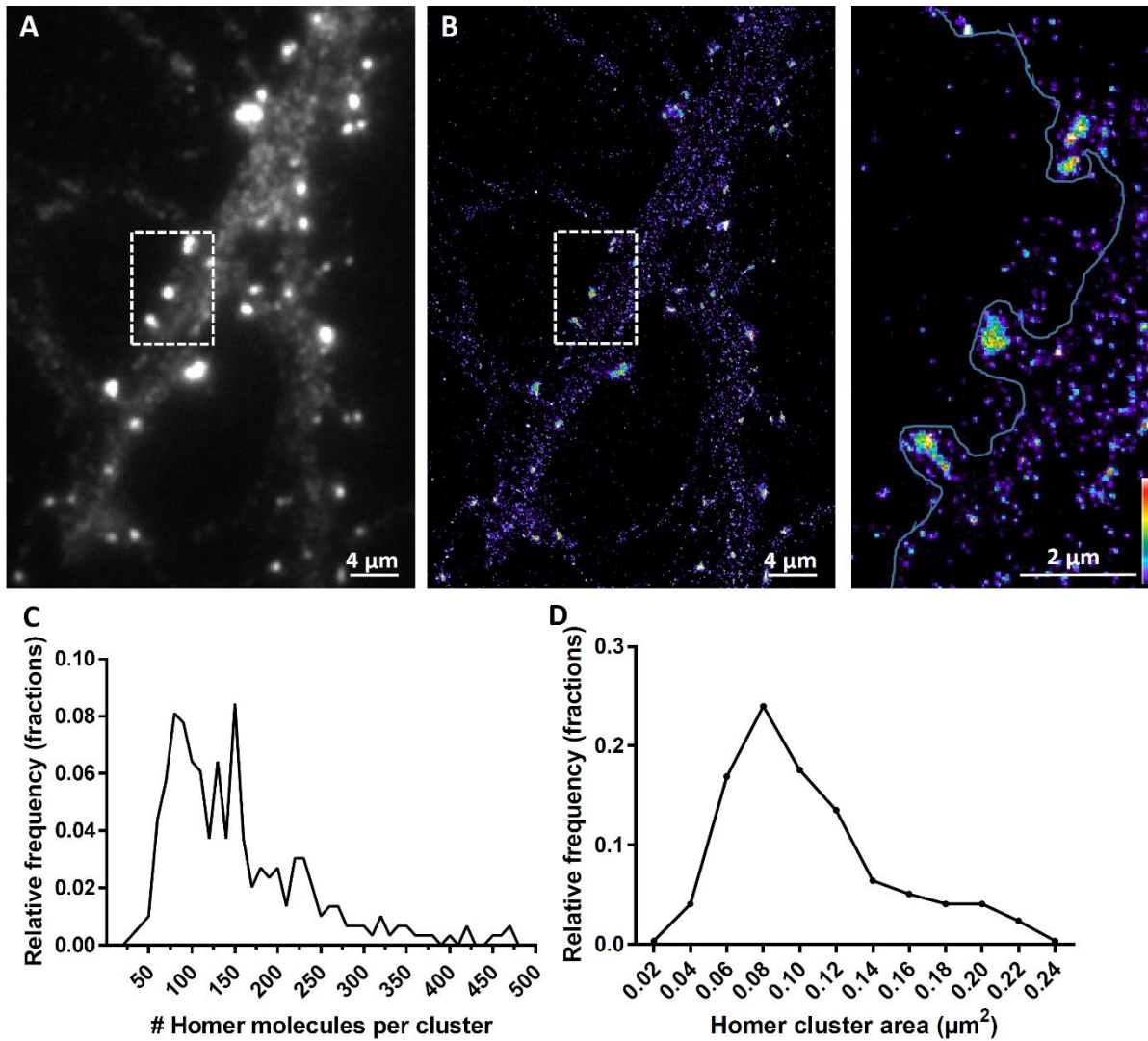
Suppl. Figure 1.1

**Suppl. Figure 1.1.** Characterization of the nano-organization of glutamate receptors. (A) Details of the process to segment nano-objects from intensity images. After d-STORM image reconstruction, the spine regions are identified. Super-resolved images are thresholded to suppress noise signal connecting individual objects. The threshold value is fixed to 5 detections per pixel of 25\*25 nm. Finally, nano-objects are segmented and their intensity divided by the averaged intensity of single receptors measured on dendrites. In example 1, we can observe a main domain containing 22 AMPAR, a second of 10 and a third of 7, etc. B, D and F represent an estimation of the number of receptors per spine, respectively for AMPAR (B), NMDAR (D) and mGluR (F). In B, the inset represents the distribution of the AMPAR number of all synaptic nano-objects. Intensity is color-coded, scale goes from 1 (purple) to 100 (white) detection per pixel. (C and E) Distribution of the synaptic cluster size of AMPAR (C) and NMDAR (E). (G) Experimental distribution of the nearest-neighbor distance (NND) between mGluR5 single objects (dark line), compared to the simulated NND when the same density of objects is either randomly distributed (blue line) or partially clustered (red line). Experimental distributions are closer to a random than to a clustered distribution.



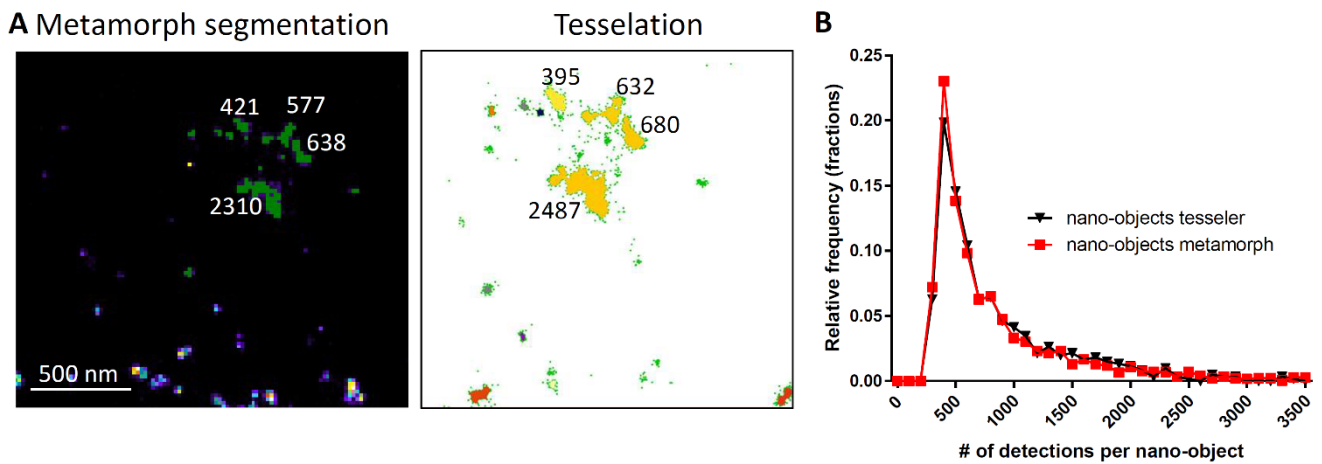
**Suppl. Figure 1.2.** Mobility of mGluR5. (A) Epifluorescence image of a neuron transfected with mGluR5-GFP, (B) super-resolution intensity image reconstructed from sptPALM experiment, and (C) example of single mGluR5 traces. (D and E) distribution of the mGluR5 diffusion properties at spines and dendrites by using MSD analysis (D) which takes into account the entire trajectory length or step analysis (E). Both analyses are unable to discriminate between mobility at spines or on dendrites. (D) dashed line represents the mobility distribution of AMPAR which presents a larger immobile fraction (with log(D) around -3).

**Suppl. Figure 1.2**

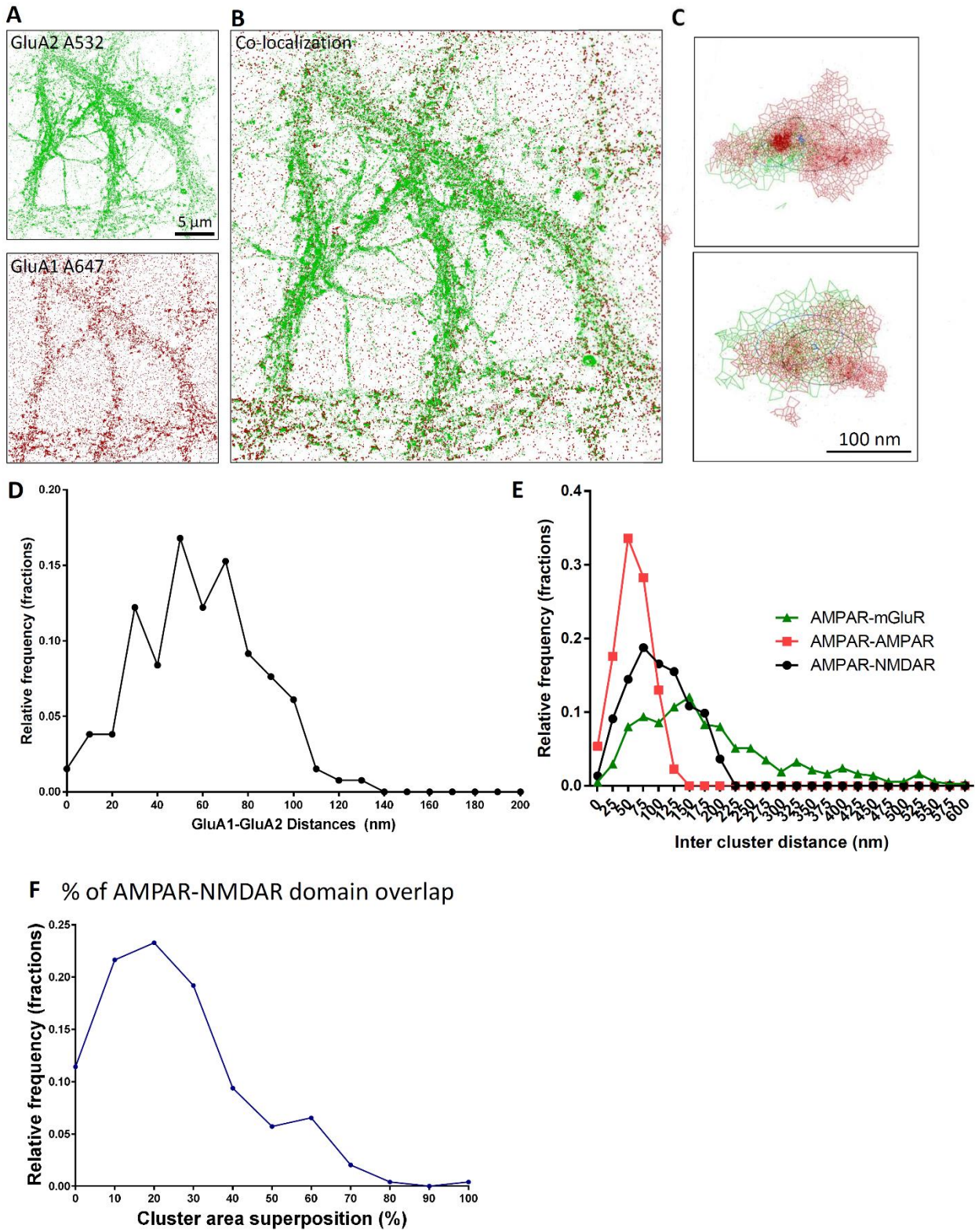


**Suppl. Figure 1.3.** Nanoscale organization of endogenous Homer 1C. (A) Epifluorescence image and (B) d-STORM image of Homer 1c labelled with Alexa 647 nm. A part of dendrite is shown (left panel) with a zoom on synapses (right panel). Homer is mainly organized in a large single synaptic cluster. Intensity is color coded, scale goes from 1 (purple) to 100 (white) detection per pixel. (C) Distribution of the number of Homer molecules per synaptic cluster, and (D) distribution of Homer cluster area.

**Suppl. Figure 1.3**

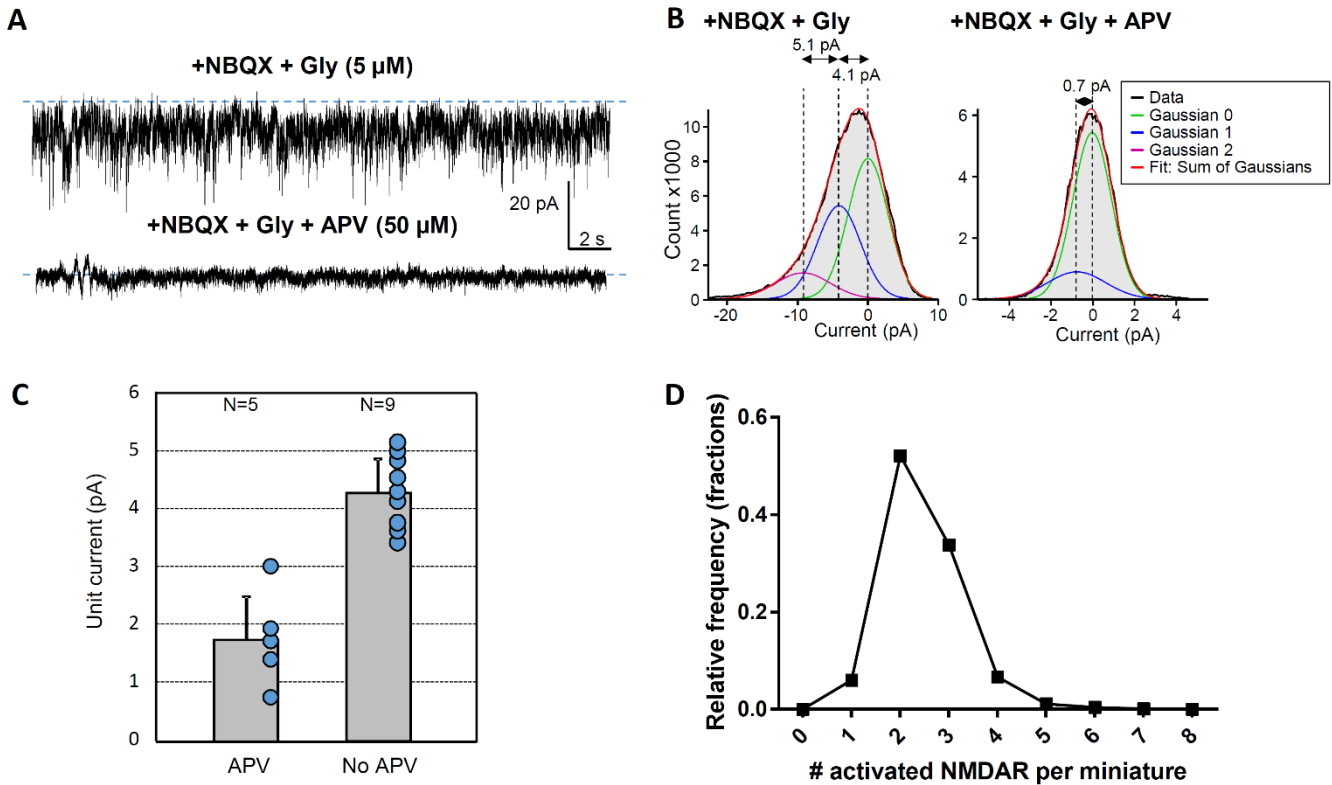


**Suppl. Figure 2.1.** Comparison between intensity-based (MetaMorph) and Tessellation-based (Coloc-Tesseler) cluster analysis. (A) AMPAR containing nano-objects are analyzed using MetaMorph and Coloc-Tesseler. The number of localizations is specified close to each segmented object. (B) Number of detections per nano-object comprising at least 5 fluorophores analyzed with MetaMorph (red line) and Coloc-Tesseler (black line). Both present similar distributions.



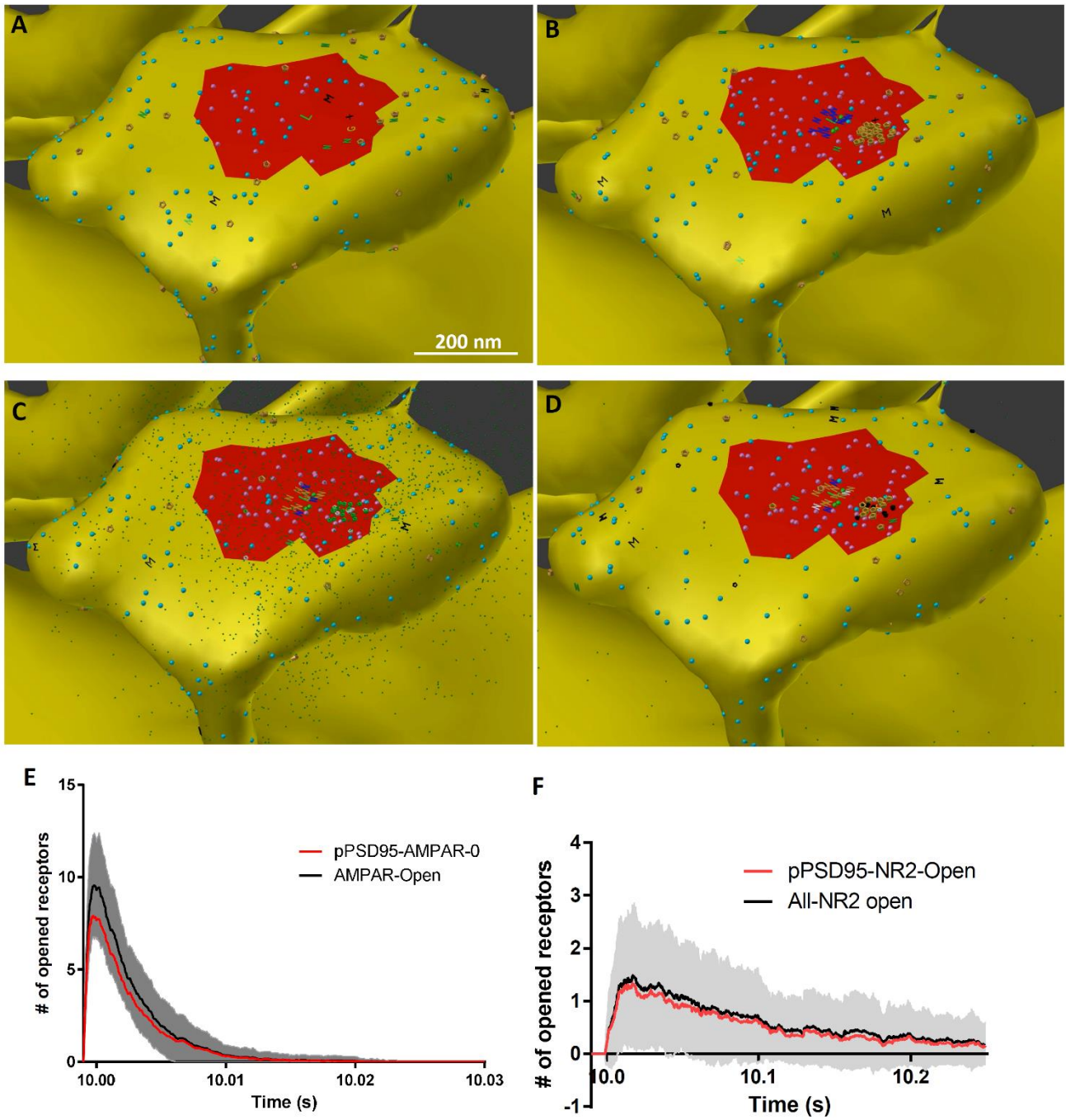
Suppl. Figure 2.2

**Suppl. Figure 2.2.** Dual-color dSTORM imaging of GluA2-containing AMPAR and GluA1-containing AMPAR represented with Coloc-Tesseler software. (A) Super-resolved image of GluA2 acquired at the 532 nm channel (upper panel) and the GluA1 acquired at 647 nm (lower panel). (B) Overlay after drift and chromatic aberration corrections. (C) Zoomed view of 2 synapses, with circles representing the cluster localization. (D) Distribution of the centroid-to-centroid distances between GluA2 and GluA1 nanodomains. The average distance is  $58 \pm 2$  nm. (E) Distribution of the centroid-to-centroid distances between GluA1 and GluA2 nanodomains (red line;  $58 \pm 2$  nm), GluA2 and NR1 nanodomains (black line;  $100 \pm 2$  nm) and GluA2 nanodomains and mGluR5 single object (green line;  $187 \pm 6$  nm). (F) Percentage of AMPAR/NMDAR overlapping clusters.



**Suppl. Figure 3.1.** Analysis of single NMDAR conductance. (A) Example of traces recorded in Tyrode's solution without  $Mg^{2+}$ , in the presence of TTX and NBQX and glycine (upper trace) and after application of APV (lower trace). (B) Distribution of current amplitude in presence and absence of APV, and fits with sums of Gaussian distribution to extract single-channel conductances. (C) Histogram representing the measured single-channel conductances in absence and presence of APV. While mainly noise is extracted in the presence of APV, a conductance of  $\sim 4$  pA is identified in absence of APV, which could correspond to NMDAR conductance. (D) Distribution of the number of NMDAR activated during a miniature current, obtained by dividing the distribution of miniature amplitude by the single-channel conductance obtained in (C).

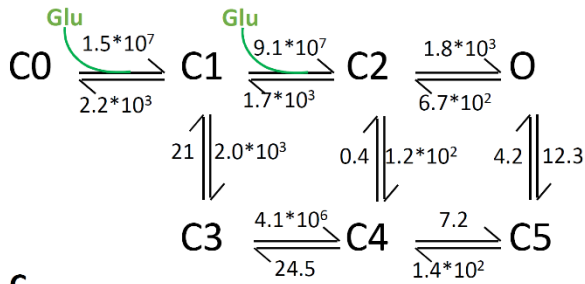




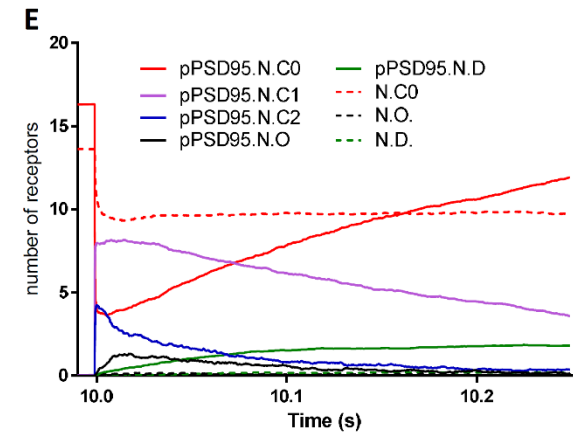
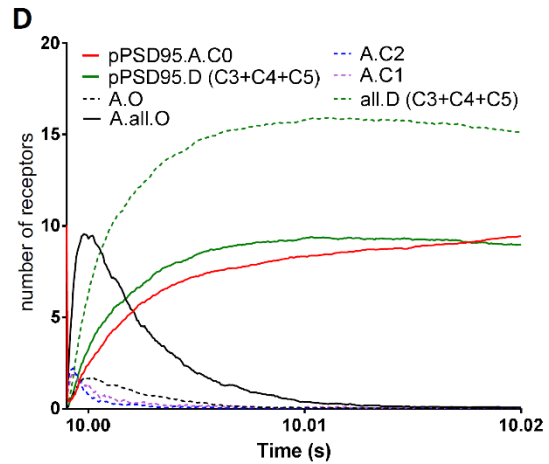
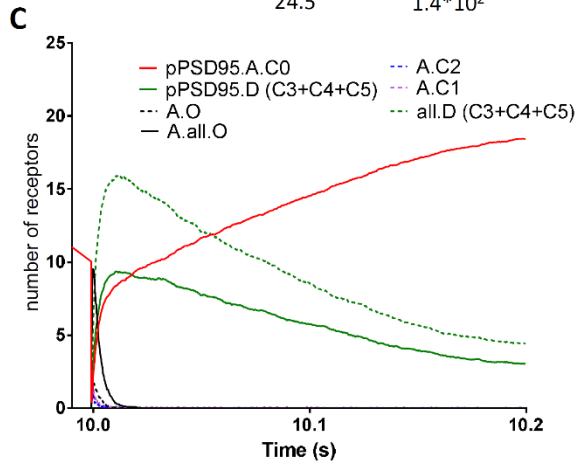
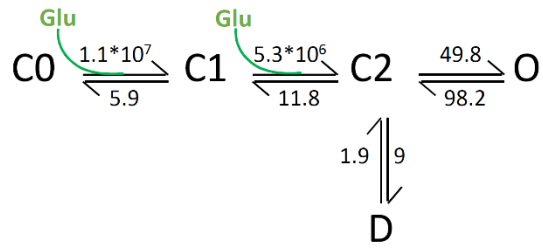
Suppl. Figure 4.1

**Suppl. Figure 4.1.** Model of glutamate receptors co-organization and activation. (A to D), Snapshot model at various iterations. Briefly, PSD95 (blue dots) can be palmitoylated inside the PSD (pPSD95, purple dots). Adhesion protein “L”, which is immobilized at the center of the PSD, can aggregate pPSD95 and trap NMDAR (N) to form a central NMDAR domain. Another adhesion protein “G” is randomly immobilized at the PSD and (i) organizes the cluster of AMPAR (pentagon), and (ii) anchor the release site at the pre-synaptic membrane facing the immobilization site. mGluR5 (M) can diffuse freely at the membrane. (A) is the initial situation. Rapidly, receptors get organized in a similar manner as when experimentally observed with d-STORM (B). When organization is set up, a determined quantity of glutamate can be released at the release site (C) and the various states of receptor activation, depending on their affinities for glutamate and various kinetic properties, can be followed (D). (E and F) represent simulated traces of AMPAR (E) and NMDAR (F) currents. The dark lines represent the total current at the synapse and the red lines, the currents mediated by trapped receptors.

**A AMPAR gating properties**



**B NMDAR gating properties**



**Suppl. Figure 4.2.** Gating properties of modeled receptors. (A and B) Detailed gating states of AMPAR (A) and NMDAR (B) with their respective association (in  $\text{M}^{-1}\cdot\text{s}^{-1}$ )/ dissociation constants (in  $\text{s}^{-1}$ ). (C) Evolution over time of the various populations of AMPAR after glutamate release. A zoom on the first 20 ms is provided (D). (E) Evolution over time of the various populations of NMDAR after glutamate release.

## Chapter 2

### NMDAR-dependent long-term depression is associated with increased short-term plasticity through autophagy mediated loss of PSD-95

Since its discovery more than a century ago, our vision of the synapse has constantly evolved. At the origin considered as a passive and fixed entity, its conceptualization has migrated to a dynamic organelle since the discovery of LTP by Bliss and Lomo in 1973. Indeed, synapses are able to tune the efficacy of synaptic transmission, through a phenomenon called synaptic plasticity. The two main forms are LTP and LTD being an increase and a decrease of synaptic strength respectively. Those forms of synaptic plasticity are thought to be the cellular substrate of learning and memory in the CNS.

During the last 45 years, hippocampal studies have provided decisive insights to the understanding of the molecular mechanisms of LTP and LTD. However, for historical reasons, most of those canonical studies have been mostly focused on LTP thought to be the principal memory engram. Nevertheless, one can also consider that LTP would be of limited use if there was no mechanism to counterbalance its effects. Indeed, during development or learning, synapses are continuously created and suppressed, both being important to refine the neuronal network and to allow cognitive function and behavioral flexibility. During development, synapses are created when an axon crosses a dendrite, through interaction between adhesion molecules, in a non-deterministic manner, meaning independently of its relevance for neuronal functioning, leading to an overproduction of synapses. The overproduced synapses will then be pruned during the network maturation. Then, learning necessitates both strengthen

and weakening of dedicated synapses, underlining the importance of both LTP and LTD for physiology. Starting from those considerations, and the constatation that comprehension of LTD has been mainly limited to reciprocal deductions from LTP findings, my PhD project aimed to understand the molecular substrate sustaining LTD at the nanoscale.

During the beginning of my PhD, I have been implicated in a project initiated by Benjamin Compans, which aimed to decipher the role of AMPARs nano-organization reshufflings during LTD.









For a long time, LTD has only been considered as a decrease of post-synaptic currents. Nonetheless, several molecular induction pathways have been described such as activation of NMDAR, mGluR, insulin or more recently P2XR. The decrease of currents has been related to a decrease of AMPARs at the membrane by increase in endocytosis rate (Rosendale et al., 2017). However, exo/endocytosis are not the only mechanisms that regulate the amount of synaptic AMPARs, they are highly mobile and exchange between synaptic and extra-synaptic sites by lateral diffusion, this parameter being crucial for synaptic transmission regulation (Constals et al., 2015). In the following paper, we thus wondered whether the LTD could be sustained by changes in the mobility of AMPARs, and if this was required for different types of LTD: NMDAR-dependent and P2XR-dependent LTD.

By combining super-resolution microscopy, electrophysiology and modelling, we demonstrated that while both LTDs are associated to a similar decrease of synaptic current due to a loss and a reorganization of synaptic AMPARs, only NMDAR-dependent LTD leads to an increase in AMPAR surface mobility. My role in this project has been to determine the molecular mechanism responsible of this modification of

diffusion properties. I found that a profound reorganization of PSD-95 occurs during NMDAR-dependent LTD, which requires the autophagy machinery to remove the T19-phosphorylated form of PSD-95 from synapses. Moreover, I demonstrated that these post-synaptic changes, that occur specifically during NMDAR-dependent LTD, affect short-term plasticity.

To conclude, our results establish that P2XR and NMDAR-mediated LTD are associated to functionally distinct forms of LTD. Beyond the changes in currents, LTD recover several forms that differentially impact the physiology of the neuron. Therefore, this project brings a new vision of the physiological role of LTD. We hypothesize that the modification of neuronal responsiveness of depressed synapses could serve as a discrimination criterion during synaptic selection. Low active synapses, unable to recover from LTD, would be suppressed later on, and active synapses, able to recover from LTD, would be maintained.

# NMDAR-dependent long-term depression is associated with increased short term plasticity through autophagy mediated loss of PSD-95

Benjamin Compans <sup>1,6</sup>, Come Camus <sup>1,6</sup>, Emmanouela Kallergi<sup>2</sup>, Silvia Sposini<sup>1</sup>, Magalie Martineau<sup>1</sup>, Corey Butler <sup>1</sup>, Adel Kechkar<sup>1</sup>, Remco V. Klaassen<sup>3</sup>, Natacha Retailleau<sup>1</sup>, Terrence J. Sejnowski<sup>4</sup>, August B. Smit <sup>3</sup>, Jean-Baptiste Sibarita <sup>1</sup>, Thomas M. Bartol Jr<sup>4</sup>, David Perrais <sup>1</sup>, Vassiliki Nikolettou<sup>2</sup>, Daniel Choquet <sup>1,5,7</sup> & Eric Hosy <sup>1,7</sup>✉

Long-term depression (LTD) of synaptic strength can take multiple forms and contribute to circuit remodeling, memory encoding or erasure. The generic term LTD encompasses various induction pathways, including activation of NMDA, mGlu or P2X receptors. However, the associated specific molecular mechanisms and effects on synaptic physiology are still unclear. We here compare how NMDAR- or P2XR-dependent LTD affect synaptic nanoscale organization and function in rodents. While both LTDs are associated with a loss and reorganization of synaptic AMPARs, only NMDAR-dependent LTD induction triggers a profound reorganization of PSD-95. This modification, which requires the autophagy machinery to remove the T19-phosphorylated form of PSD-95 from synapses, leads to an increase in AMPAR surface mobility. We demonstrate that these post-synaptic changes that occur specifically during NMDAR-dependent LTD result in an increased short-term plasticity improving neuronal responsiveness of depressed synapses. Our results establish that P2XR- and NMDAR-mediated LTD are associated to functionally distinct forms of LTD.

<sup>1</sup>Interdisciplinary Institute for Neuroscience, CNRS, Univ. Bordeaux, IINS, UMR 5297, Bordeaux, France. <sup>2</sup>Department of Fundamental Neurosciences, University of Lausanne, Lausanne, Switzerland. <sup>3</sup>Department Molecular and Cellular Neurobiology, Amsterdam, HV, The Netherlands. <sup>4</sup>Howard Hughes Medical Institute, Salk Institute for Biological Studies, La Jolla, CA, USA. <sup>5</sup>Univ. Bordeaux, CNRS, INSERM, Bordeaux Imaging Center, BIC, UMS 3420, Bordeaux, France. <sup>6</sup>These authors contributed equally: Benjamin Compans, Come Camus. <sup>7</sup>These authors jointly supervised this work: Daniel Choquet, Eric Hosy. ✉email: [eric.hosy@u-bordeaux.fr](mailto:eric.hosy@u-bordeaux.fr)

Changes in synaptic efficacy, either by strengthening through long-term potentiation (LTP) or weakening through long-term depression (LTD), are believed to underlie learning and memory. At the archetypal Schaeffer collateral to CA1 pyramidal neuron synapses, these forms of activity-dependent synaptic plasticity rely largely on the regulation of AMPA-type glutamate receptor number at synapses. In addition to endo- and exocytosis which control the total amount of receptors at the neuronal surface, the equilibrium at the membrane between freely-diffusive and immobilized AMPAR at the PSD regulates synaptic responses<sup>1–6</sup>. This equilibrium involves the binding of AMPAR associated-proteins to post-synaptic scaffolding proteins (e.g., PSD-95), which anchor AMPAR complexes at the PSD. A balanced activity of phosphatases and kinases on various targets ultimately regulates the affinities of the components of the AMPAR complexes for their scaffolds and their characteristic trapping times at synapses<sup>7–9</sup>. We, and others, have demonstrated that synaptic strength is not solely dependent on the quantity of glutamate per pre-synaptic vesicle and the number of post-synaptic AMPARs, but also rely on their nanoscale organization with respect to the pre-synaptic active zone<sup>10–13</sup>. Modeling predicts that long-term modifications in synaptic strength, as observed during LTD or LTP, can result from (i) changes in AMPAR density at synapse, (ii) variations in receptor amount per cluster or (iii) modifications of the alignment between pre-synaptic release site and AMPAR clusters<sup>10,14</sup>.

This dynamic equilibrium between mobile and trapped AMPARs regulates synaptic transmission properties at multiple timescales. Indeed, at short time scales (ms to s), we established the role of mobile AMPAR in short-term plasticity. This plasticity, observed when synapses are stimulated at tens of Hz, was previously thought to rely on both pre-synaptic mechanisms, and AMPAR desensitization properties<sup>15–17</sup>. After glutamate release, desensitized AMPARs can rapidly exchange by lateral diffusion with naive receptors, increasing the number of receptors which can be activated after a second glutamate release<sup>18–22</sup>. In various experimental paradigms, a decrease in the pool of mobile AMPARs using either receptor crosslinking<sup>18,19</sup>, CaMKII activation<sup>20</sup> or fused AMPAR-TARPs<sup>18,23</sup> enhances short-term depression. In addition to its role in short-term plasticity, AMPAR lateral diffusion and activity-dependent synaptic trapping plays a key role during LTP<sup>20,24</sup>. Specifically, altering the synaptic recruitment of AMPAR by interfering with AMPAR lateral diffusion impairs the early LTP<sup>24</sup>. These studies demonstrated that nanoscale regulation of AMPAR organization and dynamics tune individual as well as frequency dependent synaptic responses. However, few studies have yet addressed the molecular reshuffling induced by LTD.

LTD is a generic term indicating a decrease in synaptic strength, but it can be induced by different pathways. These include for example the classical glutamate-induced LTD through the activation of NMDAR or mGluR<sup>25,26</sup>, the insulin-induced LTD<sup>27</sup> or the ATP-induced LTD<sup>28,29</sup>. Each of these forms results from a specific physiological stimulus such as low frequency stimulation (LFS), which mainly involves NMDAR<sup>26</sup>, or the release of ATP by astrocytes following noradrenergic stimulation<sup>29</sup>. Interestingly, they all share intertwined molecular pathways, activating either specific or identical phosphatases/kinases<sup>27,29,30</sup>. All these pathways lead to a rapid increase of AMPAR endocytosis, responsible for synaptic depression. However, it is still unclear if all these LTD types trigger at long term, similar modification in synaptic physiology.

To investigate how various LTD protocols are associated with the dynamic reorganization of synaptic AMPAR, we combined live and fixed super-resolution microscopy, live imaging of glutamate release and measurements of exo-endocytosis of AMPARs, electrophysiology together with modeling. We tested

two well characterized LTD protocols based on the activation of either the NMDARs, by NMDA, or the P2X receptors (P2XRs), by ATP<sup>26,29,31</sup>. We observed that NMDAR-, but not P2XR-dependent LTD triggers specific changes in PSD-95 nanoscale organization in an autophagosome-dependent mechanism, responsible for an increase in AMPAR lateral diffusion. Finally, we show that the latter improves the capacity of depressed synapses to integrate high frequency stimulations. Overall, our results reveal that following the initial decrease in AMPAR synaptic content by endocytosis, the various LTD forms are not only associated to a depression of the post-synaptic response, but trigger specific modifications of the synaptic architecture and physiology affecting the ability of the post-synapse to integrate pre-synaptic inputs.

## Results

**ATP and NMDA treatments both induce a long-lasting decrease in synaptic AMPAR content and miniature amplitude.** We performed direct Stochastic Optical Reconstruction Microscopy (dSTORM) experiments and electrophysiological recordings in cultured rat primary hippocampal neurons to monitor AMPAR organization and currents following the application of either ATP or NMDA, two chemical protocols well-established to trigger a long lasting synaptic depression<sup>29,31</sup>. The fluorescent emission property of individual AMPAR was extracted from isolated receptors present at the membrane surface<sup>12</sup> and used to estimate the density and number of AMPARs in different neuronal compartments.

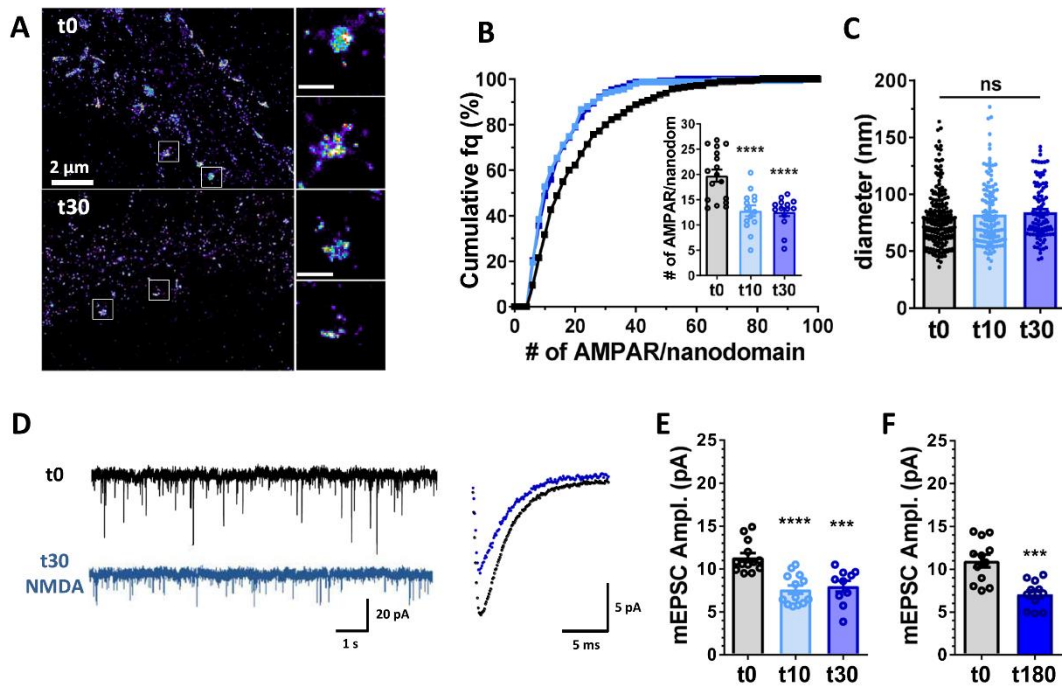
NMDA treatment (30  $\mu$ M, 3 min) led to a rapid and stable decrease in AMPAR density both in the dendritic shaft and spines (decrease of 40% in dendrites and 22% in spines, Supplementary Fig. 1A, B). As previously described, ~50% of synaptic AMPAR are organized in nanodomains facing pre-synaptic release sites<sup>11,12</sup>. NMDAR-dependent LTD was also associated with a rapid (within the first 10 min following NMDA application) and stable (up to 3 h) depletion in AMPAR content per nanodomain (estimated number of AMPAR per nanodomain (mean of the mean per cell): t0: 19.77  $\pm$  1.20, t10: 12.82  $\pm$  1.05, t30: 12.59  $\pm$  0.82) (Fig. 1A, B). In contrast, the overall nanodomain diameter was preserved as shown by the stability of their full width half maximum (t0: 79.13  $\pm$  1.82 nm, t10: 82.04  $\pm$  2.53 nm, t30: 84.35  $\pm$  2.43 nm) (Fig. 1C). This reorganization of synaptic AMPAR was associated with a depression in AMPAR-mediated miniature excitatory post-synaptic current amplitude (mEPSC; Fig. 1D, E, t0: 11.34  $\pm$  0.50 pA, t10: 7.60  $\pm$  0.49 pA, t30: 8.00  $\pm$  0.65 pA), which lasted up to 3 h after NMDA treatment (Fig. 1F, t0: 10.98  $\pm$  0.73 pA, t180: 7.06  $\pm$  0.49 pA).

In parallel, we measured the effect of ATP treatment, reported as able to induce a robust and long lasting LTD, on both AMPAR nanoscale organization and mEPSCs (Fig. 1G–L). Purinergic receptors from the P2X family were activated using ATP (100  $\mu$ M, 1 min) in the presence of CGS15943 (3  $\mu$ M) to avoid adenosine receptor activation<sup>29,32</sup>. As for NMDA, ATP treatment triggered a rapid and long-lasting decrease in AMPAR content both at dendritic shafts, spines (Supplementary Fig. 1E, F) and nanodomains (estimated number of AMPAR per nanodomain: t0: 20.36  $\pm$  1.61, t10: 13.21  $\pm$  0.46, t30: 15.38  $\pm$  0.53), without affecting their overall organization (t0: 68.19  $\pm$  2.55 nm, t10: 66.81  $\pm$  2.57 nm, t30: 70.62  $\pm$  3.11 nm) (Fig. 1G–I). In parallel, this depletion of AMPAR nanodomains was associated with a stable long-lasting decrease in mEPSC amplitude (t0: 11.93  $\pm$  0.89 pA, t10: 9.05  $\pm$  0.68 pA, t30: 8.95  $\pm$  0.70 pA) (Fig. 1J–L).

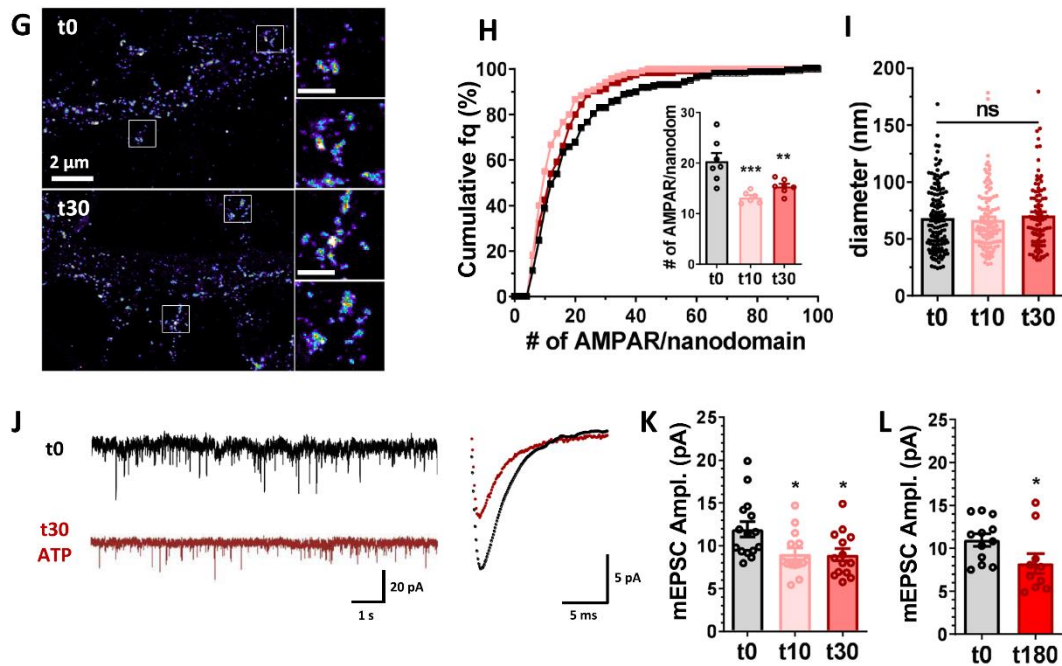
Altogether, these results indicate that both NMDA- and ATP-induced synaptic depression are associated with a reduction in the number of surface AMPARs at the synapse and on the dendrite,



### Synaptic AMPAR : NMDAR-dependent LTD



### Synaptic AMPAR : P2XR-dependent LTD



notably leading to a depletion in nanodomain content, without a change in their overall dimensions.

To determine whether the mEPSC amplitude decrease was associated with modifications in current kinetics, which might be caused by changes in the composition of AMPAR complexes, we analyzed both rise and decay times of mEPSCs. We observed no

modifications in current kinetics when LTD was induced by either NMDA or ATP (Supplementary Fig. 2). Interestingly, we observed a transient decrease in the mEPSC frequency after NMDA treatment, which might be explained by the decrease in the number of nanodomains per spine (Supplementary Figs. 1C, D and 2). This observation suggests the complete disappearance of some domains.

**Fig. 1 NMDA and ATP application triggers a rapid and long-lasting nanoscale reorganization of AMPAR at synapses associated to a long-term synaptic current depression.** **A** Example of super-resolution intensity images of a piece of dendrite obtained using dSTORM technique on live stained neurons for endogenous GluA2 containing AMPARs at basal state (t0) or 30 min (t30) following NMDA application (30  $\mu$ M, 3 min). Enlarged synapses are shown on the right. **B** Cumulative distribution of nanodomain AMPAR content ( $n = 275, 159$  and  $152$  for t0, t10 and t30 respectively), and in the inset, the mean per cell. The number of AMPARs per nanodomain was estimated 0, 10 and 30 min following NMDA treatment as explained in Nair et al. 2013 (mean  $\pm$  SEM,  $n = 17, 14$  and  $14$  respectively, one-way ANOVA,  $p < 0.0001$  and Dunnett's post-test found significant differences between t10 or t30 and t0,  $p < 0.0001$ ). Nanodomain content is significantly decreased 10 and 30 min following NMDA treatment compared to non-treated cells. **C** Diameter of AMPAR synaptic nanodomains. Nanodomain sizes were measured by anisotropic Gaussian fitting of pre-segmented clusters obtained on dSTORM images. Nanodomain diameter (mean  $\pm$  SEM) 0, 10 and 30 min following NMDA treatment are plotted ( $n = 191, 127$  and  $100$  respectively, one-way ANOVA,  $p = 0.2487$ ). Nanodomain size is not affected by NMDA application. **D** Left panel: example of miniature EPSC traces recorded on cultured neurons in basal condition (dark trace) or 30 min after NMDA treatment (blue trace). Right panel: Superposition of a mean trace of AMPAR mEPSC in basal (dark) and 30 min post-NMDA treatment (blue). **E** and **F** Average of the mEPSC amplitude recorded on neurons 0, 10 or 30 min (**E**) and 180 min (**F**) after NMDA treatment. Miniature EPSC amplitudes are significantly depressed 10 and 30 min after NMDA treatment (**E**,  $n = 13, 13$  and  $10$  respectively, one-way ANOVA  $p < 0.0001$  and Dunnett's post-test found significant differences  $p < 0.0001$  and  $p = 0.0003$  between t0 and t10, and t0 and t30 respectively), and this depression stays for at least 3 h (**F**,  $n = 12$  and  $11$  respectively,  $t$ -test  $p = 0.0003$ ). **G** Example of super-resolution intensity images of a piece of dendrite obtained using dSTORM technique on neurons live stained for endogenous GluA2 containing AMPARs at basal state (t0) or 30 min (t30) following ATP (100  $\mu$ M, 1 min). Enlarged synapses are shown on the right. **H** Cumulative distribution of nanodomain AMPAR content ( $n = 158, 120$  and  $115$  for t0, t10 and t30 respectively), and in the inset, the mean per cell. The number of AMPARs per nanodomains was estimated 0, 10 and 30 min following ATP treatment (mean  $\pm$  SEM,  $n = 7, 6$  and  $7$  respectively, one-way ANOVA,  $p = 0.0006$  and Dunnett's post-test found significant differences between t10 or t30 and t0,  $p = 0.0004$  and  $p = 0.0063$  respectively). Nanodomain content is decreased 10 and 30 min following ATP treatment compared to non-treated cells. **I** Measure of nanodomain diameter is not affected 0, 10 and 30 min following ATP treatment ( $n = 130, 112$  and  $91$  respectively, one-way ANOVA,  $p = 0.6391$ ). **J** Left panel: example of miniature EPSC traces recorded on cultured neurons in basal condition (dark trace) or 30 min after ATP treatment (red trace). Right panel: Superposition of a mean trace of AMPAR mEPSC in basal (dark) and 30 min post-ATP treatment (red). **K** and **L** Average of the mEPSC amplitude recorded on neurons 0, 10 or 30 min (**K**) and 180 min (**L**) after ATP treatment (100  $\mu$ M, 1 min). Synaptic transmission (mEPSCs) is significantly depressed 10 and 30 min after ATP treatment (mean  $\pm$  SEM, **K**,  $n = 15, 14$  and  $14$  respectively, one-way ANOVA  $p = 0.0124$  and Dunnett's post-test found significant differences  $p = 0.0214$  and  $p = 0.0172$  between t0 and t10, and t0 and t30 respectively), and this depression stays for at least 3 h (**L**,  $n = 12$  and  $10$  respectively,  $t$ -test  $p = 0.0485$ ). Scale bars (**A** and **G**) left images = 2  $\mu$ m, zoom on synapses (left panels) = 500 nm.

This effect on the nanodomains was not observed when LTD was induced by ATP (Supplementary Figs. 1G and 2).

As demonstrated in<sup>10</sup>, a decrease in synaptic response could be due to a change in pre- to post-synaptic alignment. To estimate whether NMDA treatment affected the trans-synaptic organization, we performed dual-color d-STORM experiments to measure the alignment of the pre-synaptic protein RIM1/2 with the post-synaptic AMPAR (Supplementary Fig. 3A, B). We calculated the centroid to centroid distances between RIM1/2 and GluA2-containing AMPAR clusters at t0, and 10 and 30 min after NMDA treatment (Supplementary Fig. 3A, D). NMDA treatment did not significantly change the RIM/AMPA co-organization.

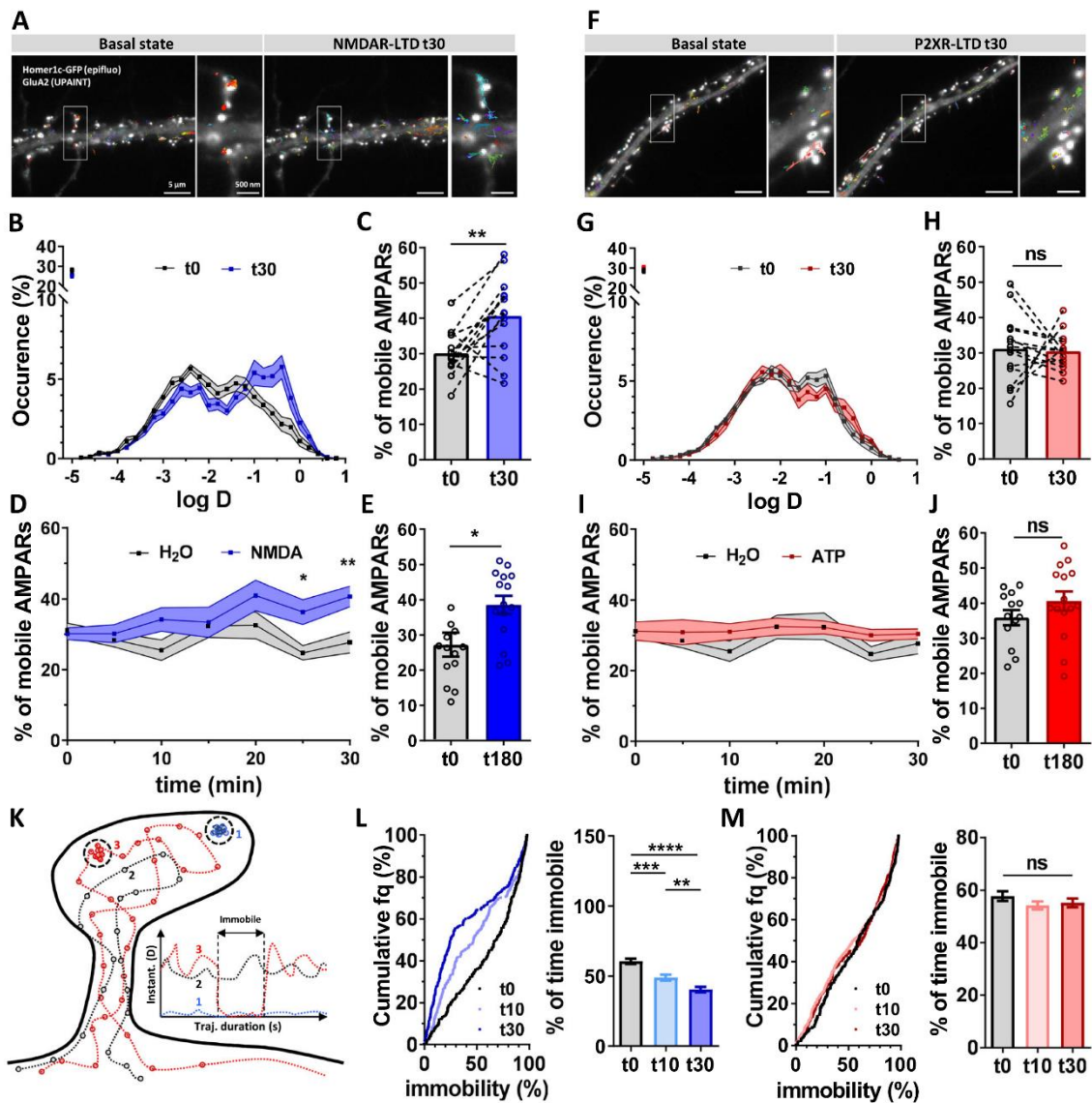
**AMPA lateral diffusion is increased during NMDAR-dependent LTD but not during P2XR-dependent LTD.** Changes in both AMPARs endocytosis and exocytosis have been involved in synaptic plasticities. More particularly, in NMDA- and ATP-induced LTD, a rapid but transient increase in endocytosis rate has been observed<sup>29,33–35</sup>. This mechanism has been proposed to primarily mediate the depression of synaptic AMPAR currents. The general view being thus that induction of both NMDAR- and P2XR-dependent LTD results from transient AMPAR endocytosis at perisynaptic sites after their escape from synapses by lateral diffusion. However, both NMDAR- and P2XR-dependent forms of LTD last at least for 3 h (Fig. 1F and L). This indicates that once synapses are depressed, they reach a new equilibrium, which is poorly characterized.

We thus aimed to first determine the status of AMPAR trafficking at the equilibrium at depressed synapses, as a function of the LTD induction protocol. To this aim, we investigated the properties of AMPAR lateral diffusion during the two LTD-inducing protocols. Using the single-particle tracking technique uPAINT<sup>36</sup>, we measured endogenous GluA2-containing AMPAR mobility at the cell surface. We acquired time lapse series consisting of 1.5 min acquisitions performed every 5 min for 30 min on cells in the basal condition and upon NMDAR- or

P2XR-dependent LTD induction. As previously described<sup>12</sup> and illustrated Fig. 2B and G (control in black line), distribution of AMPAR diffusion coefficients reveal two main populations centered approximatively at  $0.8 \cdot 10^{-2} \mu\text{m}^2 \text{s}^{-1}$  (termed immobile trapped receptors) and  $10^{-1} \mu\text{m}^2 \text{s}^{-1}$  (termed mobile receptors). 30 min following NMDA treatment, we observed a 35% increase in the AMPAR mobile fraction (D coef  $> 0.02 \mu\text{m}^2 \text{s}^{-1}$ ) (t0:  $30.11 \pm 1.69\%$ , t30:  $40.65 \pm 2.94\%$ ) (Fig. 2A–C). In contrast, we observed no change in AMPAR lateral diffusion with vehicle ( $\text{H}_2\text{O}$ ) treatment (t0:  $31.17 \pm 1.94\%$ , t30:  $27.71 \pm 2.98\%$ ) (Fig. 2D), or 30 min after an ATP treatment (t0:  $31.19 \pm 2.58\%$ , t30:  $30.44 \pm 1.40\%$ ) (Fig. 2F–J). Similar results were obtained for synaptic trajectories of the GluA2-containing AMPAR (Supplementary Fig. 6).

This increase in AMPAR mobility following NMDAR-dependent LTD induction takes place progressively along the first 20 min following NMDA treatment (Fig. 2D) and remains stable up to 3 h (Fig. 2E; t0:  $27.25 \pm 3.41\%$ , t180:  $38.57 \pm 2.56\%$ ). On the contrary, neither control nor ATP treatment induced such changes in AMPAR mobility (Fig. 2I, J). Moreover, in the presence of APV (50  $\mu$ M), a specific NMDAR antagonist, no increase in AMPAR mobility was observed after NMDA treatment (Supplementary Fig. 7).

As previously described, AMPARs alternate between two main diffusion modes at the plasma membrane: an immobile one when trapped by interaction with scaffolding proteins, and a freely diffusive one<sup>37</sup>. We calculated the instantaneous AMPAR diffusion coefficients over time from individual synaptic trajectories<sup>18</sup>. For each trajectory, we classified AMPAR movement in three categories: receptors always mobile (class I), receptors always immobile (class II) and receptors alternating between mobile and immobile states (class III) (Fig. 2K). Two parameters were computed: the percentage of class II receptors, and the duration of immobilization of the class III receptors. The immobilization duration of mobile receptors, which reflects the avidity of AMPAR for trapping slots, was significantly decreased when LTD was induced by NMDA treatment (Fig. 2L). Before NMDA application, at synapses,



GluA2-containing receptors were immobile  $\sim 60\%$  of the trajectory duration ( $60.56 \pm 1.91$ ) whereas this duration decreased to  $48.92\% \pm 2.11$  after 10 min and to  $40.37\% \pm 2.03$  30 min following NMDA treatment (Fig. 2L). In contrast, after ATP treatment, this percentage remained unchanged (t0:  $57.7\% \pm 1.83$ , t10:  $54.14\% \pm 1.54$ , t30:  $55.13\% \pm 1.71$ ) (Fig. 2M). Overall, these results demonstrate that NMDAR-dependent LTD, but not P2XR-dependent LTD, triggers an increase in AMPAR lateral mobility that takes place progressively after the LTD induction phase and remains stable for at least 3 h. At equilibrium, synapses depressed through NMDAR and P2XR thus harbor similar amounts of depression but distinct AMPAR mobility properties.

Given their supposed key role in LTD processes, we also characterized the endo/exocytosis properties at 3 h after LTD induction, when the long-term equilibrium of the depressed synapses is reached. We imaged neurons transfected with GluA1 and GluA2 labeled with pH sensitive superecliptic pHluorin (SEP) to measure directly their endocytosis (with the ppH protocol, Rosendale et al. 2017) and exocytosis rates<sup>38–40</sup>, sampled for 5 min

for endocytosis or 1 min for exocytosis, 3 h after induction of LTD (Supplementary Figs. 4 and 5). We did not detect any modification of the frequency or amplitude of endocytic and exocytic events after either NMDA or ATP treatment compared to conditions before treatment or 3 h after vehicle application (H<sub>2</sub>O) (Supplementary Figs. 4 and 5). This reveals that the maintenance of LTD is not due to a sustained modification of the endo/exocytosis balance of AMPARs.

In conclusion, the long-term equilibrium of depressed synapses seems to be maintained not by an endo/exocytosis unbalance but by a modification of AMPAR trapping at the PSD, increasing the pool of mobile receptors at the expense of the trapped ones.

**NMDAR-dependent LTD triggers a depletion of PSD-95 at synapses.** We next aimed at understanding the molecular mechanism underlying the changes in AMPAR mobility after the different LTD-inducing protocols. Various molecular modifications have been described to impact AMPAR mobility, including a diminution in the number of trapping slots, or a decrease in

**Fig. 2 NMDAR-dependent LTD but not P2XR-dependent LTD triggers a long-term increase of AMPAR lateral diffusion.** **A** Epifluorescence image of a dendritic segment expressing eGFP-Homer1c as a synaptic marker and GluA2-containing AMPAR trajectories acquired with uPAINT in basal state (left panel) and 30 min after NMDA treatment (right panel). **B** Average distribution of the  $\log(D)$  (mean  $\pm$  SEM), ( $D$  being the diffusion coefficient of endogenous AMPAR) in control condition (black line,  $n = 14$ ) and 30 min after NMDA treatment (blue line,  $n = 14$ ). **C** Average of the mobile fraction per cell, before and 30 min after NMDAR-dependent LTD induction ( $n = 14$  cells, mean  $\pm$  SEM, paired  $t$ -test,  $p = 0.0042$ ). **D** Time-lapse (from 0 to 30 min) of GluA2-containing AMPAR mobility following NMDAR-dependent LTD induction (blue line) compared to vehicle application (green line) (mean  $\pm$  SEM,  $n = 14$  and 10 respectively). A significant increase of GluA2-containing AMPAR occurs 25 min after NMDA application. **E** Average histograms of the mobile fraction per cell, before and 180 min after NMDAR-dependent LTD induction ( $n = 14$  and 15 cells, mean  $\pm$  SEM, unpaired  $t$ -test,  $p = 0.0123$ ). GluA2-containing AMPAR increased mobility remains stable for at least 3 h. **F–J** Similar experiments as from (**A–E**) has been realized with ATP-induced LTD protocol. **F** Epifluorescence image of a dendritic segment expressing eGFP-Homer1c with acquired trajectories of GluA2-containing AMPAR trajectories in basal state (left panel) and 30 min after ATP treatment (right panel). **G** Average distribution of the  $\log(D)$  before (black line,  $n = 14$ ) and 30 min (red line,  $n = 14$ ) after ATP treatment (mean  $\pm$  SEM). **H** Average of the mobile fraction per cell extracted from (**G**), ( $n = 14$  cells, mean  $\pm$  SEM, paired  $t$ -test,  $p = 0.8234$ ). Contrary to NMDA-induced LTD, ATP-induced LTD is not associated with an increase of AMPAR mobility. **I** Time-lapse (from 0 to 30 min) of AMPAR mobility following P2XR-dependent LTD induction (red line) compared to vehicle application (green line) (mean  $\pm$  SEM,  $n = 14$  and 10 respectively). **J** Average histograms of the mobile fraction per cell, before and 180 min after P2XR-dependent LTD induction ( $n = 13$  and 15 cells, mean  $\pm$  SEM, unpaired  $t$ -test,  $p = 0.1950$ ). No modification of AMPAR mobility is observed all along the 3 h experiments. **K** Scheme of the various AMPAR trajectory behaviors. AMPAR can be fully immobile (1, blue line), fully mobile (2 dark line) or alternate between mobile and immobile (3, red line). Calculation of the % of immobility all along the trajectory duration give an indication of the avidity of AMPAR for their molecular traps. **L** Variation of the % of AMPAR mobility per synaptic trajectories after NMDAR treatment (control (black line), 10 min (light blue line) and 30 min (dark blue line)). The left panel represents the cumulative distribution and the right panel the mean  $\pm$  SEM. ( $n = 252, 235$  and 280 synaptic trajectories respectively, one-way ANOVA  $p < 0.0001$  and Tukey's post-test found significant differences  $p = 0.0002$  and  $p < 0.0001$  between  $t_0$  and  $t_{10}$ , and  $t_0$  and  $t_{30}$  respectively, and  $p = 0.0081$  between  $t_{10}$  and  $t_{30}$ ). **M** Variation of the % of AMPAR mobility per synaptic trajectories during ATP-induced LTD (control (black line), 10 min (light red line) and 30 min (dark red line) following LTD induction). The left panel represents the cumulative distribution and the right panel the mean  $\pm$  SEM ( $n = 264, 434$  and 326 synaptic trajectories respectively, one-way ANOVA  $p = 0.3360$ ). Scale bars (**A** and **F**): 5  $\mu\text{m}$ , and 500 nm for the zoom image on synapses.

AMPA affinity for these slots by modifications in the AMPAR complex composition or phosphorylation status<sup>32,41</sup>. PSD-95 is the main scaffolding protein of the excitatory post-synaptic density and a major actor in AMPAR stabilization at synapses<sup>7,42</sup>. Hence, we used dSTORM to measure PSD-95 nanoscale organization following both NMDAR- and P2XR-dependent LTD induction (Fig. 3). As previously described, PSD-95 presents two levels of enrichment at synapses<sup>12,13,43</sup> the first one delineating the PSD, the second one corresponding to small domains of local over-concentration into the PSD, beneath the AMPAR nanodomains and facing the glutamate release sites (Fig. 3A)<sup>10–12</sup>. Using tessellation-based clustering analysis<sup>44</sup>, we extracted the first level (termed PSD-95 clusters), and the second level of clustering (termed PSD-95 nanoclusters) (Fig. 3A). After NMDA treatment, both PSD-95 clusters and nanoclusters displayed a decrease in number of PSD-95 (estimated number of PSD-95 per clusters (mean of the median per cell):  $t_0: 114.7 \pm 11.6$ ,  $t_{10}: 82.54 \pm 10.99$ ,  $t_{30}: 66.93 \pm 6.88$ ; per nanoclusters  $t_0: 28.12 \pm 2.79$ ,  $t_{10}: 19.91 \pm 2.02$ ,  $t_{30}: 18.99 \pm 2.36$ ) (Fig. 3B and C). We also observed a slight decrease in the nanocluster diameter (Supplementary Fig. 8). In contrast, following ATP treatment, the number of PSD-95 per clusters or nanoclusters remained unchanged (number of object per PSD-95 clusters  $t_0: 112.5 \pm 11.25$ ,  $t_{10}: 104.2 \pm 9.85$ ,  $t_{30}: 102.4 \pm 9.47$ ; per PSD-95 nanoclusters  $t_0: 23.7 \pm 2.11$ ,  $t_{10}: 25.13 \pm 3.25$ ,  $t_{30}: 21.42 \pm 1.79$ ) (Fig. 3D and E) as their overall organization (Supplementary Fig. 8).

Altogether, these results indicate that NMDAR-dependent LTD is associated with a change in PSD-95 number and cluster size, which is not the case for P2XR-dependent LTD. This could underlie the observed long-lasting increases in AMPAR mobility in the late phase of NMDAR-dependent LTD by decreasing the AMPAR trapping sites.

**Autophagosome-dependent degradation of the T19-phosphorylated form of PSD-95 is required for NMDAR-dependent LTD.** We investigated the molecular mechanism responsible of the PSD-95 loss when LTD is induced by NMDAR activation. The T19 residue of PSD-95, a GSK3 $\beta$ -phosphorylation

site, has been reported as crucial for the induction of LTD<sup>45</sup>. Thus, we investigated the impact of NMDAR-dependent LTD on both the AMPAR and PSD-95 reorganization, when expressing wild type or the phospho-null T19A mutant of PSD-95 (Fig. 4A and B). The overexpression of WT PSD-95 triggered an increase in both synaptic AMPAR and PSD-95 molecules per nanodomain correlated with an increase of mEPSC amplitude (mEPSC amplitude (pA), Ctrl:  $12.33 \pm 0.53$ , WT PSD-95:  $15.75 \pm 1.0$ ) as previously reported<sup>16,47</sup>. The induction of NMDAR-dependent LTD on neurons expressing WT PSD-95, led to a decrease of the number of synaptic AMPARs and PSD-95 (Fig. 4A) mirrored by a decrease in mEPSC amplitude (Fig. 4B) (estimated number of AMPAR per nanodomain, WT PSD-95:  $28.77 \pm 0.83$ , WT + NMDA:  $23.61 \pm 1.13$ ; estimated number of PSD-95 per cluster, WT PSD-95:  $173 \pm 8.82$ , WT + NMDA:  $128.4 \pm 9.37$ , mEPSC amplitude (pA), WT PSD-95:  $15.75 \pm 1.0$ , WT + NMDA:  $12.15 \pm 0.74$ ). In contrast, the overexpression of PSD-95 T19A blocked the NMDA-induced decrease in synaptic AMPAR and PSD-95 amounts (Fig. 4A), and suppressed the depression of the mEPSC (Fig. 4B) (estimated number of AMPAR per nanodomain, T19A PSD-95:  $25.01 \pm 0.80$ , T19A + NMDA:  $29.15 \pm 1.05$ ; estimated number of PSD-95 per cluster, T19A PSD-95:  $145.5 \pm 5.96$ , T19A + NMDA:  $148.6 \pm 8.07$ , mEPSC amplitude (pA), T19A PSD-95:  $12.21 \pm 0.52$ , T19A + NMDA:  $13.86 \pm 0.69$ ) (Fig. 4A–C). As a control, none of WT and T19A PSD-95 overexpression altered the LTD induced by ATP treatment (Supplementary Fig. 9A).

As the LTD-dependent synaptic removal of PSD-95 correlates with the increase in the diffusive fraction of AMPAR, we questioned the effect of T19A PSD-95 expression on the AMPAR lateral mobility (Fig. 4D). By using uPAINT on GluA2-containing receptors, we observed that neurons overexpressing WT PSD-95 present an increase in AMPAR mobility after NMDAR-dependent LTD induction (Mobile/immobile ratio, WT PSD-95:  $0.24 \pm 0.03$ , WT + NMDA:  $0.40 \pm 0.04$ ), similar to the control (Fig. 2A–C). In contrast, the overexpression of PSD-95 T19A occluded the NMDA-induced increase of AMPAR mobility (Mobile/immobile ratio, T19A PSD-95:  $0.23 \pm 0.04$ , T19A + NMDA:  $0.25 \pm 0.03$ ).

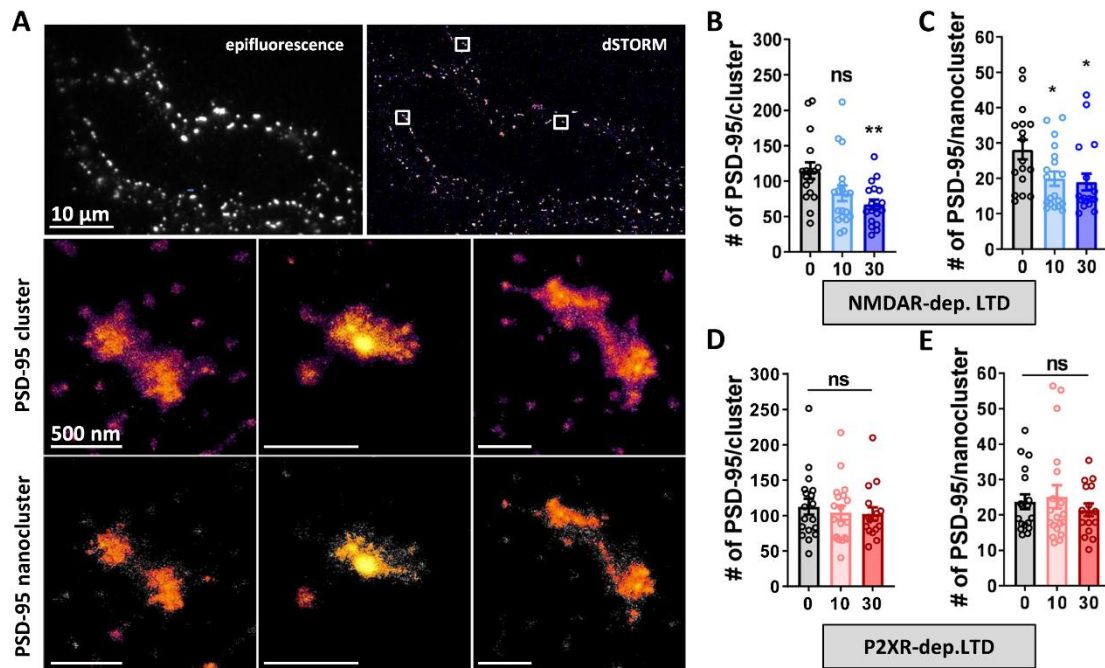


**Fig. 3 PSD-95 nanocluster organization is modified during NMDA- but not ATP-dependent LTD.** **A** Example of endogenous PSD-95 organization along a dendritic shaft observe with epifluorescence (top left) or obtained with dSTORM (top right), represented with SR-Tesseler software. Scale bars = 10  $\mu$ m. Middle panels shows a PSD-95 clusters that have an enrichment factor above the average density factor (density color coded from magenta to yellow). Down panels shows PSD-95 nanoclusters within PSD-95 cluster in the middle panels, which corresponds to a PSD-95 structure with a higher density factor than the average PSD-95 cluster's density. Scale bars for middle and bottom images (PSD-95 clusters and nanoclusters) = 500 nm (**B** and **C**) Average number of PSD-95 molecules per cluster (**B**) and per nanoclusters (**C**) in basal state, 10 and 30 min after NMDA treatment (mean  $\pm$  SEM,  $n = 17, 19$  and  $18$  respectively, one-way ANOVA  $p = 0.0059$  and Dunnett's post-test found significant between  $t_0$  and  $t_{30}$  conditions,  $p = 0.0033$  but not between  $t_0$  and  $t_{10}$  conditions,  $p = 0.0517$  for clusters; one-way ANOVA  $p = 0.0189$  and Dunnett's post-test found significant between  $t_0$  and  $t_{10}$  and between  $t_0$  and  $t_{30}$  conditions,  $p = 0.0348$  and  $p = 0.0194$  respectively, for nanoclusters). **D** and **E** Average number of PSD-95 molecules per cluster (**D**) and per nanoclusters (**E**) in basal state, 10 and 30 min after ATP treatment (mean  $\pm$  SEM,  $n = 18, 19$  and  $16$  respectively, one-way ANOVA  $p = 0.7616$  and  $p = 0.5269$  for clusters and nanoclusters respectively).

We then tried to decipher the molecular mechanism which facilitates the removal of PSD-95 when phosphorylated at T19. Previous work has identified that PSD-95 co-immunoprecipitates with LC3, the protein responsible for autophagic cargo recruitment<sup>48,49</sup>. Moreover, recent work reported that autophagy is induced in dendrites by NMDAR-dependent LTD and is required for LTD induction<sup>49</sup>. Therefore, we directly tested if autophagy could be the degradation pathway of PSD-95 during LTD. To this end, we purified autophagic vesicles (AVs) from fresh hippocampal slices (Supplementary Fig. 10), before and 30 min after ATP- or NMDA-induced LTD, and determined the amount of both total and T19 phosphorylated PSD-95 in these vesicles (Fig. 5A and B). The induction of NMDAR-dependent LTD triggered a threefold increase of the T19-phosphorylated form and total amount of PSD-95 (total intensity of PSD-95, control:  $0.71 \pm 0.07$ , NMDA:  $2.83 \pm 0.35$ ; and pT19-PSD-95, control:  $0.62 \pm 0.14$ , NMDA:  $2.89 \pm 0.77$ ) in autophagosomes, whereas P2XR-dependent LTD did not affect their abundance in the purified vesicles (total intensity of PSD-95, control:  $0.71 \pm 0.07$ , ATP:  $0.56 \pm 0.1$ ; and pT19-PSD-95, control:  $0.62 \pm 0.14$ , ATP:  $0.57 \pm 0.09$ ) (Fig. 5C).

In parallel, we performed dual-color dSTORM experiments by labeling LC3, a typical marker of AVs, with alexa 647 nm, and PSD-95 with alexa 532 nm. A PSD-95 puncta was detected in the vast majority of AVs (43 out of 45 AVs, Fig. 5D). The quantification of PSD-95 signal reveals a threefold increase after

LTD induction compare to control (PSD-95 intensity (a.u), ctrl:  $87.47 \pm 24.33$ , NMDA:  $301.6 \pm 45.26$ ).

In regard of these results, we hypothesized that NMDAR-dependent LTD triggers the activation of the GSK3 $\beta$  which phosphorylates PSD-95 at T19 to target it to autophagosomes for degradation. To validate this hypothesis, we first measured the evolution in function of time of AMPAR miniature currents following NMDAR-dependent LTD induction in the presence of TDZD8 (10  $\mu$ M), an inhibitor of GSK3 $\beta$  (Fig. 5E). In the first 10 min, NMDA treatment triggered a classical decrease of synaptic strength, despite the presence of TDZD8. However, 20 and 30 min after induction, the synaptic depression was abolished (mEPSC amplitude (pA), Ctrl:  $15.44 \pm 0.95$ , NMDA:  $10.41 \pm 0.52$ , NMDA + TDZD8 10 min:  $11.23 \pm 0.70$ , NMDA + TDZD8 20 min:  $17.07 \pm 1.16$ , NMDA + TDZD8 30 min:  $16.69 \pm 1.40$ ). Application of TDZD8 alone did not affect miniature amplitude neither at 10 min nor at 20 or 30 min (Supplementary Fig. 9B). Then, we measured mEPSC amplitude 30 min after NMDA and ATP-induced LTD in the presence of SBI (0.5  $\mu$ M), a blocker of autophagosome formation (Fig. 5F). SBI alone did not impact mEPSC amplitude, while it entirely blocked NMDAR-dependent LTD expression 30 min after NMDAR activation. In contrast, P2XR-dependent LTD was properly expressed in the presence of SBI (mEPSC amplitude (normalized to Ctrl), Ctrl:  $1.0 \pm 0.04$ , SBI:  $0.87 \pm 0.06$ , NMDA:  $0.73 \pm 0.05$ , NMDA + SBI:  $0.99 \pm 0.04$ , ATP:  $0.66 \pm 0.02$ , ATP + SBI:  $0.65 \pm 0.04$ ; Fig. 5F). A similar effect

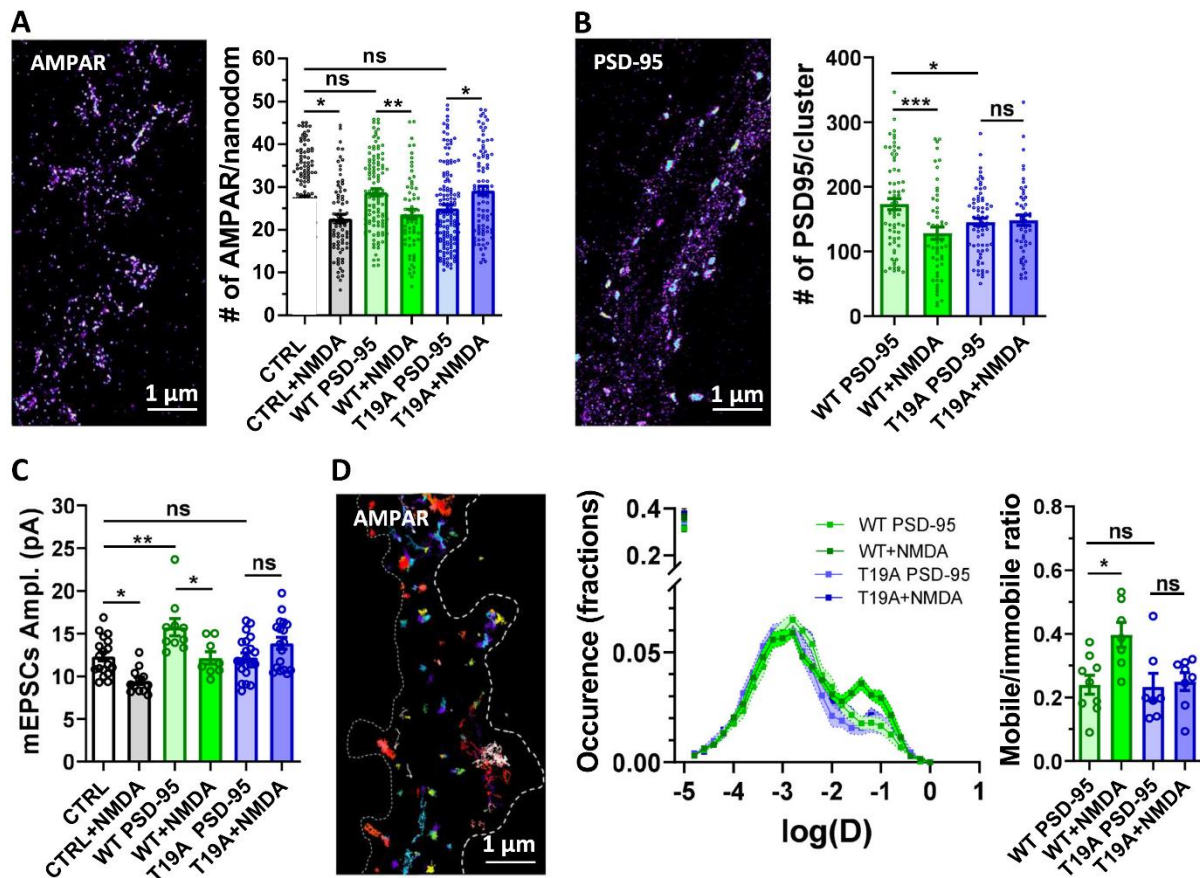


**Fig. 4** PSD-95 Phosphorylation at T19 position is essential for all the NMDAR-dependent molecular reshuffling induced by LTD. **A** and **B** Expression of T19A phospho-null mutant of PSD-95, but not WT PSD-95, suppresses the decrease of GluA2 containing AMPAR (**A**) and PSD-95 (**B**) content per nanodomain 30 min following NMDAR-dependent LTD (at left: example of super-resolution intensity images of a piece of dendrite obtained using dSTORM technique). At right, the mean per cell histogram (mean  $\pm$  SEM, one-way ANOVA,  $p < 0.0001$  and  $p = 0.0014$  respectively and Tukey's post-test results are realized between each conditions,  $N = 141, 76, 110, 65, 139, 91$  for the measure of AMPAR per nanodomain, and  $N = 65, 54, 70, 51$  for the measure of PSD-95 per cluster). **C** mEPSC amplitude is significantly decreased 30 min following NMDA treatment when both GFP or WT PSD-95 are expressed, while it is suppressed by T19A PSD-95 expression (mean  $\pm$  SEM, one-way ANOVA,  $p < 0.0001$  and Tukey's post-test results are realized between each conditions,  $N = 18, 12, 10, 8, 21, 18$ ). **D** Example of trajectories of GluA2-containing receptors with uPAINT technique (left panel) and average distribution of the log(D) (middle panel) when WT (green lines) and T19A (blue lines) mutant PSD-95 are expressed, before (dark lines) and 30 min after (light lines) NMDA treatment. Average of the mobile fraction (Right panel), before and 30 min after NMDA treatment (mean  $\pm$  SEM, one-way ANOVA,  $p = 0.009$  and Tukey's post-test results are realized between each conditions,  $N = 7, 9, 7, 8$ ). WT PSD-95 expressing neurons display an increase of AMPAR mobility following NMDAR-dependent LTD while T19A mutant expression abolished this mobility increase.

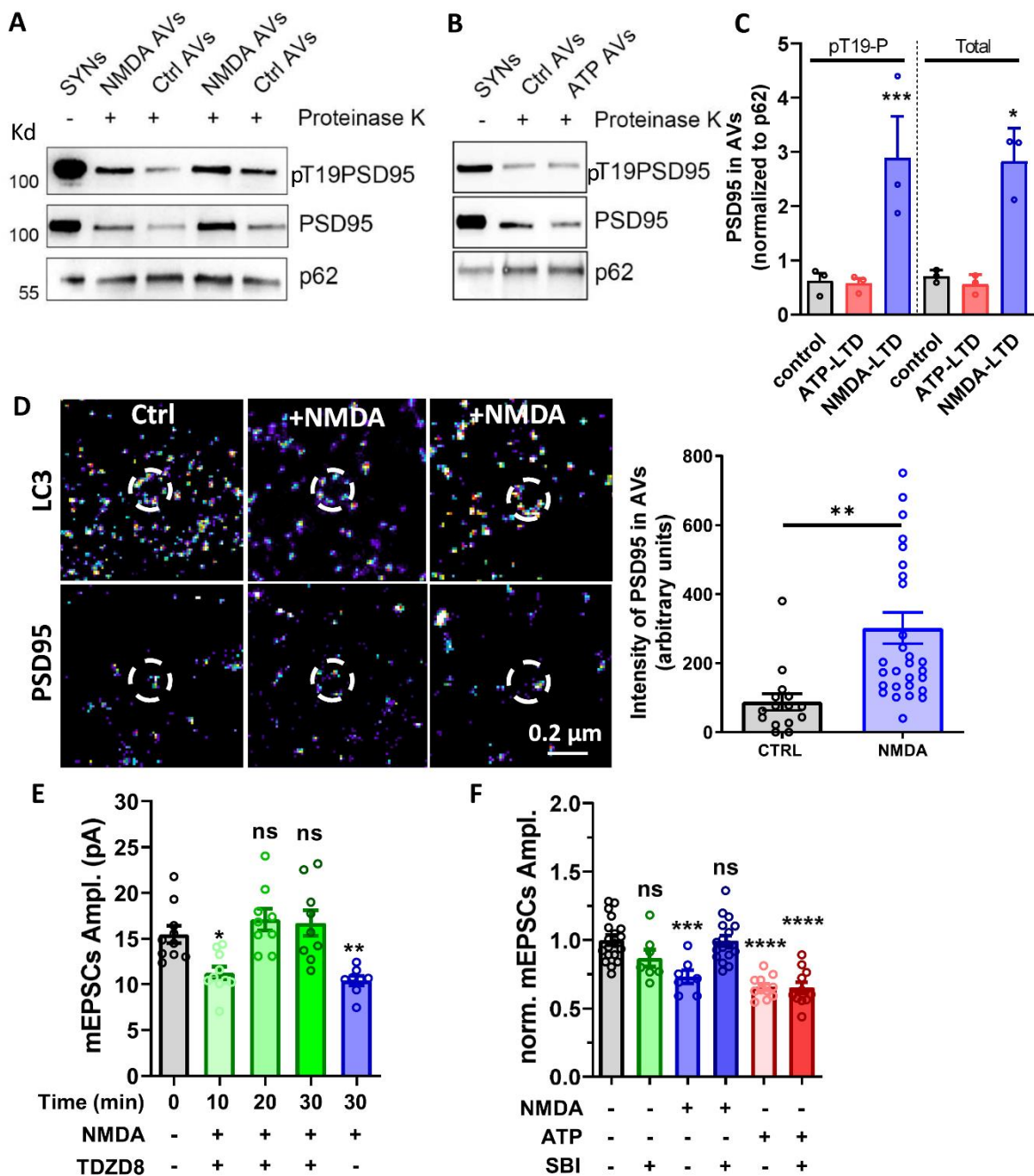
was obtained with the application of spautin-1 (10  $\mu$ M), another inhibitor of autophagy (Supplementary Fig. 9C).

Overall, these experiments suggest that specifically NMDAR-but not P2XR-dependent LTD, triggers a phosphorylation at the position T19 of PSD-95, which targets PSD-95 proteins to autophagosomes where they are degraded. We propose that this suppression of PSD-95 is responsible of the maintenance of LTD and leads to an increase of AMPAR surface mobility.

**Short-term plasticity is increased during NMDAR-dependent LTD and requires AMPAR lateral diffusion.** We then aimed to determine if the difference in mobile AMPAR proportion at depressed synapses through NMDAR vs P2XR (Fig. 2) had any functional consequences on synapse function beyond their common decreased efficacy (Fig. 6). We have previously established that the pool of mobile AMPARs favors synaptic transmission during high frequency stimulation by allowing desensitized receptors to be

replaced by naïve ones<sup>18,19,21</sup>. In contrast, a decrease in the proportion of diffusive AMPAR, as triggered by artificial crosslinking<sup>19</sup>, CaMKII activation<sup>20</sup> or by associating AMPARs with the auxiliary proteins TARPs<sup>18</sup>, leads to a significant depression of synaptic transmission during rapid trains of stimulation. Therefore, we investigated whether the increase in AMPAR mobility observed during NMDAR-dependent LTD (Fig. 2B) could affect synaptic responses to high-frequency stimulus trains (5 pulses at 20 Hz) (Fig. 6A–C). We performed whole-cell patch-clamp recordings of CA1 neurons in acute hippocampal brain slices and measured short-term synaptic plasticity upon stimulation of Schaffer collaterals. LTD was induced by either ATP or NMDA treatment and paired-pulse responses were measured 30 min after LTD induction (Fig. 6A).

We first verified whether both ATP and NMDA treatment triggered a significant decrease in EPSCs amplitude. After NMDA application, we observed a  $\sim 35\%$  decrease in evoked EPSC



amplitude (basal state:  $-37.63 \pm 2.48$  pA, 30' NMDA:  $-24.71 \pm 3.64$  pA) and ATP triggered a  $\sim 28\%$  decrease in evoked EPSC amplitude (basal state:  $-40.89 \pm 7.60$  pA, 30' ATP:  $-29.29 \pm 7.16$  pA) (Fig. 6A, B and D, E). We then analyzed paired-pulse responses. A representative trace and an average response are shown for NMDA (Fig. 6A) and for ATP treatment (Fig. 6D). Neurons expressing a P2XR-dependent LTD, which does not trigger an increase in AMPAR mobility, presented a paired-pulse

response similar to the one measured during the basal state (Fig. 6F). In contrast, neurons treated with NMDA, and thus exhibiting an increase in the proportion of mobile AMPARs, displayed a significant increase in the paired-pulse ratio compared to those at the basal state (Fig. 6C). This increase in the paired-pulse ratio was abolished when AMPAR were immobilized by antibody crosslinking (Supplementary Fig. 11), as previously described<sup>18,19</sup>.

**Fig. 5 PSD-95 Phosphorylation at T19 position by GSK3 $\beta$  targets it to autophagosomes.** **A** and **B** Western blot analysis of total PSD-95 and T19 phosphorylated PSD-95 in purified synaptosomes and in PK-treated autophagic vesicles (AVs) purified before and after induction of the LTD by NMDA (**A**) or ATP (**B**) application. PSD-95 and T19PSD-95 levels were normalized to the levels of p62, an autophagic cargo. **C** Quantification of normalized T19PSD-95 and PSD-95 levels obtained in (**A** and **B**) reveals that both phosphorylated and global form of PSD-95 is over-accumulated in autophagic vesicles after NMDA treatment but not after ATP (mean  $\pm$  SEM,  $n = 3$ , one-way ANOVA,  $p = 0.0005$  for pT19P and  $p = 0.0180$  for the Total. Dunnett's post-test results are realized between each condition and the control condition. For pT19P, control vs ATP-LTD  $p = 0.85$  and control vs NMDA-LTD  $p = 0.0008$ ; For Total, control vs ATP-LTD  $p = 0.996$  and control vs NMDA-LTD  $p = 0.022$ ). **D** Representative images of Dual-color dSTORM experiments with LC3 labelled with alexa-647 (upper panels) and PSD-95 labeled with alexa-532 (bottom panels). PSD-95 intensity inside the AVs shown a threefold increase following LTD induction by NMDA treatment (Right panel, mean  $\pm$  SEM, unpaired  $t$ -test,  $p = 0.0022$ ,  $n = 15$  and 29). **E** Evolution in function of time of the mEPSC amplitude after NMDAR-dependent LTD in the presence of TDZD8 (10  $\mu$ M), an inhibitor of GSK3 $\beta$ . After 10 min, a normal LTD is induced but TDZD8 block the maintenance of the LTD (mean  $\pm$  SEM, one-way ANOVA,  $p < 0.0001$  and Dunnett's post-test results are realized between each conditions and the control condition,  $N = 10, 10, 9, 9, 8$ ). **F** Average of the mEPSC amplitude recorded on WT neurons 0 and 30 min after NMDA or ATP treatment, in the absence or the presence of SBI (a specific blocker of autophagy, 0.5  $\mu$ M). SBI alone does not impact on mEPSC amplitude, while it fully blocks NMDAR-dependent LTD. At the opposite, ATP-induced LTD is preserved in the presence of SBI (mean  $\pm$  SEM, one-way ANOVA,  $p < 0.0001$  and Dunnett's post-test results are realized between each conditions and the control condition,  $N = 19, 7, 7, 17, 11, 11$ ).

Short-term plasticity has traditionally been attributed to changes in pre-synaptic release probability<sup>50</sup>, although it can also arise from AMPAR desensitization<sup>15–17,19</sup> and be regulated by AMPAR mobility<sup>18–21</sup>. To decipher between a pre- or post-synaptic origin of the NMDA-induced changes in short term plasticity, we directly measured the pre-synaptic probability of glutamate release before and after NMDAR- or P2XR-dependent LTD using the fluorescent glutamate reporter iGluSnFR<sup>51</sup>. We expressed iGluSnFR in cultured neurons and measured the variation in post-synaptic fluorescence upon triggering pre-synaptic action potentials by electrical field stimulations (Fig. 6G). None of the LTD protocols (ATP or NMDA) changed significantly the pre-synaptic release probability (Fig. 6H). These experiments indicate that NMDAR-dependent LTD favors the synaptic responsiveness to high-frequency stimulation through an increase in AMPAR mobility rather than a change in release probability.

Finally, we measured, in acute brain slices, the effect of synaptically induced NMDAR-dependent LTD, triggered by LFS, on paired-pulse response ratio. We first verified the proper LTD induction following LFS protocol as previously described<sup>31</sup>. After 1 Hz stimulation for 15 min, a  $23 \pm 5.1\%$  decrease of the first peak amplitude was observed (EPSC amplitude,  $t_0$ :  $-57.92 \pm 3.96$ , LFS:  $-44.74 \pm 4.03$ ) (Fig. 6J). We then analyzed paired-pulse responses, a representative trace being shown before and after LFS (Fig. 6I). 30 min after LFS-induced LTD, neurons presented a significant increase in the paired-pulse ratio compared to before induction (PPR,  $t_0$ :  $1.43 \pm 0.08$  and LFS:  $1.60 \pm 0.09$ ) (Fig. 6K), confirming that synaptically-induced LTD triggers a similar effect on synaptic responsiveness that NMDAR-dependent LTD.

**Modeling confirms that increasing AMPARs mobility improves synaptic responsiveness.** Both ATP- and NMDA-induced LTD resulted in a decrease in the overall AMPAR number at synapses. Moreover, single molecule tracking experiments (Figs. 2–4) show that LTD induced by NMDA, but not by ATP, is associated with an increase in AMPAR mobility. These changes in AMPAR diffusion can be related to a decrease in AMPAR complex affinity for their traps and/or a decrease in the number of synaptic traps (as reported by the decrease of total PSD-95 per synapses)<sup>7,20,42,52,53</sup>.

To theoretically evaluate the impact of AMPAR endocytosis or untrapping on AMPAR mobility, organization and synaptic responses, we performed Monte-Carlo simulations using the MCell software (Fig. 7). The synaptic shape and perisynaptic environment were obtained from 3D electron microscopy images of hippocampal CA1 stratum radiatum area<sup>10,54–56</sup>.

The simulation was divided in two sequences. The initial part simulates for 50 s, at the ms resolution, the dynamic

organization of proteins inside the synapse (Supplementary Fig. 12). The second part simulates for 250 ms, at the  $\mu$ s resolution, the AMPAR currents following 5 synaptic glutamate releases at 20 Hz (Fig. 7B to J, see methods). The protein properties, such as number and diffusion coefficient, were implemented into the model based on the results obtained with super-resolution imaging techniques and in agreement with previous papers<sup>57</sup>, i.e., 200 PSD-95 and 120 AMPAR molecules (half in an internal pool, half at the surface, these values correspond to the mean of the mean per cell obtained in Supplementary Fig. 1 for AMPAR and Fig. 3 for PSD-95). Interactions between proteins were implemented following the scheme (Fig. 7A), and affinity constants ( $k$ ) were adjusted to reach, at the equilibrium, a distribution similar to the one observed by microscopy (Supplementary Fig. 12).

Based on the literature and our experimental results, we tested the relation between simulated AMPAR current amplitudes and variations of two different interaction constants: (i) the endocytosis rate ( $k_8^*3$ ), and (ii) the removal of PSD-95 into the PSD named PSD-95 inactivation rate ( $k_6^*4$ ) (Fig. 7A).

A threefold increase in the endocytosis rate (noticed  $k_8^*3_{\text{Endo}}$ ) which would correspond to the initial phase of both ATP- and NMDA-induced LTD, triggered a 25% decrease in the number of activated AMPAR (Fig. 7B). This value is similar to the current amplitude decrease measured with electrophysiology. In parallel, the increase in PSD-95 inactivation ( $k_6^*4_{\text{Inact}}$ ) led to a 30% decrease in AMPAR current amplitude at the first glutamate release (Fig. 7C). Interestingly, this modification triggered a net increase in the number of mobile AMPAR (as illustrated in Supplementary Fig. 12B, blue line), mimicking the results observed during the late phase of NMDAR-dependent LTD (30 min and 3 h after LTD induction).

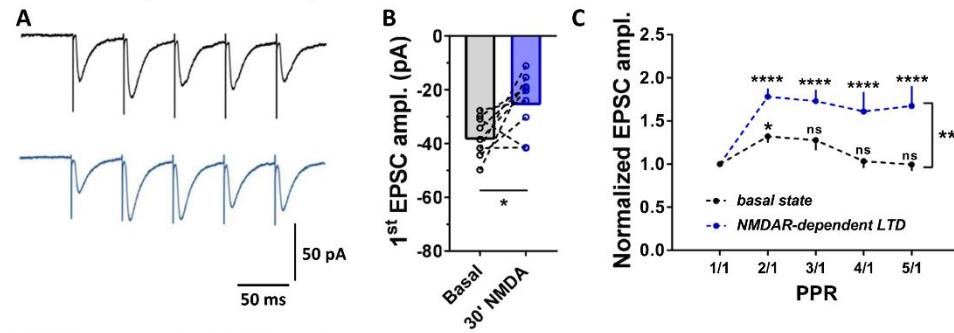
In another set of modeling experiments, we induced an AMPAR depletion into domains by increasing endocytosis rate ( $k_8^*3$ ) and then put back this rate at its initial value. A rapid replenishment of nanodomains is observed (Supplementary Fig. 13A). Interestingly, this replenishment could be counter-balanced by an increase of AMPAR untrapping ( $k_4^*4$ ) (Supplementary Fig. 13B).

We then determined the synaptic responses following trains of 5 stimulations at 20 Hz in these various conditions.  $k_6^*4_{\text{Inact}}$  conditions triggered an increase in paired-pulse ratio, with a 18.7% increase in AMPAR activation for the second release and a 20.4% for the third one (Fig. 7C). While the  $k_8^*3_{\text{Endo}}$  condition, which does not impact AMPAR mobility, did not modify the synaptic response in frequency (Fig. 7B).

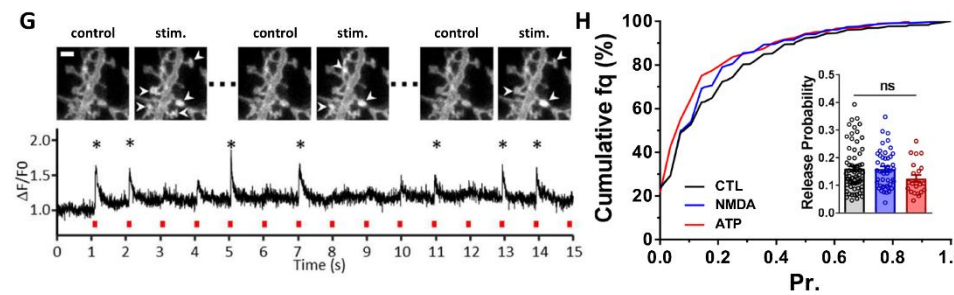
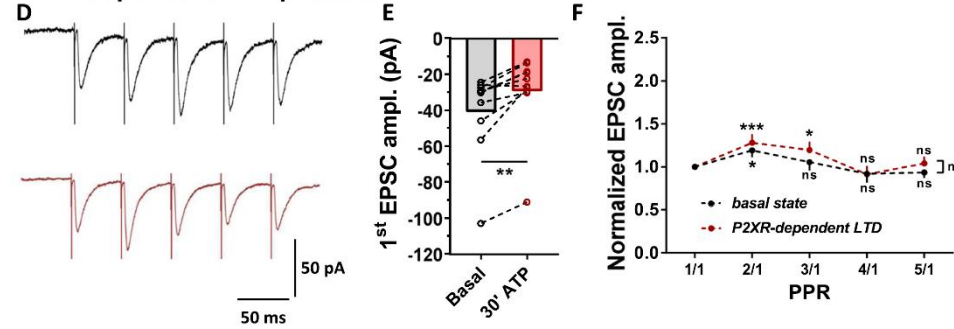
These simulations demonstrate that using a realistic model of AMPAR organization, an increase in the pool of freely diffusing



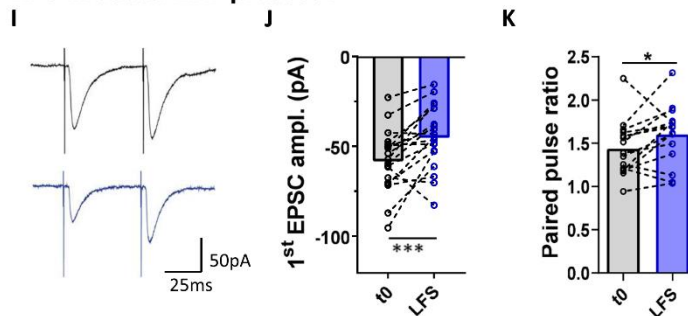
**NMDAR-dependent LTD protocol**



**P2XR-dependent LTD protocol**



**LFS-induced LTD protocol**



AMPA induced by a decrease in the number of traps, is sufficient to trigger a paired-pulse facilitation similar to the one observed on brain slices by electrophysiological experiments.

Altogether, these experiments indicate that an increase in AMPAR mobility induced by the activation of NMDARs triggers an increase of synaptic responsiveness. Here we show that the plasticity paradigm (here the NMDAR-dependent LTD) regulates neuronal responsiveness through a post-synaptic mechanism that requires the degradation of PSD-95 by autophagosome and AMPAR surface mobility increases.

**Discussion**

Using single molecule localization-based super-resolution microscopy on live and fixed neurons, combined with electrophysiology and modeling, we characterized the nanoscale modifications in AMPAR organization and dynamic triggered by two different types of LTD-inducing stimuli and estimated their impact on frequency-dependent synaptic current properties. We identified a common induction phase going through a depletion of AMPAR content both in nanodomains and at synapses, leading to a decrease in synaptic strength. A subsequent phase,

**Fig. 6 NMDAR-dependent LTD is associated to a frequency stimulation facilitation without affecting release probability.** **A** Representative traces of synaptic EPSCs in response to 5 stimulations at 20 Hz before (dark line) and 30 min after (blue line) NMDAR treatment. **B** Paired-average amplitude of the first response before and 30 min after treatment ( $n = 9$  cells, mean  $\pm$  SEM, paired  $t$ -test,  $p = 0.0263$ ). The decrease of the first response demonstrates the efficiency of the LTD protocol. **C** Average of the 5 EPSC amplitudes, normalized by the first response intensity ( $n = 9$  cells, mean  $\pm$  SEM, two-way ANOVA. For PPR variation,  $F(4,32) = 10.36$ ,  $p < 0.0001$ , Dunnett's post-test found significant differences increase of PPR between PPR1/1 and PPR2/1,  $p = 0.0234$  at basal state, and between PPR1/1 and either PPR2/1, PPR3/1, PPR4/1 or PPR5/1,  $p < 0.0001$ , 30 min after NMDAR-dependent LTD induction. For basal state vs NMDAR-dependent LTD,  $F(1,8) = 12.85$ ,  $p = 0.0071$  and Sidak's post-test found significant difference between the basal state and 30 min after NMDAR-dependent LTD induction for PPR2/1, PPR3/1, PPR4/1 and PPR5/1,  $p = 0.0011$ ,  $p = 0.0013$ ,  $p < 0.0001$  and  $p < 0.0001$  respectively). A clear facilitation of the currents appears after induction of a NMDAR-dependent LTD. **D–F** Similar experiments has been realized when LTD is induced by ATP application, with example of traces in **(D)**. The significant decrease of the first response represented in **(E)** validate the depression of the synaptic response ( $n = 10$  cells, mean  $\pm$  SEM, paired  $t$ -test,  $p = 0.0012$ ). The average of the 5 responses **(F)** reveals no facilitation compared to control condition after ATP treatment ( $n = 10$  cells, mean  $\pm$  SEM, two-way ANOVA. For PPR variation,  $F(4,36) = 7.73$ ,  $p < 0.0001$ , Dunnett's post-test found significant differences increase of PPR between PPR1/1 and PPR2/1,  $p = 0.0163$  at basal state, and between PPR1/1 and PPR2/1 or PPR3/1,  $p < 0.0004$  and  $p = 0.0138$  for P2XR-dependent LTD. For basal state vs P2XR-dependent LTD,  $F(1,9) = 1.197$ ,  $p = 0.03023$ ). **G** Example of the fluorescence increase at a synapse expressing iGluSnFR construct during a field stimulation. Responding synapses are labelled with an arrow (upper part). At the bottom, example of the  $\Delta F/F$  signal obtained at a single synapse. Stars indicate when the synapse is considered as stimulated (scale bar =  $2 \mu\text{m}$ ). **H** Cumulative distribution of the release probability per synapse in control condition (black line) or after LTD induction with either NMDA (Blue line) or ATP (red line) treatment. The mean values per recorded dendrites has been represented in the insert with the same color code. None of the conditions affects significantly the release probability ( $n = 64$ , 44 and 22 respectively, mean  $\pm$  SEM, one-way ANOVA,  $p = 0.1520$ ). **I** Representative traces of synaptic EPSCs in response to 2 stimulations at 20 Hz before (dark line) and 30 min after (blue line) LFS protocol. **J** Paired-average amplitude of the first response before and 30 min after treatment ( $n = 19$  cells, paired  $t$ -test,  $p = 0.0009$ ). The decrease of the first response demonstrates the efficiency of the LTD protocol. **K** Average of the paired-pulse ratio before and 30 min after LFS-induced LTD ( $n = 15$ ; paired  $t$ -test,  $p = 0.046$ ).

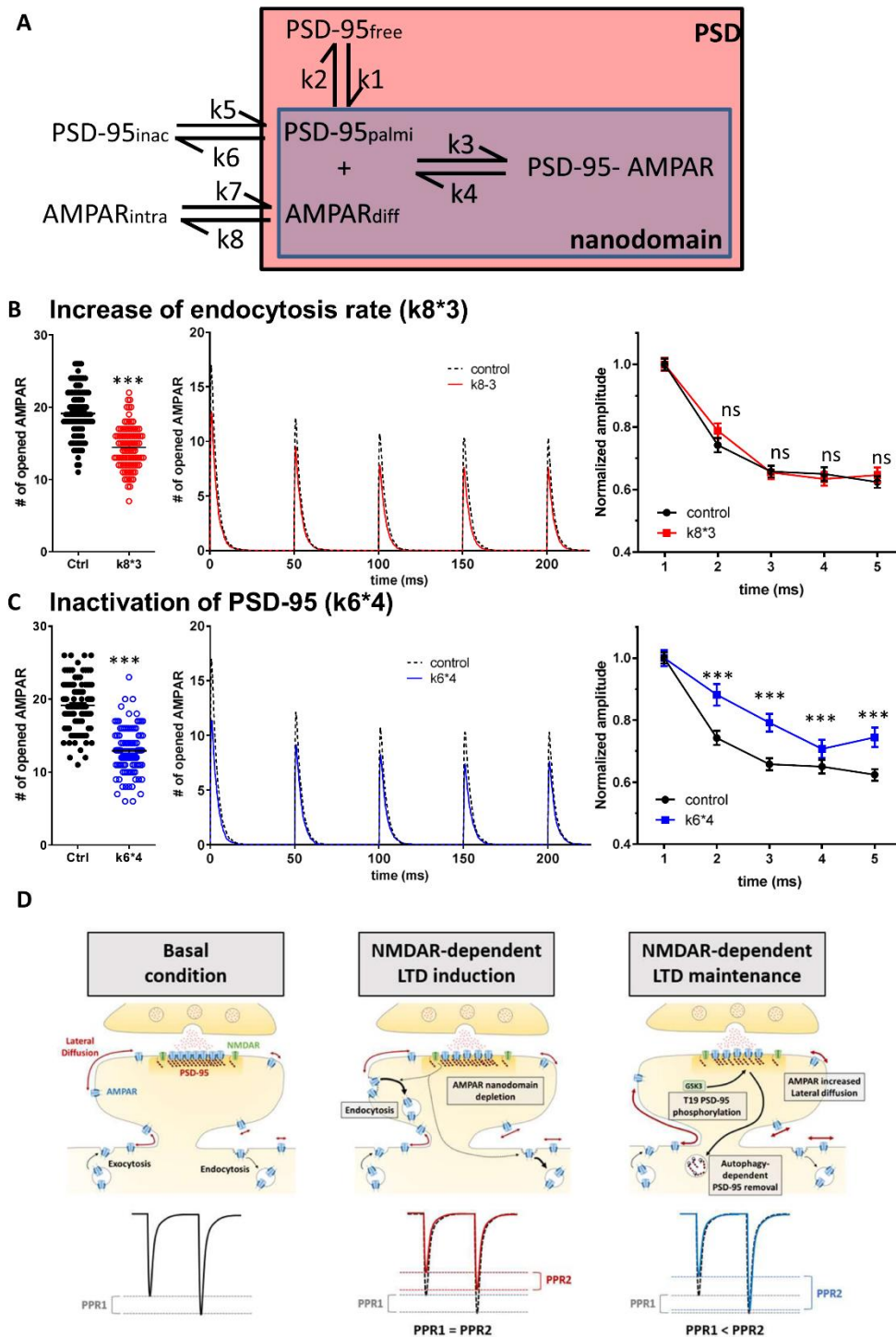
specific to NMDAR-dependent LTD, is associated with a net increase in the proportion of mobile AMPAR, and a depletion in PSD-95 clusters. The PSD-95 cluster modification is due to its phosphorylation at T19 position, driving it to autophagosome for degradation. Importantly, our experimental data and simulations using a realistic model indicate that this change in AMPAR dynamic allows synapses to improve their responsiveness to high frequency stimulations. Altogether, our data uncover an unexpected level of synaptic integration, where various LTD types do not similarly impact on synaptic molecular organization and function. This argues for a mechanism through which regulation of AMPAR surface density and diffusion following specific post-synaptic signaling to express LTD allows to adjust the capacity of synapses to encode pre-synaptic activity.

**P2XR- and NMDAR-dependent LTD are associated with nanodomain depletion proportional to the decrease in AMPAR mEPSC amplitudes.** Since the discovery that AMPARs are organized in nanodomains<sup>12,13,43</sup> and that AMPAR clusters are aligned with pre-synaptic release sites<sup>10,11</sup>, our view of synapse function, and how it could be plastic, has strongly evolved. Together with previous findings<sup>14,19,58,59</sup>, this has introduced the concept that post-synaptic plasticity could arise not only from absolute changes in AMPAR content, but also from their local reorganization regarding glutamate release site at the nanoscale. Thus, it became important to revisit LTD through this new prism. AMPAR-mediated current amplitude changes observed during LTD could arise from (i) a modification of the domain structure leading to a decrease in the packing of receptor;<sup>14</sup> (ii) a misalignment between the pre- and the post-synaptic machinery<sup>10,59</sup> or more simply (iii) a depletion of the domains and overall decrease in synaptic AMPAR content. Here we report that both NMDA and ATP treatments induce a synaptic depression based, at least partially, on post-synaptic nanoscale modifications. Super-resolution experiments revealed no modification in the overall nanodomain dimensions, and no pre-post synaptic misalignment. However, we observed a rapid (<10 min) depletion in the number of AMPAR per nanodomain. Interestingly, the extent of synaptic AMPAR depletion (around 30%) is proportional to the extent of mEPSC depression. This

suggests that synaptic depression can be mainly attributed to a decrease in post-synaptic AMPAR content per nanodomain.

**PSD-95 degradation through autophagy maintained the NMDAR-dependent LTD by decreasing the AMPAR trapping at domains.** The existence of various phases during NMDAR-dependent LTD has been described previously. A large increase in the AMPAR endocytosis rate after NMDA treatment has been reproducibly reported, but Rosendale et al. demonstrated that this increase is transient and goes back to its original value after ~10 min<sup>34,35,60</sup>. Sanderson et al. 2016, reported in parallel a rapid and transient increase in calcium-permeable AMPARs<sup>61</sup>. Modeling (Supplementary Fig. 13) reports that transient increase in endocytosis rate is able to induce but not to maintain a LTD. Because the consequence of endocytosis is to overfill the intracellular pool of receptors, the non-maintenance of this increased endocytosis rate should, if receptors are not degraded, lead to a replenishment of synapses by slow exocytosis of these receptors (recycling). This means that the long-term maintenance of LTD requires additional mechanisms to the fast and transient increase in endocytosis. Endocytosis and exocytosis rates 3 h after LTD induction displayed a return to normal, demonstrating that neurons do not maintain a long-lasting unbalance between endocytosis and exocytosis to stabilize LTD. Modeling confirmed that the non-maintenance of this unbalance should lead to a replenishment of synaptic AMPAR and suppress the depression of synaptic currents, if receptors are not degraded. Here we observed a delayed increase in the proportion of mobile AMPAR, developing 20 min after NMDAR-dependent LTD induction. This mobility increase is correlated to a depletion of PSD-95 both inside the nanocluster and inside the entire PSD.

The expression of the T19A phospho-null mutant form of PSD-95 abolished both the PSD-95 reshuffling and the AMPAR increased mobility, favoring the hypothesis that the AMPAR mobility increase is directly due to the decrease in the number of their traps. Interestingly, inhibition of GSK3 $\beta$  during NMDAR-dependent LTD did not occlude the induction of LTD, as a ~27% decrease of miniature EPSC amplitude was observed 10 min after LTD induction in the presence of TDZD8. In contrast, inhibition of GSK3 $\beta$  blocked LTD maintenance (20 and 30 min after induction with NMDA).



Previous work demonstrated how posttranslational modifications of PSD-95 can regulate its amount at the PSD and thus be important for LTD. As an example, PSD-95 ubiquitination by the E3 ligase Mdm2 removes it from the PSD and rapidly targets it to degradation by the proteasome<sup>62</sup>. Our results, combined to previous publications, allowed to sketch another quite complete

scheme of the molecular mechanisms implicated in PSD-95 reshuffling during NMDAR-dependent LTD. Synaptic activity favors PSD-95 depalmitoylation<sup>63</sup> and activates GSK3 $\beta$  which phosphorylates PSD-95 at the T19 position<sup>45</sup>. Calcium bound calmodulin interacts with PSD-95 when phosphorylated at T19 and antagonizes palmitoylation, promoting release of PSD-95 out

**Fig. 7** *In silico* simulations confirm that AMPAR untrapping induced both a depression of synaptic currents and an increase of synaptic responsiveness. **A** Representation of the main interactions which define the AMPAR organization/ trapping. PSD-95 can diffuse freely, be slowly mobile and confined into nanodomain when palmitoylated, or be inactivated. AMPAR can be endocytosed, freely mobile at the surface or being trapped by palmitoylated PSD-95 into the domain. Two various kinetic rate constant modifications trigger a synaptic depression, (1) an increase of endocytosis rate, mimicking the initial phase of the NMDAR-dependent LTD and the P2XR-dependent LTD (**B**). (2) A decrease of the total number of PSD through an increase of their inactivation rate (**C**), mimicking the depletion of PSD-95 observed during NMDAR-dependent LTD. For each condition, we report in the right panel, the number of open AMPARs during the first glutamate release (mean  $\pm$  SEM), before (dark dots) and after (color dots) modification of the parameter. A significant decrease of AMPAR response similar to the depression experimentally measured is observed in all conditions. Middle panel, the average traces of the equivalent AMPAR current following 5 glutamate releases at 20 Hz. Right panel, the average of the AMPAR equivalent current following the 5 releases (mean  $\pm$  SEM), normalized by the initial response. 96 independent simulations are realized in each condition. When depletion of synaptic AMPAR is induced by increasing the endocytosis, there is no modification of simulated paired-pulse ratio while PSD-95 inactivation condition triggers a significant increase of PPR. **D** Schematic summary of the molecular processes responsible of NMDAR-dependent LTD induction and maintenance. From basal state (left panel), NMDAR activation triggers an increase of endocytosis rate, responsible of the initiation of the depression (middle panel). Then the activation of the GSK3 $\beta$  phosphorylates PSD-95 at T19, targeting it to autophagosomes for degradation. This decrease of traps releases AMPAR out of the PSD, increase the amount of mobile receptors and favoring synaptic responsiveness (left panel).

of the PSD<sup>64–66</sup>. PSD-95 is then targeted to autophagosomes for degradation. This decrease in PSD-95 amount at the PSD limits the trapping of AMPAR, maintaining the depression after the initial induction phase. Regarding PSD-95, previous papers hypothesized that the role of autophagy during NMDAR-dependent LTD was to degrade AMPARs<sup>48,49</sup>. Here we demonstrate that during NMDAR-dependent LTD, there is also an autophagy of PSD-95 favoring the untrapping of AMPARs, which is not observed during P2XR-dependent LTD.

**The AMPAR mobility increase induced during NMDAR-dependent LTD mediates an improvement in synaptic responsiveness.** Short term synaptic plasticity (STP) depends on many factors, including pre-synaptic transmitter release<sup>50</sup>, post-synaptic AMPAR desensitization<sup>15–17,19</sup>, and AMPAR surface diffusion<sup>18–21</sup>. The latter mechanism potentiates synaptic responses to sequential stimuli by allowing desensitized receptors to be exchanged by naive ones, hence improving the rate of recovery of synaptic depression due to AMPAR desensitization. Strikingly, we observed that following NMDAR activation, either by direct NMDA application or by synaptic activation through LFS stimulation, but not ATP, the ability of synapses to follow high frequency stimulation is improved. This differential effect between NMDA and ATP on STP mirrors their effect observed on AMPAR mobility. Therefore, it is attractive to suggest that NMDAR-dependent LTD increases STP through the increase in AMPAR mobility. This hypothesis is supported by the observation that: (i) NMDA does not modify pre-synaptic release probability, (ii) the time course of STP potentiation parallels that of the NMDA-induced increase in mobility, i.e., both processes only happen 20–30 min after NMDAR-dependent LTD, (iii) blocking the NMDA-induced increase in AMPAR mobility by AMPAR X-linking prevents the potentiation of STP, (iv) P2XR-dependent LTD, which does not affect AMPAR mobility, does not modify STP and (v) modeling confirmed that increasing the AMPAR mobile pool by decreasing the number of traps, favors the ability of synapses to follow high frequency stimulation. Of note, a similar increase in the paired-pulse ratio upon an increase in the proportion of mobile AMPAR has already been observed upon digestion of the extracellular matrix<sup>21</sup>. Here, our data suggest that a physiological increase in AMPAR mobility, after a protocol that induces LTD, triggers an improvement in synaptic responsiveness through potentiation of STP.

The comparison between P2XR- and NMDAR-dependent LTD reveals that LTD is a generic term, which comprises various physiological consequences. By definition, they all correspond to a net decrease of the amplitude of post-synaptic currents, and they are both induced by a transient increase in AMPAR

endocytosis. However, while ATP-induced LTD just scales down the overall synaptic transmission properties, the NMDAR-dependent LTD affects more drastically the entire synaptic physiology. Indeed, the reshuffling of PSD-95 and AMPAR nanoscale organization induced by NMDAR-dependent LTD does not solely correspond to a decrease in the synaptic response amplitude but to deeper changes which modify the capacity of the depressed synapses to encode pre-synaptic inputs.

## Methods

**Hippocampal neuron culture and transfection.** The experimental designs and all procedures were in accordance with the European guide for the care and use of laboratory animals and the animal care guidelines issued by the animal experimental committee of Bordeaux Universities. Primary hippocampal cultures were prepared from E18 rat embryos of Sprague-Dawley rats according to the Banker protocol<sup>67</sup>. Briefly, hippocampi were dissected in Petri dishes filled with HBSS and HEPES, and dissociated by trypsin treatment (0.05%; Gibco) at 37 °C. For uPAINT experiments, neurons were electroporated (4D-Nucleofector system, Lonza, Switzerland) just after dissection with eGFP-Homer1c. 4 poly-L-lysine pre-coated 1.5H 18 mm coverslips were introduced in 60 mm dishes, which were pre-plated with 75,000 non-electroporated cells. Then, each dish was plated with electroporated neurons at the density of 250,000. After 2 h, coverslips were transferred to dishes containing an astrocyte feeder layer, plated at a density of 40,000 cells and cultured in MEM (Fisher scientific, cat No. 21090-022) containing 4.5 g/l Glucose, 2 mM L-glutamine and 10% horse serum (Invitrogen) for 14 days. Neuron cultures were maintained in Neurobasal medium supplemented with 2 mM L-glutamine and 1X NeuroCult SMI Neuronal supplement (STEMCELL technologies) at 37 °C and 5% CO<sub>2</sub> for 14–16 days.

Banker neurons were transfected with WT and T19A mutant of PSD-95, as well as GFP and SEP-GluA1 and SEP-GluA2 plasmids via calcium phosphate protocol (described in<sup>10</sup>).

**Sample preparation and immuno-labeling.** For dSTORM imaging of GluA2-containing AMPARs, primary neuronal cultures were treated with 30  $\mu$ M NMDA (Tocris) for 3 min<sup>31</sup> or with 100  $\mu$ M ATP (Sigma-aldrich) for 1 min in presence of CGS15943 (3  $\mu$ M)<sup>29,32</sup>. After 10 or 30 min, neurons were incubated with a monoclonal mouse anti-GluA2 antibody (mouse antibody, diluted 1/100, provided by E. Gouaux, Portland, USA)<sup>10,12,18</sup> for 7 min at 37 °C and then fixed with 4% PFA. Then, cells were washed three times for 5 min in 1 $\times$  PBS. PFA was quenched with NH<sub>4</sub>Cl 50 mM for 10 min. Unspecific staining was blocked by incubating coverslips in 1% BSA for 1 h at room temperature. Primary antibodies were revealed with Alexa 647 coupled anti-mouse IgG secondary antibodies (ThermoFisher, A21235).

For dSTORM and confocal imaging of PSD-95, primary neuronal cultures were treated either with 30  $\mu$ M NMDA (Tocris) for 3 min or with 100  $\mu$ M ATP (Sigma-aldrich) for 1 min and fixed with PFA 10 or 30 min after. PFA was quenched with NH<sub>4</sub>Cl 50 mM for 10 min. A permeabilization step with 0.2% triton X100 for 5 min was performed. Cells were washed three times for 5 min in 1 $\times$  PBS. After three washes with 1 $\times$  PBS, unspecific staining was blocked by incubating coverslips in 1% BSA for 1 h at room temperature. Cells were then incubated with monoclonal mouse anti-PSD-95 antibody (MA1-046, ThermoFisher), diluted in 1% BSA at 1/500, at room temperature for 1 h. Coverslips were rinsed three times in 1% BSA solution and incubated in 1% BSA for 1 h at room temperature. Primary antibodies were revealed with Alexa 647 (dSTORM) or Alexa 488 (confocal) coupled anti-mouse IgG secondary antibodies (ThermoFisher, A21235 and A11001).

Similar protocol is applied for LC3 labeling with incubation after permeabilization with polyclonal rabbit LC3 primary antibody (Sigma-aldrich, L8918, diluted at 1/500), revealed by anti-rabbit Alexa-647 nm antibodies.

For dSTORM imaging of pre- to post-synaptic alignment, primary neuronal cultures were incubated 0, 10 or 30 min after NMDA treatment with monoclonal mouse anti-GluA2 antibody<sup>12</sup> for 7 min at 37 °C and then fixed with 4% PFA. After permeabilization, unspecific staining was blocked by incubating coverslips in 1% BSA for 1 h at room temperature. Cells were then incubated with a polyclonal rabbit anti-RIM 1/2 antibody (synaptic systems, 140 203, diluted 1/200). Primary antibodies were revealed with Alexa 532 coupled anti-mouse IgG secondary antibodies (ThermoFisher, A21235) and with Alexa 647 coupled anti-rabbit IgG secondary antibodies (ThermoFisher, A21244).

**direct Stochastic optical reconstruction microscopy (dSTORM).** dSTORM experiments were done on fixed immunolabeled neurons. dSTORM imaging was performed on a LEICA DMi8 mounted on an anti-vibrational table (TMC, USA), using a Leica HXC PL APO 160 × 1.43 NA oil immersion TIRF objective and fiber-coupled laser launch (405 nm, 488 nm, 532 nm, 561 nm and 642 nm) (Roper Scientific, Evry, France). Fluorescent signal was collected with a sensitive EMCCD camera (Evolve, Photometrics, Tucson, USA). The 18 mm coverslips containing neurons were mounted on a Ludin chamber (Life Imaging Services, Switzerland) and 600 µL of imaging buffer was added<sup>88</sup>. Another 18 mm coverslip was added on top of the chamber to minimize oxygen exchanges during the acquisition to limit contact with the oxygen of the atmosphere. Image acquisition and control of microscope were driven by Metamorph software (Molecular devices, USA). Image stack contained typically 40,000–80,000 frames. Selected ROI (region of interest) had dimension of 512 × 512 pixels (one pixel = 100 nm).

The power of the 405 nm laser was adjusted to control the density of single molecules per frame, keeping the 642 nm laser intensity constant. Multicolor fluorescent microspheres (Tetraspeck, Invitrogen) were used as fiducial markers to register long-term acquisitions and correct for lateral drifts.

Super-resolution images with a pixel size of 25 nm were reconstructed using WaveTracer software<sup>69</sup> operating as a plugin of MetaMorph software.

**Cluster analysis.** AMPAR nanodomain analysis: localization of Alexa-647 signals was performed using PalmTracer, a software developed as a MetaMorph plugin by J.B. Sibarita group (Interdisciplinary Institute for Neuroscience). AMPAR nanodomain properties were extracted from super-resolution images corrected for lateral drift as described in previous studies<sup>12,18</sup>.

**PSD-95 cluster analyses:** PSD-95 clusters and nanoclusters were then identified using SR-Tesseler software<sup>44</sup>. A first automatic threshold of normalized density  $DF = 1$  was used to extract clusters of PSD-95 (cluster of level 1) having an enrichment factor higher than the average localization density, corresponding to Post-Synaptic Densities (PSD). A second threshold of  $DF = 1$  applied on the localizations inside these clusters was used to identify the PSD-95 nanoclusters corresponding to domains.

**AMPAR-RIM1/2 cluster distance measurement:** localizations of Alexa-532 and Alexa-647 were corrected for chromatic aberration using a correction matrix calibrated from a set of tetraspeck beads imaged both with 642 nm and 532 nm excitation wavelengths. Clusters of AMPARs and clusters of RIM1/2 proteins were detected using the multicolor version of SR-Tesseler software<sup>70</sup> as described previously for single color SR-Tesseler, and distances between clusters detected in each color were measured within each synaptic ROI in order to solely measure the distances between objects belonging to the same synaptic contact.

#### universal Point Accumulation Imaging in Nanoscale Topography (uPAINT).

For u-PAINT experiments, the 18 mm coverslip containing neurons was mounted on a Ludin chamber (Life Imaging Services, Switzerland). Cells were maintained in a Tyrode solution equilibrated at 37 °C and composed of the following (in mM): 15 D-Glucose, 100 NaCl, 5 KCl, 2 MgCl<sub>2</sub>, 2 CaCl<sub>2</sub>, 10 HEPES (pH7.4; 247 mOsm). Imaging was performed on a Nikon Ti-Eclipse microscope equipped with an APO 100 × 1.49 NA oil immersion TIRF objective and laser diodes with following wavelength: 405 nm, 488 nm, 561 nm and 642 nm (Roper Scientific, Evry, France). A TIRF device (Ilas, Roper Scientific, Evry, France) was placed on the laser path to modify the angle of illumination. Fluorescence signal was detected with sensitive EMCCD camera (Evolve, Roper Scientific, Evry, France). Image acquisition and control of microscope were driven by Metamorph software (Molecular devices, USA). The microscope was caged and heated in order to maintain the biological sample at 37 °C.

The first step consisted to find a transfected neuron (eGFP-Homer1c, soluble GFP, soluble GFP + WT PSD-95 or soluble GFP + PSD-95 TA). This construct was used in order to visualize the neuron of interest and the synaptic area for more synaptic trajectory analysis. After selection of the dendritic segment of interest, ATTO647N coupled-anti-GluA2 antibody (mouse antibody, provided by E. Gouaux, Portland, USA) at low concentration was added in the Ludin chamber to sparsely and stochastically label endogenous GluA2-containing AMPARs at the cell surface. The TIRF angle was adjusted in oblique configuration to detect ATTO647N signal at the cell surface and to decrease background noise due to freely moving ATTO647N coupled antibodies. 647 nm laser was activated at a low

power to avoid photo-toxicity but allowing a pointing accuracy of around 50 nm, and 4000 frames at 50 Hz were acquired to record AMPAR lateral diffusion at basal state.

For LTD experiments lasting 30 min, chemical treatments to induce LTD were added into the Ludin chamber after the first movie acquisition. NMDAR-dependent LTD was induced using NMDA (Tocris Bioscience) at 30 µM for 3 min, while P2XR-dependent LTD was induced using ATP (Sigma-Aldrich) at 100 µM for 1 min in presence of CGS15943 (3 µM) as described in<sup>29</sup>. Imaging solution was washed and replaced by fresh Tyrode solution and ATTO647N coupled-anti-GluA2 antibody at low concentration was added. A 4000 frames movie of the same dendritic segment was recorded at 50 Hz every 5 min for 30 min.

LTD experiments lasting 3 h were performed in non-paired conditions. Some coverslips were treated with the chemical compound inducing LTD while control are treated with water. Coverslips were placed into the culture dish at 37 °C and 5% CO<sub>2</sub> and were imaged as previously described for uPAINT experiments. A single movie of 4000 frames at 50 Hz was acquired.

**Single-particle tracking analysis.** Single molecule localization, tracking and Mean Square Displacement (MSD) of ATTO-647N signals (uPAINT) were computed using PALMTracer software like in Nair et al 2013. From the MSD, two parameters were extracted: (i) the diffusion coefficient (D) corresponding to the global diffusion of the trajectory were calculated by linear fit of the first four points of the MSD plots. (ii) The instantaneous diffusion, corresponds to the variations of the D values all along the trajectory duration (see<sup>18</sup>).

#### Biochemical purification of autophagic vesicles from hippocampal slices after NMDA and ATP treatment.

200 µm-thick hippocampal sections were prepared from the brains of five C57BL/6 adult mice, using a vibratome (Leica, VT1200S), in the presence of ice-cold oxygenated a-CSF (124 mM NaCl, 74.55 mM KCl, 26 mM NaHCO<sub>3</sub>, 1.25 mM NaH<sub>2</sub>PO<sub>4</sub>, 10 mM glucose, 1 mM MgSO<sub>4</sub> and 2 mM CaCl<sub>2</sub>). The sections were then incubated in a-CSF or were treated with an ATP pulse (100 µM for 1 min) or an NMDA pulse (50 µM for 10 min), followed by a 30 min incubation in oxygenated a-CSF containing 10 nM of BafilomycinA1. After centrifugation for 2 min at 1,000 g at 4 °C, the supernatant was discarded and the pelleted sections were collected in 10 ml of 10% (w/v) sucrose, 10 mM Hepes and 1 mM EDTA pH 7.4, for homogenization using a glass homogenizer (20 ounces). Following a centrifugation for 2 min at 2,000 g at 4 °C, the post-nuclear supernatant was collected and AVs were purified as previously described<sup>48,49</sup>. Briefly, mitochondria and peroxisomes are removed with discontinuous Nycodenz gradients. The supernatant was placed on the top of the gradients and was centrifuged at 72,000 g for 1 h at 4 °C. The interface (Aps and endoplasmic reticulum) was isolated and diluted with an equal volume of HB buffer to be loaded on Nycodenz-Percoll gradients in order to remove the small-vesicular and non-membraneous material followed by a 51,000 g centrifugation for 30 min at 4 °C. The interface was collected and diluted with 0.7 V of 60% buffered Optiprep and the removal of Percoll silica particles followed by placing 8.5 ml of the diluted material in SW40 tubes overlaid with 1.5 ml of 30% iodixanol and a top layer of 2.5 ml of HB buffer. The material was then centrifuged at 51,000 g for 30 min at 4 °C resulting in the sedimented Percoll particles at the bottom of the tube and the autophagosomes band floated to the iodixanol/HB interface. Autophagosomes were collected for western blot analysis.

All fractions of the purification procedure were collected and analyzed by western blot with antibodies against the ER marker GRP78Bip (1:1000, ab21685), the nuclear marker Histone-H3 (1:1000, ab1791) and the autophagic vesicle LC3B-II (1:1000, L7543, Sigma). The purified vesicles were subjected to proteinase K (20 µg/ml) treatment for 20 min on ice to digest proteins associated with the outer membrane. Proteinase K was then inactivated with 4 mM PMSF for 10 min on ice and the material was centrifuged at 16,000 g for 20 min at 4 °C to pellet the AVs. The vesicles were lysed and boiled in laemmli buffer and analyzed by western blot using the following antibodies: a-PSD-95 (1:2000, MA1-046, Invitrogen), a-T19PSD-95 (1:1000, ab16496), a-p62 (1:2000, ab56416).

**Electrophysiological recordings.** mEPSC recordings in neuronal culture: coverslips of eGFP-Homer1c, soluble GFP, soluble GFP + WT PSD-95 or soluble GFP + PSD-95 T19A electroporated neurons were placed in a Ludin Chamber on an inverted motorized microscope (Nikon Eclipse Ti) and transfected neurons were identified under epifluorescence from the GFP signal. Extracellular recording solution was composed of the following (in mM): 110 NaCl, 5.4 KCl, 1.8 CaCl<sub>2</sub>, 0.8 MgCl<sub>2</sub>, 10 HEPES, 10 D-Glucose, 0.001 Tetrodotoxin and 0.05 Picrotoxin (pH 7.4; ~245 mOsm/L). For specific experiments, the extracellular solution was supplemented with an autophagy inhibitor, SBI (0.5 µM, Sigma-Aldrich) or GSK3β inhibitor, TDZD8 (10 µM, abcam). Patch pipettes were pulled using a horizontal puller (P-97, Sutter Instrument) from borosilicate capillaries (GB150F-8P, Science Products GmbH), and parameters are adjusted to reach a resistance of 4–6 MΩ. The pipettes are filled with intracellular solution composed of the following (in mM): 100 K-gluconate, 10 HEPES, 1.1 EGTA, 3 ATP, 0.3 GTP, 0.1 CaCl<sub>2</sub>, 5 MgCl<sub>2</sub> (pH 7.2; 230 mOsm). Recordings were performed using an EPC10 patch-clamp amplifier operated with Patchmaster software (HEKA Elektronik). Whole-cell voltage clamp recordings were performed at room temperature and at a holding

potential of  $-70$  mV. Unless specified otherwise, all chemicals were purchased from Sigma-Aldrich except for drugs, which were from Tocris Bioscience.

Miniature EPSC analysis was performed using a software developed by Andrew Penn, the matlab script is available on MATLAB File Exchange, ID: 61567; <http://uk.mathworks.com/matlabcentral/fileexchange/61567-peaker-analysis-toolbox>.

Paired-Pulse Response recordings in acute slices: acute slices were prepared from P16–18 Sprague-Dawley rats of both sexes. Rats were anesthetized with 5% isoflurane prior to decapitation according to the European Directive rules (2010/63/EU). Brain were quickly extracted and the two hemispheres were separated and placed in ice-cold, oxygenated (95% O<sub>2</sub>, 5% CO<sub>2</sub>) sucrose-based artificial cerebrospinal fluid (ACSF) containing (in mM): 250 Sucrose, 2 KCl, 7 MgCl<sub>2</sub>, 0.5 CaCl<sub>2</sub>, 11 Glucose, 1.15 NaH<sub>2</sub>PO<sub>4</sub> and 26 NaHCO<sub>3</sub> (pH 7.4;  $\sim 305$  mOsm/L). Sagittal slices were cut (350  $\mu$ m thick) and incubated for 30 min at 32 °C in carbonated ACSF (95% O<sub>2</sub>, 5% CO<sub>2</sub>) containing (in mM): 126 NaCl, 3.5 KCl, 2 CaCl<sub>2</sub>, 1 MgCl<sub>2</sub>, 1.2 NaH<sub>2</sub>PO<sub>4</sub>, 25 NaHCO<sub>3</sub> and 12.1 Glucose (pH 7.4;  $\sim 310$  mOsm/L). Subsequently, slices were incubated for 30 min at room temperature and used until 5 h after preparation. Experiments were performed in a submerged recording chamber at 30–32 °C with continuous perfusion of carbonated ACSF added with Gabazine (2  $\mu$ M) and CGP52432 (2  $\mu$ M). The intracellular solution was composed of (in mM): 130 Cs methane sulfonate, 10 HEPES, 10 EGTA, 2 MgCl<sub>2</sub>, 1 CaCl<sub>2</sub>, 4 Na<sub>2</sub>-ATP, 0.4 Na-GTP and 5 QX314. Synaptic responses were obtained by five stimulations of Schaffer collateral with 0.2 ms pulses at 50 Hz. 20 series spaced by 20 s were performed. LTD was induced by perfusion of NMDA (30  $\mu$ M, 3 min), or ATP (100  $\mu$ M, 1 min), in presence of CGS15943 3  $\mu$ M. Another 20 series of 5 stimulations at 50 Hz were performed 30 min after LTD induction or LFS (15 min 1 Hz stimulation at the Schaffer collateral). Average of each 20 series were calculated. Each response was normalized to the first one. Paired-Pulse Ratios were measured using Stimfit software taking into account fully successful paired-pulse response (trials with failures were rejected from analysis).

**iGluSnFR imaging and release probability measurement.** Transfection of iGluSnFR (Marvin et al., 2013) was performed on banker neuronal culture at 6 days in vitro (DIV) by a calcium phosphate transfection procedure. Experiments were carried out at 15–18 DIV. Thirty minutes after induction of LTD or water application for control, the neuronal preparation was placed under continuous perfusion in a Tyrode solution containing 100 mM NaCl, 5 mM KCl, 2 mM CaCl<sub>2</sub>, 2 mM MgCl<sub>2</sub>, 15 mM glucose, 10 mM HEPES pH 7.4. Experiments were performed at 35 °C on an inverted microscope (IX83, Olympus) equipped with an Apochromat N oil  $\times 100$  objective (NA 1.49). Samples were illuminated by a 473 nm laser (Cobolt) and emitted fluorescence was detected after passing a 525/50 nm filter (Chroma Technology Corp.). Images were acquired at a resolution of 100  $\times$  100 pixels every 3 ms with a sCMOS camera (Prime 95B; Photometrics) controlled by MetaVue7.1 (Roper Scientific). Neurons were stimulated by electric field stimulation (platinum electrodes, 10 mm spacing, 1 ms pulses of 50 mA and alternating polarity at 1 or 10 Hz) applied by constant current stimulus isolator (SIU-102, Warner Instruments) in the presence of 10  $\mu$ M 6-cyano-7-nitroquinoxaline-2,3-dione (CNQX) and 50  $\mu$ M d,l-2-amino-5-phosphonovaleric acid (AP5) to prevent recurrent activity.

Image analysis was performed with custom-written macros in MATLAB (MathWorks) using an automated detection algorithm. At the end of the experiments, a 10 Hz stimulus was delivered for 5 s while images are acquired at 2 Hz in order to select only active synapses. A differential image was constructed by subtracting a five-frame average obtained immediately before the test train of stimulation from a five-frame average obtained just after stimulation. This difference image highlighting the stimulus-dependent increase of fluorescence was subjected to segmentation based on wavelet transform. All identified masks and calculated time courses were visually inspected for correspondence to individual functional pre-synaptic boutons. The mask was then transferred to the images acquired every 3 ms during a 1 Hz electrical stimulation. Successful fusion events were those where the fluorescence intensity of the first point following stimulation was greater than thrice the standard deviation of 200 points prior the increase in fluorescence. The measurement of release probability was made according to the number of successful responses over the total number of stimulations applied.

**Fluorescence imaging of exocytosis and endocytosis events.** Neurons (14–17 DIV, transfected at 7 DIV with SEP-GluA2 and SEP-GluA1) were perfused with HEPES buffered saline solution (HBS) at 37 °C. HBS contained, in mM: 120 NaCl, 2 KCl, 2 MgCl<sub>2</sub>, 2 CaCl<sub>2</sub>, 5 D-glucose and 10 HEPES, and was adjusted to pH 7.4 and 260–270 mOsm. For the pH assay, MES buffered saline solution (MBS) was prepared similarly by replacing HEPES with MES and adjusting the pH to 5.5. All salts were from Sigma-Aldrich. HBS and MBS were perfused locally around the recorded cell using a 2-way borosilicate glass pipette. Chemical LTD was induced by incubating cells at 37 °C with either ATP (100  $\mu$ M, 1 min) or NMDA (30  $\mu$ M, 3 min) in culture medium, rinsed once and then incubated for further 3 h at 37 °C. When ATP treatment was used, cells were pre-incubated with CGS (3  $\mu$ M, 10 min) to block adenosine receptors. For control experiments, water was used instead of ATP or NMDA.

Imaging was performed with an Olympus IX71 inverted microscope equipped with TIRF microscopy with a 150 $\times$ , 1.45 NA objective (UAPON150XOTIRF), a

Laser source (Cobolt Laser 06-DPL 473 nm, 100 mW) and an Ilas2 illuminator (Gataca Systems) with a penetration depth set to 100 nm. Emitted fluorescence was filtered with a dichroic mirror (R405/488/561/635) and an emission filter (ET525/50 m, Chroma Technology) and recorded by an EMCCD camera (QuantEM 512 C, Princeton Instruments). Movies were acquired for 5 min at 0.5 Hz for endocytosis and for 1 min at 10 Hz for exocytosis. To achieve good signal/noise ratio required for event detection and further analysis, fluorescence was bleached by high laser power illumination prior to acquisition of the full movie. For imaging of exocytosis, this was done in the regular imaging buffer (HBS) to remove signal from fluorescent receptors localized at the plasma membrane or in non-acidic intracellular compartments<sup>71</sup> that could mask the appearance of newly exocytosed receptors. For imaging of endocytosis, bleaching was conducted while applying MBS at pH 5.5. At this pH, plasma membrane receptors are no longer fluorescent and protected from bleaching while intracellular receptors in non-acidic compartments are bleached (Rosendale et al. 2017).

Detection of both exocytic and endocytic events and their analyses was conducted using custom made Matlab scripts previously described<sup>34,40</sup>, apart from kymographs which were obtained using ImageJ. Semi-automatic detection of endocytic events was performed as described previously<sup>34</sup>. In short, a sudden, punctate, fluorescence increase appearing in pH 5.5 images was detected as being an endocytic event if (1) it was visible for more than three frames (i.e., 8 s), and (2) it appeared at the same location as a pre-existing fluorescence cluster detectable in pH 7.4 images. Candidate events (768 events in 18 cells) were then validated by visual inspection in a random order to avoid any bias during cell stimulation (280 validated events,  $48.87 \pm 5.94\%$  per cell). This dataset was then used to train a support vector machine to validate the 47 remaining cells automatically to give 1447 validated events. Event frequency was expressed per cell surface area measured on the cell mask. Fluorescence quantification of events was performed as in<sup>72</sup>. In short, each value is calculated as the mean intensity in a 2-pixel radius circle centred on the detection to which the local background intensity is subtracted (the local background is taken as the 20–80th percentile of fluorescence in an annulus of 5–2 pixel outer and inner radii centred on the detection).

Semi-automatic detection of exocytic events was performed as described previously<sup>40</sup>. Fast fluorescence increases reporting exocytosis events were detected by generating a differential movie (imagen+1 - imagen + constant). A manual threshold was used to select candidate events (objects bigger than 2 pixels), with additional criteria to exclude moving clusters, variations in intense clusters, or tubule contraction. For each candidate event, a mini-movie and a series of background-subtracted images were generated. Events were validated or discarded by the user based on these two visualization tools. For fluorescence quantification, a ROI and a region surrounding the ROI (SR) are defined as follows. The five background-subtracted images before exocytosis define an SD of pixel values. A threshold is defined as seven times the SD to define putative ROIs. In case of multiple objects, the one closest to image center is chosen. If no object is detected, the ROI is defined as a 2.2 pixel radius circle centred on the centroid of the original detection. If an object is detected, the ROI is the reunion of the object and a 2.2 pixel radius circle centred on the object. The SR is obtained by a dilation of the ROI by two pixels. For the following frame, the same object detection procedure is applied, and a new ROI and SR are defined. The centroid of the new ROI must be  $<5$  pixels away. If no object is defined, the ROI is kept the same. For images before exocytosis, the ROI used is the one defined at time 0, the time of exocytosis. For each event, we compute  $FR - S = FROI - FSR$ , where FROI and FSR represent the average fluorescence of the original images in the ROI and the SR, respectively. For the SR, the 20% lowest and highest pixel values are removed to limit environmental variations (out of the cell, bright cluster). For each event,  $FR - S$  is normalized by subtracting the average of values before exocytosis and divided by  $FR - S$  at the time of exocytosis. Events for which normalized  $FR - S$  was 50% for 2 s were sorted as burst events, and the other ones were sorted as display events.

**Modeling.** Computer modeling was performed using the MCell/CellBlender simulation environment (<http://mcell.org>) with MCell version 3.3, CellBlender version 1.1, and Blender version 2.77a (<http://blender.org>). The realistic model of glutamatergic synaptic environment was constructed from 3D-EM of hippocampal area CA1 neuropil as described in<sup>54–56</sup>. The 3D-EM reconstruction contains all plasma membrane bounded components including dendrites, axons, astrocytic glia and the extracellular space itself, in a  $6 \times 6 \times 5 \mu\text{m}^3$  volume of hippocampal area CA1 stratum radiatum from adult rat. The AMPAR chemical kinetic properties were obtained from the well-established model published in Jonas et al., 1993, and the kinetic parameters were adjusted to fit with the recorded mEPSCs (see<sup>10</sup>).

Three surface properties are defined. The synapse, the PSD (identified on EM data) and a 100 nm domain inside the PSD which correspond to the AMPAR nanodomain. According to literature and to our dSTORM data, 200 PSD-95 molecules were released. They freely diffuse inside the PSD and are palmitoylated at a certain rate ( $k_{\text{on}} = 35$ ,  $k_{\text{off}} = 0.7$ ) when they enter inside the nanodomain area. These kinetic rate constants result in a steady-state accumulation of around 70 palmitoylated PSD-95 inside the nanodomain according to experimental results. PSD-95 can be also inactivated with a certain rate to mimic LTD.

Concerning AMPAR, a total of 120 receptors were released at time zero and were distributed in two separate pools as follow: one pool of 60 AMPARs were allowed to diffuse on the membrane surface and a second pool of 60 AMPARs

represented the endocytosed state. Individual receptors exchange between the pools at equal forward and backward rates to maintain equilibrium. To mimic LTD induction, the rate of exchange to the endocytosed state was increased. At the surface, AMPARs are mobile with a diffusion coefficient of  $0.5 \mu\text{m}^2 \text{s}^{-1}$ , and can interact inside the nanodomain with palmitoylated PSD-95 ( $k_{\text{on}} = 5$ ,  $k_{\text{off}} = 1$ ). This interaction slows down the AMPAR to  $0.005 \mu\text{m}^2 \text{s}^{-1}$  and slows down the AMPAR diffusion constant to retain the molecular complex within the nanodomain leading to an equilibrium of around 20–25 AMPAR trapped into the domain (similar to results described in the literature). All this organization of PSD-95 and AMPAR at the synapse were simulated at a time step of 1 ms for 50,000 iterations (50 ms), until reaching an equilibrium (as illustrated Supplementary Fig. 13). Then the simulations were switched to a time step of 1  $\mu\text{s}$  for 250,000 iterations to model the AMPAR responses when the glutamate is released at the pre-synaptic level, in front of the nanodomain.

We tested three individual modifications of the kinetic rate constants to mimic LTD. (1) A multiplication by 3 of the endocytosis rate mimics the endocytosis-dependent LTD (ATP type or initial phase of NMDA type of LTD). (2) A four times increase of the PSD-95 + AMPAR  $k_{\text{off}}$ , which favors the untrapping of AMPAR. (3) A four-time increase of the inactivation rate of PSD-95, mimicking the decrease of PSD-95 experimentally observed. 100 simulation trials are averaged for each condition, and 2500 glutamate are releases for each release event.

**Sampling and statistics.** All data showing AMPARs and PSD-95 organization, AMPAR lateral diffusion, PSD-95 autophagy and synaptic currents, AMPAR endocytosis are pooled from at least three independent experiments. Summary statistics are presented as mean  $\pm$  SEM (Standard Error of the Mean). Statistical significance tests were performed using GraphPad Prism software (San Diego, CA). Normality tests were performed with D'Agostino and Pearson omnibus tests. For non-normally distributed data, we applied Mann–Whitney test or Wilcoxon matched-pairs signed rank tests for paired observations. When the data followed normal distribution, we used paired or unpaired *t*-test for paired observations unless stated otherwise. All statistics are two-sided tests comparing groups of biological replicates. ANOVA test was used to compare means of several groups of normally distributed variables. Indications of significance correspond to *p* values  $< 0.05$  (\*),  $p < 0.005$  (\*\*), and  $p < 0.0005$  (\*\*\*). After ANOVA analysis, we apply a Dunnett's post test to determine the *p* value between two conditions, results of these tests are noted Anova post-test.

**Ethical approval.** All experiments were approved by the Regional Ethical Committee on Animal Experiments of Bordeaux.

**Reporting summary.** Further information on research design is available in the Nature Research Reporting Summary linked to this article.

### Data availability

Source Data that support the findings of this study are available in the online version of the paper and from the corresponding author upon reasonable request.

Received: 1 September 2020; Accepted: 7 April 2021;

Published online: 14 May 2021

### References

- Borgdorff, A. J. & Choquet, D. Regulation of AMPA receptor lateral movements. *Nature* **417**, 649–653 (2002).
- Tardin, C., Cognet, L., Bats, C., Lounis, B. & Choquet, D. Direct imaging of lateral movements of AMPA receptors inside synapses. *EMBO J.* **22**, 4656–4665 (2003).
- Ehlers, M. D., Heine, M., Groc, L., Lee, M. C. & Choquet, D. Diffusional Trapping of GluR1 AMPA Receptors by Input-Specific Synaptic Activity. *Neuron* **54**, 447–460 (2007).
- Makino, H. & Malinow, R. AMPA Receptor Incorporation into Synapses during LTP: the Role of Lateral Movement and Exocytosis. *Neuron* **64**, 381–390 (2009).
- Groc, L. & Choquet, D. Linking glutamate receptor movements and synapse function. *Science* **368**, 1204–1213 (2020).
- Goncalves, J. et al. Nanoscale co-organization and coactivation of AMPAR, NMDAR, and mGluR at excitatory synapses. *Proc. Natl Acad. Sci. U. S. A.* **117**, 14503–14511 (2020).
- Schnell, E. et al. Direct interactions between PSD-95 and stargazin control synaptic AMPA receptor number. *Proc. Natl Acad. Sci.* **99**, 13902–13907 (2002).
- Schwenk, J. et al. Regional diversity and developmental dynamics of the AMPA-receptor proteome in the mammalian brain. *Neuron* **84**, 41–54 (2014).

- Huganir, R. L. & Nicoll, R. A. AMPARs and synaptic plasticity: the last 25 years. *Neuron* **80**, 704–717 (2013).
- Haas, K. T. et al. Pre-post synaptic alignment through neuroligin-1 tunes synaptic transmission efficiency. *Elife* **7**, 1–22 (2018).
- Tang, A. H. et al. A trans-synaptic nanocolumn aligns neurotransmitter release to receptors. *Nature* **536**, 210–214 (2016).
- Nair, D. et al. Super-Resolution Imaging Reveals That AMPA Receptors Inside Synapses Are Dynamically Organized in Nanodomains Regulated by PSD95. *J. Neurosci.* **33**, 13204–13224 (2013).
- MacGillavry, H. D., Song, Y., Raghavachari, S. & Blanpied, T. A. Nanoscale scaffolding domains within the postsynaptic density concentrate synaptic ampa receptors. *Neuron* **78**, 615–622 (2013).
- Savtchenko, L. P. & Rusakov, D. A. Moderate AMPA receptor clustering on the nanoscale can efficiently potentiate synaptic current. *Philos. Trans. R. Soc. B Biol. Sci.* **369**, 20130167 (2014).
- Brenowitz, S. & Trussell, L. O. Minimizing synaptic depression by control of release probability. *J. Neurosci.* **21**, 1857–1867 (2001).
- Chen, C., Blitz, D. M. & Regehr, W. G. Contributions of receptor desensitization and saturation to plasticity at the retinogeniculate synapse. *Neuron* **33**, 779–788 (2002).
- Turecek, R. & Trussell, L. O. Control of synaptic depression by glutamate transporters. *J. Neurosci.* **20**, 2054–2063 (2000).
- Constals, A. et al. Glutamate-Induced AMPA Receptor Desensitization Increases Their Mobility and Modulates Short-Term Plasticity through Unbinding from Stargazin. *Neuron* **85**, 787–803 (2015).
- Heine, M. et al. Surface mobility of postsynaptic AMPARs tunes synaptic transmission. *Science* **320**, 201–205 (2008).
- Opazo, P. et al. CaMKII triggers the diffusional trapping of surface AMPARs through phosphorylation of stargazin. *Neuron* **67**, 239–252 (2010).
- Frischknecht, R. et al. Brain extracellular matrix affects AMPA receptor lateral mobility and short-term synaptic plasticity. *Nat. Neurosci.* **12**, 897–904 (2009).
- Compans, B., Choquet, D. & Hossy, E. Review on the role of AMPA receptor nano-organization and dynamic in the properties of synaptic transmission. *Neurophotonics* **3**, 041811 (2016).
- Klaassen, R. V. et al. Shisa6 traps AMPA receptors at postsynaptic sites and prevents their desensitization during synaptic activity. *Nat. Commun.* **7**, 10682 (2016).
- Penn, A. C. et al. Hippocampal LTP and contextual learning require surface diffusion of AMPA receptors. *Nature* **549**, 384–388 (2017).
- Oliet, S. H., Malenka, R. C. & Nicoll, R. A. Two distinct forms of long-term depression coexist in CA1 hippocampal pyramidal cells. *Neuron* **18**, 969–982 (1997).
- Dudek, S. M. & Bear, M. F. Homosynaptic long-term depression in area CA1 of hippocampus and effects of N-methyl-D-aspartate receptor blockade. *Proc. Natl Acad. Sci. U. S. A.* **89**, 4363–4367 (1992).
- Beattie, E. C. et al. Regulation of AMPA receptor endocytosis by a signaling mechanism shared with LTD. *Nat. Neurosci.* **3**, 1291–1300 (2000).
- Cavaccini, A., Durkee, C., Kofuji, P., Tonini, R. & Araque, A. Astrocyte signaling gates long-term depression at corticostriatal synapses of the direct pathway. *J. Neurosci.* **40**, JN-RM-2369–19 (2020).
- Pougnat, J. T. et al. ATP P2X receptors downregulate AMPA receptor trafficking and postsynaptic efficacy in hippocampal neurons. *Neuron* **83**, 417–430 (2014).
- Collingridge, G. L., Peineau, S., Howland, J. G. & Wang, Y. T. Long-term depression in the CNS. *Nat. Rev. Neurosci.* **11**, 459–473 (2010).
- Lee, H. K., Kameyama, K., Huganir, R. L. & Bear, M. F. NMDA induces long-term synaptic depression and dephosphorylation of the GluR1 subunit of AMPA receptors in hippocampus. *Neuron* **21**, 1151–1162 (1998).
- Pougnat, J.-T. et al. P2X-mediated AMPA receptor internalization and synaptic depression is controlled by two CaMKII phosphorylation sites on GluA1 in hippocampal neurons. *Sci. Rep.* **6**, 31836 (2016).
- Fuji, S., Tanaka, H. & Hirano, T. Suppression of AMPA receptor exocytosis contributes to hippocampal LTD. *J. Neurosci.* **38**, 5523–5537 (2018).
- Rosendale, M., Jullié, D., Choquet, D. & Perrais, D. Spatial and Temporal Regulation of Receptor Endocytosis in Neuronal Dendrites Revealed by Imaging of Single Vesicle Formation. *Cell Rep.* **18**, 1840–1847 (2017).
- Carroll, R. C., Lissin, D. V., von Zastrow, M., Nicoll, R. A. & Malenka, R. C. Rapid redistribution of glutamate receptors contributes to long-term depression in hippocampal cultures. *Nat. Neurosci.* **2**, 454–460 (1999).
- Giannone, G. et al. Dynamic superresolution imaging of endogenous proteins on living cells at ultra-high density. *Biophys. J.* **99**, 1303–1310 (2010).
- Hossy, E., Butler, C. & Sibarita, J. B. Organization and dynamics of AMPA receptors inside synapses-nano-organization of AMPA receptors and main synaptic scaffolding proteins revealed by super-resolution imaging. *Curr. Opin. Chem. Biol.* **20**, 120–126 (2014).
- Yudowski, G. A. & Puthenveedu, M. A. & Von Zastrow, M. Distinct modes of regulated receptor insertion to the somatodendritic plasma membrane. *Nat. Neurosci.* **9**, 622–627 (2006).

39. Kennedy, M. J., Davison, I. G., Robinson, C. G. & Ehlers, M. D. Syntaxin-4 defines a domain for activity-dependent exocytosis in dendritic spines. *Cell* **141**, 524–535 (2010).
40. Jullié, D., Choquet, D. & Perraiss, D. Recycling endosomes undergo rapid closure of a fusion pore on exocytosis in neuronal dendrites. *J. Neurosci.* **34**, 11106–11118 (2014).
41. Opazo, P., Sainlos, M. & Choquet, D. Regulation of AMPA receptor surface diffusion by PSD-95 slots. *Curr. Opin. Neurobiol.* **22**, 453–460 (2012).
42. Bats, C., Groc, L. & Choquet, D. The Interaction between Stargazin and PSD-95 Regulates AMPA Receptor Surface Trafficking. *Neuron* **53**, 719–734 (2007).
43. Fukata, Y. et al. Local palmitoylation cycles define activity-regulated postsynaptic subdomains. *J. Cell Biol.* **202**, 145–161 (2013).
44. Levet, F. et al. SR-Tesseler: a method to segment and quantify localization-based super-resolution microscopy data. *Nat. Methods* **12**, 1065–1071 (2015).
45. Nelson, C. D., Kim, M. J., Hsin, H., Chen, Y. & Sheng, M. Phosphorylation Threonine-19 PSD-95 GSK-3 $\alpha$  is Required PSD-95 Mobilization and Long-Term Depression. *J. Neurosci.* **33**, 12122–12135 (2013).
46. Ehrlich, I. & Malinow, R. Postsynaptic Density 95 controls AMPA Receptor Incorporation during Long-Term Potentiation and Experience-Driven Synaptic Plasticity. *J. Neurosci.* **24**, 916–927 (2004).
47. Stein, V., House, D. R. C., Bredt, D. S. & Nicoll, R. A. Postsynaptic density-95 mimics and occludes hippocampal long-term potentiation and enhances long-term depression. *J. Neurosci.* **23**, 5503–5506 (2003).
48. Nikolettou, V., Sidropoulou, K., Kallergj, E., Daleziou, Y. & Tavernarakis, N. Modulation of Autophagy by BDNF Underlies Synaptic Plasticity. *Cell Metab.* **26**, 230–242.e5 (2017).
49. Kallergj, E. et al. Long-term synaptic depression triggers local biogenesis of autophagic vesicles in dendrites and requires autophagic degradation. Preprint at *bioRxiv* <https://doi.org/10.1101/2020.03.12.983965> (2020).
50. Zucker, R. S. & Regehr, W. G. Short-Term Synaptic Plasticity. *Annu. Rev. Physiol.* **64**, 355–405 (2002).
51. Marvin, J. S. et al. An optimized fluorescent probe for visualizing glutamate neurotransmission. *Nat. Methods* **10**, 162–170 (2013).
52. Sainlos, M. et al. Biomimetic divalent ligands for the acute disruption of synaptic AMPAR stabilization. *Nat. Chem. Biol.* **7**, 81–91 (2011).
53. Tomita, S. et al. Stargazin modulates AMPA receptor gating and trafficking by distinct domains. *Nature* **435**, 1052–1058 (2005).
54. Bartol, T. M. et al. Computational reconstitution of spine calcium transients from individual proteins. *Front. Synaptic Neurosci.* **7**, 1–24 (2015).
55. Bartol, T. M. Jr et al. Nanoconnectomic upper bound on the variability of synaptic plasticity. *Elife* 1–18 (2015). <https://doi.org/10.7554/eLife.10778.001>
56. Kinney, J. P. et al. Extracellular sheets and tunnels modulate glutamate diffusion in hippocampal neuropil. *J. Comp. Neurol.* **521**, 448–464 (2013).
57. Sheng, M. & Hoogenraad, C. C. The postsynaptic architecture of excitatory synapses: a more quantitative view. *Annu. Rev. Biochem.* **76**, 823–847 (2007).
58. Tarusawa, E. et al. Input-Specific Intrasympatric Arrangements of Ionotropic Glutamate Receptors and Their Impact on Postsynaptic Responses. *J. Neurosci.* **29**, 12896–12908 (2009).
59. Xie, X., Liaw, J. S., Baudry, M. & Berger, T. W. Novel expression mechanism for synaptic potentiation: alignment of presynaptic release site and postsynaptic receptor. *Proc. Natl Acad. Sci. U. S. A.* **94**, 6983–6988 (1997).
60. Lüscher, C. et al. Role of AMPA Receptor Cycling in Synaptic Transmission and Plasticity. *Neuron* **24**, 649–658 (1999).
61. Sanderson, J. L., Gorski, J. A. & Dell'Acqua, M. L. NMDA Receptor-Dependent LTD Requires Transient Synaptic Incorporation of Ca $^{2+}$  -Permeable AMPARs Mediated by AKAP150-Anchored PKA and Calcineurin. *Neuron* **89**, 1000–1015 (2016).
62. Colledge, M. et al. Ubiquitination regulates PSD-95 degradation and AMPA receptor surface expression. *Neuron* **40**, 595–607 (2003).
63. El-Husseini, A. E. D. et al. Synaptic strength regulated by palmitate cycling on PSD-95. *Cell* **108**, 849–863 (2002).
64. Zhang, Y. et al. Capping of the N-terminus of PSD-95 by calmodulin triggers its postsynaptic release. *EMBO J.* **33**, 1341–1353 (2014).
65. Chowdhury, D. & Hell, J. W. Ca $^{2+}$ /Calmodulin Binding to PSD-95 Downregulates Its Palmitoylation and AMPARs in Long-Term Depression. *Front. Synaptic Neurosci.* **11**, 1–10 (2019).
66. Chowdhury, D. et al. Ca $^{2+}$ /calmodulin binding to PSD-95 mediates homeostatic synaptic scaling down. *EMBO J.* **37**, 122–138 (2018).
67. Kaech, S. & Banker, G. Culturing hippocampal neurons. *Nat. Protoc.* **1**, 2406–2415 (2006).
68. Linde, S. VanDe. et al. Direct stochastic optical reconstruction microscopy with standard fluorescent probes. *Cell* **141**, 34–38 (2011).
69. Kechkar, A., Nair, D., Heilemann, M., Choquet, D. & Sibarita, J. B. Real-Time Analysis and Visualization for Single-Molecule Based Super-Resolution Microscopy. *PLoS ONE* **8**, e62918 (2013).
70. Levet, F. et al. A tessellation-based colocalization analysis approach for single-molecule localization microscopy. *Nat. Commun.* **10**, 1–12 (2019).
71. Petri, E. M. et al. Endocytic trafficking and recycling maintain a pool of mobile surface AMPA receptors required for synaptic potentiation. *Neuron* **63**, 92–105 (2009).
72. Shen, Y., Rosendale, M., Campbell, R. E. & Perraiss, D. pHuji, a pH-sensitive red fluorescent protein for imaging of exo- and endocytosis. *J. Cell Biol.* **207**, 419–432 (2014).

## Acknowledgements

We acknowledge E. Gouaux for the anti-GluA2 antibody and J.S. Marvin for the iGluSnFR plasmid; the Bordeaux Imaging Center, part of the FranceBioImaging national infrastructure (ANR-10INBS-04-0, for support in microscopy; E. Normand and the IINS in vivo facility for animal husbandry. We thank the IINS cell biology core facilities (LABEX BRAIN [ANR-10-LABX-43]) and in particular C. Breillat, E. Verdier, and N. Retailleau for cell culture and plasmid production, and Jorge Aldana from the Salk institute for computing support. This work was supported by funding from the Ministère de l'Enseignement Supérieur et de la Recherche (ANR NanoDom and AMPAR-T), Fulbright and Philippe foundation to E.H. and D.C., Centre National de la Recherche Scientifique (CNRS), ERC grant ADOS (339541) and DynSynMem (787340) to D.C., Fondation pour la Recherche Médicale fellowship to B.C.

## Author contributions

B.C. and C.C. performed all dSTORM and single-particle tracking experiments, culture and slice electrophysiology. M.M. performed iGluSnFR experiments, D.P. and S.S. performed the endo/exocytosis experiments. E.H., T.M.B. and T.J.S. created the MCell model and E.H. performed the simulations. C.B., A.K. and J.B.S. developed the super-resolution analysis software. R.V.K. and A.B.S. participate to conception and validation of some hypothesis. E.K. and V.N. realized biochemical experiments on autophagosomes. N.R. performed molecular biology constructs. E.H. conceived and supervised the study. D.C. financed the study. E.H., B.C. and D.C. wrote the paper. All authors contributed to the revision of the paper.

## Competing interests

The authors declare no competing interests.

## Additional information

**Supplementary information** The online version contains supplementary material available at <https://doi.org/10.1038/s41467-021-23133-9>.

**Correspondence** and requests for materials should be addressed to E.H.

**Peer review information** *Nature Communications* thanks the anonymous reviewer(s) for their contribution to the peer review of this work. Peer reviewer reports are available.

**Reprints and permission information** is available at <http://www.nature.com/reprints>

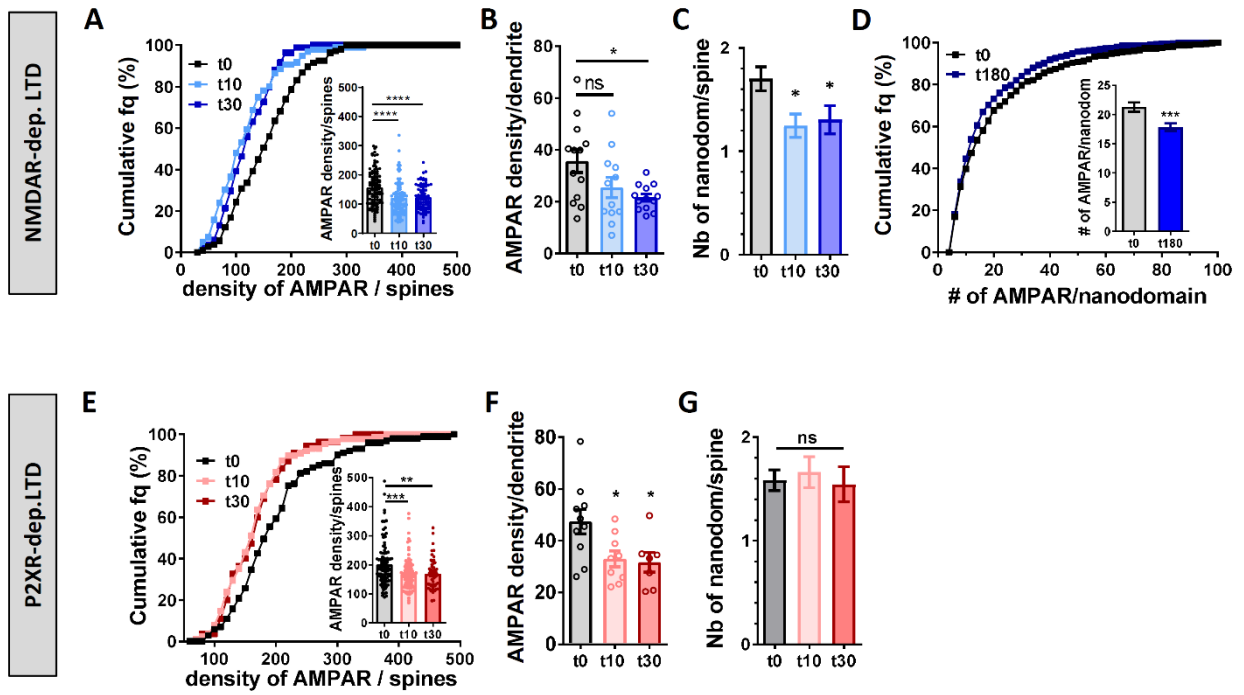
**Publisher's note** Springer Nature remains neutral with regard to jurisdictional claims in published maps and institutional affiliations.



**Open Access** This article is licensed under a Creative Commons Attribution 4.0 International License, which permits use, sharing, adaptation, distribution and reproduction in any medium or format, as long as you give appropriate credit to the original author(s) and the source, provide a link to the Creative Commons license, and indicate if changes were made. The images or other third party material in this article are included in the article's Creative Commons license, unless indicated otherwise in a credit line to the material. If material is not included in the article's Creative Commons license and your intended use is not permitted by statutory regulation or exceeds the permitted use, you will need to obtain permission directly from the copyright holder. To view a copy of this license, visit <http://creativecommons.org/licenses/by/4.0/>.

© The Author(s) 2021



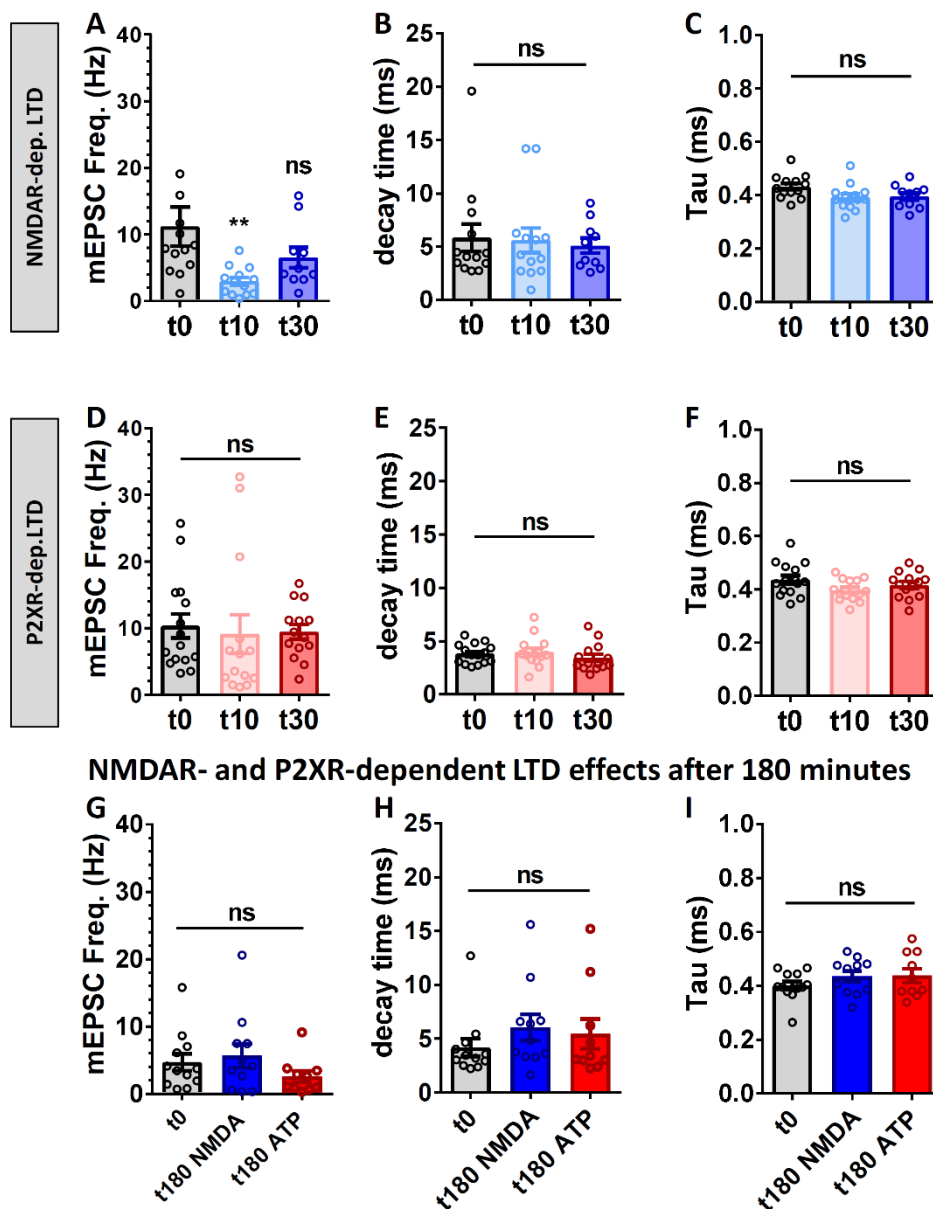


Supplementary Figure 1

**Supplementary Figure 1. NMDA and ATP application triggers a rapid and long-lasting decrease of AMPAR surface expression and nanoscale organization.**

(A) Cumulative distribution of AMPAR density per dendritic spine ( $n=107$ , 96 and 84 for  $t_0$ ,  $t_{10}$  and  $t_{30}$  respectively), and in the inset, the average histogram. The density of AMPARs per spine was measured 0, 10 and 30 minutes following NMDA treatment (mean  $\pm$  SEM, one-way ANOVA,  $p<0.0001$  and Dunnett's post-test found significant differences between  $t_0$  and  $t_{10}$  or  $t_{30}$ ,  $p<0.0001$ ). AMPAR surface expression is significantly decreased in dendritic spines 10 and 30 minutes following NMDA treatment compared to non-treated cells. (B) Average of AMPAR density per dendrite measured 0, 10 and 30 minutes following NMDA treatment (mean  $\pm$  SEM,  $n=13$ , 12 and 13 respectively, one-way ANOVA,  $p=0.0183$  and Dunnett's post-test found significant difference between  $t_0$  and  $t_{30}$   $p=0.0118$  but not between  $t_0$  and  $t_{10}$ ,  $p=0.0851$ ). AMPAR surface expression is significantly decreased in neuronal dendritic shafts 30 minutes following NMDA treatment compared to non-treated cells. (C) Average of AMPAR nanodomain number per dendritic spine measured 0, 10 and 30 minutes following NMDA treatment (mean  $\pm$  SEM,  $n=107$ , 105 and 79 respectively, one-way ANOVA,  $p=0.0123$  and Dunnett's post-test found significant difference between  $t_0$  and  $t_{10}$  or  $t_{30}$ ,  $p=0.0112$  and  $p=0.0465$  respectively). AMPAR nanodomain number per dendritic spine is significantly decreased in neuronal dendritic shafts 10 and 30 minutes following NMDA treatment compared to non-treated cells. (D) Cumulative distribution of nanodomain AMPAR content ( $n=556$  and 544 for  $t_0$  and  $t_{180}$  respectively), and in the inset, the average histogram. The number of AMPARs per nanodomains was measured at basal state ( $t_0$ ) and 180 minutes following NMDA treatment (mean  $\pm$  SEM,  $n=556$  and 544, unpaired t-test,  $p=0.0010$ ). Nanodomain content is significantly decreased 180 minutes following NMDA treatment compared to non-treated cells.

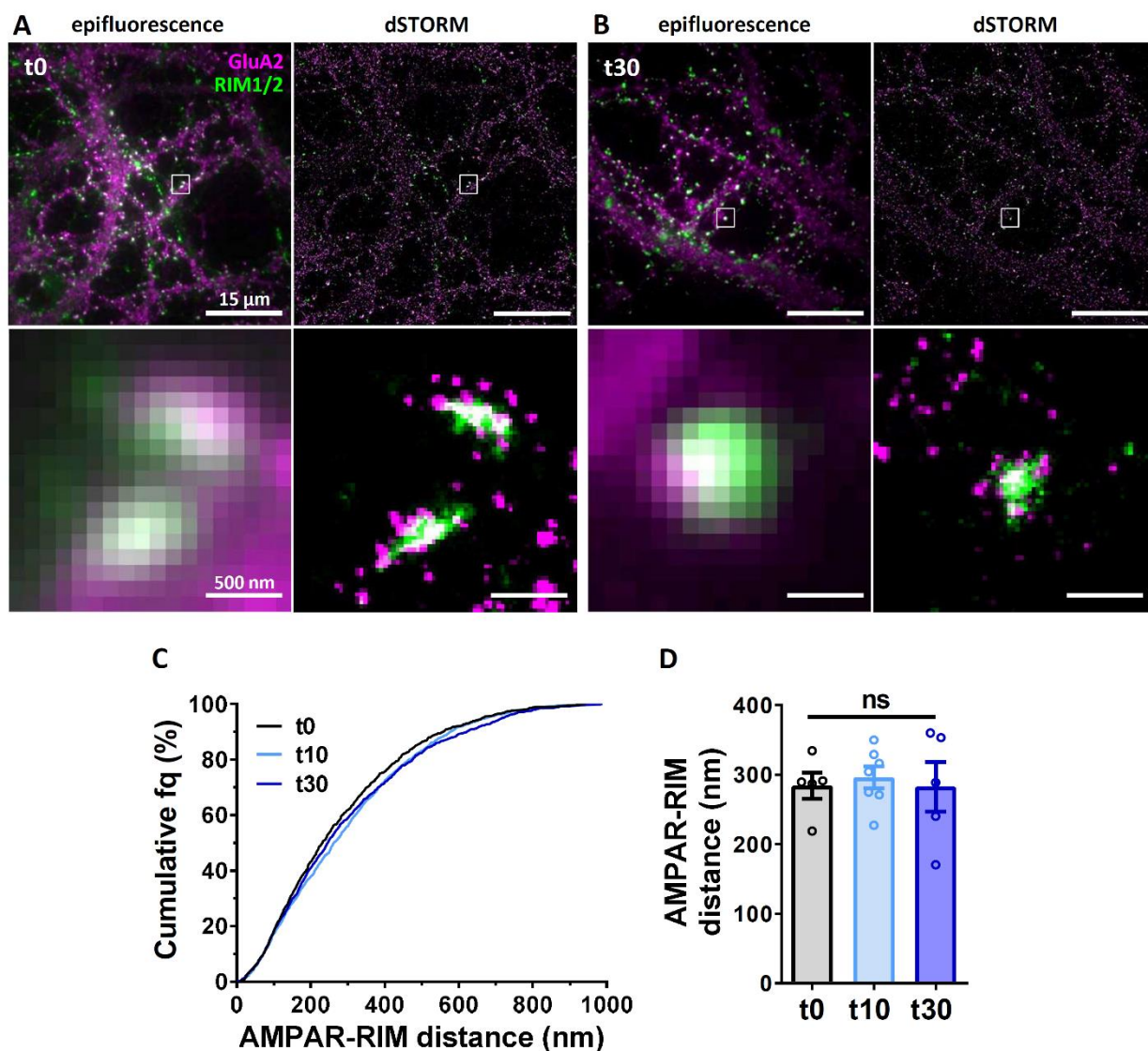
(E-G) Similar experiments as from A to C has been realized using ATP treatment to trigger LTD. (E) Cumulative distribution of AMPAR density per dendritic spine ( $n=101$ , 88 and 55 for  $t_0$ ,  $t_{10}$  and  $t_{30}$  respectively), and in the inset, the average histogram. The density of AMPARs per spines was measured 0, 10 and 30 minutes following ATP treatment (mean  $\pm$  SEM, one-way ANOVA,  $p=0.0005$  and Dunnett's post-test found significant differences between  $t_0$  and  $t_{10}$  or  $t_{30}$ ,  $p=0.0008$  and  $p=0.0052$  respectively). AMPAR surface expression is significantly decreased in dendritic spines 10 and 30 minutes following ATP treatment compared to non-treated cells. (F) Average of AMPAR density per dendrite measured 0, 10 and 30 minutes following ATP treatment (mean  $\pm$  SEM,  $n=10$ , 9 and 7 respectively, one-way ANOVA,  $p=0.0186$  and Dunnett's post-test found significant difference between  $t_0$  and  $t_{10}$  or  $t_{30}$   $p=0.0304$  and  $p=0.0266$  respectively). AMPAR surface expression is significantly decreased in neuronal dendritic shafts 10 and 30 minutes following ATP treatment compared to non-treated cells. (G) Average of AMPAR nanodomain number per dendritic spine measured 0, 10 and 30 minutes following ATP treatment (mean  $\pm$  SEM,  $n=82$ , 68 and 55 respectively, one-way ANOVA,  $p=0.8399$ ). AMPAR nanodomain number per dendritic spine is maintained 10 and 30 minutes following ATP treatment compared to non-treated cells.



**Supplementary Figure 2. Impact of NMDA and ATP treatment on mEPSC properties.**

(A-C) mEPSC frequency (A), decay time (B) and tau (C) at basal state (t0) or 10 and 30 minutes after NMDA treatment (mean +/- SEM, n=13, 13 and 10 respectively, (A) one-way ANOVA,  $p=0.0179$  with Dunnett's post-test showing a significant difference between t0 and t10,  $p=0.0094$ ; (B,C) one-way ANOVA,  $p=0.9033$  and  $p=0.0707$  respectively). (D-F) mEPSC frequency (D), decay time (E) and tau (F) at basal state (t0) or 10 and 30 minutes after ATP treatment (n=15, 14 and 14 respectively, one-way ANOVA,  $p=0.0905$ ,  $p=0.4583$  and  $p=0.1274$  respectively). (G-I) mEPSC frequency (G), decay time (H) and tau (I) at basal state (t0) or 180 minutes after NMDA (t180 NMDA) or ATP (t180 ATP) treatments (n=12, 11 and 10 respectively, one-way ANOVA,  $p=0.2920$ ,  $p=0.4848$  and  $p=0.3639$  respectively).

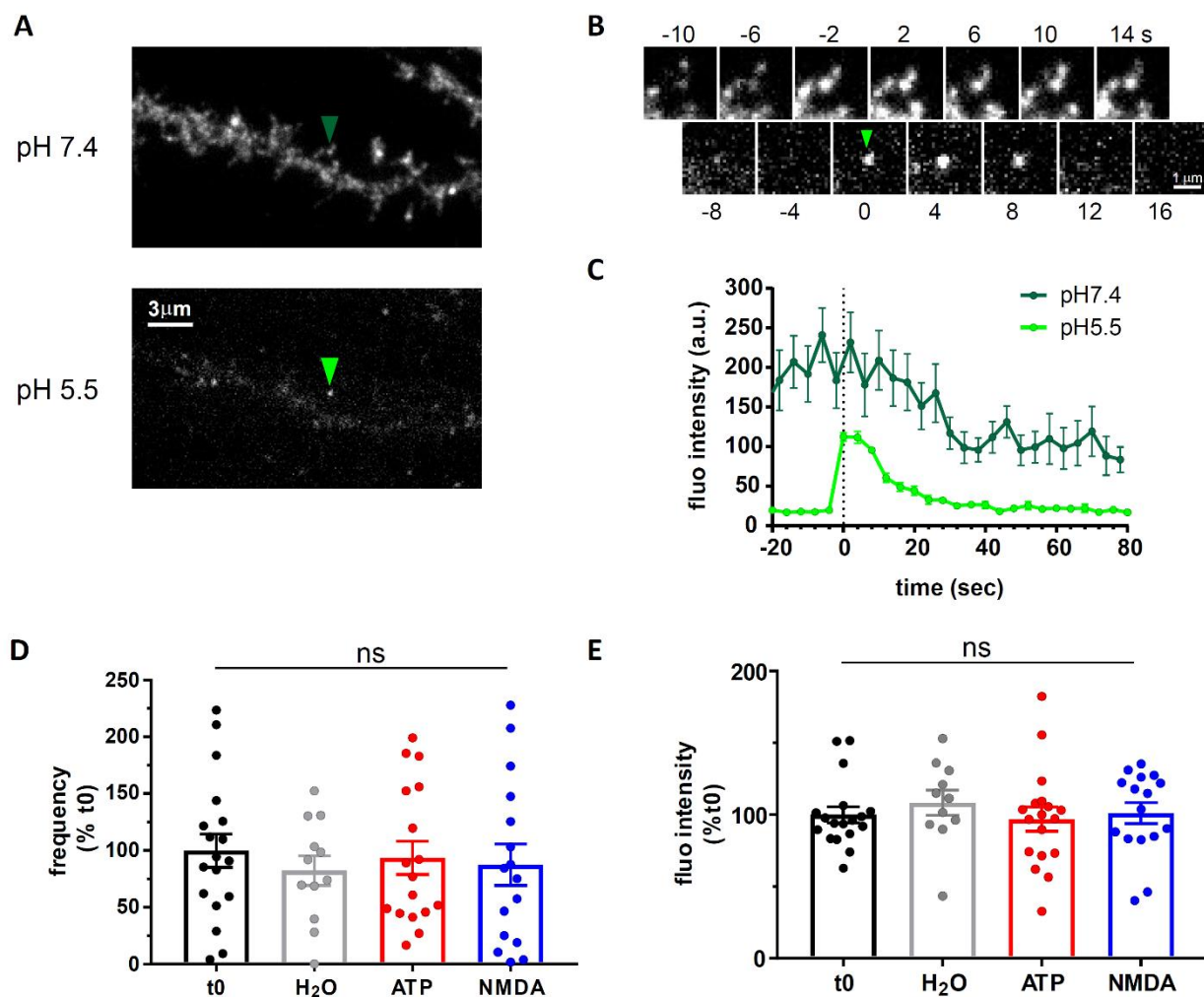
**Supplementary Figure 2**



**Supplementary Figure 3. NMDA treatment does not impact on the colocalization of the pre-synaptic RIM and the post-synaptic AMPAR domains**

(A and B) Example of dual color D-STORM images with RIM1/2 in green and GluA2-containing AMPARs in purple before treatment (A) and 30 minutes after NMDA application (B). Top Right panels are low resolution images, top left panels are dSTORM reconstructed images, bottom are zoom on synapses from both low and high resolution images. Cumulative distribution (C) and Average per cell (D) of the AMPAR-RIM cluster distances (centroid to centroid) at t0 and 10 and 30 minutes following NMDA treatment. No significant differences are measured (one-way ANOVA,  $p=0.897$ ). Scale bars for A and B top panels are 15 $\mu$ m and bottom panels are 500nm.

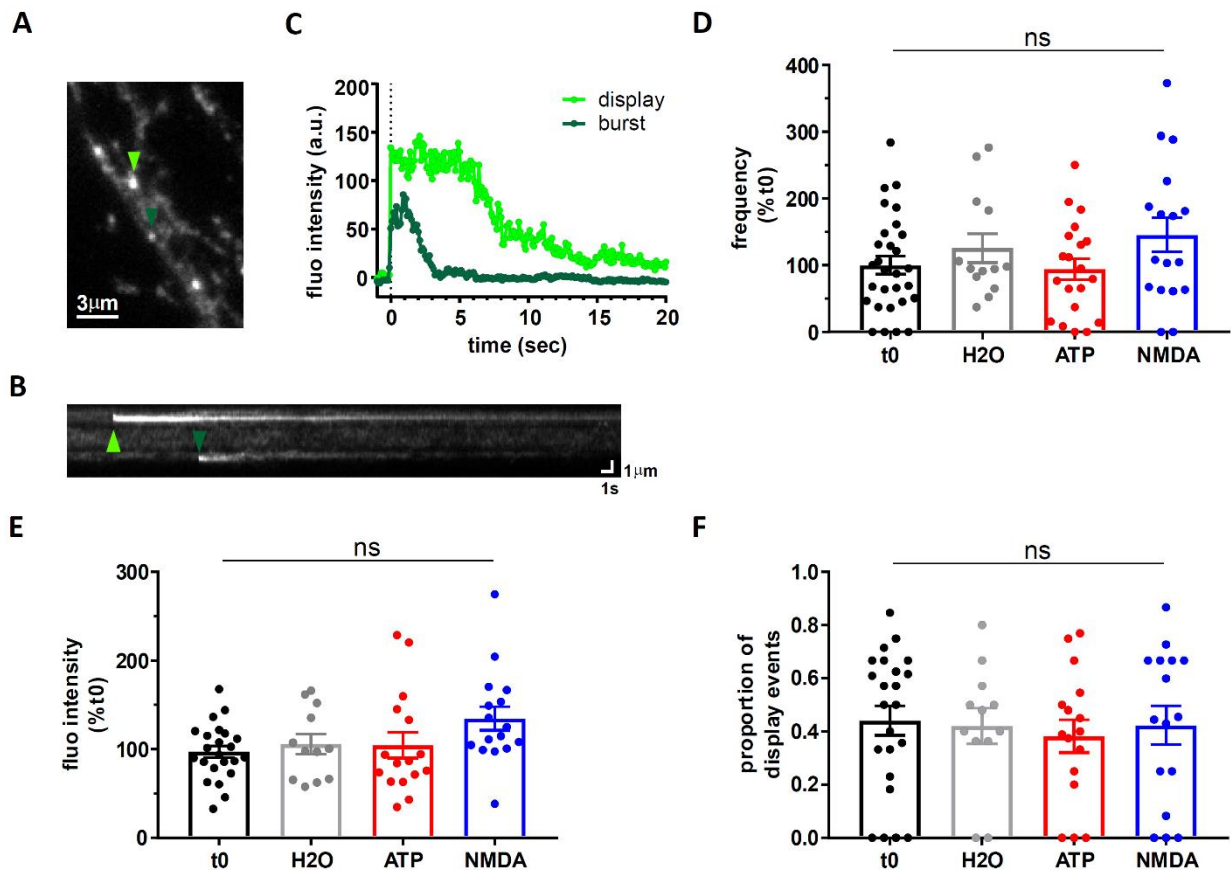
**Supplementary Figure 3**



### Supplementary Figure 4. NMDA or ATP do not alter endocytosis of AMPAR 3 hours post application.

(A) Dendrite of a neuron transfected with SEP-GluA1 and SEP-GluA2 and imaged with TIRF microscopy at pH 7.4 and pH 5.5 (4x contrast). Spots visible at pH 5.5 are intracellular receptors; green arrowhead highlights an endocytic vesicle with its corresponding cluster at pH 7.4. Scale bar = 3  $\mu$ m. (B) Example of the endocytic event, illustrated in A, detected with the ppH assay. Images taken at pH 7.4 (top) and 5.5 (bottom) at times relative to time 0, the moment of vesicle detection at pH 5.5. Scale bar = 1  $\mu$ m. (C) Average fluorescence intensity (fluo.) of all the endocytic events detected in the cell shown in A, aligned to the time of vesicle detection (frame 0). (D) Frequency of endocytosis (in events.min<sup>-1</sup>.m<sup>-2</sup>) measured prior any stimulation (t0) or 3h after application of H<sub>2</sub>O, ATP or NMDA, normalized to t0 of each session to correct for differences in basal activity of neuronal cultures; not normalized numbers are (mean  $\pm$  SEM): t0, 0.0157  $\pm$  0.0034, n=18; H<sub>2</sub>O, 0.0143  $\pm$  0.0031, n=12; ATP, 0.0088  $\pm$  0.0017, n=16; NMDA, 0.0146  $\pm$  0.00286, n=17. (E) Average fluorescence intensity (fluo.) at time of vesicle formation of 621, 317, 264, 525 events in 18, 12, 16, 17 cells imaged prior any stimulation (t0), 3h after H<sub>2</sub>O, ATP or NMDA application, respectively.

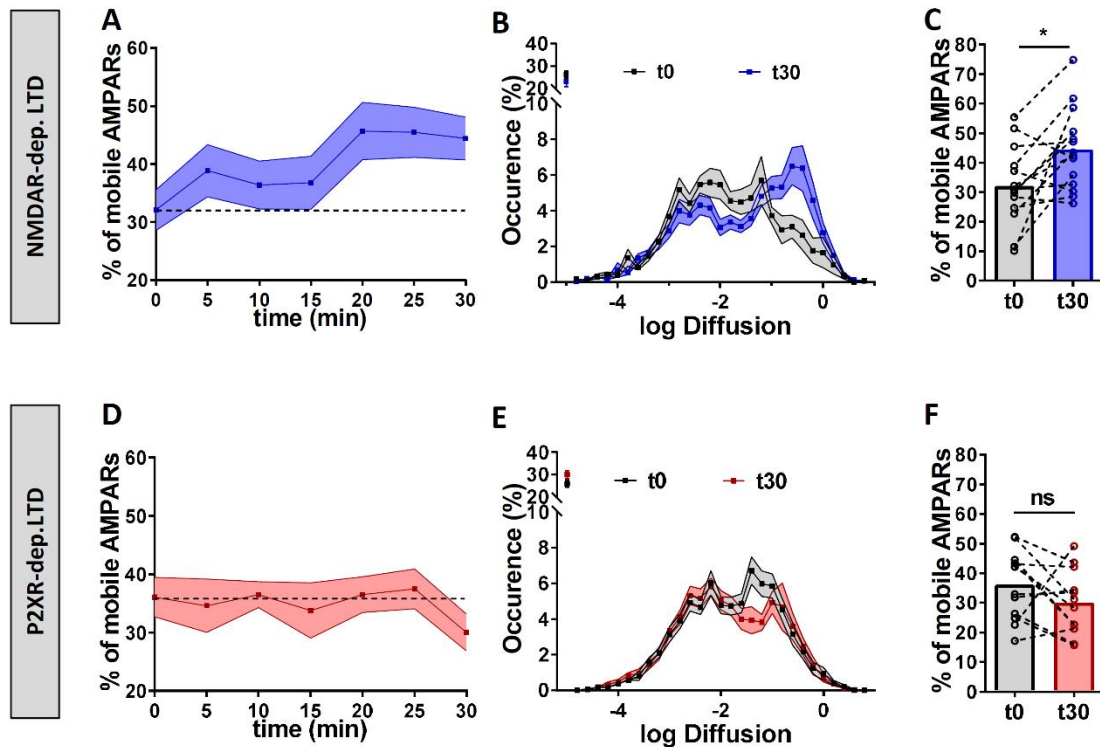
## Supplementary Figure 4



**Supplementary Figure 5. NMDA or ATP do not alter exocytosis of AMPAR 3 hours post application.**

(A) Dendrite of a neuron transfected with SEP-GluA1 and SEP-GluA2 and imaged with TIRF microscopy showing the two types of exocytic events: burst (dark green arrow) and display (light green arrow). (B) Kymograph from the line scan on the two events shown in B in which the display event remains visible for many seconds (light green arrow) and the burst event in which receptors quickly diffuse in the plasma membrane after exocytosis (light green arrow). (D) Fluorescence intensity of the two exocytic events from B, aligned to the time of detection (time 0). Note that fluorescence of burst event (dark green) decays to half of its maximal fluorescence within 2 seconds. (E) Frequency of exocytosis (in events.min<sup>-1</sup>.m<sup>-2</sup>) measured prior to any stimulation (t0) or 3h after application of H<sub>2</sub>O, ATP or NMDA, normalized to t0 of each session to correct for differences in basal activity of neuronal cultures; not normalized numbers are: t0, 0.0242 ± 0.0037, n=29; H<sub>2</sub>O: 0.0370 ± 0.0082, n=14; ATP, 0.0324 ± 0.0060, n=19; NMDA, 0.0257 ± 0.0043, n=17. (F) Average fluorescence intensity at time of detection of 183, 142, 148, 169 exocytic events in 23, 12, 16, 16 cells imaged prior any stimulation (t0), 3h after H<sub>2</sub>O, ATP or NMDA application, respectively. (G) Proportion of display events from the same sample as in F.

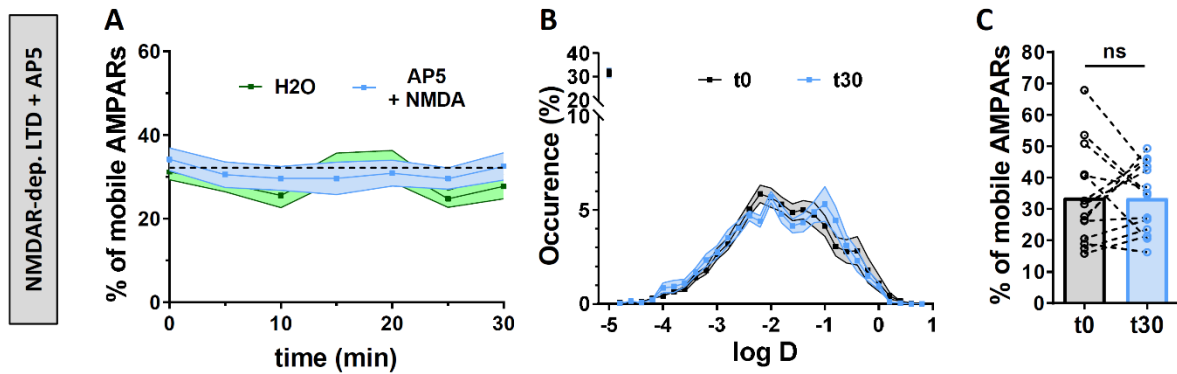
**Supplementary Figure 5**



**Supplementary Figure 6. NMDAR-dependent LTD but not P2XR-dependent LTD is associated to a long-term increase of synaptic AMPAR lateral diffusion.**

(A) Time-lapse (from 0 to 30 minutes) of synaptic GluA2-containing AMPAR mobility following NMDAR-dependent LTD induction protocol (blue line) (mean  $\pm$  SEM,  $n=14$ ). (B) Average distribution of the  $\log(D)$ , ( $D$  being the diffusion coefficient of endogenous AMPAR synaptic trajectories) in control condition (black line,  $n=14$ ) and 30 minutes after NMDA treatment (blue line,  $n=14$ ) (mean  $\pm$  SEM). (C) Average of the mobile fraction at synapses per cell, before and 30 minutes after NMDA treatment ( $n=14$  cells, mean  $\pm$  SEM, paired  $t$ -test,  $p=0.0115$ ). (D) Time-lapse (from 0 to 30 minutes) of synaptic GluA2-containing AMPAR mobility following P2XR-dependent LTD induction (red line) (mean  $\pm$  SEM,  $n=14$ ). (E) Average distribution of the  $\log(D)$  in control condition (black line,  $n=14$ ) and 30 minutes after ATP treatment (red line,  $n=14$ ) (mean  $\pm$  SEM). (F) Average of the mobile fraction at synapses per cell, before and 30 minutes after ATP treatment ( $n=14$  cells, mean  $\pm$  SEM, paired  $t$ -test,  $p=0.1563$ ).

**Supplementary Figure 6**

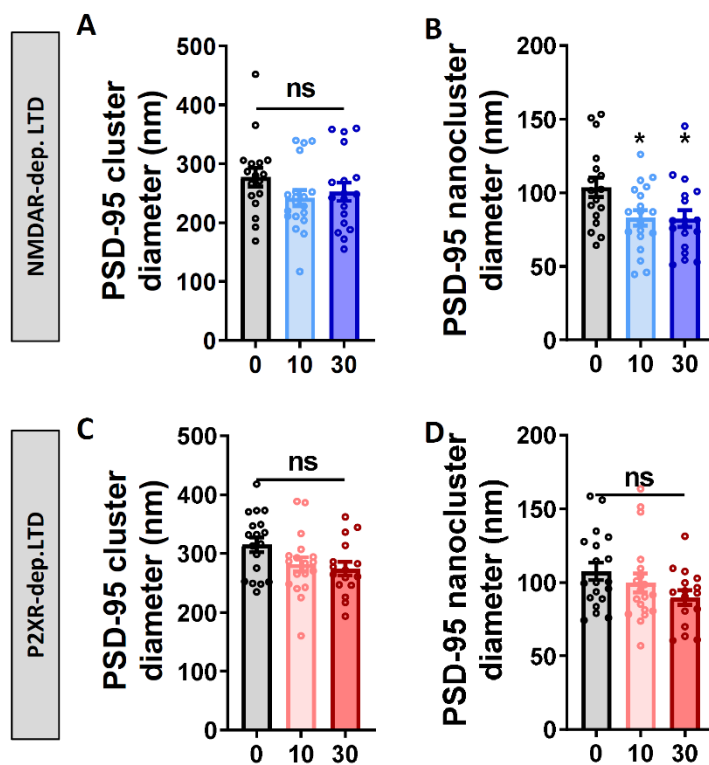


**Supplementary Figure 7. AMPAR increased mobility after NMDA treatment is dependent of NMDAR specific activation.**

(A) Time-lapse (from 0 to 30 minutes) of GluA2-containing AMPAR mobility following NMDAR-dependent LTD induction in the presence of AP5 (a specific NMDAR antagonist, light blue line) compared to vehicle application (green line) ( $n=12$  and  $10$  respectively). No change in GluA2-containing AMPAR mobility occurs after NMDA application in the presence of AP5 ( $50 \mu\text{M}$ ). (B) Average distribution of the  $\log(D)$  in control condition (black line) and 30 minutes after NMDA treatment in presence of AP5 (light blue line). (C) Average of the mobile fraction per cell, before and 30 minutes after NMDA treatment with AP5 ( $n=14$  cells, mean  $\pm$  SEM, paired t-test,  $p=0.9697$ ).

**Supplementary Figure 7**

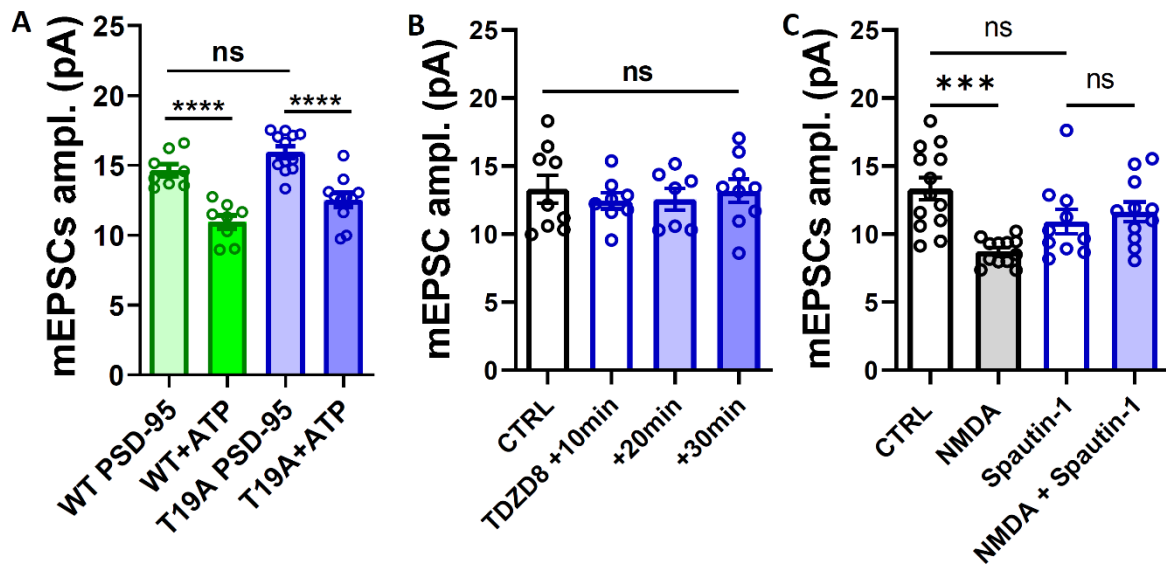




**Supplementary Figure 8. Impact of NMDA or ATP treatment on PSD-95 cluster and nanocluster properties.**

(A and B) Average size of PSD-95 molecules per cluster (A) and per nanoclusters (B) in basal state, 10 and 30 minutes after NMDA treatment (mean +/- SEM, n=17, 19 and 18 respectively, one-way ANOVA p=0.2338 for clusters; one-way ANOVA p=0.0212 and Dunnett's post-test found significant between t0 and t10 and between t0 and t30 conditions, p=0.0297 and p=0.0268 respectively, for nanoclusters). (C and D) Average size of PSD-95 molecules per cluster (C) and per nanoclusters (D) in basal state, 10 and 30 minutes after ATP treatment (mean +/- SEM, n=18, 19 and 16 respectively, one-way ANOVA p=0.0504 for clusters; one-way ANOVA p=0.1165 for nanoclusters).

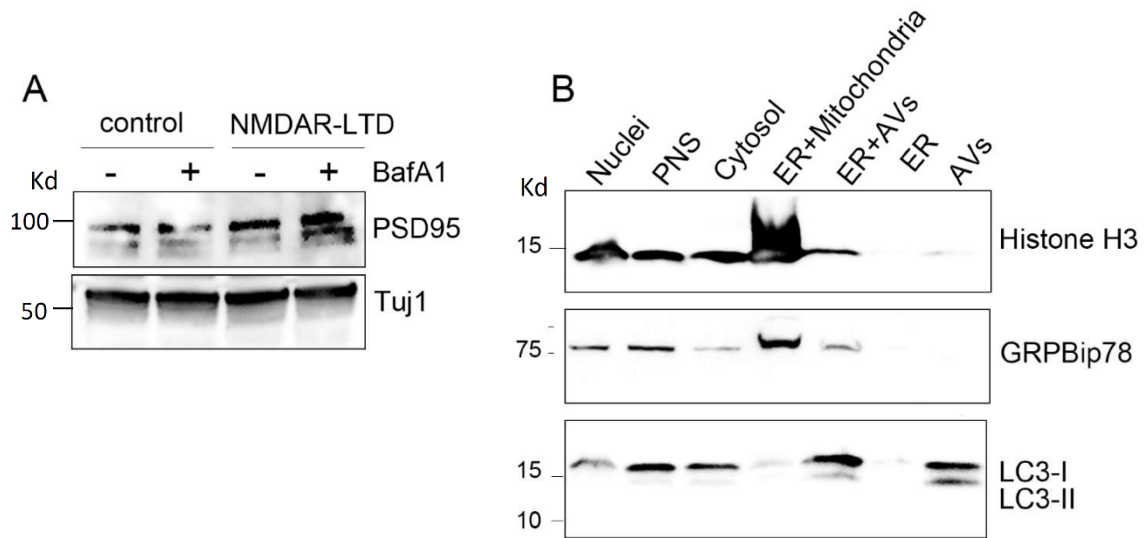
**Supplementary Figure 8**



**Supplementary Figure 9. PSD95 degradation by autophagy is specific of NMDAR-dependent LTD.**

(A) Average of the mEPSC amplitude recorded on neurons expressing WT or T19A mutant PSD-95, 0 and 30 minutes after ATP treatment. Both neuron types present a significant decrease of mEPSC amplitude following LTD induction (mean +/- SEM, one-way ANOVA,  $p < 0.0001$  and Tukey's post-test results are realized between each conditions,  $N=8, 8, 12, 11$ ). (B) Average of the mEPSC amplitude recorded on neurons, 0, 10, 20 and 30 minutes after TDZD8 application. The presence of TDZD8 does not affect mEPSC amplitude (mean +/- SEM, one-way ANOVA,  $p < 0.0001$  and Tukey's post-test results are realized between each conditions,  $N=9, 8, 7, 9$ ). (C) Average of the mEPSC amplitude recorded on neurons, before and after induction of LTD by NMDA application, in the absence or the presence of spautin (an autophagy inhibitor,  $10 \mu\text{M}$ ). The presence of spautin suppresses the LTD induction (mean +/- SEM, one-way ANOVA,  $p < 0.001$  and Tukey's post-test results are realized between each conditions,  $N=13, 12, 10, 11$ ).

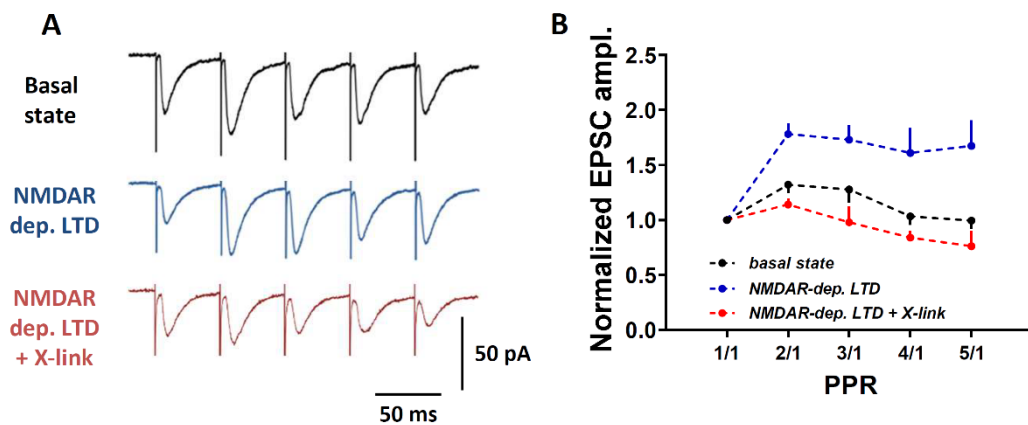
**Supplementary Figure 9**



**Supplementary Figure 10. Validation of the autophagic vesicle purification quality.**

(A) Western blot analysis for PSD95 and the loading control  $\beta$ -III tubulin (Tuj1) in lysates of cultured control neurons or one hour after NMDAR-dependent LTD, in the presence or absence of Bafilomycin A1 (BafA1). BafA1 was applied fifteen minutes before, during the LTD induction and for one hour after it. The same total duration was used for the application of BafA1 in the control neurons. Note the accumulation of PSD95 in the BafA1-treated neurons after LTD induction. (B) Western blot analysis of the fractions collected during the autophagic vesicle purification procedure for an ER marker (GRP97Bip), a nuclear marker (Histone-H3) and an autophagic vesicle marker (LC3B-II). Note the absence of ER and nuclear markers from the final AV purified sample, which is instead enriched for LC3B-II.

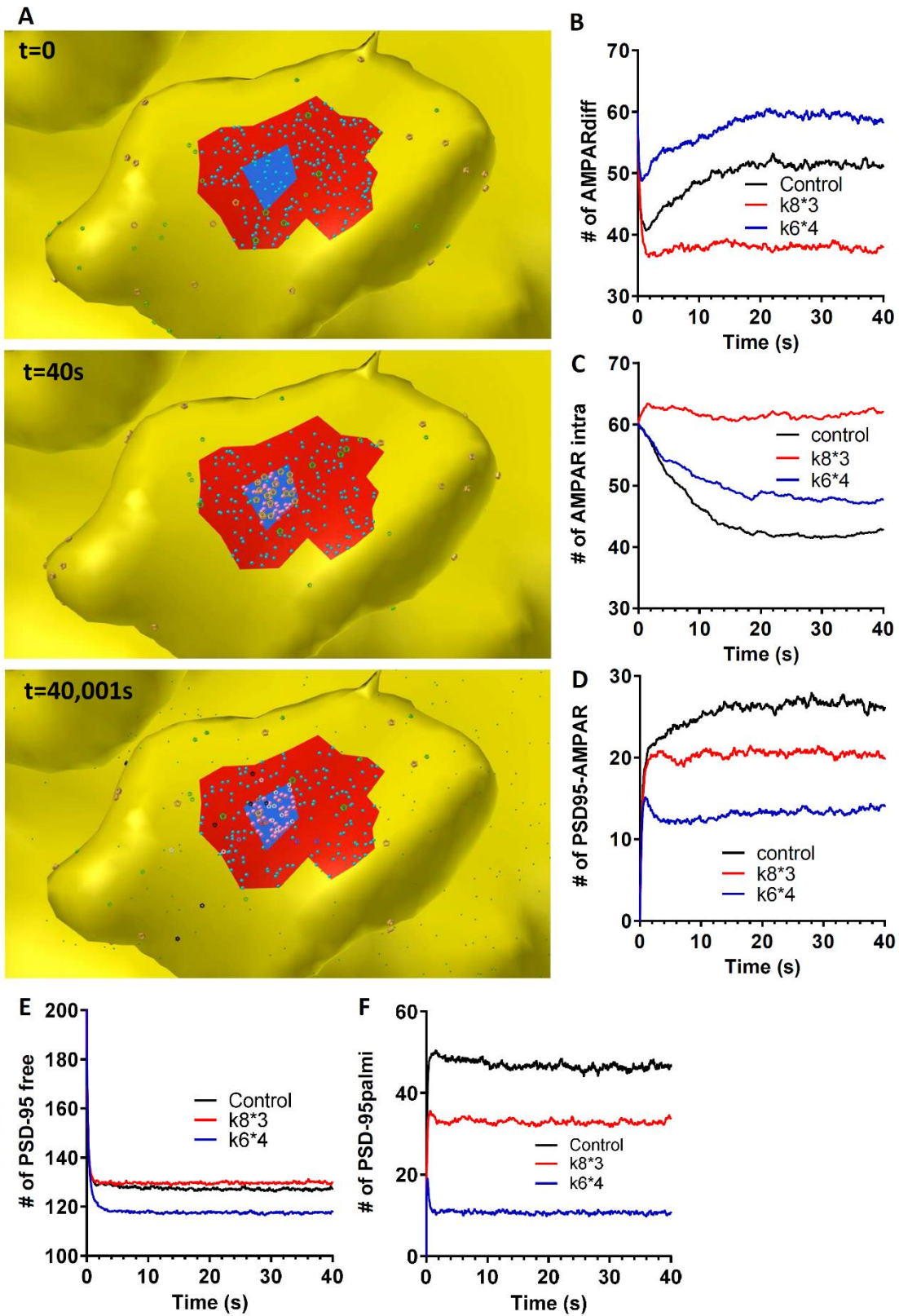
**Supplementary Figure 10**



**Supplementary Figure 11.**

(A) Average of the 5 EPSC amplitudes, normalized by the first response intensity. Paired-pulse stimulation was performed on acute hippocampal slices either untreated (basal state, n=9), or 30 minutes after NMDAR-dependent LTD induction in presence of anti-GFP antibody (control, n=9) or anti-GluA2 antibody (0.3 $\mu$ g/ $\mu$ L, inducing AMPAR cross-link, n=2). Injection of antibodies have been done in the stratum radiatum area of the whole-cell patch neuron 20 minutes after the NMDAR-dependent LTD induction (mean  $\pm$  SEM). As described in Heine et al. 2008 and Constals et al. 2015, GluA2 cross-linking decrease the PPR.

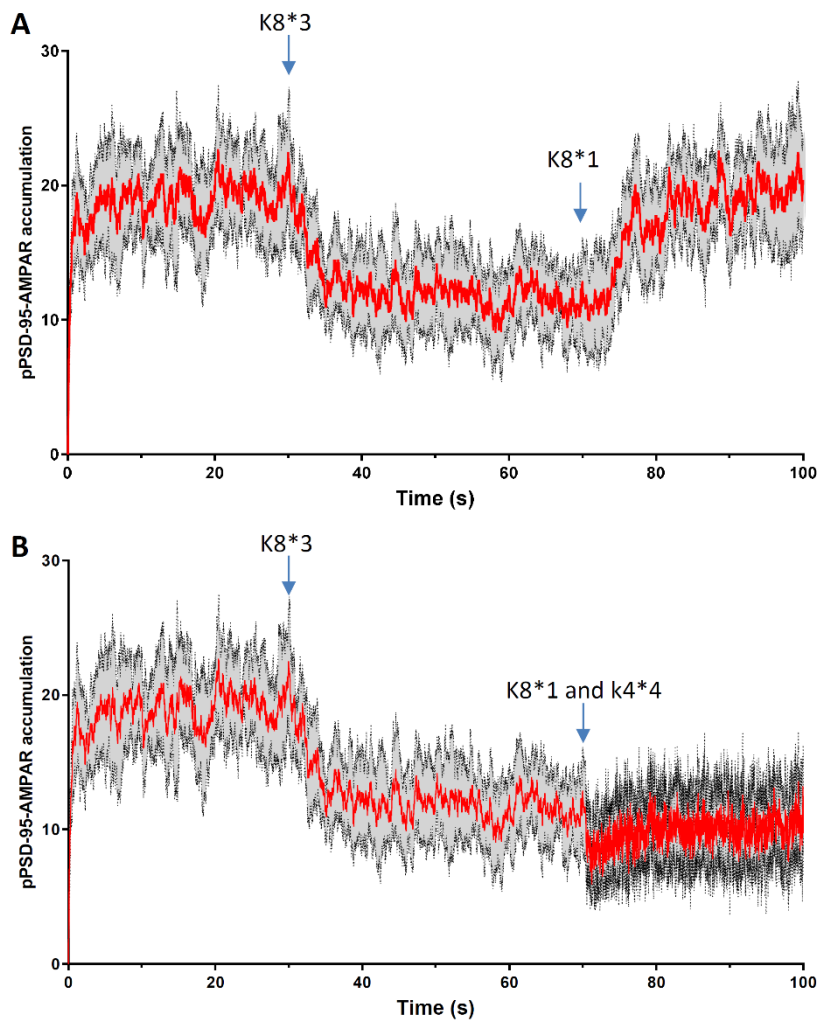
**Supplementary Figure 11**



Supplementary Figure 12

**Supplementary Figure 12. Effect of *in silico* LTD on the equilibrium between various state of both PSD-95 and AMPAR**

(A) Example of images obtained with the model at  $t=0$  (top panel),  $t=40$  s when protein organization reach a stable state (middle panel) and at  $t=40.001$  s, 1 ms after first glutamate release (bottom panel). Icosahedrons represent AMPAR, and colors differ in function of their states: orange for the closed, green for the endocytosed, white for the opened, black for the desensitized, etc. Dots represent PSD-95, blue for the freely diffusive and pink for the palmitoylated. (B-F) Kinetics of accumulation of the various protein species in control or when LTD is mimicked by either an increase of endocytosis (red line,  $k_8 \times 3$ ) or by an inactivation of PSD-95 (blue line,  $k_6 \times 4$ ). We report, the evolution of the number of diffusive AMPAR (B), internalized AMPAR (C), PSD-95 coupled to AMPAR (D), free PSD-95 (E) and palmitoylated PSD-95 (F). The proportion of each species at the equilibrium are closed to the values experimentally obtained.



**Supplementary Figure 13. Simulation shows that LTD-induced increase of endocytosis needs to be maintained or compensate to stabilize depression of AMPAR**

(A) Simulation of AMPAR accumulation in nanodomain. For the first 30 s we observe the recruitment of AMPAR. At 30 s, the endocytosis rate is multiplied by 3 to mimic an LTD. At 70 s the endocytosis rate is returned to its initial value, triggering to a progressive replenishment of the AMPAR nanodomain. (B) Similar simulations are realized but at 70 s, we re-initiate endocytosis rate and in parallel we decreased the affinity of AMPAR for the traps (as shown Figure 6C). We observed a stabilization of the nanodomain depletion, and interestingly, to an increase of the noise due to the more rapid exchange of AMPAR.

**Supplementary Figure 13**

## Chapter 3

### Synaptic pruning following NMDAR-dependent LTD preferentially affects isolated PSD-95-depleted synapses

In the brain, neurons are included into a network where they communicate with partners (Sigoillot et al., 2015). The level of integration in the network can evolve to enable the brain to adapt to new conditions. This can happen by a regulation of synaptic strength, notably through long term synaptic plasticity, but this can also be done by changing the number of connections between a neuron and its partners (Scholl et al., 2021). This is achieved through the phenomenon of structural plasticity that shapes the number of synapses that a neuron makes, which can evolve all along life, from development until adulthood (Holtmaat and Svoboda, 2009). This can lead to the suppression (pruning) or creation of synapses and, as mentioned above, is crucial for the good refinement of brain connectivity. Synaptic pruning has been shown to sustain learning and is necessary for the refinement of cortical networks during development. It is rather noting that structural plasticity mainly occurs in parallel of changes in synaptic strength and that LTD is followed by synaptic pruning (Wiegert and Oertner, 2013). This observation led to two major hypotheses concerning the relation between LTD and pruning. They could be considered as two distinct phenomena being related by some common molecular player, or as the same phenomenon observed at different time-lapse. This lead to very exiting studies such as Colgan and colleagues, where PKC has been investigated to relate input integration to neuronal plasticity (Colgan et al., 2018). The last part of my PhD is in direct line with



this question and aims to understand the interaction LTD-pruning by taking advantage of our molecular knowledge on LTD.

I initiated this project by questioning the requested conditions for LTD to be followed by synaptic pruning. Indeed, it has been already suggested that the level of integration of a synapse could determine the fact that, following NMDAR-dependent LTD, it would be pruned or not (Wiegert and Oertner, 2013). This could explain as well data showing that LTD is not always followed by pruning. Moreover, as showed in the previous paper, LTD is a broad notion, and the different types of LTD do not trigger the same molecular reshuffling. Therefore, it is logical to interrogate which molecular modifications occurring during LTD are necessary for pruning, and which determinants could influence the synaptic selection.

To answer these questions, I combined live and fixed confocal imaging with electrophysiology. We found that unlike P2XR-LTD, NMDAR-LTD is followed by synaptic pruning, and that the removal of PSD-95 from synapses is necessary for synaptic pruning. Then, we reported that specific determinants of synaptic integration determine the fate of synapses following LTD, where proximity of active synapses help less active ones to recover from depression.

This project shows a new side of synaptic selection. Indeed, this model is more “peaceful” than classical view of synaptic selection. The studies of LTP-dependent pruning implied a competition between synapses, where low activity is seen as a punishment signal triggering suppression. Here, we show that LTD-mediated pruning is more collaborative and it is not only the level of activity *per se* that determines the fate of a synapse, but its contribution to coordinated dendritic activity.

Interestingly, *in vivo* data report a constant turnover of synapses at basal state. It still remains unclear whether these prunings are dependent of synaptic plasticities or if they correspond to another mode of spine selection, happening spontaneously in basal conditions. This last point should be further investigated.

This project is the major conclusion of my PhD work. It proposes a new vision of LTD, and suggests a new physiological role of LTD. We hypothesize that LTD enables the selective suppression of weakly integrated synapses, following specific synaptic re-organization at the nanoscale.

# Synaptic pruning following NMDAR-dependent LTD preferentially affects isolated PSD-95-depleted synapses

Camus Côme, Compans Benjamin, Choquet Daniel and Hosy Eric.

## Introduction

The overall number of synapses per neuron is constantly regulated all along life. As for the synaptic strength which is modulated by synaptic plasticity, the structural plasticity shapes the number of synaptic connections. This particular mechanism does not equally affect all synapses, but follow specific rules (Holtmaat and Svoboda, 2009) and seems mainly evolve jointly with synaptic strength (Yang et al., 2009). For example, during the human brain development, activity-dependent synapse elimination reduces synaptic density by about 50% and results in the typical microarchitecture of the mature cortex (Huttenlocher, 1990). Synaptic pruning, defined as a suppression of synapses, occurs subsequently to a period of axonal pruning that takes place during the first months after birth (LaMantia and Rakic, 1990). As a consequence of its implication in development, the dysfunction of synaptic pruning can lead to neurodevelopmental disorders such as Autism Spectrum Disorder (Bourgeron, 2009).

In parallel of the development phase of spine selection, activity-driven changes in neuronal connectivity are essential for experience-dependent remodeling of brain circuitry, as learning. *In vivo* studies have shown that learning is associated with pruning, and that the level of spine loss is directly correlated with improved behavioral performance (Lai et al., 2012; Yang et al., 2009). However as both synaptic and structural plasticities are intermingled mechanisms, it is difficult to determine their specific role during learning and memory (Nishiyama and Yasuda, 2015). Indeed, loss of dendritic spines is driven by glutamatergic signaling mechanisms responsible of synaptic weakening through induction of long-term depression (LTD), even if it happens hours to days after LTD induction (Wiegert and Oertner, 2013).

Physiologically, LTD is a generic term based on electrophysiological recording, which reflects a global decrease of the synaptic response when multiple pre-synaptic neurons are activated. This plasticity can be induced through different stimulation pathways, including for example the classical glutamate-induced LTD through the activation of NMDAR or mGluR (Dudek and Bear, 1992; Oliet et al., 1997), or the activation of secondary pathway as insulin application (Huang et al., 2003), or activation of ATP-gated P2X receptors (Cavaccini et al., 2020; Pougnet et al., 2016, 2014). Each of these forms results from a specific physiological stimulus such as low frequency stimulation, which mainly involves NMDAR (Dudek and Bear, 1992), or the release of ATP by astrocytes following noradrenergic stimulation (Pougnet et al., 2014).

Previous works found that induction of NMDAR-dependent LTD is followed by a synaptic pruning happening hours to days after induction (Thomazeau et al., 2020; Wiegert and Oertner, 2013; Wiegert et al., 2018). However, it remains unknown

whether these two phenomena are two sides of the same re-organization or whether they only share some common signaling pathways (Nishiyama and Yasuda, 2015; Piochon et al., 2016). It is also rather noting that induction of LTD doesn't trigger necessarily suppression of all synapses but that "failure" in the sequence LTD-pruning occurs frequently (Wiegert et al., 2018). Other works indicated as well that the initial state of synapse, in term of activity, size and integration into the network, influences its fate (Oh et al., 2013; Wiegert and Oertner, 2013; Wiegert et al., 2018). However, the precise conditions necessary for LTD to trigger synaptic pruning remain far from being elucidated. In parallel, it is impossible for now to determine if LTD is necessary for synaptic pruning, for example, does the constant turnover of synapses (Holtmaat et al., 2006) is always initiated by a long term depression or can it be induced independently of synaptic plasticity.

In the present work, we aimed to understand which elements are necessary to trigger the sequence NMDAR-dependent LTD to synaptic pruning. By combining live and fixed sample confocal imaging with electrophysiology recordings, we first observed that following NMDAR activation, all molecular reshufflings occurring during LTD induction have to be maintained to trigger pruning. Then, we identified various characteristics drawing the portrait-robot of a synapse that will be pruned following NMDAR-dependent LTD. We observed that suppressed synapses presented low to moderate activity. It appears that the other parameters are the presence and the properties of neighboring synapses. If the synapse has few or far neighbors or/ and if these neighbors are weakly active, the pruning is favored. Interestingly, the presence of multiple pre-synaptic boutons from the same axon on a dendrite tend to protect synapses from pruning. These experiments are in favor that after LTD induction, neighboring synapses tend to protect each other from pruning by their activities.

## Results

### **NMDAR activation but not P2XR induces synaptic pruning**

LTD has previously been widely related to synaptic pruning following hours to days (Oh et al., 2013; Wiegert and Oertner, 2013; Wiegert et al., 2018). However, it remains unclear whether it is the subsequent decrease of post-synaptic currents by itself or the activation of a specific molecular pathway that induces pruning.

To investigate if chem-LTD triggers a pruning, independently of the molecular pathway being activated, we treated hippocampal neuronal cultures with two different chemical induction protocols characterized previously (Compans et al., 2021). LTD induced by the application of the NMDAR agonist NMDA (30  $\mu$ M for 3 minutes), or the P2XR agonist ATP (100  $\mu$ M for 1 minute) triggers a similar decrease (about 25%) of miniature EPSC amplitude and similar decrease of AMPAR content per synapse and per nanodomain. However, NMDAR and P2XR-dependent LTD have been shown previously to induce different molecular pathways and to present additive effects (Pougnnet et al., 2014, 2016, Compans et al., 2021).

Electrophysiological recordings showed, as previously described, that both treatments induced a similar decrease of mEPSCs after 30 minutes (mean amplitude  $\pm$  SEM, 11.88  $\pm$  0.57 vs 8.4  $\pm$  0.4 following NMDA treatment and 9.23  $\pm$  0.52 following ATP

treatment; fig.1A-C), confirming the induction of synaptic depression in our experimental conditions. We then assessed the presence of synaptic pruning at 30 minutes and 3 hours after LTD induction by realizing an immunostaining against the post-synaptic protein PSD95 to reveal the position of post-synaptic densities (fig.1D). Then, using confocal imaging, we found that only NMDA application induced a decrease of PSD95 puncta after 3 hours, but not at 30 minutes (mean PSD-95 puncta density +/- SEM, for ATP treatment: 0.9136 +/- 0.022 at t0, 0.9211 +/- 0.022 at t30, 0.9367 +/- 0.02 at t180; for NMDA treatment: 0.8806 +/- 0.026 at t0, 0.8626 +/- 0.016 at t30, 0.6021 +/- 0.015 at t180; fig.1E-F). This indicates that the specific activation of NMDAR is required to induce synaptic pruning, rather than the only decrease of synaptic currents.

### **Synaptic pruning requires PSD-95 removal from synapses**

Activation of NMDAR lead to the activation of a wide range of signaling pathways (Dudek and Bear, 1992; Traynelis et al., 2010). Amongst them, we described previously that during NMDAR-dependent LTD, PSD-95 is phosphorylated at T19 position by GSK3beta, targeting PSD95 to autophagosomes. This removal of PSD95 facilitates the mobilization of AMPAR out of nanodomains, leading to a measurable decrease of synaptic currents. Thus, we next investigated if the pruning observed following NMDA application was related to the activation of NMDAR only, or if molecular reshufflings induced afterward were necessary (Compans et al., 2021).

We first studied whether NMDAR activation is sufficient to induce synaptic pruning. We and others have previously shown that T19A mutation of PSD-95 is able to block induction of NMDAR-dependent LTD by suppressing the phosphorylation site by the GSK3beta (Compans et al., 2021; Nelson et al., 2013). We found that the expression of the T19A mutated form of PSD95 suppressed the decrease of PSD-95 puncta observed in control 3 hours after NMDA application, indicating the absence of pruning. This result indicates that even though NMDAR were activated this was insufficient to trigger a suppression of synapses, if a proper LTD is not set up.

Thus, we next wondered if a transient expression of LTD (with complete re-organization of the synapse) was sufficient to induce a pruning 3 hours after NMDA application. We reported previously that the presence of inhibitor of either the GSK3beta activity by applying TDZD8 (10µM) or the formation of autophagosomes by applying SBI-0206965 (0.5µM), during and after LTD induction, results in a full blockade of late-phase of LTD that is dependent of PSD-95 removal from synapses. Here we first induced a classical chemical LTD by NMDA treatment, and let the full LTD to set for 30 minutes. Then, we applied for 2.5 hours the inhibitors TDZD8 or SBI-0206965. We found that application of these drugs suppressed the decrease in PSD-95 puncta density and so the synaptic pruning (normalized mean of PSD-95 puncta density +/- SEM, for NMDA + TDZD8: 1.186 +/- 0.06 vs NMDA alone: 0.7179 +/- 0.027; for NMDA + SBI: 1.031 +/- 0.045 vs NMDA alone: 0.7492 +/- 0.022).

Taken together, these results indicate that the solely induction of LTD is not enough to induce the spine selection mechanism, the LTD pathway need to be maintained active until the end of the pruning mechanism.

### **Increase in synaptic activity suppresses pruning**

After LTD induction all synapses does not disappear even if the vast majority presents a depression of their AMPAR currents which is stable for more than 3 hours. This reveals that all synapses in a LTD state does not behave similarly. Previous studies reported a direct relationship between the level of synaptic activity and lifespan of synapses (Oh et al., 2013; Wiegert and Oertner, 2013; Wiegert et al., 2018).

To investigate the effect of the neuronal activity on the LTD-induced spine selection, we increased, 30 minutes after LTD induction with NMDA, the neuronal activity by inhibiting the inhibitory neurons by applying the GABA<sub>A</sub> inhibitor Gabazine (2  $\mu$ M) or by increasing the glutamate release probability by increasing the calcium concentration to 4 mM in the culture dish. The neurons are incubated in these medium for 2.5 hours and then synapse density is measured. Both conditions resulted in a complete suppression of the decrease in PSD95 puncta density 3 hours after NMDA application (normalized mean of PSD-95 puncta density  $\pm$  SEM, for NMDA: 0.7159  $\pm$  0.021, for NMDA + Gabazine: 0.9473  $\pm$  0.024, for NMDA + 4 mM calcium: 1.016  $\pm$  0.057) (fig.3A-B). This seems to indicate that a high synaptic activity is able to counteract the LTD-dependent synaptic pruning pathway.

### **Network activity is weakly affected by LTD-dependent synaptic pruning**

In a network and without external stimulation, neuronal activity presents various electrical responses, (i) the miniature currents which correspond to a single synapse response, (ii) the coordinated poly-synaptic response, where multiple synapses from the same axon release together, and (iii) the sequential poly-synaptic response, when the network burst, the recorded neuron receives multiple stimulus from various axons all along the burst duration (see suppl. fig. 4.1). It has been previously suggested that weakly integrated synapses are pruned following LTD (Wiegert and Oertner, 2013). This conclusion would imply that there is not a linear effect between the amount of pruning (around 40% of spine disappearance 3 hours after NMDA treatment) and the number of inputs received by the neuron because pruned synapses are not the active ones.

To investigate this question, we measured spontaneous EPSCs in control conditions and 3 hours after NMDA application (fig.4A), with three calcium concentrations in the extracellular medium to vary release probability (0.2, 2 and 4 mM). At 2 and 4 mM of extracellular calcium in the recording chamber, we were able to identify two different populations of EPSCs (fig.4B and 4E). The first population, with a  $\log(\text{area}/\text{duration}) < 1.5$ , correspond to single synapse responses, as revealed when comparing their area with the miniature currents (in presence of TTX, dashed line figure 4B). This population, which represents the only current type observed at 0.2 mM of calcium, present a shift toward small areas after NMDA treatment, corresponding to the decrease of AMPAR content induced by LTD. This area goes from (mean  $\log(\text{area}/\text{duration}) \pm$  SEM, see supp. Fig.4.1), 0.9249  $\pm$  0.009 to 0.8271  $\pm$  0.008, 3 hours after LTD induction, meaning a decrease of 10.6 % as expected.

The second population of synaptic response with a  $\log(\text{area}/\text{duration}) > 1.5$  corresponds to polysynaptic responses. We see that after LTD, neither their frequency nor their

average intensity is affected, this seems indicate that LTD-dependent pruning, which suppress 40% of total synapses, affects mainly synapses that do not contribute to responses implicated in the network activity.

### **Isolated synapses are preferentially pruned**

If low integrated synapses are preferentially pruned, they should share some predictive characteristics related to activity that determines their behavior in response to LTD. To first test the implication of initial activity of synapses, we measured the uptake of synaptotagmin-1. Synaptotagmin-1 is a vesicular transmembrane protein, which get a transient access to the pre-synaptic membrane when the vesicle fusion before to be recycled into new vesicle. Living neurons are incubated with an anti-synaptotagmin-1 antibody coupled to a pH-sensitive fluorescent probe (CypHer 5E) for 30 minutes, the antibody will be loaded inside the pre-synapse proportionally to the number of glutamate releases. Using live imaging we were able to determine the initial level of activity of a synapse (Schneider et al., 2015) and to compare it with its fate (pruned or maintained) 3 hours later (fig.5A). Briefly, LTD is induced by NMDA treatment and neurons were putted back for 30 minutes into culture medium to allow the full LTD to set. Then pre-synapses are loaded with synaptotagmin fluorescent antibody for 30 minutes, and an image of post-synapse (GFP) and Synaptotagmin labeling (CypHer) is taken. Two hours later, another GFP image is taken to determine which synapse has been pruned. Finally we quantified the synaptic fate 3 hours after LTD induction regarding the measured pre-synaptic activity. When the intensity of synaptotagmin labelling is compared to the maintained and pruned synapses, we found similar median intensity (12,168 for maintained synapses and 11,609 for pruned synapses). However, the maintained synapses presented a population of high activity, which was absent for the pruned synapses (fig.5B). This indicate that except for highly active synapses, the level of pre-synapse activity is not a determinant parameter to explain the suppression or the maintenance of a spine following LTD.

Then we determined the distance between the pruned or maintained synapses regarding their closest neighbors (fig.5C-E). It clearly appears that pruned synapses present a broader distribution of neighbor distance than the maintained ones (Fig 5D). 89% of maintained synapses have a neighbor closer than 4  $\mu\text{m}$ , while it represents only 46 % of pruned synapses. These results go in favor of a protection by the neighboring synapses following a LTD, which seems a different mechanism that the observed one after LTP (Oh et al., 2015).

To determine if the activity of the neighboring synapses was important for the protection to pruning, we represented the activity level of neighboring synapse and their impact on the synaptic fate (fig.5F). For pruned and maintained synapses presenting a similar level of activity, the activity of neighboring synapses plays a crucial role for synaptic fate. Synapses surrounding maintained synapses presented a 30% higher level of activity than the ones around the pruned spines (mean +/- SEM, for maintained synapses: 15,633 +/- 264.8; for pruned synapses: 12,213 +/- 402). This reinforced the notion of protection to pruning by the neighboring synapses. To avoid pruning, the proper synapse activity is not essential if it is surrounded by active and closed neighboring synapses.

To complete the description of the synaptic environment which determines spine maintenance or suppression, we counted the number of neighbors within the 20  $\mu\text{m}$

around the pruned or maintain synapses (fig. 5G). The pruned synapses were found to be more isolated than the maintained synapses. 63% of pruned spines were surrounded by only one synapse, 29% by two and 8 % by three spines, whereas the maintained ones were comprised in groups with two (37%) or three (63%) other synapses, and none with only one spine (fig.5G).

All these results indicate that synapses tend to protect each other from pruning by both being close and active.

Finally, we determined if for a synapse, to belong to a cluster of spines receiving inputs from the same axon improves the protection to pruning (fig.5I). In order to study the number of synapses that axons were making with dendrites, we estimated based on synaptotagmin-1 labeling, the number of pre-synaptic bouton per axon on a dedicated dendrite. We identified cases where a unique (single) synapse is connected to the dendrite, or some multiple "en passant" synapses that were made all along the dendrite. We found that 60 % of pruned synapses were single-made synapses, whereas the maintained ones were at 81 % multiple-made synapses (fig.5H). This resulted in the fact that after pruning, the fraction of single-made synapses decreased from 32 to 20% (fig.5I).

Taken together, these results demonstrate the protection role of neighboring synapses following a NMDA-dependent LTD induction. After LTD, the mid-low activity synapses surrounded by low activity synapses, and constituting the single synapse of a dedicated axon are the most susceptible synapses to be pruned.

### **AMPA and L-type calcium channels activation is related to the maintenance of synapses**

After the determination of the structural organization which drives the LTD-dependent synapse selection, we questioned the molecular mechanism responsible of this protection / suppression of the spine. So, we assessed pruning efficiency 3 hours after LTD induction, by blocking various ion channels responsible of synapse depolarization or calcium entry (fig.6A). The protocol consisted to first induce a complete LTD by NMDA treatment and incubation following the treatment, and then we apply after 30 minutes inhibitors of AMPAR receptors (NBQX (10 $\mu$ M); Fig 6B), or specifically calcium permeable AMPAR (IEM 1460 (100 $\mu$ M); Fig 6C), or L-type voltage dependent calcium channel (Amlodipine (5 $\mu$ M); Fig 6D) and NMDAR (D-AP5 (50 $\mu$ M); Fig 6E).

Application of the AMPAR antagonist, 30 minutes after NMDA, reduced the decrease of PSD95 puncta density at 3 hours (fig.6B). At the opposite, application of the Ca<sup>2+</sup>-permeable AMPAR antagonist or NMDAR antagonist did not counteract the pruning mechanism (fig.6C and 6E). This indicates that the entry of calcium which is probably responsible of the synapse protection from pruning, is not mediated by NMDAR or AMPAR themselves. The application of the L-type voltage-dependent calcium channel inhibitor 30 minutes after NMDA significantly increased the intensity of the pruning (mean density of PSD95 puncta +/- SEM, for NMDA alone: 0.749 +/- 0.004; for NMDA + amlodipine: 0.602 +/- 0.03) (fig.6D). Taken together, these results indicate that the maintenance signal, which counteract the LTD-dependent synaptic pruning, is mediated by the AMPAR-induced depolarization, leading to the activation of L-type calcium channels that enables the entry of calcium.



## Figures

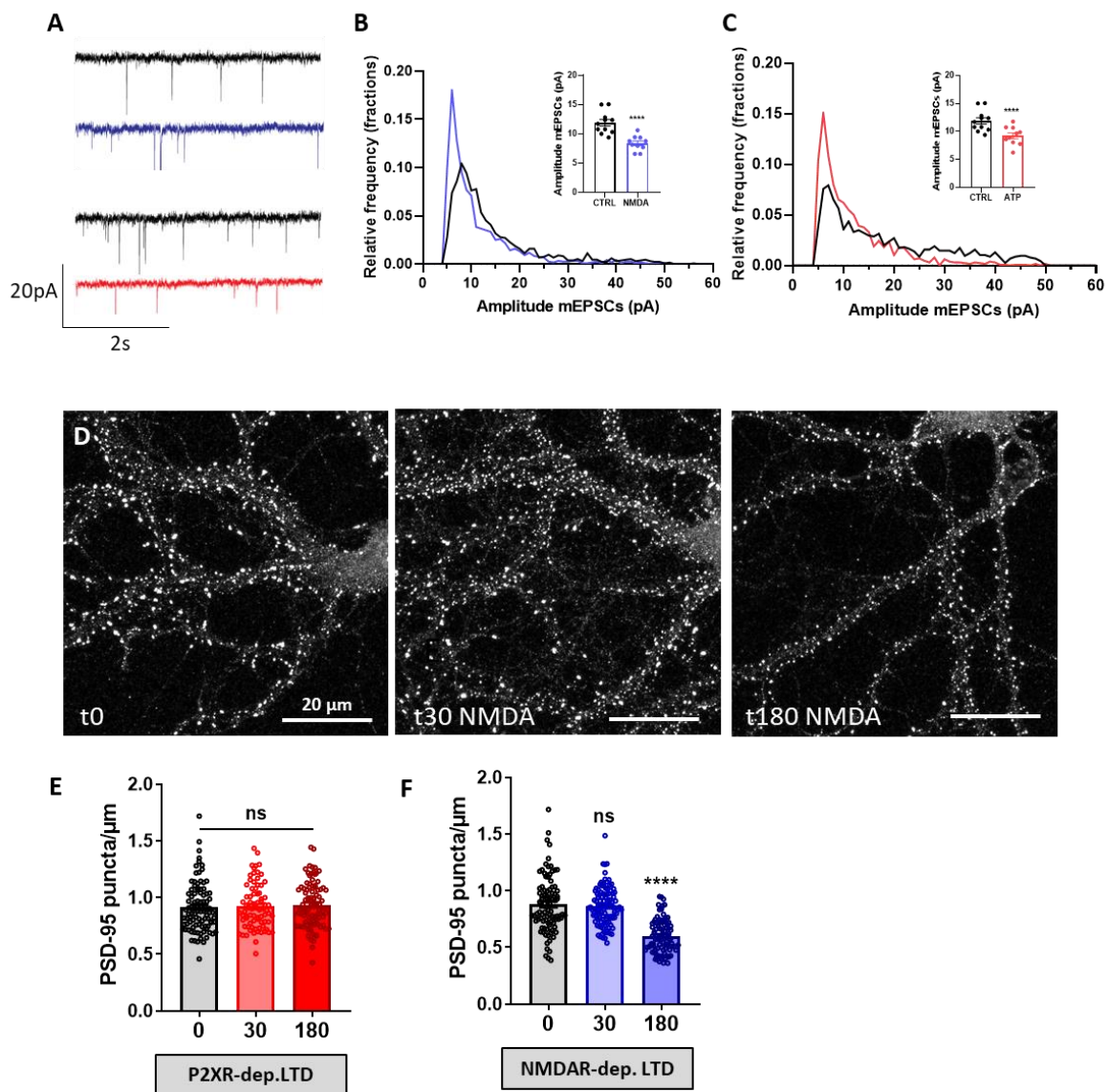


**Figure 1: NMDAR-dependent but not ATP-dependent LTD induces synaptic pruning.** A: example traces of mEPSCs recordings. Control in black, NMDA + 30 min in blue and ATP + 30 min in red. B and C: left, frequency distribution of mEPSCs amplitude corresponding to A. Right: median of mEPSCs amplitudes, one dot representing a median of a cell. (B: mean  $\pm$  SEM, t-test,  $p = 0.0001$ , C: mean  $\pm$  SEM, t-test,  $p < 0.0001$ ). D: example of confocal images after immunostaining of PSD-95. Left: control, middle: NMDA + 30 min, right: NMDA + 3 hours. E and F: quantification of PSD-95 puncta density obtained from D. Black: control, red: ATP + 30 or 180 minutes, blue: NMDA + 30 or 180 minutes. Mean  $\pm$  SEM, one dot represents one portion of dendrite (E: one-way ANOVA, F: one-way ANOVA, at +180 min Dunnett's multiple comparisons test gives  $p < 0.0001$ ).

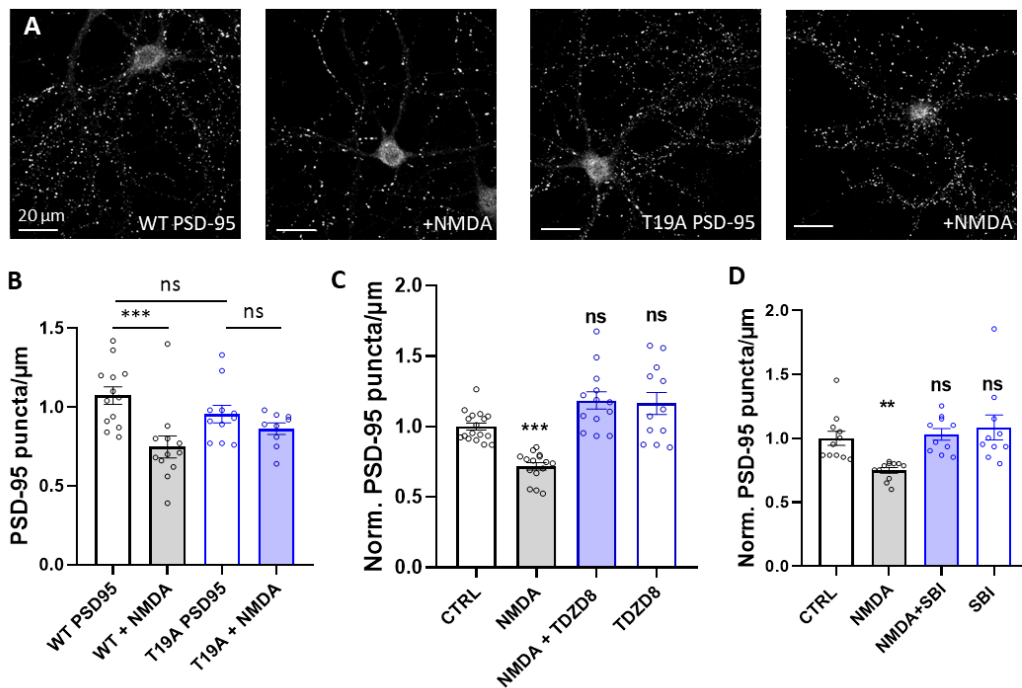


**Figure 2 : PSD-95 synaptic depletion is required for pruning.** A: example of confocal images after PSD-95 immunostaining. From left to right: WT PSD-95 overexpression, WT PSD-95 overexpression and NMDA + 3 hours, T19A PSD-95 overexpression, T19A overexpression and NMDA + 3 hours. B, C and D: quantification of PSD-95 puncta density 3 hours after beginning of treatments, one dot represents the mean of a cell. B: from left to right: WT PSD-95 overexpression, WT PSD-95 overexpression and NMDA + 3 hours, T19A PSD-95 overexpression, T19A overexpression and NMDA + 3 hours. Mean +/- SEM, one-way ANOVA, for WT + NMDA, Dunnett's multiple comparisons test gives  $p=0.0008$ . C: from left to right: control, NMDA, NMDA + TDZD8 30 minutes later, TDZD8. Normalized data to control, mean +/- SEM, for NMDA Turkey's multiple comparisons test gives  $p=0.0001$ . D: from left to right: control, NMDA, NMDA and SBI-0206965 30 minutes later, SBI-0206965. Mean +/- SEM, one-way ANOVA, for NMDA, Dunnett's multiple comparisons test gives  $p=0.01$ .)

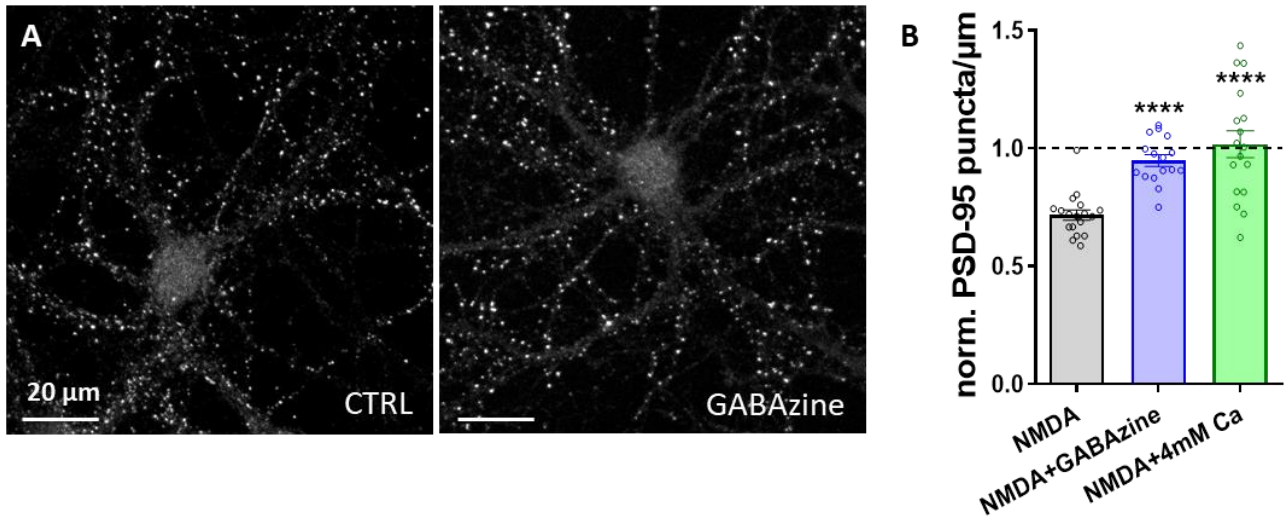


**Figure 3 : Increase in activity level suppresses pruning.** A: example of confocal images after PSD-95 immunostaining, left: control, right: NMDA and GABAazine + 3 hours. B: quantification of PSD-95 puncta density, normalized data to control, grey: NMDA+ 3h, blue: NMDA + GABAazine + 3h, green: NMDA+ 3h in 4mM Ca<sup>2+</sup> condition. Each dot represents the mean of a cell, mean  $\pm$  SEM, one-way ANOVA, for comparison between NMDA and GABAazine or 4mM Ca<sup>2+</sup>, Dunnett's multiple comparisons test gives  $p < 0.0001$ .

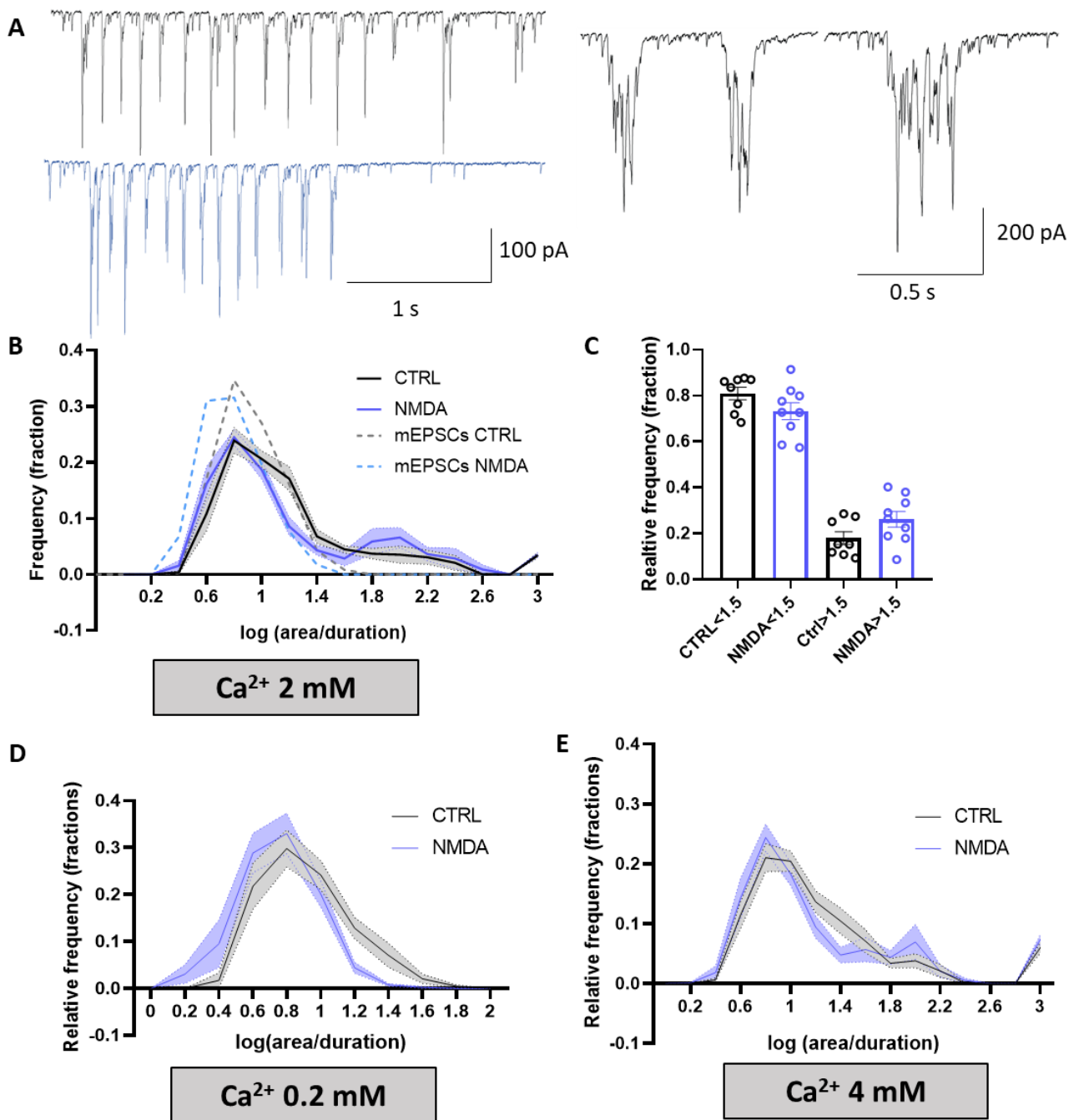
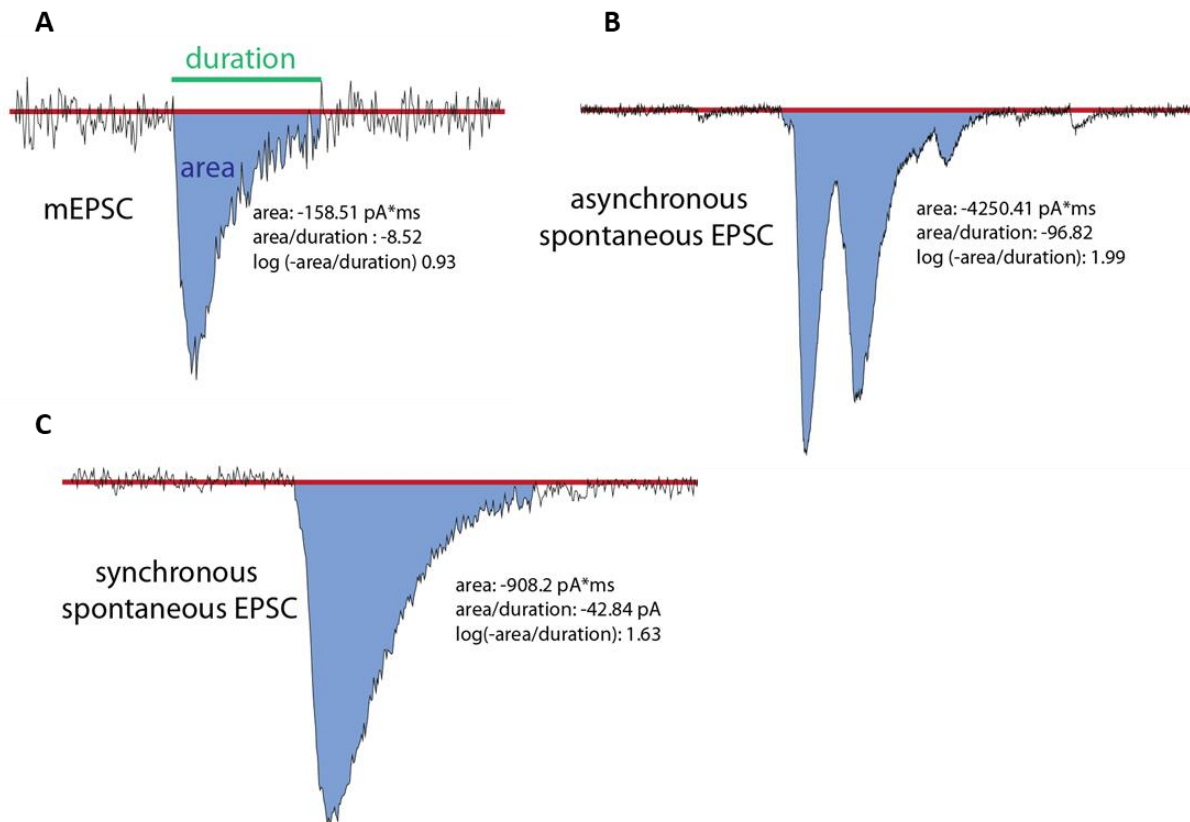


**Figure 4 : Pruning does not affect poly-synaptic responses.** A. Example traces of spontaneous EPSCs recordings. Left: control in black, NMDA +3h in blue. Right: zoomed trace showing from left to right: two poly-synaptic EPSCs and one action potential. B. Frequency distribution of  $\log(\text{area}/\text{duration})$  of spontaneous EPSCs recorded with extracellular  $\text{Ca}^{2+}$  at 2mM. Mean  $\pm$  SEM. C. Fractions from B were cumulated and separated with a threshold to distinguish <1.5 mEPSCs and >1.5 macroscopic EPSCs. No difference was found. D and E. Frequency distribution of  $\log(\text{area}/\text{duration})$  of spontaneous EPSCs recorded with extracellular  $\text{Ca}^{2+}$  at 0.2mM (D) or 4mM (E). Mean  $\pm$  SEM



**Supplementary figure 4.1: example traces of the different types of recorded EPSCs.** A. Example trace of a mEPSC. The area used for analysis correspond to the blue part, and is determined as the surface between the baseline (in red) and the line of current of the event. The duration (green line) is the length of the mEPSC. B: example trace of an asynchronous spontaneous EPSC, and C: example trace of a synchronous spontaneous EPSC. Data on the right of each trace correspond to the extracted parameters of the shown event.

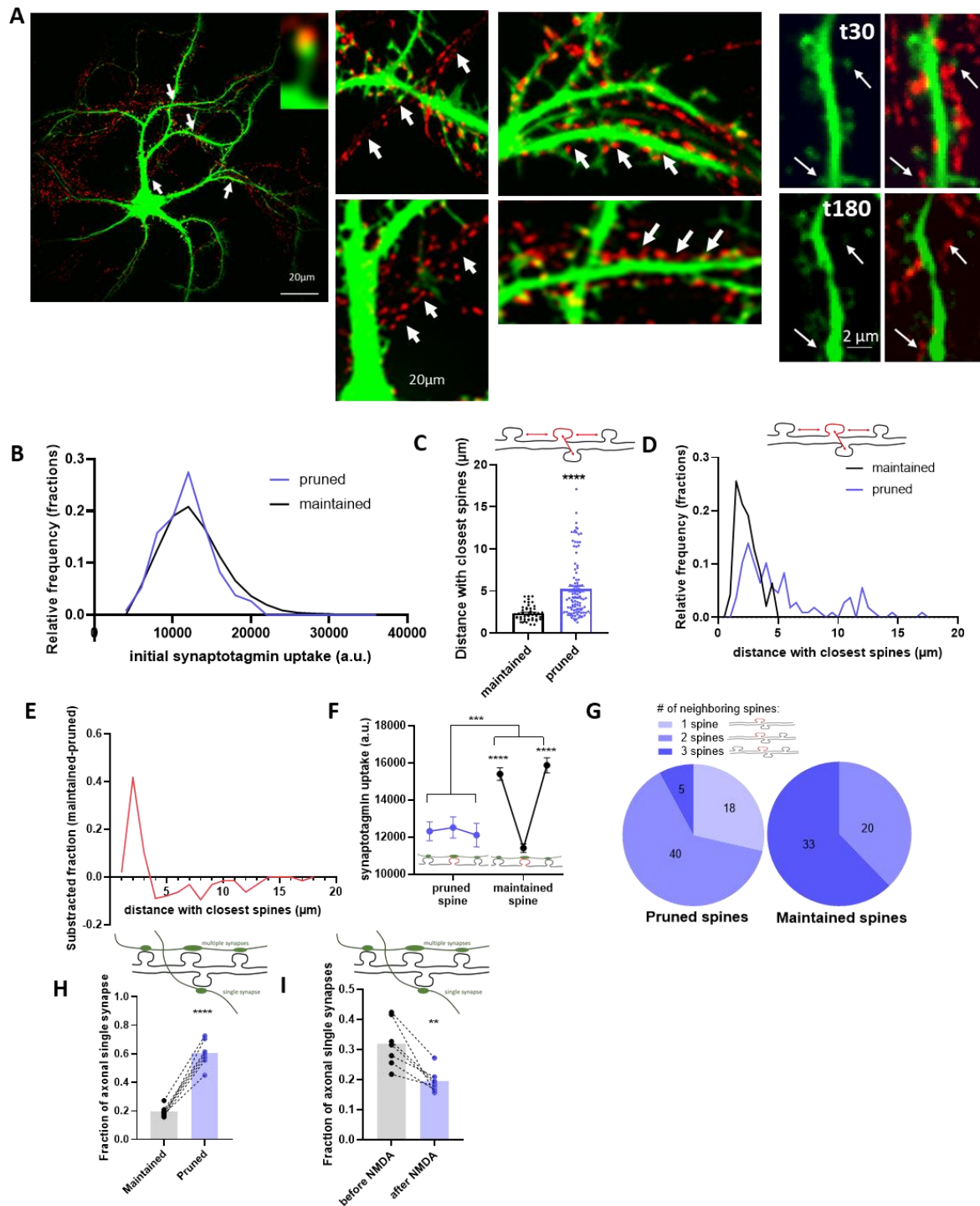


**Figure 5: Proximity of active synapses protects from pruning** A. Example images of synaptotagmin-1 uptake measurements. Left: arrows indicate portions of dendrites zoomed in on the middle and right panels. Middle: arrows indicate axons making single synapses (right) or multiple synapses (left). Right: images of the same portion of dendrite, on left for EGFP signal alone and right merged with anti-synaptotagmin signal. Arrows indicate synapses pruned at 3 hours (bottom). B. Frequency distribution of initial synaptotagmin uptake for maintained spines at 3h (black) and pruned spines at 3h (blue). C. Distance between the spine of interest and

the closest spines, for maintained spines at 3h (black) and pruned spines (blue). Maintained spines were selected to present similar level of activity than the pruned ones (mean spines +/- 2000 au). Mean +/- SEM, t-test gives  $p < 0.0001$ . D. Frequency distribution of the distance between the spine of interest and the closest spines, for maintained spines at 3h (black) and pruned spines (blue). E. Curves obtained in D were subtracted: data of maintained spines-pruned spines. F. Comparison of synaptotagmin uptake of neighboring spines (at less than  $5\mu\text{m}$  of the central spine) for maintained (black) or pruned spines at 3h. The spine of interest is at the center of the triplet, and on left and right are the neighbors. Mean +/- SEM, Turkey's multiple comparisons test gives  $p < 0.0001$  for neighbors of pruned spines, and  $p = 0.0004$  for comparison between neighbors of pruned and maintained spines. G. Count of the number of spines in the vicinity of spines, constituting clusters of spines. H and I., H: Comparison of fraction of single synapses made by an axon for maintained and pruned ones. Dashed lines connect groups of spines from the same neuron, t-test gives  $p < 0.0001$ . I: fraction of single-synapses by neuron before and 3 hours after NMDA treatment. Paired experiments, paired t-test gives  $p = 0.0036$ .

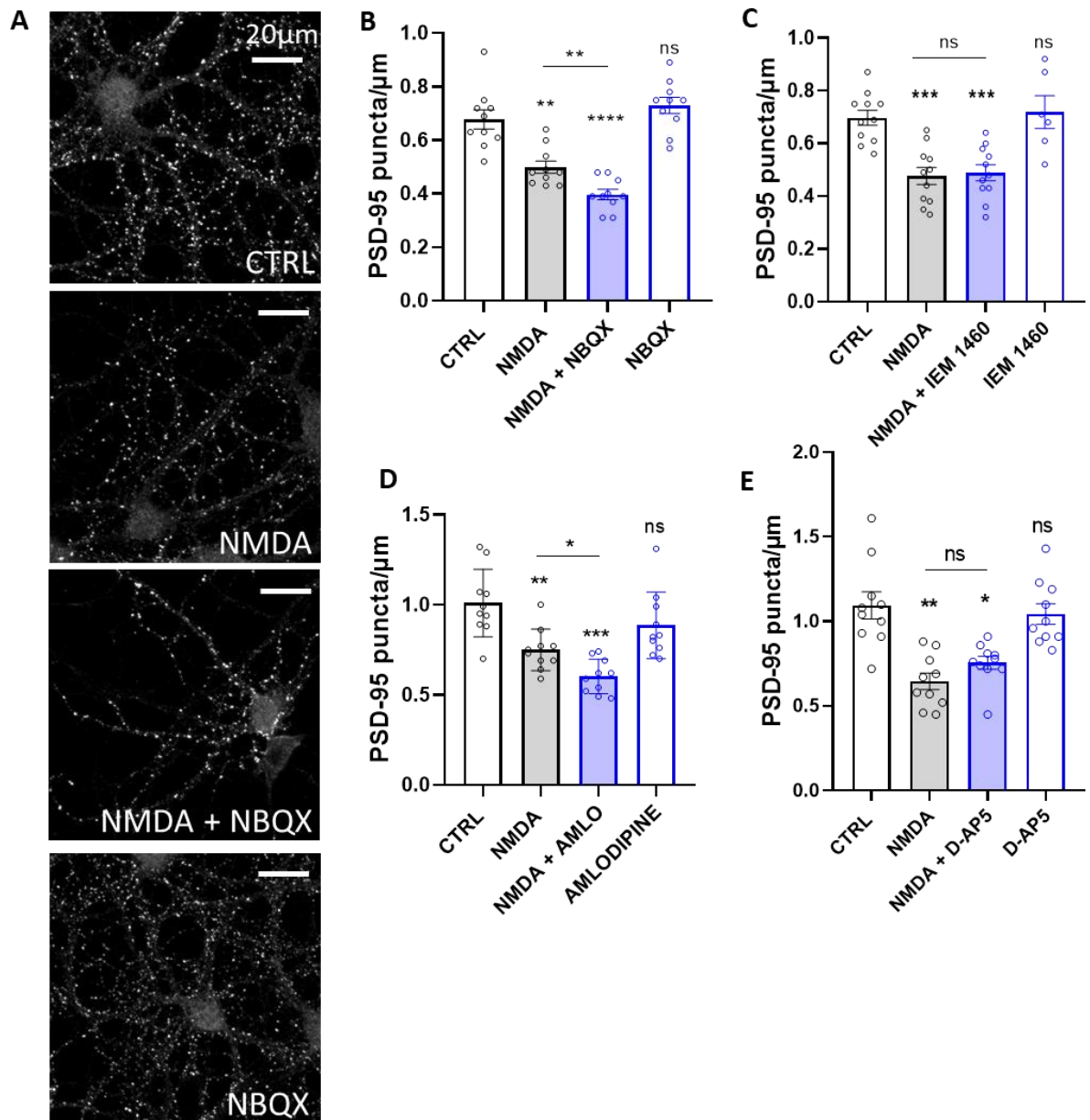


**Figure 6: Blockade of AMPAR and L-type calcium channels increases pruning.** A. Example of confocal images of PSD-95 immunolabeling. B to E: quantification of PSD-95 puncta density 3 hours after beginning of treatments, one dot represents the mean of a cell. B: from left to right: control, NMDA, NMDA and NBQX after 30 min, NBQX. Mean +/-SEM, one-way ANOVA, Turkey's multiple comparisons test gives  $p=0.0003$ ,  $p<0.0001$  and  $p=0.56$  respectively, and t-test between NMDA and NMDA+NBQX gives  $p=0.003$ . C: from left to right: control, NMDA, NMDA and IEM1460 after 30 min, IEM1460. Mean +/-SEM, one-way ANOVA, Turkey's multiple comparisons test gives  $p=0.0002$ ,  $0.0005$  and  $0.98$  respectively. D: from left to right: control, NMDA, NMDA and Amlodipine after 30 min, Amlodipine. Mean +/-SEM, one-way ANOVA, Turkey's multiple comparisons test gives  $p=0.0026$ ,  $<0.0001$ , and  $0.28$  respectively. T-test between NMDA and NMDA+Amlodipine gives  $p=0.0062$ . E: from left to right: control, NMDA, NMDA and APV after 30 min, APV. Mean +/-SEM, one-way ANOVA, Turkey's multiple comparisons test gives  $p<0.0001$ ,  $p=0.0014$ ,  $0.93$  respectively.



## Material and methods

### Hippocampal neuron culture

Sprague-Dawley pregnant rats (Janvier Labs, Saint-Berthevin, France) were sacrificed according to the European Directive rules (2010/63/EU). Dissociated hippocampal neurons from E18 Sprague-Dawley rats embryos of either sex were prepared as described previously (Kaech and Banker, 2006) at a density of 200,000 cells per 60-mm dish on poly-L-lysine pre-coated 1.5H coverslips (Marienfeld, cat. No. 117 580). Neurons cultures were maintained in Neurobasal Plus medium supplemented with 0.5 mM GlutaMAX and 1X B-27 Plus supplement (Thermo Fischer Scientific). 2 $\mu$ M Ara-C is added after 72 hours. Neurons were kept at 37°C and 5% CO<sub>2</sub>, for 14–16 days.

### Plasmids/transfection

Banker neurons were transfected with WT and T19A mutant of PSD-95, as well as soluble EGFP plasmids via calcium phosphate protocol (described in (Haas et al., 2018)).

### Electrophysiology

mEPSC recordings in neuronal culture were performed as described in Haas et al. Extracellular recording solution was composed of the following (in mM): 110 NaCl, 5 KCl, 2 CaCl<sub>2</sub>, 2 MgCl<sub>2</sub>, 10 HEPES, 10 D-Glucose, 0.0005 Tetrodotoxin, 0.1 Picrotoxin (pH 7.4; ~256 mOsm/L). The pipettes were filled with intracellular solution composed of the following (in mM): 100 K-gluconate, 10 HEPES, 1.1 EGTA, 3 ATP, 0.3 GTP, 0.1 CaCl<sub>2</sub>, 5 MgCl<sub>2</sub> (pH 7.3; 230 mOsm). Recordings were performed using an EPC10 patch clamp amplifier operated with Patchmaster software (HEKA Elektronik). Whole-cell voltage clamp recordings were performed at room temperature and at a holding potential of -70mV. Unless specified otherwise, all chemicals were purchased from Sigma-Aldrich except for drugs, which were from Tocris Bioscience.

Miniature EPSC analysis was performed using a software developed by Michel Goillandeau, Detection Mini. Briefly, the principle of the detection used is the median filter. The program takes a window with a width sets by the experimenter. For each point of the biological signal, the software calculates the median of values in the window before and after the point. The detection is not made on the biological signal but on another signal (called Detection Signal), calculated from the difference between the filtered signal and the baseline signal. For further analysis, only detected events with an amplitude comprised between 5 and 50 pA are taken into account.

Similar methods were used for spontaneous EPSCs in neuronal culture. Extracellular recording solution was composed of the following (in mM): 110 NaCl, 5 KCl, 0.2 / 2 / 4 CaCl<sub>2</sub>, 10 HEPES, 10 D-Glucose, 0.1 Picrotoxin (pH 7.4; ~256 mOsm/L). The pipettes

are filled with intracellular solution composed of the following (in mM): 100 K-gluconate, 10 HEPES, 1.1 EGTA, 3 ATP, 0.3 GTP, 0.1 CaCl<sub>2</sub>, 5 MgCl<sub>2</sub> (pH 7.3; 230 mOsm). The area and duration from individual events were measured using the software Clampfit 10.7 (Molecular Devices). A template-based search of events was used to obtain the parameters.

### **Labeling**

For confocal imaging of PSD-95, primary neuronal cultures were treated either with 30 μM NMDA (Tocris) for 3 minutes or with 100 μM ATP in presence of CGS15943 (3 μM) (Pougnnet et al., 2016, 2014) (Sigma-aldrich) for 1 minute and fixed with PFA 30 minutes or 3 hours after. PFA was quenched with NH<sub>4</sub>Cl 50 mM for 5 minutes. A permeabilization step with 0.2% triton X100 for 5 minutes was then performed. Cells were washed 3 times for 5 min in 1x PBS. After 3 washes with 1x PBS, unspecific staining was blocked by incubating coverslips in 1% BSA for 1h at room temperature. Cells were then incubated with monoclonal mouse anti-PSD-95 antibody (MA1-046, ThermoFischer), diluted in 1% BSA at 1/500, at room temperature for 4 hours. Coverslips were rinsed 3 times in 1% BSA solution and incubated in 1% BSA for 1h at room temperature. Primary antibodies were revealed with Alexa 647 coupled anti-mouse IgG secondary antibodies (ThermoFisher, A21235).

### **Confocal imaging**

Images were acquired with a microscope Leica TCS SP8 confocal head mounted on an upright stand DM6 FS (Leica Microsystems, Mannheim, Germany), an objective HC Plan Apo CS2 40X oil NA 1.3 and an internal hybrid detector.

Images were acquired on different Z plans and reconstructed as Z projections using the software ImageJ. Reconstructed images were then analyzed using the software MetaMorph (Molecular Devices). For puncta density measurement, puncta were manually counted and labelled as regions of interest on three to five portions of dendrites of around 25μm length each.

### **Live imaging**

For live imaging of EGFP transfected primary neuronal cultures and synaptogamin-1 uptake measurement, neurons were treated with 30 μM NMDA (Tocris) for 3 minutes. After 30 minutes of incubation, they were placed in a Ludin chamber with culture media from their original dish, and a fluorescently labelled mouse anti-Synaptotagmin-1 (Synaptic System, 105311CpH monoclonal) was applied in the bath at 1/200 for 30 minutes.

Images were acquired 3 hours after treatment using spinning disk microscope Leica DMI8 (Leica Microsystems, Wetzlar, Germany) equipped with a confocal Scanner Unit CSU-W1 T2 (Yokogawa Electric Corporation, Tokyo, Japan) using a HCX PL Apo CS2 63X oil NA 1.4 TIRF objective. The system comprised a sCMOS Prime 95B camera (Photometrics, Tucson, USA). The LASER diodes used were at 488 nm (400 mW), and 642 nm (100 mW). Z stacks were done with a galvanometric stage (Leica

Microsystems, Wetzlar, Germany). The 37°C and 5% CO<sub>2</sub> atmosphere was created with an incubator box and an air heating system (PeCon GmbH, Germany). This system was controlled by MetaMorph software (Molecular Devices, Sunnyvale, USA).

Images were analyzed using the software MetaMorph. Using the EGFP signal, spines were manually selected as region of interests of a size sufficient to comprise the full spine. All visible spines from a neuron were selected.

To rule out cross-interactions between the parameters of activity and distance of neighboring spines, we selected spines presenting similar parameters between maintained and pruned spines, except the one of interest. For neighboring spines activity analysis, maintained spines were selected to present similar activity than pruned spines (mean pruned spines  $\pm$  2000 au) and only pruned spines with neighbors closer than 5 $\mu$ m were used. For distance analysis with surrounding spines, spines with similar level of activity and surrounded by middle active synapses (activity of the spine of interest  $\pm$  1000 au) were selected for the maintained group.

## Discussion

In the present study, we showed, by combining live and fixed sample confocal imaging with electrophysiology recordings, that following NMDAR activation, all molecular reshufflings occurring during LTD induction have to be maintained to trigger pruning. Then, we identified conditions necessary for NMDAR-dependent LTD to trigger pruning. We found that to counteract pruning, synapses need either a high activity, or be protected by neighbors. This protection by the surrounding synapses can be due to their close proximity, to their high activity or to a coordinated activity if they are connected to the same axon.

### PSD-95 reshuffling mediates the relation LTD-synaptic pruning

Chemical LTD on neuronal cell culture triggers, 3 hours following NMDA treatment, to a 40% decrease of synaptic density. The maintained synapses are depressed as revealed by miniature amplitudes recorded at 3 hours (figure 1 and 4), meaning that after LTD induction, some synapses are maintained and some are pruned. To decipher the mechanism which determine the synaptic fate, we first studied if the intensity of synaptic response could be important. Indeed, as seen on the distribution of miniature currents, LTD lead to a shift of all the synaptic response currents toward lower currents. It could be possible that only the synapses presenting the lower intensity of current went through pruning. So, we induced LTD not by NMDAR but by P2XR activation. This LTD type, described almost ten years ago, triggers a similar decrease of synaptic current without leading to important reshuffling of synaptic proteins. Our results indicate that unlike NMDAR-dependent LTD, P2XR-dependent LTD does not trigger a synaptic pruning after 3 hours (fig.1). The observed differences for pruning between these two protocols probably resides in the PSD-95 removal from synapses as it has previously been described as an important marker of LTD-induced synaptic pruning (Cane et al., 2014; Wu et al., 2017).

As the effective decrease of AMPAR currents at the synapse seems not to be the determinant factor which is responsible of pruning induction, we tried to determine if an induction of the LTD for 30 minutes followed by an inhibition of the late phase of the LTD, corresponding to PSD95 removal and targeting to the autophagic pathway, was able to trigger spine selection (fig.2). Blocking the PSD95 reshuffling by expression of the T19A mutant, or interrupting PSD-95 removal 30 minutes after treatment with either GSK3 or autophagy inhibitor, blocks the pruning. These experiments underlined the direct relation between LTD and synaptic pruning. We can even hypothesize that the role of LTD is to initiate the pruning, putting the synapse in a waiting state to determine if it has to be maintained or pruned.

### **Rules for LTD-dependent synaptic pruning protection**

Once the LTD induced, what could determine the synaptic fate? Previous studies have shown that induction of LTD doesn't necessarily trigger synaptic pruning (Oh et al., 2013; Stein et al., 2020; Wiegert and Oertner, 2013; Wiegert et al., 2018), and it has been suggested that synapses could recover from synaptic depression (Wiegert and Oertner, 2013). Consistent with these findings, our experiments showed that following NMDAR-dependent LTD, 30% to 40% of spines are suppressed (fig.1), meaning that in 60 to 70% of the cases, there is an interruption of the "LTD-pruning" sequence.

We investigated which conditions favor the synaptic maintenance following LTD induction. We first modulated the level of activity of the network and determined in what extent it modified the proportion of pruned synapses. Both increase of release probability by increasing extracellular calcium concentration and inhibition of the inhibitory neurons fully suppress the synaptic pruning, revealing that a high network activity is able to counteract the LTD-dependent pruning.

Then we determined the activity dependence of pruning at the synaptic level. We found that a small part of synapses was very active, and this high activity protects synapses from suppression. However, for the vast majority of synapses, individual activity is not a parameter which seems determinant to explain their suppression or maintenance.

Then we studied the effect of the environment and more particularly of neighboring synapse distances and activity on the spine selection. Cooperation and interaction between neighboring synapses are more and more reported in the literature as fundamental parameters in the dendritic integration and modulation of signal (Oh et al., 2015; Zhang et al., 2015). We first found that maintained synapses presented neighboring synapses that were closer from them than the neighbors of pruned synapses (fig.5), and second that these neighboring synapses presented higher levels of activity. These findings raise the hypothesis that clustered synapses collaborate together to recover and avoid their suppression.

This protection by closed and active synapses are probably related to local calcium influx. Previous work has shown that the balance of GABAergic inhibition was responsible for a limitation in space of the diffusion of calcium into dendritic branches (Hayama et al., 2013). Thus, influx and then diffusion of calcium in the neighborhood of active spines could promote the maintenance of surrounding synapses. However,

calcium is known to be a very important secondary messenger that could in turn activate myriad of molecular pathways (Brini et al., 2014). Thus, another hypothesis could be that it is not the local diffusion of calcium that constitutes a maintenance signal but the activation and then the diffusion all along the dendritic branch of a calcium sensible protein.

However, it is rather noting that these findings seem contradictory with other studies. In fact, it has been previously reported that induction of LTP at several surrounding synapses triggered synaptic pruning of the only non-potentiated synapse of the group (Oh et al., 2015). Recent work also showed that during development, the proximity of active spines was favoring suppression of low active spines, instead of their maintenance (Yasuda et al., 2021). Nonetheless, heterosynaptic shrinkage and pruning, as well as developmental specific selection of synapses are supported by different molecular reshufflings and molecular pathways activation than homosynaptic pruning (Nishiyama and Yasuda, 2015). This could explain the different influence that neighboring spines exert on each other. It is therefore exciting to observe that depending on the paradigm of synaptic plasticity and selection, rules regulating interaction between synapses and recovery signal are different, underlying the brain complexity.

### **Activation of VGCCs constitutes a maintenance signal for synapses**

When looking for the molecular source of calcium which is responsible of the spine maintenance, we initially thought about the NMDAR. Indeed, the main dependent activity calcium entry at spines is the NMDA receptor. But inhibition of this receptor 30 minutes after LTD induction and for all the duration of the pruning induction does not affect the number of pruned and maintained synapses. So, we prospected from the AMPAR side, it appeared to be AMPAR dependent but not through the Calcium permeant AMPAR. Finally, it seems that the calcium entry comes from the activation by the AMPAR-induced depolarization of the L-type voltage dependent calcium channel. These results are consistent with the principle of local dendritic depolarization with local synaptic integration. In this case the spine cooperation, moreover when they are activated in the same time because belonging to the same axon, favors the activation of CAV which are present both at spine and on the dendrite.

### **Circuit refinement and the theory of noise reduction**

Beyond deciphering the mechanisms of pruning, we also investigated the consequences for neuronal integration of synaptic pruning. Our study of spontaneous synaptic activity revealed that pruning tends to increase the segregation of the population of currents (fig.4). Unlike multi-synaptic signaling, mono-synaptic currents tend to disappear after pruning. This can be putted in relation with the fact that pruning preferentially affects single-made axonal synapses (fig.5H) and that therefore after pruning the total amount of single-made axonal synapse is decreased compared to multiple-made synapses (fig. 5I). What could be the consequence of such refinement of inputs for a neuron? To address this question, one should consider the notions of

synchrony and aberrance of synaptic signaling for neuronal integration. It is known that not all synaptic events contribute to a depolarization at the soma, and then at the axonal initial segment, to generate an action potential (Spruston, 2008). This phenomenon is notably at the origin of the concept of spike-timing short term plasticity, where the timing of synaptic signaling in relation with the spike propagation determines the depression or potentiation of individual synapses (Tazerart et al., 2020). In this specific paradigm, synapses that fire before the spike propagation are weakened. In the present situation we found that pruning affected isolated synapses: spatially isolated because they have few neighboring synapses, and isolated in activity because they fire alone and therefore in an aberrant manner in regard to the activity of the neuron. We can thus hypothesize that pruning refines the network and the inputs that a neuron receives, to suppress aberrant signaling that can be imagined as noise compared to pluri-synaptic coordinated signaling. As a consequence, synaptic pruning will increase the efficacy and the specificity of information transmission in a neuronal network.

We first showed that LTD-related pruning is not related to the decrease of synaptic currents, but to the NMDAR-induced removal of PSD-95 from synapses. However, we reported here that synapses can recover from LTD induction through the activation of L-type calcium channels. Moreover, co-operation between highly active and low active synapses is at the basis of this maintenance pathway, where pruning affects specifically isolated synapses in space and activity. To our knowledge, it is the first time that data suggest so strongly the implication of synaptic pruning in the promotion of coordinated synaptic inputs.

## **CONCLUSION AND PERSPECTIVES**

For the last ten years, the application of super-resolution techniques to neuroscience, improves our synaptic physiology understanding through the tries to integrate nanoscale molecular organization to synaptic function. My PhD belong to this general movement of re-interpretation of the concept of synapse.

Indeed, through my PhD, I have learned the importance to decipher the precise molecular organization of synaptic proteins to understand the synaptic physiology. Although the synaptic input is only the first actor in the input/output relationship, and that several studies still need to be done to fully understand the functioning of synapses, I think that my PhD work helps to improve our current vision of synaptic transmission both in basal state and during synaptic and structural plasticities.

### **1. Deciphering the basal synaptic nano-organization**

The principal aim of my thesis was to understand how the nanoscale organization of glutamate receptors determine the synaptic function a basal state and during plasticity.

I started my PhD by characterizing the co-organization of AMPAR, NMDAR, and mGluR, and understanding how this organization tunes the synaptic transmission. In this work, by combining single-molecule super-resolution microscopy, electrophysiology, and modeling, we determined (i) the average amount of each glutamate receptor type per spine, (ii) their nanoscale organization and co-organization, and (iii) their respective activation. We observed that NMDARs form a unique cluster mainly at the center of the PSD, while AMPARs segregate in clusters surrounding the NMDARs. mGluR5 presents a different organization and is homogenously distributed at the synaptic surface. From these results, we built a model predicting the synaptic transmission properties of a unitary synapse, allowing better



understanding of synaptic physiology. The continuity of this project is to inject into the model, the physiological input received by a CA1 synapse, at rest or during activity or learning task, to determine the level of activation of each receptor type. These data have been already given by Jack Mellor, but I will not have the opportunity to take part of this new project.

After having studied the nanoscale organization of glutamate receptors in basal conditions, I have been interested also to the mechanisms by which synapses were able to adapt synaptic transmission during synaptic plasticity.

## **2. Importance of the dynamic nanoscale organization for neuronal plasticity**

Synapses are plastic compartments of neurons. They can be strengthened or weakened through specific input patterns. These changes have been extensively shown to be dependent on a regulation of the number of AMPARs at synapses through exocytosis and endocytosis. However, the new level of complexity regarding the molecular surface dynamic organization has driven us to go deeper in the understanding of the precise rearrangement of protein in the control of synaptic strength. The aim of my PhD has been to investigate the role of the nanoscale organization of AMPAR during chemical LTD. Comparing two forms of synaptic depression, we have demonstrated that the classical definition of LTD, meaning a decrease of synaptic strength through an internalization of AMPARs is not sufficient to describe this phenomenon. Although it is true that the initial phase, at the origin of synaptic weakening, is correlated with AMPAR endocytosis, it is also linked to a precise reorganization of AMPARs at synapses. This initial phase is followed, specifically during NMDAR-dependent LTD, by an entire molecular reorganization of synapses, increasing AMPAR diffusion, removing PSD95, and so changing the synaptic capacity

to respond to high-frequency inputs. It is interesting in this study to observe the difference between NMDAR- and P2XR-dependent LTD. These two depression types lead to a similar decrease of synaptic strength but does not produce the same reshuffling of synaptic components. We did not have time during this study to fully characterize the mGluR-dependent LTD, which is another synaptic and glutamate-dependent form of LTD. Measure of AMPAR mobility after DHPG treatment revealed an increase of the proportion of mobile receptor, as observed after NMDA treatment. However, we did not determine the molecular causes of such increase mobility neither its effect on synaptic currents (STP). However, through a collaboration project with Vassiliki Nikolettou in Lausanne, we demonstrated that both mGluR and NMDAR activation triggered a similar long-lasting increase of autophagy (paper in revision at Nature Communication). The similarity of both increase in AMPAR mobility and in autophagy could indicate that both NMDAR and mGluR-dependent LTD activate similar molecular pathway, at least partly. It could be interesting to study the particularity of each of these two ways to induce glutamate dependent LTD.

In parallel to molecular re-organization, LTD triggers morphological changes: either spine shrinkage or pruning. This network reorganization during LTD is thought to be at the origin of its physiological role. During development, LTD is required to select the pertinent synapses when too many of them have been created. Later on, LTD plays an important role within circuits to trigger the selective elimination of weaker synapses. This spine selection could be important for LTD function, meaning behavioral flexibility, experience-dependent adaptation, and memory erasing.

Therefore, I interested myself to the relation LTD-dependent synaptic pruning. In fact, previous work found that induction of NMDAR-dependent LTD is followed by a synaptic pruning hours to days after induction, depending on the model and the method of

induction (Thomazeau et al., 2020; Wiegert and Oertner, 2013; Wiegert et al., 2018). However, it remains unknown whether these two phenomena are two sides of the same re-organization or whether they only share some signaling pathways (Nishiyama and Yasuda, 2015; Piochon et al., 2016). It is also rather noting that induction of LTD does not trigger necessarily suppression of all synapses but that “failure” in the “LTD-pruning” sequence occurs frequently (Wiegert et al., 2018). Other works indicate as well that the initial state of synapse, in activity, size and integration, influences the fate of synapses (Oh et al., 2013; Wiegert and Oertner, 2013; Wiegert et al., 2018).

From my point of view, one of the main discoveries through this project around LTD and pruning is that similar LTD amplitude induced by ATP or NMDA does not trigger the same effect of pruning. This is not the decrease of synaptic current by decreasing the local depolarization, leading to a decrease of Calcium channel or NMDAR receptor activity which will induce the pruning. The second is that even if synapses receive NMDA treatment, when we specifically block LTD with genetical tools, we suppress the pruning, so LTD and pruning are not two independent molecular pathways but two sides of the same mechanism.

Finally, I succeeded to identify which determinants of a synapse, notably concerning its activity, can modulate the LTD-induced synaptic pruning. Indeed, we identified 5 characteristics of synapses that influence their pruning or maintenance. Suppressed synapses 1) presented low-middle activity, 2) were the single synapse that an axon makes with a given dendrite, 3) had few neighboring synapses, 4) these neighbors were far from the pruned synapse and 5) had a low activity level.

Altogether, this gives us rules to predict if following LTD a synapse will be pruned. I would like to find a way to test these rules at the spine level, without using massive

chemical protocol to induce LTD, and in a more physiological context as slices or in vivo, but this step is technically highly challenging.

### **3. A unified model of synaptic regulation**

For my PhD, I aimed to understand how the nanoscale organization of synapses tunes the ability of a neuron to adapt to new situations. Indeed, a neuron has the possibility to increase or decrease its communication with partners. For this, a simple rule resumes the different parameters that a neuron can influence in order to change the sum of the currents at the soma:  $I = N \cdot Pr \cdot Q$ .

In the last three years, I studied how these three parameters N, Pr and Q could be modulated during LTD to decrease I.

When looking at the literature, which of those parameters is able to be modulated during LTD is far from being consensual. Moreover, measurement with electrophysiology of EPSC is probably not the best way to get access to the individual synapse level, because the stimulation of a large number of axons with a sub-threshold intensity, recruit a very large N with a low Pr and too much variability to clearly obtain the Q. Moreover, it is difficult to follow, with electrophysiology, a neuron for multiple hours avoiding to get access to the effect of the pruning on EPSC.

Historically, LTD has been described in the hippocampus as a post-synaptic mechanism dependent on NMDAR activation (Dudek and Bear, 1992). Few studies investigated the role of the pre-synaptic element in the weakening of synaptic transmission. The existence of pre-synaptic mechanisms has been reported following a retrograde signaling (endocannabinoids, nitric oxide ...) and they are thought to modify the Pr or the readily releasable pool size. However, this pre-synaptic

mechanism is controversial, probably because the studies were performed in various brain regions and at different developmental stages (Collingridge et al., 2010; Goda and Stevens, 1998; Hjelmstad et al., 1997; Kreitzer and Malenka, 2007).

We propose, thanks to our different projects a more unified model of the depressed synapse. Indeed, by iGluSnFR experiments we showed that NMDAR-dependent LTD does not change the release probability ( $Pr$ ). Concerning the  $Q$  parameters, it is determined by the organization and the composition of glutamate receptor complexes. We reported that LTD decreases the  $Q$  by decreasing the AMPARs content inside of the nanodomains. Interestingly, we observed a linear correlation between the 25 to 30% decrease of AMPAR amount per synapse (and per nanodomain), with the 25% to 30% decrease of AMPAR amplitude.

Finally, the last parameter of the equation is the  $N$ , the number of synapses. The fact that LTD was able to induce the suppression of spines and therefore decrease the  $N$  was already described. However, our data brought the important notion that if LTD is induced, the pruning will happen only if the synapse is weakly integrated because of isolation in distance or activity from the rest of the dendrite. This property renders electrophysiology inefficient to study the LTD-dependent pruning, because only low activity synapses (which can represent until 40% of the overall synapses) will be pruned, meaning the one which mainly does not participate to the EPSC.

Here we propose that if a neuron needs to decrease synaptic strength at one synapse, meaning induction of LTD:  $Pr$  will be unchanged,  $Q$  will decrease, and  $N$  will decrease if weakly integrated synapses are present.

In this model, we propose that initial molecular reorganization of synapses could be the first step for structural plasticity. After LTD induction, the synapse will be in a

transient state to determine if it needs to be maintained or suppressed. Probably, when this decision will be taken, the maintained synapses will be de-depressed to reach back to a normal activity, as described in Wiegert et al. 2013.

Our hypothesis is that synaptic depression allows, by specific modifications of AMPAR dynamic organization, to suppress weakly integrated synapses and to maintain important synapses based on their input patterns. In this way, the Q and N values, important for neuronal signal integration, appear to be regulated by nanoscale organization of synaptic proteins. Although parallel mechanisms such as change in neuronal excitability or change in the inhibitory inputs, could play a role, this suggests a key role of the organization at the nanoscale in the input/output balance which should be further investigated.

To finish, my thesis work is included in a research group dynamic aiming to decipher the impact of nanoscale organization of receptors on synaptic transmission. Indeed, over the last years, our group notably characterized the dynamic (Constals et al., 2015; Frischknecht et al., 2009; Groc et al., 2004; Borgdorff and Choquet, 2002) and the nanodomains organization of AMPARs in basal conditions (Nair et al., 2013b) and how this tunes synaptic inputs (Haas et al., 2018; Heine et al., 2008; Klaassen et al., 2016; Penn et al., 2017). In the direct line of these studies, my PhD work brought important information about co-organization and co-activation of glutamate receptors, to finally revisit the regulation of LTD by synaptic nano-organization reshufflings, and its role for neuronal functioning.

## **BIBLIOGRAPHY**

# A

Abbott, L.F., Varela, J.A., Sen, K., and Nelson, S.B. (1997). Synaptic depression and cortical gain control. *Science* (80- ). 275, 220–224.

Abraham, W.C., and Goddard, G. V. (1983). Asymmetric relationships between homosynaptic long-term potentiation and heterosynaptic long-term depression. *Nature* 305, 717–719.

Arellano, J.I., Benavides-Piccione, R., DeFelipe, J., and Yuste, R. (2007). Ultrastructure of Dendritic Spines: Correlation Between Synaptic and Spine Morphologies. *Front. Neurosci.* 1, 131–143.

Axelrod, D., Ravdin, P., Koppel, D.E., Schlessinger, J., Webb, W.W., Elson, E.L., and Podleski, T.R. (1976b). Lateral motion of fluorescently labeled acetylcholine receptors in membranes of developing muscle fibers. *Proc. Natl. Acad. Sci. U. S. A.* 73, 4594–4598.

Axelrod, D., Koppel, D.E., Schlessinger, J., Elson, E., and Webb, W.W. (1976a). Mobility measurement by analysis of fluorescence photobleaching recovery kinetics. *Biophys. J.* 16, 1055–1069.

# B

Bashir, Z.I., Jane, D.E., Sunter, D.C., Watkins, J.C., and Collingridge, G.L. (1993). Metabotropic glutamate receptors contribute to the induction of long-term depression in the CA1 region of the hippocampus. *Eur. J. Pharmacol.* 239, 265–266.

Bassani, S., Cingolani, L.A., Valnegri, P., Folci, A., Zapata, J., Gianfelice, A., Sala, C., Goda, Y., and Passafaro, M. (2012). The X-Linked Intellectual Disability Protein TSPAN7 Regulates Excitatory Synapse Development and AMPAR Trafficking. *Neuron* 73, 1143–1158.

Bats, C., Groc, L., and Choquet, D. (2007). The Interaction between Stargazin and PSD-95 Regulates AMPA Receptor Surface Trafficking. *Neuron* 53, 719–734.

Bats, C., Soto, D., Studniarczyk, D., Farrant, M., and Cull-Candy, S.G. (2012). Channel properties reveal differential expression of TARPed and TARPlless AMPARs in stargazer neurons. *Nat. Neurosci.* 15, 853–861.

Bhattacharyya, S., Biou, V., Xu, W., Schlüter, O., and Malenka, R.C. (2009). A critical role for PSD-95/AKAP interactions in endocytosis of synaptic AMPA receptors. *Nat. Neurosci.* 12, 172–181.

Bliss, T.V.P. & Collingridge, G.L. (1993). A synaptic model of memory: LTP in the hippocampus. *Nature* 361, 31–39.

Bliss, T.V.P., and Lømo, T. (1973). Long-lasting potentiation of synaptic transmission in the dentate area of the anaesthetized rabbit following stimulation of the perforant path. *J. Physiol.* 232, 331–356.

Borgdorff, A.J., and Choquet, D. (2002). Regulation of AMPA receptor lateral



movements. *Nature* 417, 649–653.

Bosch, M., Castro, J., Saneyoshi, T., Matsuno, H., Sur, M., and Hayashi, Y. (2014). Structural and molecular remodeling of dendritic spine substructures during long-term potentiation. *Neuron* 82, 444–459.

Bourgeron, T. (2009). A synaptic trek to autism. *Curr. Opin. Neurobiol.* 19, 231–234.

Brenowitz, S., and Trussell, L.O. (2001). Minimizing synaptic depression by control of release probability. *J. Neurosci.* 21, 1857–1867.

Brini, M., Cali, T., Ottolini, D., and Carafoli, E. (2014). Neuronal calcium signaling: Function and dysfunction. *Cell. Mol. Life Sci.* 71, 2787–2814.

Broadhead, M.J., Horrocks, M.H., Zhu, F., Muresan, L., Benavides-Piccione, R., DeFelipe, J., Fricker, D., Kopanitsa, M. V., Duncan, R.R., Klenerman, D., et al. (2016). PSD95 nanoclusters are postsynaptic building blocks in hippocampus circuits. *Sci. Rep.* 6, 1–14.

Buonarati, O.R., Hammes, E.A., Watson, J.F., Greger, I.H., and Hell, J.W. (2019). Mechanisms of postsynaptic localization of AMPA-type glutamate receptors and their regulation during long-term potentiation. *Sci. Signal.* 12, 1–10.

Burrone, J., and Lagnado, L. (2000). Synaptic depression and the kinetics of exocytosis in retinal bipolar cells. *J. Neurosci.* 20, 568–578.

## C

Campelo, T., Augusto, E., Chenouard, N., de Miranda, A., Kouskoff, V., Camus, C., Choquet, D., and Gambino, F. (2020). AMPAR-Dependent Synaptic Plasticity Initiates Cortical Remapping and Adaptive Behaviors during Sensory Experience. *Cell Rep.* 32.

Cane, M., Maco, B., Knott, G., and Holtmaat, A. (2014). The relationship between PSD-95 clustering and spine stability In Vivo. *J. Neurosci.* 34, 2075–2086.

Carroll, R.C., Lissin, D. V, von Zastrow, M., Nicoll, R. a, and Malenka, R.C. (1999). Rapid redistribution of glutamate receptors contributes to long-term depression in hippocampal cultures. *Nat. Neurosci.* 2, 454–460.

Carroll, R.C., Beattie, E.C., Zastrow, M. Von, Malenka, R.C., and Einstein, A. (2001). Role of ampa receptor endocytosis in synaptic plasticity. *Nat. Rev. Neurosci.* 2.

Casimiro, T.M., Sossa, K.G., Uzunova, G., Beattie, J.B., Marsden, K.C., and Carroll, R.C. (2011). MGluR and NMDAR activation internalize distinct populations of AMPARs. *Mol. Cell. Neurosci.* 48, 161–170.

Castillo, B.Y.J.D.E.L., and Katz, B. (1954). From the Department of Biophysics , University College , London in frog muscle ( Fatt & Katz , 1952a ), and their relation to the end-plate are identical in size with the spontaneous ' miniature e . p . p . ' s ' . The latter , say , 70-80 mV is provided by. *Quantum* 560–573.

Cavaccini, A., Durkee, C., Kofuji, P., Tonini, R., and Araque, A. (2020). Astrocyte signaling gates long-term depression at corticostriatal synapses of the direct pathway. *J. Neurosci.* 40, 5757–5768.

Chen, C., Blitz, D.M., and Regehr, W.G. (2002). Contributions of receptor desensitization and saturation to plasticity at the retinogeniculate synapse. *Neuron* 33, 779–788.

- Chen, G., Harata, N.C., and Tsien, R.W. (2004). Paired-pulse depression of unitary quantal amplitude at single hippocampal synapses. *Proc. Natl. Acad. Sci. U. S. A.* *101*, 1063–1068.
- Chen, L., Chetkovich, D.M., Petralia, R.S., Sweeney, N.T., Kawasaki, Y., Wenthold, R.J., Brecht, D.S., and Nicoll, R.A. (2000). Stargazin regulates synaptic targeting of AMPA receptors by two distinct mechanisms. *Nature* *408*, 936–943.
- Chen, S.X., Kim, A.N., Peters, A.J., and Komiyama, T. (2015). Subtype-specific plasticity of inhibitory circuits in motor cortex during motor learning. *Nat. Neurosci.* *18*, 1109–1115.
- Chen, X., Nelson, C.D., Li, X., Winters, C.A., Azzam, R., Sousa, A.A., Leapman, R.D., Gainer, H., Sheng, M., and Reese, T.S. (2011). PSD-95 is required to sustain the molecular organization of the postsynaptic density. *J. Neurosci.* *31*, 6329–6338.
- Chin, A.C., and Lau, A.Y. (2021). Structural biology and thermodynamics of GluD receptors. *Neuropharmacology* *191*, 108542.
- Cho, K.O., Hunt, C.A., and Kennedy, M.B. (1992). The rat brain postsynaptic density fraction contains a homolog of the drosophila discs-large tumor suppressor protein. *Neuron* *9*.
- Choquet, D., and Triller, A. (2013). The Dynamic Synapse. *Neuron* *80*, 691–703.
- Colgan, L.A., Hu, M., Mislér, J.A., Parra-Bueno, P., Moran, C.M., Leitges, M., and Yasuda, R. (2018). PKC $\alpha$  integrates spatiotemporally distinct Ca<sup>2+</sup> and autocrine BDNF signaling to facilitate synaptic plasticity. *Nat. Neurosci.* *21*, 1027–1037.
- Collingridge, G.L., Peineau, S., Howland, J.G., and Wang, Y.T. (2010). Long-term depression in the CNS. *Nat. Rev. Neurosci.* *11*, 459–473.
- Colquhoun, B.Y.D., Jonas, P., and Sakmann, B. (1992). *Zellphysiologie*, 6900. 261–287.
- Compans, B., Choquet, D., and Hosy, E. (2016). Review on the role of AMPA receptor nano-organization and dynamic in the properties of synaptic transmission. *Neurophotonics* *3*, 041811.
- Compans, B., Camus, C., Kallergi, E., Sposini, S., Martineau, M., Butler, C., Kechkar, A., Klaassen, R. V., Retailleau, N., Sejnowski, T.J., et al. (2021). NMDAR-dependent long-term depression is associated with increased short term plasticity through autophagy mediated loss of PSD-95. *Nat. Commun.* 1–18.
- Constals, A., Penn, A.C., Compans, B., Toulmé, E., Phillipat, A., Marais, S., Retailleau, N., Hafner, A.S., Coussen, F., Hosy, E., et al. (2015). Glutamate-Induced AMPA Receptor Desensitization Increases Their Mobility and Modulates Short-Term Plasticity through Unbinding from Stargazin. *Neuron* *85*, 787–803.
- Coombs, I.D., Soto, D., McGee, T.P., Gold, M.G., Farrant, M., and Cull-Candy, S.G. (2019). Homomeric GluA2(R) AMPA receptors can conduct when desensitized. *Nat. Commun.* *10*.
- Coultrap, S.J., Freund, R.K., O’Leary, H., Sanderson, J.L., Roche, K.W., Dell’Acqua, M.L., and Bayer, K.U. (2014). Autonomous CaMKII mediates both LTP and LTD using a mechanism for differential substrate site selection. *Cell Rep.* *6*, 431–437.
- Cummings, J.A., Mulkey, R.M., Nicoll, R.A., and Malenka, R.C. (1996). Ca<sup>2+</sup> signaling requirements for long-term depression in the hippocampus. *Neuron* *16*, 825–833.

# D

Dan, Y., and Poo, M.M. (2004). Spike timing-dependent plasticity of neural circuits. *Neuron* *44*, 23–30.

Dani, A., Huang, B., Bergan, J., Dulac, C., and Zhuang, X. (2010). Superresolution Imaging of Chemical Synapses in the Brain. *Neuron* *68*, 843–856.

Derkach, V.A., Oh, M.C., Guire, E.S., and Soderling, T.R. (2007). Regulatory mechanisms of AMPA receptors in synaptic plasticity. *Nat. Rev. Neurosci.* *8*, 101–113.

Deschout, H., Zanicchi, F.C., Mlodzianoski, M., Diaspro, A., Bewersdorf, J., Hess, S.T., and Braeckmans, K. (2014). Precisely and accurately localizing single emitters in fluorescence microscopy. *Nat. Methods* *11*, 253–266.

Diering, G.H., Nirujogi, R.S., Roth, R.H., Worley, P.F., Pandey, A., and Huganir, R.L. (2017). During Sleep. *Science* (80-. ). *515*, 511–515.

Dittman, J.S., Kreitzer, A.C., and Regehr, W.G. (2000). Interplay between facilitation, depression, and residual calcium at three presynaptic terminals. *J. Neurosci.* *20*, 1374–1385.

Dobrunz, L.E., and Stevens, C.F. (1997). Heterogeneity of release probability, facilitation, and depletion at central synapses. *Neuron* *18*, 995–1008.

Dudek, S.M., and Bear, M.F. (1992). Homosynaptic long-term depression in area CA1 of hippocampus and effects of N-methyl-D-aspartate receptor blockade. *Proc. Natl. Acad. Sci. U. S. A.* *89*, 4363–4367.

Dürr, K.L., Chen, L., Stein, R.A., De Zorzi, R., Folea, I.M., Walz, T., McHaourab, H.S., and Gouaux, E. (2014). Structure and dynamics of AMPA receptor GluA2 in resting, pre-open, and desensitized states. *Cell* *158*, 778–792.

# E

Ehlers, M.D., Heine, M., Groc, L., Lee, M.C., and Choquet, D. (2007). Diffusional Trapping of GluR1 AMPA Receptors by Input-Specific Synaptic Activity. *Neuron* *54*, 447–460.

El-Husseini, A.E., Schnell, E., Chetkovich, D.M., Nicoll, R.A., and Brecht, D.S. (2000). PSD-95 involvement in maturation of excitatory synapses. *Science* *290*, 1364–1368.

El-Husseini, A.E.D., Schnell, E., Dakoji, S., Sweeney, N., Zhou, Q., Prange, O., Gauthier-Campbell, C., Aguilera-Moreno, A., Nicoll, R.A., and Brecht, D.S. (2002). Synaptic strength regulated by palmitate cycling on PSD-95. *Cell* *108*, 849–863.

Elegheert, J., Cvetkovska, V., Clayton, A.J., Heroven, C., Vennekens, K.M., Smukowski, S.N., Regan, M.C., Jia, W., Smith, A.C., Furukawa, H., et al. (2017). Structural Mechanism for Modulation of Synaptic Neuroligin-Neurexin Signaling by MDGA Proteins. *Neuron* *95*, 896–913.e10.

Elias, G.M., Funke, L., Stein, V., Grant, S.G., Brecht, D.S., and Nicoll, R.A. (2006). Synapse-Specific and Developmentally Regulated Targeting of AMPA Receptors by a Family

of MAGUK Scaffolding Proteins. *Neuron* 52, 307–320.

Engelhardt, J. Von, Mack, V., Sprengel, R., Kavenstock, N., Li, K.W., Sternbach, Y., Smit, A.B., Seeburg, P.H., and Monyer, H. (2010). Plasticity in the Dentate Gyrus. *Situ* 60, 1518–1522.

Von Engelhardt, J., Mack, V., Sprengel, R., Kavenstock, N., Li, K.W., Stern-Bach, Y., Smit, A.B., Seeburg, P.H., and Monyer, H. (2010). CKAMP44: A brain-specific protein attenuating short-term synaptic plasticity in the dentate gyrus. *Science* (80-. ). 327.

## F

Fatt, B.P., and Katz, B. (1951). An analysis of the end-plate potential recorded with an intra-cellular electrode. *Biophysics (Oxf)*. 320–370.

De Felipe, J., Marco, P., Fairén, A., and Jones, E.G. (1997). Inhibitory synaptogenesis in mouse somatosensory cortex. *Cereb. Cortex* 7, 619–634.

Ferraguti, F., and Shigemoto, R. (2006). Metabotropic glutamate receptors. *Cell Tissue Res.* 326, 483–504.

Fortune, E.S., and Rose, G.J. (2000). Short-term synaptic plasticity contributes to the temporal filtering of electrosensory information. *J. Neurosci.* 20, 7122–7130.

Fortune, E.S., and Rose, G.J. (2001). Short-term synaptic plasticity as a temporal filter. *Trends Neurosci.* 24, 381–385.

Franks, K.M., Bartol, T.M., and Sejnowski, T.J. (2002). A Monte Carlo model reveals independent signaling at central glutamatergic synapses. *Biophys. J.* 83, 2333–2348.

Franks, K.M., Stevens, C.F., and Sejnowski, T.J. (2003). Independent sources of quantal variability at single glutamatergic synapses. *J. Neurosci.* 23, 3186–3195.

Frischknecht, R., Heine, M., Perrais, D., Seidenbecher, C.I., Choquet, D., and Gundelfinger, E.D. (2009). Brain extracellular matrix affects AMPA receptor lateral mobility and short-term synaptic plasticity. *Nat. Neurosci.* 12, 897–904.

Fukata, Y., Tzingounis, A. V., Trinidad, J.C., Fukata, M., Burlingame, A.L., Nicoll, R.A., and Brecht, D.S. (2005). Molecular constituents of neuronal AMPA receptors. *J. Cell Biol.* 169, 399–404.

Fukata, Y., Dimitrov, A., Boncompain, G., Vielemeyer, O., Perez, F., and Fukata, M. (2013). Local palmitoylation cycles define activity-regulated postsynaptic subdomains. *J. Cell Biol.* 202, 145–161.

Fukata, Y., Chen, X., Chiken, S., Hirano, Y., Yamagata, A., and Inahashi, H. (2021). Nanoalignment for Synaptic Transmission and Epilepsy Prevention. 118.

# G

Gambino, F., Pagès, S., Kehayas, V., Baptista, D., Tatti, R., Carleton, A., and Holtmaat, A. (2014). Sensory-evoked LTP driven by dendritic plateau potentials in vivo. *Nature* *515*, 116–119.

Giannone, G., Hosy, E., Levet, F., Constals, A., Schulze, K., Sobolevsky, A.I., Rosconi, M.P., Gouaux, E., Tampe, R., Choquet, D., et al. (2010). Dynamic superresolution imaging of endogenous proteins on living cells at ultra-high density. *Biophys. J.* *99*, 1303–1310.

Gladding, C.M., Fitzjohn, S.M., and Molnár, E. (2009). Metabotropic glutamate receptor-mediated long-term depression: Molecular mechanisms. *Pharmacol. Rev.* *61*, 395–412.

Goda, Y., and Stevens, C.F. (1998). Readily releasable pool size changes associated with long term depression. *Proc. Natl. Acad. Sci. U. S. A.* *95*, 1283–1288.

González-Calvo, I., Iyer, K., Carquin, M., Khayachi, A., Giuliani, F.A., Sigoillot, S.M., Vincent, J., Séveno, M., Veleanu, M., Tahraoui, S., et al. (2021). Sushi domain-containing protein 4 controls synaptic plasticity and motor learning. *Elife* *10*, 1–34.

Gonzalez-Islas, C., Bölow, P., and Wenner, P. (2018). Regulation of synaptic scaling by action potential-independent miniature neurotransmission. *J Neurosci Res.* *96*, 348–353.

Goodell, D.J., Zaegel, V., Coultrap, S.J., Hell, J.W., and Bayer, K.U. (2017). DAPK1 Mediates LTD by Making CaMKII/GluN2B Binding LTP Specific. *Cell Rep.* *19*, 2231–2243.

Granger, A.J., Shi, Y., Lu, W., Cerpas, M., and Nicoll, R.A. (2013). LTP requires a reserve pool of glutamate receptors independent of subunit type. *Nature* *493*, 495–500.

Grant, S.G.N. (2013). SnapShot: Organizational principles of the postsynaptic proteome. *Neuron* *80*.

Greger, I.H., and Esteban, J.A. (2007). AMPA receptor biogenesis and trafficking. *Curr. Opin. Neurobiol.* *17*, 289–297.

Greger, I.H., Khatri, L., Kong, X., and Ziff, E.B. (2003). AMPA receptor tetramerization is mediated by Q/R editing. *Neuron* *40*, 763–774.

Greger, I.H., Akamine, P., Khatri, L., and Ziff, E.B. (2006). Developmentally Regulated, Combinatorial RNA Processing Modulates AMPA Receptor Biogenesis. *Neuron* *51*, 85–97.

Greger, I.H., Watson, J.F., and Cull-Candy, S.G. (2017). Structural and Functional Architecture of AMPA-Type Glutamate Receptors and Their Auxiliary Proteins. *Neuron* *94*, 713–730.

Groc, L., Heine, M., Cognet, L., Brickley, K., Stephenson, F.A., Lounis, B., and Choquet, D. (2004). Differential activity-dependent regulation of the lateral mobilities of AMPA and NMDA receptors. *Nat. Neurosci.* *7*, 695–696.

Groc, L., Heine, M., Cousins, S.L., Stephenson, F.A., Lounis, B., Cognet, L., and Choquet, D. (2006). NMDA receptor surface mobility depends on NR2A-2B subunits. *Proc. Natl. Acad. Sci. U. S. A.* *103*, 18769–18774.

# H

Haas, K.T., Compans, B., Letellier, M., Bartol, T.M., Grillo-Bosch, D., Sejnowski, T.J., Sainlos, M., Choquet, D., Thoumine, O., and Hosy, E. (2018). Pre-post synaptic alignment through neuroligin-1 tunes synaptic transmission efficiency. *Elife* 7, 1–22.

Hamill, O.P., Marty, A., Neher, E., Sakmann, B., and Sigworth, F.J. (1981). Improved patch-clamp techniques for high-resolution current recording from cells and cell-free membrane patches. *Pflügers Arch. Eur. J. Physiol.* 391.

Harris, K.M., and Stevens, J.K. (1989). Dendritic spines of CA1 pyramidal cells in the rat hippocampus: Serial electron microscopy with reference to their biophysical characteristics. *J. Neurosci.* 9, 2982–2997.

Harris, K.M., and Weinberg, R.J. (2012). Ultrastructure of synapses in the mammalian brain. *Cold Spring Harb. Perspect. Biol.* 4, 7.

Hasegawa, S., Sakuragi, S., Tominaga-Yoshino, K., and Ogura, A. (2015). Dendritic spine dynamics leading to spine elimination after repeated inductions of LTD. *Sci. Rep.* 5, 1–6.

Hayama, T., Noguchi, J., Watanabe, S., Takahashi, N., Hayashi-Takagi, A., Ellis-Davies, G.C.R., Matsuzaki, M., and Kasai, H. (2013). GABA promotes the competitive selection of dendritic spines by controlling local Ca<sup>2+</sup> signaling. *Nat. Neurosci.* 16, 1409–1416.

Hayashi, T., Rumbaugh, G., and Huganir, R.L. (2005). Differential regulation of AMPA receptor subunit trafficking by palmitoylation of two distinct sites. *Neuron* 47, 709–723.

Hebb, D.O. (1949). *The Organization of Behavior; A Neuropsychological Theory*. *Am. J. Psychol.* 63, 633.

Heine, M., Groc, L., Frischknecht, R., Béïque, J.-C., Lounis, B., Rumbaugh, G., Huganir, R.L., Cognet, L., and Choquet, D. (2008). Surface mobility of postsynaptic AMPARs tunes synaptic transmission. *Science* 320, 201–205.

Henley, J.M., and Wilkinson, K.A. (2016). Synaptic AMPA receptor composition in development, plasticity and disease. *Nat. Rev. Neurosci. advance on*, 337–350.

Hjelmstad, G.O., Nicoll, R.A., and Malenka, R.C. (1997). Synaptic refractory period provides a measure of probability of release in the hippocampus. *Neuron* 19, 1309–1318.

Hofer, S.B., Mrsic-Flogel, T.D., Bonhoeffer, T., and Hübener, M. (2009). Experience leaves a lasting structural trace in cortical circuits. *Nature* 457, 313–317.

Hollmann, M. (1994). Cloned Glutamate Receptors. *Annu. Rev. Neurosci.* 17, 31–108.

Holtmaat, A., and Svoboda, K. (2009). Experience-dependent structural synaptic plasticity in the mammalian brain. *Nat. Rev. Neurosci.* 10, 647–658.

Holtmaat, A., Wilbrecht, L., Knott, G.W., Welker, E., and Svoboda, K. (2006). Experience-dependent and cell-type-specific spine growth in the neocortex. *Nature* 441, 979–983.

Hosy, E., Butler, C., and Sibarita, J.B. (2014). Organization and dynamics of AMPA receptors inside synapses-nano-organization of AMPA receptors and main synaptic scaffolding proteins revealed by super-resolution imaging. *Curr. Opin. Chem. Biol.* 20, 120–

126.

Hruska, M., Henderson, N.T., Xia, N.L., Le Marchand, S.J., and Dalva, M.B. (2015). Anchoring and synaptic stability of PSD-95 is driven by ephrin-B3. *Nat. Neurosci.* *18*, 1594–1605.

Hruska, M., Henderson, N., Le Marchand, S.J., Jafri, H., and Dalva, M.B. (2018). Synaptic nanomodules underlie the organization and plasticity of spine synapses. *Nat. Neurosci.* *21*, 671–682.

Huang, C.C., You, J.L., Lee, C.C., and Hsu, K. Sen (2003). Insulin induces a novel form of postsynaptic mossy fiber long-term depression in the hippocampus. *Mol. Cell. Neurosci.* *24*, 831–841.

Hubel, D.H., and Wiesel, T.N. (1965). Binocular interaction reared in striate artificial cortex squint. *J. Neurophysiol.* *28*, 1041–1059.

Huganir, R.L., and Nicoll, R.A. (2013). AMPARs and synaptic plasticity: The last 25 years. *Neuron* *80*, 704–717.

Hunt, C.A., Schenker, L.J., and Kennedy, M.B. (1996). PSD-95 is associated with the postsynaptic density and not with the presynaptic membrane at forebrain synapses. *J. Neurosci.* *16*.

Huttenlocher, P.R. (1990). Morphometric study of human cerebral cortex development. *Neuropsychologia* *28*, 517–527.

## I

Isaac, J.T.R., Nicoll, R.A., and Malenka, R.C. (1995). Evidence for silent synapses: Implications for the expression of LTP. *Neuron* *15*, 427–434.

## J

Jackson, A.C., and Nicoll, R.A. (2011). The Expanding Social Network of Ionotropic Glutamate Receptors: TARPs and Other Transmembrane Auxiliary Subunits. *Neuron* *70*, 178–199.

Jacobi, E., and von Engelhardt, J. (2018). AMPA receptor complex constituents: Control of receptor assembly, membrane trafficking and subcellular localization. *Mol. Cell. Neurosci.* *91*, 67–75.

Jeyifous, O., Lin, E.I., Chen, X., Antinone, S.E., Mastro, R., Drisdell, R., Reese, T.S., and Green, W.N. (2016). Palmitoylation regulates glutamate receptor distributions in Postsynaptic densities through control of PSD95 conformation and orientation. *Proc. Natl. Acad. Sci. U. S. A.* *113*, E8482–E8491.

Jung, J.H., Kirk, L.M., Bourne, J.N., and Harris, K.M. (2021). Shortened tethering filaments stabilize presynaptic vesicles in support of elevated release probability during LTP in

rat hippocampus. *Proc. Natl. Acad. Sci. U. S. A.* 118, 1–8.

## K

Kaech, S., and Banker, G. (2006). Culturing hippocampal neurons. *Nat. Protoc.* 1, 2406–2415.

Kavalali, E.T. (2015). The mechanisms and functions of spontaneous neurotransmitter release. *Nat. Rev. Neurosci.* 16, 5–16.

Kellermayer, B., Ferreira, J.S., Dupuis, J., Levet, F., Grillo-Bosch, D., Bard, L., Linares-Loyez, J., Bouchet, D., Choquet, D., Rusakov, D.A., et al. (2018). Differential Nanoscale Topography and Functional Role of GluN2-NMDA Receptor Subtypes at Glutamatergic Synapses. *Neuron* 100.

Kim, M.J., Futai, K., Jo, J., Hayashi, Y., Cho, K., and Sheng, M. (2007). Synaptic Accumulation of PSD-95 and Synaptic Function Regulated by Phosphorylation of Serine-295 of PSD-95. *Neuron* 56, 488–502.

Klaassen, R. V, Stroeder, J., Coussen, F., Hafner, A.-S., Petersen, J.D., Renancio, C., Schmitz, L.J.M., Normand, E., Lodder, J.C., Rotaru, D.C., et al. (2016). Shisa6 traps AMPA receptors at postsynaptic sites and prevents their desensitization during synaptic activity. *Nat. Commun.* 7, 10682.

Knott, G.W., Holtmaat, A., Wilbrecht, L., Welker, E., and Svoboda, K. (2006). Spine growth precedes synapse formation in the adult neocortex in vivo. *Nat. Neurosci.* 9, 1117–1124.

Ko, J., Fuccillo, M. V., Malenka, R.C., and Südhof, T.C. (2009). LRRTM2 Functions as a Neurexin Ligand in Promoting Excitatory Synapse Formation. *Neuron* 64, 791–798.

Koehl, A., Hu, H., Feng, D., Sun, B., Zhang, Y., Robertson, M.J., Chu, M., Kobilka, T.S., Laermans, T., Steyaert, J., et al. (2019). Structural insights into the activation of metabotropic glutamate receptors. *Nature* 566, 79–84.

Koike-Tani, M., Kanda, T., Saitoh, N., Yamashita, T., and Takahashi, T. (2008). Involvement of AMPA receptor desensitization in short-term synaptic depression at the calyx of Held in developing rats. *J. Physiol.* 586, 2263–2275.

Kornau, H.C., Schenker, L.T., Kennedy, M.B., and Seeburg, P.H. (1995). Domain interaction between NMDA receptor subunits and the postsynaptic density protein PSD-95. *Science* (80- ). 269.

Kreitzer, A.C., and Malenka, R.C. (2007). Endocannabinoid-mediated rescue of striatal LTD and motor deficits in Parkinson's disease models. *Nature* 445, 643–647.

Kuriu, T., Inoue, A., Bito, H., Sobue, K., and Okabe, S. (2006). Differential control of postsynaptic density scaffolds via actin-dependent and -independent mechanisms. *J. Neurosci.* 26, 7693–7706.



# L

Lai, C.S.W., Franke, T.F., and Gan, W.B. (2012). Opposite effects of fear conditioning and extinction on dendritic spine remodelling. *Nature* 483, 87–92.

LaMantia, A.S., and Rakic, P. (1990). Axon overproduction and elimination in the corpus callosum of the developing rhesus monkey. *J. Neurosci.* 10, 2156–2175.

Lang, C., Barco, A., Zablow, L., Kandel, E.R., Siegelbaum, S.A., and Zakharenko, S.S. (2004). Transient expansion of synaptically connected dendritic spines upon induction of hippocampal long-term potentiation. *Proc. Natl. Acad. Sci. U. S. A.* 101, 16665–16670.

Lanoue, V., Usardi, A., Sigoillot, S.M., Talleur, M., Iyer, K., Mariani, J., Isope, P., Vodjdani, G., Heintz, N., and Selimi, F. (2013). The adhesion-GPCR BAI3, a gene linked to psychiatric disorders, regulates dendrite morphogenesis in neurons. *Mol. Psychiatry* 18, 943–950.

Lee, H.-K., Takamiya, K., Han, J.-S., Man, H., Kim, C.-H., Rumbaugh, G., Yu, S., Ding, L., He, C., Petralia, R.S., et al. (2003). Phosphorylation of the AMPA Receptor GluR1 Subunit Is Required for Synaptic Plasticity and Retention of Spatial Memory. *Cell* 112, 631–643.

Lee, H.K., Kameyama, K., Huganir, R.L., and Bear, M.F. (1998). NMDA induces long-term synaptic depression and dephosphorylation of the GluR1 subunit of AMPA receptors in hippocampus. *Neuron* 21, 1151–1162.

Lee, H.K., Barbarosie, M., Kameyama, K., Bear, M.F., and Huganir, R.L. (2000). Regulation of distinct AMPA receptor phosphorylation sites during bidirectional synaptic plasticity. *Nature* 405, 955–959.

Lee, H.K., Takamiya, K., He, K., Song, L., and Huganir, R.L. (2010). Specific roles of AMPA receptor subunit GluR1 (GluA1) phosphorylation sites in regulating synaptic plasticity in the CA1 region of hippocampus. *J. Neurophysiol.* 103, 479–489.

Levet, F., Hosy, E., Kechkar, A., Butler, C., Beghin, A., Choquet, D., and Sibarita, J.-B. (2015). SR-Tesseler: a method to segment and quantify localization-based super-resolution microscopy data. *Nat. Methods* 12, 1065–1071.

Levy, W.B., and Steward, O. (1983). Temporal contiguity requirements for long-term associative potentiation/depression in the hippocampus. *Neuroscience* 8.

Levy, J.M., Chen, X., Reese, T.S., and Nicoll, R.A. (2015). Synaptic Consolidation Normalizes AMPAR Quantal Size following MAGUK Loss. *Neuron* 87, 534–548.

Li, S., Raychaudhuri, S., Lee, S.A., Brockmann, M.M., Wang, J., Kusick, G., Prater, C., Syed, S., Falahati, H., Ramos, R., et al. (2021). Asynchronous release sites align with NMDA receptors in mouse hippocampal synapses. *Nat. Commun.* 12, 1–13.

Li, W., Ma, L., Yang, G., and Gan, W.B. (2017). REM sleep selectively prunes and maintains new synapses in development and learning. *Nat. Neurosci.* 20, 427–437.

Liao, D., Zhang, X., O'Brien, R., Ehlers, M.D., and Huganir, R.L. (1999). Regulation of morphological postsynaptic silent synapses in developing hippocampal neurons. *Nat. Neurosci.* 2, 37–43.

Lisman, J.E., and Spruston, N. (2005). Postsynaptic depolarization requirements for

LTP and LTD: A critique of spike timing-dependent plasticity Molecular mechanism of synaptic memory View project EM tomography View project. *Nat. Neurosci.* 8, 839–841.

Lisman, J., Yasuda, R., and Raghavachari, S. (2012). Mechanisms of CaMKII action in long-term potentiation. *Nat. Rev. Neurosci.* 13, 169–182.

Lisman, J.E., Raghavachari, S., and Tsien, R.W. (2007). The sequence of events that underlie quantal transmission at central glutamatergic synapses. *Nat. Rev. Neurosci.* 8, 597–609.

Lledo, P.M., Zhang, X., Südhof, T.C., Malenka, R.C., and Nicoll, R.A. (1998). Postsynaptic membrane fusion and long-term potentiation. *Science* (80-. ). 279, 399–403.

Lodge, D. (2009). The history of the pharmacology and cloning of ionotropic glutamate receptors and the development of idiosyncratic nomenclature. *Neuropharmacology* 56, 6–21.

Lu, W., Shi, Y., Jackson, A.C., Bjorgan, K., During, M.J., Sprengel, R., Seeburg, P.H., and Nicoll, R.A. (2009). Subunit Composition of Synaptic AMPA Receptors Revealed by a Single-Cell Genetic Approach. *Neuron* 62, 254–268.

Lu, W.Y., Man, H.Y., Ju, W., Trimble, W.S., MacDonald, J.F., and Wang, Y.T. (2001). Activation of synaptic NMDA receptors induces membrane insertion of new AMPA receptors and LTP in cultured hippocampal neurons. *Neuron* 29, 243–254.

Lua, W., Isozaki, K., Roche, K.W., and Nicoll, R.A. (2010). Synaptic targeting of AMPA receptors is regulated by a CaMKII site in the first intracellular loop of GluA1. *Proc. Natl. Acad. Sci. U. S. A.* 107, 22266–22271.

Lüscher, C., Nicoll, R.A., Malenka, R.C., and Muller, D. (2000). Synaptic plasticity and dynamic modulation of the postsynaptic membrane The biochemical composition of the postsynaptic membrane and the structure of dendritic spines may be rapidly modulated by synaptic activity. Here we review these findings, discuss th. *Nat. Rev. Neurosci.* 545–550.

Lynch, G.S., Dunwiddie, T., and Gribkoff, V. (1977). Heterosynaptic depression: A postsynaptic correlate of long-term potentiation [31]. *Nature* 266, 737–739.

## M

MacGillavry, H.D., Song, Y., Raghavachari, S., and Blanpied, T.A. (2013). Nanoscale scaffolding domains within the postsynaptic density concentrate synaptic ampa receptors. *Neuron* 78, 615–622.

Magee, J.C., and Johnston, D. (1997). A synaptically controlled, associative signal for Hebbian plasticity in hippocampal neurons. *Science* (80-. ). 275, 209–213.

Makino, H., and Malinow, R. (2009). AMPA Receptor Incorporation into Synapses during LTP: The Role of Lateral Movement and Exocytosis. *Neuron* 64, 381–390.

Man, H.Y., Lin, J.W., Ju, W.H., Ahmadian, G., Liu, L., Becker, L.E., Sheng, M., and Wang, Y.T. (2000). Regulation of AMPA receptor-mediated synaptic transmission by clathrin-dependent receptor internalization. *Neuron* 25, 649–662.

Markram, H., Lübke, J., Frotscher, M., and Sakmann, B. (1997). Regulation of synaptic efficacy by coincidence of postsynaptic APs and EPSPs. *Science* (80-. ). 275, 213–215.

- Martineau, M., Baux, G., and Mothet, J.P. (2006). d-Serine signalling in the brain: friend and foe. *Trends Neurosci.* 29, 481–491.
- Matsuda, S., Kakegawa, W., Budisantoso, T., Nomura, T., Kohda, K., and Yuzaki, M. (2013). Stargazin regulates AMPA receptor trafficking through adaptor protein complexes during long-term depression. *Nat. Commun.* 4.
- Matsuzaki, M., Ellis-Davies, G.C.R., Nemoto, T., Miyashita, Y., Iino, M., and Kasai, H. (2001). Dendritic spine geometry is critical for AMPA receptor expression in hippocampal CA1 pyramidal neurons. *Nat. Neurosci.* 4, 1086–1092.
- Matsuzaki, M., Honkura, N., Ellis-Davies, G.C.R., and Kasai, H. (2004). Structural basis of long-term potentiation in single dendritic spines. *Nature* 429, 761–766.
- Matt, L., Kim, K., Chowdhury, D., and Hell, J.W. (2019). Role of palmitoylation of postsynaptic proteins in promoting synaptic plasticity. *Front. Mol. Neurosci.* 12, 1–19.
- Meier, J., Vannier, C., Sergé, A., Triller, A., and Choquet, D. (2001). Fast and reversible trapping of surface glycine receptors by gephyrin. *Nat. Neurosci.* 4, 253–260.
- Meyerson, J.R., Kumar, J., Chittori, S., Rao, P., Pierson, J., Bartesaghi, A., Mayer, M.L., and Subramaniam, S. (2014). Structural mechanism of glutamate receptor activation and desensitization. *Nature* 514, 328–334.
- Mignogna, M.L., Giannandrea, M., Gurgone, A., Fanelli, F., Raimondi, F., Mapelli, L., Bassani, S., Fang, H., Van Anken, E., Alessio, M., et al. (2015). The intellectual disability protein RAB39B selectively regulates GluA2 trafficking to determine synaptic AMPAR composition. *Nat. Commun.* 6.
- Miguez-Cabello, F., Sánchez-Fernández, N., Yefimenko, N., Gasull, X., Gratacòs-Batlle, E., and Soto Del Cerro, D. (2020). AMPAR/TARP stoichiometry differentially modulates channel properties. *Elife* 9, 1.
- Moretto, E., Longatti, A., Murru, L., Chamma, I., Sessa, A., Zapata, J., Hosy, E., Sainlos, M., Saint-Pol, J., Rubinstein, E., et al. (2019). TSPAN5 Enriched Microdomains Provide a Platform for Dendritic Spine Maturation through Neuroligin-1 Clustering. *Cell Rep.* 29, 1130–1146.e8.
- Mothet, J.P., Parent, A.T., Wolosker, H., Brady, R.O., Linden, D.J., Ferris, C.D., Rogawski, M.A., and Snyder, S.H. (2000). D-serine is an endogenous ligand for the glycine site of the N-methyl-D-aspartate receptor. *Proc. Natl. Acad. Sci. U. S. A.* 97, 4926–4931.
- Mulkey, R.M., and Malenka, R.C. (1992). Mechanisms underlying induction of homosynaptic long-term depression in area CA1 of the hippocampus. *Neuron* 9, 967–975.
- Mulkey, R.M., Herron, C.E., and Malenka, R.C. (1993). An essential role for protein phosphatases in hippocampal long-term depression. *Science* (80-. ). 261, 1051–1055.
- Mulkey, R.M., Endo, S., Shenolikar, S., and Malenka, R.C. (1994). Involvement of a calcineurin/inhibitor-1 phosphatase cascade in hippocampal long-term depression. *Nature* 369, 486–488.
- Murakoshi, H., Shin, M.E., Parra-Bueno, P., Szatmari, E.M., Shibata, A.C.E., and Yasuda, R. (2017). Kinetics of Endogenous CaMKII Required for Synaptic Plasticity Revealed by Optogenetic Kinase Inhibitor. *Neuron* 94, 37–47.e5.

# N

Nabavi, S., Fox, R., Proulx, C.D., Lin, J.Y., Tsien, R.Y., and Malinow, R. (2014). Engineering a memory with LTD and LTP. *Nature* 511, 348–352.

Nägerl, U.V., Eberhorn, N., Cambridge, S.B., and Bonhoeffer, T. (2004). Bidirectional activity-dependent morphological plasticity in hippocampal neurons. *Neuron* 44, 759–767.

Nägerl, U.V., Köstinger, G., Anderson, J.C., Martin, K.A.C., and Bonhoeffer, T. (2007). Protracted synaptogenesis after activity-dependent spinogenesis in hippocampal neurons. *J. Neurosci.* 27, 8149–8156.

Nair, D., Hosy, E., Petersen, J.D., Constals, A., Giannone, G., Choquet, D., and Sibarita, J.-B. (2013). Super-resolution imaging reveals that AMPA receptors inside synapses are dynamically organized in nanodomains regulated by PSD95. *J. Neurosci.* 33, 13204–13224.

Nakayama, D., Iwata, H., Teshirogi, C., Ikegaya, Y., Matsuki, N., and Nomura, H. (2015). Long-delayed expression of the immediate early gene *Arc/Arg3.1* refines neuronal circuits to perpetuate fear memory. *J. Neurosci.* 35, 819–830.

Naur, P., Hansen, K.B., Kristensen, A.S., Dravid, S.M., Pickering, D.S., Olsen, L., Vestergaard, B., Egebjerg, J., Gajhede, M., Traynelis, S.F., et al. (2007). Ionotropic glutamate-like receptor  $\delta 2$  binds D-serine and glycine. *Proc. Natl. Acad. Sci. U. S. A.* 104, 14116–14121.

Nelson, C.D., Kim, M.J., Hsin, H., Chen, Y., and Sheng, M. (2013). Phosphorylation of Threonine-19 of PSD-95 by GSK-3 is Required for PSD-95 Mobilization and Long-Term Depression. *J. Neurosci.* 33, 12122–12135.

Nicholls, R.E., Alarcon, J.M., Malleret, G., Carroll, R.C., Grody, M., Vronskaya, S., and Kandel, E.R. (2008). Transgenic Mice Lacking NMDAR-Dependent LTD Exhibit Deficits in Behavioral Flexibility. *Neuron* 58, 104–117.

Nicoll, R.A., Tomita, S., and Brecht, D.S. (2006). Auxiliary subunits assist AMPA-type glutamate receptors. *Science* (80- ). 311, 1253–1256.

Nimchinsky, E.A., Sabatini, B.L., and Svoboda, K. (2002). Structure and function of dendritic spines. *Annu. Rev. Physiol.* 64, 313–353.

Nishiyama, J., and Yasuda, R. (2015). Biochemical Computation for Spine Structural Plasticity. *Neuron* 87, 63–75.

Noguchi, J., Hayama, T., Watanabe, S., Ucar, H., Yagishita, S., Takahashi, N., and Kasai, H. (2016). State-dependent diffusion of actin-depolymerizing factor/cofilin underlies the enlargement and shrinkage of dendritic spines. *Sci. Rep.* 6, 1–9.

Nosov, G., Kahms, M., and Klingauf, J. (2020). The Decade of Super-Resolution Microscopy of the Presynapse. *Front. Synaptic Neurosci.* 12, 1–17.

# O

Oh, W.C., Hill, T.C., and Zito, K. (2013). Synapse-specific and size-dependent mechanisms of spine structural plasticity accompanying synaptic weakening. *Proc. Natl. Acad. Sci. U. S. A.* *110*.

Oh, W.C., Parajuli, L.K., and Zito, K. (2015). Heterosynaptic structural plasticity on local dendritic segments of hippocampal CA1 neurons. *Cell Rep.* *10*, 162–169.

Okabe, S. (2007). Molecular anatomy of the postsynaptic density. *Mol. Cell. Neurosci.* *34*, 503–518.

Okamoto, K.I., Nagai, T., Miyawaki, A., and Hayashi, Y. (2004). Rapid and persistent modulation of actin dynamics regulates postsynaptic reorganization underlying bidirectional plasticity. *Nat. Neurosci.* *7*, 1104–1112.

Oliet, S.H.R., Malenka, R.C., and Nicoll, R.A. (1997). Two distinct forms of long-term depression coexist in CA1 hippocampal pyramidal cells. *Neuron* *18*, 969–982.

Opazo, P., Labrecque, S., Tigaret, C.M., Frouin, A., Wiseman, P.W., De Koninck, P., and Choquet, D. (2010). CaMKII triggers the diffusional trapping of surface AMPARs through phosphorylation of stargazin. *Neuron* *67*, 239–252.

Otis, T., Zhang, S., and Trussell, L.O. (1996). Direct measurement of AMPA receptor desensitization induced by glutamatergic synaptic transmission. *J. Neurosci.* *16*, 7496–7504.

# P

Palay, S.L. (1956). Synapses in the central nervous system. *J. Biophys. Biochem. Cytol.* *2*.

Palay, S.L., and Palade, G.E. (1955). The fine structure of neurons. *J. Biophys. Biochem. Cytol.* *1*.

Panatier, A., Theodosis, D.T., Mothet, J.P., Touquet, B., Pollegioni, L., Poulain, D.A., and Oliet, S.H.R. (2006). Glia-Derived d-Serine Controls NMDA Receptor Activity and Synaptic Memory. *Cell* *125*, 775–784.

Panatier, A., Vallée, J., Haber, M., Murai, K.K., Lacaille, J.C., and Robitaille, R. (2011). Astrocytes are endogenous regulators of basal transmission at central synapses. *Cell* *146*, 785–798.

Park, M., Penick, E.C., Edwards, J.G., Kauer, J.A., and Ehlers, M.D. (2004). Recycling endosomes supply AMPA receptors for LTP. *Science (80- )*. *305*, 1972–1975.

Pascual, O., Casper, K.B., Kubera, C., Zhang, J., Revilla-Sanchez, R., Sul, J.Y., Takano, H., Moss, S.J., McCarthy, K., and Haydon, P.G. (2005). Neurobiology: Astrocytic purinergic signaling coordinates synaptic networks. *Science (80- )*. *310*, 113–116.

Penn, A.C., Balik, A., Wozny, C., Cais, O., and Greger, I.H. (2012). Activity-Mediated AMPA Receptor Remodeling, Driven by Alternative Splicing in the Ligand-Binding Domain.

Neuron 76, 503–510.

Penn, A.C., Zhang, C.L., Georges, F., Royer, L., Breillat, C., Hosy, E., Petersen, J.D., Humeau, Y., and Choquet, D. (2017). Hippocampal LTP and contextual learning require surface diffusion of AMPA receptors. *Nature* 549, 384–388.

Petrini, E.M., Lu, J., Cognet, L., Lounis, B., Ehlers, M.D., and Choquet, D. (2009). Endocytic trafficking and recycling maintain a pool of mobile surface AMPA receptors required for synaptic potentiation. *Neuron* 63, 92–105.

Piochon, C., Kano, M., and Hansel, C. (2016). LTD-like molecular pathways in developmental synaptic pruning. *Nat. Neurosci.* 19, 1299–1310.

Pougnnet, J.-T., Compans, B., Martinez, A., Choquet, D., Hosy, E., and Boué-Grabot, E. (2016). P2X-mediated AMPA receptor internalization and synaptic depression is controlled by two CaMKII phosphorylation sites on GluA1 in hippocampal neurons. *Sci. Rep.* 6, 31836.

Pougnnet, J.T., Toulme, E., Martinez, A., Choquet, D., Hosy, E., and Boué-Grabot, E. (2014). ATP P2X receptors downregulate AMPA receptor trafficking and postsynaptic efficacy in hippocampal neurons. *Neuron* 83, 417–430.

## R

Raghavachari, S., and Lisman, J.E. (2004). Properties of quantal transmission at CA1 synapses. *J. Neurophysiol.* 92, 2456–2467.

Reid, C.A., Dixon, D.B., Takahashi, M., Bliss, T.V.P., and Fine, A. (2004). Optical Quantal Analysis Indicates that Long-Term Potentiation at Single Hippocampal Mossy Fiber Synapses is Expressed through Increased Release Probability, Recruitment of New Release Sites, and Activation of Silent Synapses. *J. Neurosci.* 24, 3618–3626.

Robert, A., and Howe, J.R. (2003). How AMPA receptor desensitization depends on receptor occupancy. *J. Neurosci.* 23, 847–858.

De Robertis, E.D.P., and Bennett, H.S. (1954). A submicroscopic vesicular component of Schwann cells and nerve satellite cells. *Exp. Cell Res.* 6.

De Robertis, E.D.P., and Bennett, H.S. (1955). Some features of the submicroscopic morphology of synapses in frog and earthworm\*. *J. Biophys. Biochem. Cytol.* 1.

Rosendale, M., Jullié, D., Choquet, D., and Perrais, D. (2017). Spatial and Temporal Regulation of Receptor Endocytosis in Neuronal Dendrites Revealed by Imaging of Single Vesicle Formation. *Cell Rep.* 18, 1840–1847.

Rosenmund, C., Stern-Bach, Y., and Stevens, C.F. (1998). The tetrameric structure of a glutamate receptor channel. *Science* (80-. ). 280, 1596–1599.

Rotman, Z., Deng, P.Y., and Klyachko, V.A. (2011). Short-term plasticity optimizes synaptic information transmission. *J. Neurosci.* 31, 14800–14809.

# S

Sainlos, M., Tigaret, C., Poujol, C., Olivier, N.B., Bard, L., Breillat, C., Thiolon, K., Choquet, D., and Imperiali, B. (2011). Biomimetic divalent ligands for the acute disruption of synaptic AMPAR stabilization. *Nat. Chem. Biol.* 7, 81–91.

Salin, P.A., Scanziani, M., Malenka, R.C., and Nicoll, R.A. (1996). Distinct short-term plasticity at two excitatory synapses in the hippocampus. *Proc. Natl. Acad. Sci. U. S. A.* 93, 13304–13309.

Sanders, J., Cowansage, K., Baumgärtel, K., and Mayford, M. (2012). Elimination of dendritic spines with long-term memory is specific to active circuits. *J. Neurosci.* 32, 12570–12578.

Sanderson, J.L., Gorski, J. a., and Dell'Acqua, M.L. (2016). NMDA Receptor-Dependent LTD Requires Transient Synaptic Incorporation of Ca<sup>2+</sup>-Permeable AMPARs Mediated by AKAP150-Anchored PKA and Calcineurin. *Neuron* 89, 1000–1015.

Savtchenko, L.P., and Rusakov, D.A. (2014). Moderate AMPA receptor clustering on the nanoscale can efficiently potentiate synaptic current. *Philos. Trans. R. Soc. B Biol. Sci.* 369.

Scheefhals, N., and MacGillavry, H.D. (2018). Functional organization of postsynaptic glutamate receptors. *Mol. Cell. Neurosci.* 91, 82–94.

Scheefhals, N., Catsburg, L.A.E., Westerveld, M.L., Blanpied, T.A., Hoogenraad, C.C., and MacGillavry, H.D. (2019). Shank Proteins Couple the Endocytic Zone to the Postsynaptic Density to Control Trafficking and Signaling of Metabotropic Glutamate Receptor 5. *Cell Rep.* 29, 258–269.e8.

Schneggenburger Ralf, and Neher Erwin (2000). Intracellular calcium dependence of transmitter release rates at a fast central synapse. *Nature* 406, 889–893.

Schneider, R., Hosy, E., Kohl, J., Klueva, J., Choquet, D., Thomas, U., Voigt, A., and Heine, M. (2015). Mobility of Calcium Channels in the Presynaptic Membrane. *Neuron* 86, 672–679.

Schnell, E., Sizemore, M., Karimzadegan, S., Chen, L., Bredt, D.S., and Nicoll, R.A. (2002). Direct interactions between PSD-95 and stargazin control synaptic AMPA receptor number. *Proc. Natl. Acad. Sci.* 99, 13902–13907.

Scholl, B., Thomas, C.I., Ryan, M.A., Kamasawa, N., and Fitzpatrick, D. (2021). Cortical response selectivity derives from strength in numbers of synapses. *Nature* 590, 111–114.

Schwenk, J., Harmel, N., Brechet, A., Zolles, G., Berkefeld, H., Müller, C.S., Bildl, W., Baehrens, D., Hüber, B., Kulik, A., et al. (2012). High-Resolution Proteomics Unravel Architecture and Molecular Diversity of Native AMPA Receptor Complexes. *Neuron* 74, 621–633.

Schwenk, J., Baehrens, D., Haupt, A., Bildl, W., Boudkkazi, S., and Roeper, J. (2014). Regional Diversity and Developmental Dynamics of the AMPA-Receptor Proteome in the Mammalian Brain. *Neuron* 1–14.

Scimemi, A., and Diamond, J.S. (2012). The number and organization of Ca<sup>2+</sup> channels in the active zone shapes neurotransmitter release from schaffer collateral synapses. *J. Neurosci.* 32, 18157–18176.

Sharma, K., Fong, D.K., and Craig, A.M. (2006). Postsynaptic protein mobility in dendritic spines: Long-term regulation by synaptic NMDA receptor activation. *Mol. Cell. Neurosci.* *31*, 702–712.

Sharonov, A., and Hochstrasser, R.M. (2006). Wide-field subdiffraction imaging by accumulated binding of diffusing probes. *Proc. Natl. Acad. Sci. U. S. A.* *103*, 18911–18916.

Sheng, M., and Kim, E. (2011). The postsynaptic organization of synapses. *Cold Spring Harb. Perspect. Biol.* *3*.

Sigoillot, S.M., Iyer, K., Binda, F., González-Calvo, I., Talleur, M., Vodjdani, G., Isope, P., and Selimi, F. (2015). The secreted protein C1QL1 and its receptor BAI3 control the synaptic connectivity of excitatory inputs converging on cerebellar purkinje cells. *Cell Rep.* *10*, 820–832.

Singer, S.J., and Nicolson, G.L. (1972). The fluid mosaic model of the structure of cell membranes. *Science* (80-. ). *175*.

Sjöström, P.J., Turrigiano, G.G., and Neslon, S.B. (2001). Rate, Timing, and Cooperativity Jointly Determine Cortical Synaptic Plasticity. *Proc. Zool. Soc. London* *79*, 897–912.

Sjöström, P.J., Rancz, E.A., Roth, A., and Häusser, M. (2008). Dendritic excitability and synaptic plasticity. *Physiol. Rev.* *88*, 769–840.

Sobolevsky, A.I., Rosconi, M.P., and Gouaux, E. (2009). X-ray structure, symmetry and mechanism of an AMPA-subtype glutamate receptor. *Nature* *462*, 745–756.

Spruston, N. (2008). Pyramidal neurons: Dendritic structure and synaptic integration. *Nat. Rev. Neurosci.* *9*, 206–221.

Stanton, P.K., and Sejnowski, T.J. (1989). Associative long-term depression in the hippocampus induced by hebbian covariance. *Nature* *339*, 215–218.

Stein, I.S., and Zito, K. (2019). Dendritic Spine Elimination: Molecular Mechanisms and Implications. *Neuroscientist* *25*, 27–47.

Stein, I.S., Park, D.K., Flores, J.C., Jahncke, J.N., and Zito, K. (2020). Molecular Mechanisms of Non-ionotropic NMDA Receptor Signaling in Dendritic Spine Shrinkage. *J. Neurosci.* *40*, 3741–3750.

Stent, G.S. (1973). A physiological mechanism for Hebb's postulate of learning. *Proc. Natl. Acad. Sci. U. S. A.* *70*, 997–1001.

Subramanian, J., Michel, K., Benoit, M., and Nedivi, E. (2019). CPG15/Neuritin Mimics Experience in Selecting Excitatory Synapses for Stabilization by Facilitating PSD95 Recruitment. *Cell Rep.* *28*, 1584–1595.e5.

Südhof, T.C. (2017). Synaptic Neurexin Complexes: A Molecular Code for the Logic of Neural Circuits. *Cell* *171*, 745–769.

Sumioka, A., Yan, D., and Tomita, S. (2010). TARP Phosphorylation Regulates Synaptic AMPA Receptors through Lipid Bilayers. *Neuron* *66*, 755–767.

Sumioka, A., Brown, T.E., Kato, A.S., Bredt, D.S., Kauer, J.A., and Tomita, S. (2011). PDZ binding of TARPy-8 controls synaptic transmission but not synaptic plasticity. *Nat. Neurosci.* *14*, 1410–1412.

Sun, Y., Olson, R., Horning, M., Armstrong, N., Mayer, M., and Gouaux, E. (2002). Mechanism of glutamate receptor desensitization. *Nature* *417*, 245–253.



Swanson, G.T., Kamboj, S.K., and Cull-Candy, S.G. (1997). Single-channel properties of recombinant AMPA receptors depend on RNA editing, splice variation, and subunit composition. *J. Neurosci.* *17*, 58–69.

## T

Tang, A.-H., Chen, H., Li, T.P., Metzbower, S.R., MacGillavry, H.D., and Blanpied, T.A. (2016). A trans-synaptic nanocolumn aligns neurotransmitter release to receptors. *Nature* *536*, 210–214.

Tardin, C., Cognet, L., Bats, C., Lounis, B., and Choquet, D. (2003). Direct imaging of lateral movements of AMPA receptors inside synapses. *EMBO J.* *22*, 4656–4665.

Tarusawa, E., Matsui, K., Budisantoso, T., Molnar, E., Watanabe, M., Matsui, M., Fukazawa, Y., and Shigemoto, R. (2009). Input-Specific Intrasympaptic Arrangements of Ionotropic Glutamate Receptors and Their Impact on Postsynaptic Responses. *J. Neurosci.* *29*, 12896–12908.

Tazerart, S., Mitchell, D.E., Miranda-Rottmann, S., and Araya, R. (2020). A spike-timing-dependent plasticity rule for dendritic spines. *Nat. Commun.* *11*.

Thomazeau, A., Bosch, M., Essayan-Perez, S., Barnes, S.A., De Jesus-Cortes, H., and Bear, M.F. (2020). Dissociation of functional and structural plasticity of dendritic spines during NMDAR and mGluR-dependent long-term synaptic depression in wild-type and fragile X model mice. *Mol. Psychiatry*.

Tomita, S., Chen, L., Kawasaki, Y., Petralia, R.S., Wenthold, R.J., Nicoll, R.A., and Brecht, D.S. (2003). Functional studies and distribution define a family of transmembrane AMPA receptor regulatory proteins. *J. Cell Biol.* *161*, 805–816.

Tomita, S., Adesnik, H., Sekiguchi, M., Zhang, W., Wada, K., Howe, J.R., Nicoll, R. a, and Brecht, D.S. (2005a). Stargazin modulates AMPA receptor gating and trafficking by distinct domains. *Nature* *435*, 1052–1058.

Tomita, S., Stein, V., Stocker, T.J., Nicoll, R.A., and Brecht, D.S. (2005b). Bidirectional synaptic plasticity regulated by phosphorylation of stargazin-like TARPs. *Neuron* *45*, 269–277.

Tønnesen, J., and Nägerl, U.V. (2016). Dendritic spines as tunable regulators of synaptic signals. *Front. Psychiatry* *7*.

Tønnesen, J., Katona, G., Rózsa, B., and Nägerl, U.V. (2014). Spine neck plasticity regulates compartmentalization of synapses. *Nat. Neurosci.* *17*, 678–685.

Traynelis, S.F., Wollmuth, L.P., McBain, C.J., Menniti, F.S., Vance, K.M., Ogden, K.K., Hansen, K.B., Yuan, H., Myers, S.J., and Dingledine, R. (2010). Glutamate Receptor Ion Channels: Structure, Regulation, and Function. *Pharmacol. Rev.* *62*, 405–496.

Trommald, M., and Hulleberg, G. (1997). Dimensions and density of dendritic spines from rat dentate granule cells based on reconstructions from serial electron micrographs. *J. Comp. Neurol.* *377*, 15–28.

Trussell, L.O., Zhang, S., and Ramant, I.M. (1993). Desensitization of AMPA receptors upon multiquantal neurotransmitter release. *Neuron* *10*, 1185–1196.

Tschida, K.A., and Mooney, R. (2012). Deafening Drives Cell-Type-Specific Changes

to Dendritic Spines in a Sensorimotor Nucleus Important to Learned Vocalizations. *Neuron* 73, 1028–1039.

Turecek, R., and Trussell, L.O. (2000). Control of synaptic depression by glutamate transporters. *J. Neurosci.* 20, 2054–2063.

## V

Valnegri, P., Khelifaoui, M., Dorseuil, O., Bassani, S., Lagneaux, C., Gianfelice, A., Benfante, R., Chelly, J., Billuart, P., Sala, C., et al. (2011). A circadian clock in hippocampus is regulated by interaction between oligophrenin-1 and Rev-erba. *Nat. Neurosci.* 14, 1293–1301.

De Vivo, L., Bellesi, M., Marshall, W., Bushong, E.A., Ellisman, M.H., Tononi, G., and Cirelli, C. (2017). Ultrastructural evidence for synaptic scaling across the wake/sleep cycle. *Science* (80-. ). 355, 507–510.

Vyklicky, V., Korinek, M., Smejkalova, T., Balik, A., Krausova, B., Kaniakova, M., Lichnerova, K., Cerny, J., Krusek, J., Dittert, I., et al. (2014). Structure, function, and pharmacology of NMDA receptor channels. *Physiol. Res.* 63.

## W

Wagner, W., Lippmann, K., Heisler, F.F., Gromova, K. V., Lombino, F.L., Roesler, M.K., Pechmann, Y., Hornig, S., Schweizer, M., Polo, S., et al. (2019). Myosin VI Drives Clathrin-Mediated AMPA Receptor Endocytosis to Facilitate Cerebellar Long-Term Depression. *Cell Rep.* 28, 11–20.e9.

Wiegert, J.S., and Oertner, T.G. (2013). Long-Term depression triggers the selective elimination of weakly integrated synapses. *Proc. Natl. Acad. Sci. U. S. A.* 110.

Wiegert, J.S., Pulin, M., Gee, C.E., and Oertner, T.G. (2018). The fate of hippocampal synapses depends on the sequence of plasticity-inducing events. *Elife* 7, 1–18.

Wiesel, T.N., and Hubel, D.H. (1965). Comparison of the effects of unilateral and bilateral eye closure on cortical unit responses in kittens. *J. Neurophysiol.* 28, 1029–1040.

de Wit, J., Sylwestrak, E., O’Sullivan, M.L., Otto, S., Tiglio, K., Savas, J.N., Yates, J.R., Comoletti, D., Taylor, P., and Ghosh, A. (2009). LRRTM2 Interacts with Neurexin1 and Regulates Excitatory Synapse Formation. *Neuron* 64, 799–806.

Woods, G.F., Oh, W.C., Boudewyn, L.C., Mikula, S.K., and Zito, K. (2011). Loss of PSD-95 enrichment is not a prerequisite for spine retraction. *J. Neurosci.* 31, 12129–12138.

Wu, Q., Sun, M., Bernard, L.P., and Zhang, H. (2017). Postsynaptic density 95 (PSD-95) serine 561 phosphorylation regulates a conformational switch and bidirectional dendritic spine structural plasticity. *J. Biol. Chem.* 292, 16150–16160.

Wu, X., Morishita, W.K., Riley, A.M., Hale, W.D., Südhof, T.C., and Malenka, R.C.

(2019). Neuroligin-1 Signaling Controls LTP and NMDA Receptors by Distinct Molecular Pathways. *Neuron* 102, 621–635.e3.

## X

Xiao, M.Y., Zhou, Q., and Nicoll, R.A. (2001). Metabotropic glutamate receptor activation causes a rapid redistribution of AMPA receptors. *Neuropharmacology* 41, 664–671.

Xu-Friedman, M.A., and Regehr, W.G. (2004). Structural Contributions to Short-Term Synaptic Plasticity. *Physiol. Rev.* 84, 69–85.

Xu, T., Yu, X., Perlik, A.J., Tobin, W.F., Zweig, J.A., Tennant, K., Jones, T., and Zuo, Y. (2009). Rapid formation and selective stabilization of synapses for enduring motor memories. *Nature* 462, 915–919.

## Y

Yamazaki, Y., Fujii, S., Kato, H., Ito, K.I., Nakamura, T., Miyakawa, H., and Kudo, Y. (2002). Changes in  $[Ca^{2+}]_i$  during adenosine triphosphate-induced synaptic plasticity in hippocampal CA1 neurons of the guinea pig. *Neurosci. Lett.* 324, 65–68.

Yan, D., and Tomita, S. (2012). Defined criteria for auxiliary subunits of glutamate receptors. *J. Physiol.* 590, 21–31.

Yang, G., Pan, F., and Gan, W.B. (2009). Stably maintained dendritic spines are associated with lifelong memories. *Nature* 462, 920–924.

Yang, Y., Ge, W., Chen, Y., Zhang, Z., Shen, W., Wu, C., Poo, M., and Duan, S. (2003). Contribution of astrocytes to hippocampal long-term potentiation through release of D-serine. *Proc. Natl. Acad. Sci. U. S. A.* 100, 15194–15199.

Yasuda, M., Nagappan-Chettiar, S., Johnson-Venkatesh, E.M., and Umemori, H. (2021). An activity-dependent determinant of synapse elimination in the mammalian brain. *Neuron* 1–17.

Yu, J., Rao, P., Clark, S., Mitra, J., Ha, T., and Gouaux, E. (2021). Hippocampal AMPA receptor assemblies and mechanism of allosteric inhibition. *Nature* 2021.

## Z

Zhang, Y., Cudmore, R.H., Lin, D.T., Linden, D.J., and Huganir, R.L. (2015). Visualization of NMDA receptor - Dependent AMPA receptor synaptic plasticity in vivo. *Nat. Neurosci.* 18, 402–409.

Zhou, Q., Homma, K.J., and Poo, M.M. (2004). Shrinkage of dendritic spines associated with long-term depression of hippocampal synapses. *Neuron* *44*, 749–757.

Zucker, R.S., and Regehr, W.G. (2002). Short-Term Synaptic Plasticity. *Annu. Rev. Physiol.* *64*, 355–405.

Zuo, Y., Lin, A., Chang, P., and Gan, W.B. (2005). Development of long-term dendritic spine stability in diverse regions of cerebral cortex. *Neuron* *46*, 181–189.